



Delft University of Technology

Valorization of Wood Biomass Fly Ash for the Development of Sustainable Low-carbon Cementitious Materials

Liang, X.

DOI

[10.4233/uuid:b17dda4d-a804-447c-9278-7b85026da167](https://doi.org/10.4233/uuid:b17dda4d-a804-447c-9278-7b85026da167)

Publication date

2024

Document Version

Final published version

Citation (APA)

Liang, X. (2024). *Valorization of Wood Biomass Fly Ash for the Development of Sustainable Low-carbon Cementitious Materials*. [Dissertation (TU Delft), Delft University of Technology].
<https://doi.org/10.4233/uuid:b17dda4d-a804-447c-9278-7b85026da167>

Important note

To cite this publication, please use the final published version (if applicable).

Please check the document version above.

Copyright

Other than for strictly personal use, it is not permitted to download, forward or distribute the text or part of it, without the consent of the author(s) and/or copyright holder(s), unless the work is under an open content license such as Creative Commons.

Takedown policy

Please contact us and provide details if you believe this document breaches copyrights.
We will remove access to the work immediately and investigate your claim.

Valorization of Wood Biomass Fly Ash for the Development of Sustainable Low-carbon Cementitious Materials



Xuhui Liang
梁旭辉

Valorization of Wood Biomass Fly Ash for the Development of Sustainable Low-carbon Cementitious Materials

Dissertation

For the purpose of obtaining the degree of doctor
at Delft University of Technology

by the authority of the Rector Magnificus Prof.dr.ir. T.H.J.J. van der Hagen
chair of the Board for Doctorates
to be defended publicly on
Thursday 05 December 2024 at 10:00 o'clock

By

Xuhui LIANG

Master of Science in Materials Science and Engineering
Chongqing University, China
Born in Sichuan Province, China

This dissertation has been approved by the promotores

Composition of the doctoral committee:

Rector Magnificus

Chairperson

Prof. dr. G. Ye

Delft University of Technology, promotor

Prof. dr. ir. H.E.J.G. Schlangen

Delft University of Technology, promotor

Independent Members:

Prof. dr. H.M. Jonkers

Delft University of Technology

Prof. dr. ir. J.M.C. Mol

Delft University of Technology

Prof. dr. M. Cyr

University of Toulouse, France

Prof. dr. Ö. Cizer

KU Leuven, Belgium

Dr. J. Visser

TNO



Keywords: wood biomass fly ash; cementitious materials; pretreatment; reaction kinetics; carbonation; microstructure; life cycle analysis

Printed by: Ipskamp, the Netherlands

Thesis format by: Xuhui Liang

Cover design: Xuhui Liang

Copyright © 2024 by Xuhui Liang

All rights reserved. No part of the material protected by this copyright notice may be reproduced or utilized in any form or by any means, electronic or mechanical, including photocopying, recording or by any information storage and retrieval system, without written consent from the author

- *To my family*

Contents

List of Abbreviations	V
Summary	VII
Samenvatting.....	IX
Chapter 1	
<i>Introduction</i>	1
1.1 Research background.....	1
1.2 Research goal and objectives.....	4
1.3 Research scope and strategy.....	4
1.4 Outline of this thesis	5
Chapter 2	
<i>Literature review on the valorization of WBFA for the development of cementitious materials</i>	7
2.1 Introduction.....	7
2.2 Fuels type, incineration techniques and ash collection.....	7
2.3 Characteristics of WBFA	8
2.3.1 <i>Physical properties</i>	9
2.3.2 <i>Chemical compositions</i>	10
2.3.3 <i>Mineral compositions</i>	13
2.4 Pretreatment of WBFA.....	15
2.5 Valorization of WBFA in cementitious materials	15
2.5.1 <i>Clinker production</i>	15
2.5.2 <i>Blended cement</i>	17
2.5.3 <i>Alkali-activated materials preparation</i>	22
2.6 WBFA classification towards cementitious materials development	24
2.7 Research gap and problem definition.....	26
2.8 Summary	27
Chapter 3	
<i>Characterization, pretreatment, and evaluation of wood biomass fly ash as a binder component</i>	29
3.1 Introduction.....	29
3.2 Materials and Methods.....	29
3.2.1 <i>Raw materials</i>	29
3.2.2 <i>BFA characterization and screen-out</i>	30
3.2.3 <i>Ash pretreatment</i>	34
3.2.4 <i>Dissolution test</i>	35
3.3 Results and discussion.....	35
3.3.1 <i>Pretreatment of WBFA1</i>	35
3.3.2 <i>Characteristics of treated WBFA1</i>	37
3.3.3 <i>Ash dissolution</i>	41

3.3.4	<i>Comments on the utilization approaches for treated WBFA1</i>	45
3.4	Conclusion	46
	Appendix	47

Chapter 4

Cement clinker-free binder: wood biomass fly ash-blast furnace slag binary material..... 49

4.1	Introduction	49
4.2	Materials and experiments	49
4.2.1	<i>Materials and mixtures</i>	49
4.2.2	<i>Experimental methods</i>	50
4.3	Results	53
4.3.1	<i>Heat evolution</i>	53
4.3.2	<i>Pore solution chemistry</i>	54
4.3.3	<i>Solid phases</i>	59
4.3.4	<i>Microstructure development</i>	62
4.3.5	<i>Compressive strength development</i>	66
4.4	Discussions	67
4.4.1	<i>Reaction kinetics of binary pastes</i>	67
4.4.2	<i>Thermodynamics modelling</i>	72
4.5	Conclusion	73
	Appendix	75

Chapter 5

Wood biomass fly ash as slag substitute in slag blended cement..... 77

5.1	Introduction	77
5.2	Materials and methods	77
5.2.1	<i>Materials</i>	77
5.2.2	<i>Experiments</i>	78
5.3	Results	79
5.3.1	<i>Heat evolution measured by isothermal calorimeter</i>	79
5.3.2	<i>Pore solutions</i>	81
5.3.3	<i>Solid phases</i>	85
5.3.4	<i>Microstructure analysis</i>	92
5.3.5	<i>Compressive strength</i>	96
5.4	Discussions	97
5.4.1	<i>Reaction contribution from WBFA</i>	97
5.4.2	<i>Phase evolution prediction of BFS blended cement containing WBFA</i>	98
5.5	Conclusions	101

Chapter 6

Carbonation of cementitious materials containing wood biomass fly ash 103

6.1	Introduction	103
6.2	Materials and experiments	103
6.2.1	<i>Materials and mixtures</i>	103

6.2.2	<i>Experimental methods</i>	104
6.3	Results	105
6.3.1	<i>Carbonation Rate</i>	105
6.3.2	<i>Phases alteration via carbonation</i>	107
6.3.3	<i>Microstructure alteration via carbonation</i>	115
6.3.4	<i>Compressive strength</i>	122
6.4	Discussions	123
6.4.1	<i>Hydrates vs. carbonation</i>	123
6.4.2	<i>Pore structure vs. carbonation</i>	125
6.5	Conclusions.....	126
	Appendix	128

Chapter 7

Utilization of wood biomass fly ash as a construction material and environmental assessment - Case studies in brick and cement production .. 131

7.1	Introduction.....	131
7.2	Products development and technical properties.....	132
7.2.1	<i>Materials and products development</i>	132
7.2.2	<i>Products testing methods</i>	133
7.2.3	<i>Technical properties of construction products</i>	134
7.3	Life cycle assessment (LCA)	137
7.3.1	<i>Goal and scope</i>	137
7.3.2	<i>Life cycle inventory (LCI)</i>	137
7.3.3	<i>Environmental cost indicator (ECI)</i>	139
7.4	Life cycle impact assessment	139
7.4.1	<i>Bio-ash brick</i>	139
7.4.2	<i>Bio-ash composite cement (BCC)</i>	143
7.5	Discussions	144
7.5.1	<i>Recommendations for improvement</i>	144
7.5.2	<i>Limitation of the LCA</i>	146
7.6	Conclusions.....	146
	Appendix	148

Chapter 8

Retrospection, conclusions, and prospects .. 153

8.1	Retrospection	153
8.2	Conclusions.....	154
8.3	Contributions of this thesis	156
8.4	Prospects	157

Reference .. 159

Acknowledgements .. 179

Curriculum Vitae .. 181

List of Abbreviations

AAMs	Alkali-activated materials
ADPE	Abiotic depletion potential-non fossil fuel
ADPFF	Abiotic depletion potential-fossil fuel
AP	Acidification potential
ASTM	American Society for Testing and Materials
BCC	Bio-ash composite cement
BFS	Blast furnace slag
BSE	Backscattered electron microscopy
CFA	Coal fly ash
C-S-H	Calcium-silicate-hydrate
DoH	Degree of hydration
DTG	Derivative thermogravimetry
ECI	Environmental cost indicator
EDS	Electron dispersive spectroscopy
EN	European Standards
EP	Eutrophication potential
ESI	Effective saturation indices
ESP	Electrostatic precipitators
FAETP	Freshwater Aquatic Eco-toxicity potential
FTIR	Fourier transform infrared spectroscopy
GEMs	Gibbs Energy Minimization Software
GWP	Global Warming potential
HTP	Human toxicity potential
LCA	Life cycle assessment
LCI	Life cycle inventory
ICP-OES	Inductively coupled plasma optical emission spectroscopy
LOI	Loss on ignition
LSF	Lime saturating factor
MAETP	Marine Aquatic Eco-toxicity potential
MIP	Mercury Intrusion Porosimetry

MS	Mass spectroscopy
ODP	Ozone layer Depletion potential
POCP	Photochemical Oxidation potential
PSD	Particle size distribution
RH	Relative humidity
SCM	Supplementary cementitious materials
SEM	Scanning electron microscope
TETP	Terrestrial Eco-toxicity potential
TGA	Thermogravimetric analysis
w/b	Water to binder ratio
WBFA	Wood biomass fly ash
XRF	X-ray fluorescence
XRD	X-ray diffraction

Summary

With growing concern for global warming, the electricity industry is actively promoting the transition from coal to renewable energy sources. Due to the carbon neutrality of wood biomass energy, it has become one of the most popular options of renewable energy sources. However, the by-products resulting from biomass combustion, particularly wood biomass fly ash (WBFA), have not received sufficient attention. Direct disposal of WBFA poses environmental threats and causes pollution. From the perspective of the construction industry, the energy transition has led to a scarcity of coal fly ash (CFA) that is intensively used as supplementary cementitious materials (SCMs) in construction industry. With the increasing demand for raw materials in construction industry, it is of great interest to explore whether WBFA can be integrated as a new material in construction industry. This motivates the initiative of this research, driven by significant industry demand.

This thesis aims to enlarge the utilization efficiency of WBFA by recirculating WBFA as a valuable mineral to develop sustainable low-carbon cementitious materials. Prior to the experiment, a literature review on the properties of WBFA and current WBFA utilization methodologies in cementitious materials are summarized. An application-oriented WBFA classification was proposed, providing a guideline for the utilization of WBFA in preparing cementitious materials.

For the experimental research, three types of WBFA were initially characterized and screened based on their physicochemical properties, i.e., the content of unfavoured metallic aluminum and reactive components. One type of WBFA with representative properties was selected as the most suitable candidate for further investigation. To remove the metallic aluminum in WBFA, a two-step pretreatment method is proposed. The feasibility of WBFA for binder formulation was then evaluated through dissolution tests.

Based on the characteristics of WBFA, two types of binders were proposed. In chapter 4, considering the high alkalinity of WBFA, WBFA was used to enhance the reaction of aluminosilicates. An innovative clinker-free binary binder with WBFA and blast furnace slag (BFS) was developed. The effects of different WBFA to BFS ratios on reaction kinetics, hydration products, and microstructure evolution were studied. Following this, WBFA was further used as a mineral additive for BFS replacement in BFS blended cement. The effects of WBFA on both BFS and cement reactions were comprehensively studied using different characterization techniques. These two chapters together provide new solutions for the valorization of WBFA in novel binder formulations.

The carbonation of WBFA-containing binders investigated in chapter 4 and 5 was studied in chapter 6. The carbonation kinetics of pastes were calculated based on the carbonation depth development. It was found that in WBFA-BFS binary pastes, mixture with 50% of WBFA and 50% of BFS showed the best carbonation resistance, although the carbonation coefficient was much larger than cement pastes. When WBFA was introduced in BFS blended cement, it was observed that there was a decreased carbonation resistance in pastes with more WBFA.

By analysing the microstructure evolution, it was concluded that pore connectivity played the key role in governing the carbonation process of pastes. Further grinding of WBFA to reduce its porous structure was recommended to reduce the pore connectivity and improve the carbonation resistance of pastes with WBFA.

The environmental impact evaluation is of great significance for waste utilization in the construction industry, as it can, to a certain extent, help quantify the sustainability of specific products. In chapter 7, bio-ash bricks and bio-ash composite cement were developed based on the mixtures studied in Chapters 4 and 5, respectively. A cradle-to-gate life cycle analysis (LCA) was conducted to evaluate the contribution of integrating WBFA for the production of these construction products. Possible improvements regarding further reducing the environmental impact of these products are discussed.

In summary, this thesis offers novel options for the utilization of WBFA in the construction sector as a binder component. Binary paste containing up to 70% WBFA demonstrates satisfactory mechanical properties for low-strength applications. In BFS-blended cement, substituting up to 30% of BFS with WBFA enhances early compressive strength, only a 7.67% reduction in compressive strength after 90 days. These findings indicate high utilization efficiency for WBFA. The investigations in the reaction kinetics and microstructure evolution of pastes with different WBFA to BFS ratios in the binders yield valuable insights into the function of WBFA in binder reaction. This knowledge can serve as a valuable reference for engineering practitioners seeking to customize the properties of these binders. The development of building products such as bio-ash bricks and bio-ash cement exemplifies the conversion of WBFA into construction materials. This emphasizes the notable ecological advantages of WBFA as a resource for the construction sector, highlighting the academic and industrial interests in utilizing WBFA for the development of sustainable low-carbon cementitious materials.

Samenvatting

Vanwege de toenemende bezorgdheid over klimaatverandering, stimuleert de elektriciteitssector actief de overgang van kolen naar hernieuwbare energiebronnen. Dankzij de koolstof neutrale aard van houtbiomassa-energie is het een van de populairste opties voor hernieuwbare energie geworden. Echter hebben de bijproducten die vrijkomen bij biomassaverbranding, met name houtbiomassa-vliegas (WBFA), nog niet voldoende aandacht gekregen, hoewel de directe afvoer van WBFA milieuproblemen oplevert en vervuiling veroorzaakt. Vanuit het perspectief van de bouwsector heeft de energietransitie geleid tot een schaarse aan kolenvliegas (CFA), dat intensief wordt gebruikt als cementachtig toeslagmateriaal (SCMs) in de bouwsector. Met de toenemende vraag naar grondstoffen in de bouwsector is het van groot belang om te onderzoeken of WBFA kan worden geïntegreerd als nieuw SCM in de bouwsector. Dit motiveert ook het initiatief van dit onderzoek, gedreven door een aanzienlijke vraag vanuit de industrie.

Dit proefschrift heeft als doel de toepassingsefficiëntie van WBFA te vergroten door WBFA toe te passen als een waardevol mineraal om zo duurzame, koolstofarme cementachtige materialen te ontwikkelen. Voorafgaand aan het experiment is een literatuuronderzoek uitgevoerd naar de eigenschappen van WBFA en de huidige methoden voor de inzet van WBFA in cementachtige materialen. Een toepassingsgerichte classificatie van WBFA werd voorgesteld, die richtlijnen biedt voor het gebruik van WBFA bij de bereiding van cementachtige materialen.

Voor het experimentele onderzoek werden aanvankelijk drie soorten WBFA gekarakteriseerd en geselecteerd op basis van hun fysisch-chemische eigenschappen, namelijk het gehalte aan ongewenst metaalaluminium en reactieve componenten. Eén type WBFA met representatieve eigenschappen werd geselecteerd als de meest geschikte kandidaat voor verder onderzoek. Om het metaalaluminium in WBFA te verwijderen, wordt een twee-staps voorbehandelmethode voorgesteld. De toepasbaarheid van WBFA in bindmiddelen werd vervolgens geëvalueerd door middel van oplosbaarheid experimenten.

Op basis van de eigenschappen van WBFA werden twee soorten bindmiddelen voorgesteld. In hoofdstuk 4, rekening houdend met de hoge alkaliteit van WBFA, werd WBFA toegepast om de reactie van aluminosilicaat te verbeteren. Een innovatief klinkervrij binair bindmiddel met WBFA en hoogoven Slak (BFS) werd ontwikkeld. De effecten van verschillende WBFA- tot BFS-verhoudingen op de reactiekinetica, de hydratatieproducten en de microstructuurontwikkeling werden bestudeerd. Vervolgens werd WBFA verder toegepast als mineraal toeslagmateriaal ter vervanging van BFS in BFS-gebonden cement. De effecten van WBFA op zowel BFS- als cementreacties werden uitgebreid bestudeerd met verschillende karakteriseringstechnieken. Deze twee hoofdstukken bieden samen nieuwe oplossingen voor de valorisatie van WBFA in nieuwe bindmiddelen.

De carbonatie van WBFA-bevattende bindmiddelen die in hoofdstuk 4 en 5 zijn onderzocht, werd bestudeerd in hoofdstuk 6. De carbonatie kinetica van pasta's werden

berekend op basis van de ontwikkeling van de carbonatiediepte. Het werd vastgesteld dat in WBFA-BFS-binaire pasta's de mengsels met 50% WBFA en 50% BFS de beste carbonatieweerstand vertoonden, hoewel de carbonatiecoëfficiënt veel groter was dan die van cementpasta's. Wanneer WBFA werd geïntroduceerd in BFS-gebonden cement, werd geobserveerd dat er een verlaagde carbonatieweerstand was in pasta's met een hogere hoeveelheid WBFA. Door de microstructuurontwikkeling te analyseren, werd geconcludeerd dat porieconnectiviteit een bepalende rol speelde bij het bepalen van het carbonatieproces van de pasta's. Het verder fijnmalen van WBFA om de poreuze structuur te verlagen werd aanbevolen, om zo de porieconnectiviteit te verminderen en de carbonatieweerstand van pasta's met WBFA te verbeteren.

De beoordeling van de milieu-impact is van groot belang voor het verwerken van afvalstromen in de bouwsector, aangezien het tot op zekere hoogte kan helpen de duurzaamheid van specifieke producten te kwantificeren. In hoofdstuk 7 werden bio-as betonstenen en bio-as composietcement ontwikkeld op basis van de mengsels die in hoofdstukken 4 en 5 zijn bestudeerd. Een cradle-to-gate levenscyclusanalyse (LCA) werd uitgevoerd om de invloed van de integratie van WBFA voor de productie van deze bouwproducten te evalueren. Mogelijke verbeteringen om de milieu-impact van deze producten verder te verminderen worden behandeld.

Kort samengevat biedt dit proefschrift nieuwe opties voor de inzet van WBFA in de bouwsector als bindmiddelcomponent. Binaire pasta's die tot 70% WBFA bevatten, tonen gunstige mechanische eigenschappen voor lage sterkte toepassingen. In BFS-gebonden cement verbetert het vervangen van tot 30% van BFS door WBFA de vroege druksterkte, terwijl de druksterkte na 90 dagen slechts met 7,67% afneemt. Deze bevindingen wijzen op een hoge toepassingsefficiëntie voor WBFA. Het onderzoek naar de reactiekinetica en microstructuurontwikkeling van pasta's met verschillende WBFA- en BFS-verhoudingen biedt waardevolle inzichten in de rol van WBFA in de bindmiddelreactie. Deze kennis kan dienen als een waardevolle referentie voor ingenieurs die de eigenschappen van deze bindmiddelen willen aanpassen. De ontwikkeling van bouwproducten zoals bio-as bakstenen en bio-as cement is een voorbeeld van de toepassing van WBFA in bouwmateriaal. Dit benadrukt de aanzienlijke ecologische voordelen van WBFA als grondstof voor de bouwsector en benadrukt de academische en industriële belangen bij het gebruik van WBFA voor de ontwikkeling van duurzame, koolstofarme cementachtige materialen.

Chapter 1

Introduction

1.1 Research background

Global warming is to date one of the most pressing challenges worldwide. This is primarily due to the substantial emissions of greenhouse gases (GHG), especially CO₂, with the escalating industrial production [1]. Statistical results show that approximately 30-40% of CO₂ emissions originate from the energy sector (referring to Figure 1.1). This should be predominantly attributed to the combustion of fossil fuels, particularly coal, for electricity generation [2]. Efforts aimed at reducing carbon emissions in the energy sector have led to a shift from fossil fuels to renewable energy sources. An illustrative instance is the European energy industry, which launched the coal phase-out initiative in 2015, proposing the closure of all coal-fired electricity plants by 2030 while promoting the development of renewable energy sources [3,4].

Similar strategies have been adopted in the Netherlands, where there has been a notable increase in the development of renewable energy sources. As depicted in Figure 1.2, the percentages of renewable energy sources have progressively risen in recent decades in the Netherlands, with biomass energy accounting for the largest share. This trend is echoed in other countries, where biomass energy holds a significant position and is widely utilized [5].

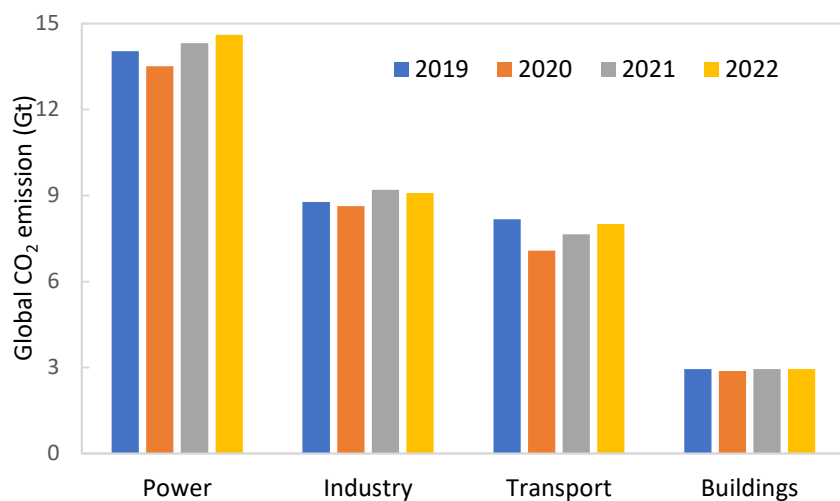


Figure 1.1 Global CO₂ emissions by sector from 2019 to 2022 (adapted from [2])

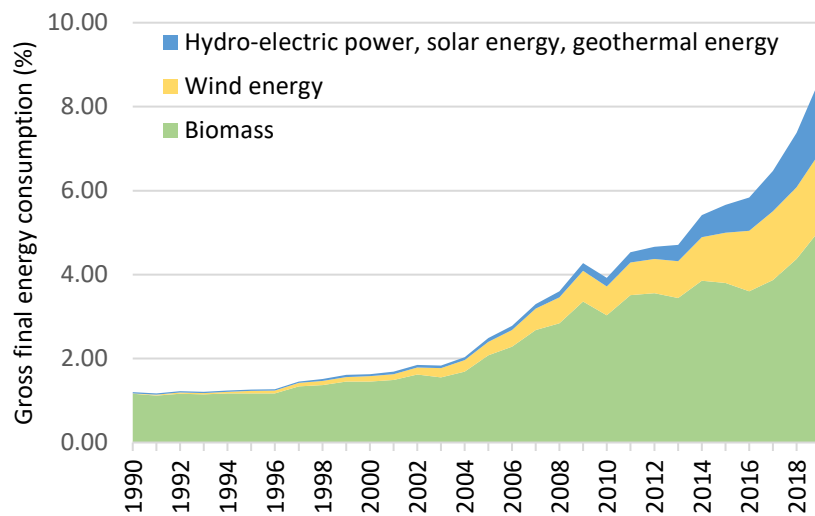


Figure 1.2 Renewable energy consumption and shares in the Netherlands (retrieved from CBS [6], with respect to the total energy from both renewable and non-renewable energy)

With the wide sources of biomass in the energy sector, wood biomass has emerged as the primary source of biomass energy and has been largely promoted in the last decades [7]. One of the main advantages of wood biomass energy is its carbon-neutral characteristic. It is recognized that with sustainable forest management, energy produced from wood biomass can achieve net-zero carbon emissions, as carbon circulates within the wood growth through the photosynthesis process [8]. In addition, biomass combustion techniques have been well developed, enabling their integration into existing coal-fired plants after proper retrofitting. This facilitates a seamless transition for the energy industry towards bioenergy orientation without extra costs and overhauls, which is a privilege from an industrial perspective. Based on these advantages, a prospective development of the wood biomass energy industry can be anticipated. An estimation of wood biomass-derived energy can reach about 18% of total energy consumption by 2050 [9].

While the carbon neutrality of wood biomass energy greatly benefits the decarbonization of energy sectors, there are critical issues worth attention, particularly in the post-biomass electricity production stage. Similar to coal combustion, it is inevitable for the generation of by-products after biomass incineration. As illustrated in Figure 1.3, two types of by-products, namely bottom ash and fly ash, are generated. The weight proportions between biomass bottom ash and fly ash vary depending on the incineration techniques and feedstocks. For example, grate boilers tend to yield larger amounts of biomass bottom ash than fly ash, while fluidized bed incineration techniques lead to higher shares of biomass fly ash. In the Netherlands, the issues with fly ash are much more severe, as it constitutes the main by-product in biomass energy production. The annual biomass fly ash generation is reported to be 146,000 tons in 2018, compared to 23,000 tons of bottom ash [10]. Currently, most of the biomass fly ash is under improper management. The landfilling or disposal of biomass fly ash becomes problematic as this will lead to secondary pollution of the environment. Given the rapid development of the biomass energy industry, a surge in biomass fly ash generation is anticipated. Thus, there is an urgent need to implement effective utilization methods for biomass fly ash to integrate the sustainability of biomass energy.

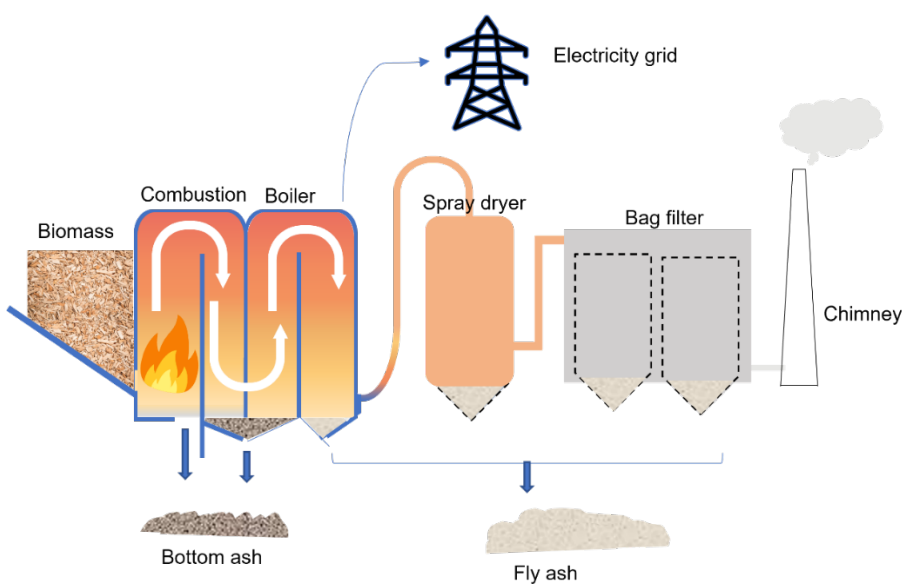


Figure 1.3 Schematic figure of biomass combustion and ash collection

The construction industry has become a preferred destination for a wide range of industrial by-products recycling [11–15], mainly due to its imperative to reduce carbon footprints and the high demand for raw materials. For now, the construction sector accounts for about 8–10% of global CO₂ emissions, primarily due to the carbon-intensive production process of Portland cement, which involves limestone decomposition, clinkering at high temperatures, and grinding [16]. Thus, there are considerable interests in scientific research and engineering practices to diminish the carbon footprint in the construction sector. Viable solutions, such as the partial substitution of cement clinker with industrial by-products, often referred to as secondary or supplementary cementitious materials (SCMs), and the formulation of new alternative binders, have been proposed in recent decades, integrating industrial by-products to fulfil the raw material needs of the construction sector. Previous successes in utilizing blast furnace slag and pulverized coal fly ash have established these by-products as valuable mineral sources [17]. However, given the increasing demand for raw materials and the depletion of those ‘well-studied’ minerals, there is a pressing need to explore mineral sources from other industries. Wood biomass fly ash, on the other hand, emerges as a potential candidate in this regard.

As of now, the use of wood biomass fly ash is in its infancy in both research and industrial practice, which is mainly because of the less attention it has received. Besides, it is reported that in most cases, wood biomass fly ash shows limited pozzolanic reactivity [18–20], rendering it less favourable for direct use as SCMs to replace cement. The negative impact of wood biomass fly ash on the performance of cementitious materials, such as reduced strength and weakened durability [21–23], diminishes its attractiveness for integration into the construction industry. To effectively utilize wood biomass fly ash in cementitious materials, further investigations into alternative solutions are urgently needed. However, there is currently a lack of systematic research in this regard.

1.2 Research goal and objectives

The aim of this research is to propose innovative approaches for valorizing wood biomass fly ash (WBFA) as a mineral resource in cementitious materials, thereby enhancing its utilization efficiency as a value-added mineral. To accomplish this goal, the following objectives should be achieved:

- To study the properties of WBFA, further evaluate the feasibility and potential of WBFA in developing cementitious materials.
- To develop low-carbon cementitious materials with WBFA, further understand the roles of wood biomass fly ash in the reaction kinetics and microstructure evolution of cementitious materials.
- To extend the understanding of WBFA-containing binders from a durability perspective. Since carbonation is an inevitable process during the service life of binders, the effects of carbonation on the properties of binders containing WBFA are specifically investigated.
- To evaluate the environmental impact of construction products developed by the WBFA-containing binders, further compare them with the commercially available products.

1.3 Research scope and strategy

Firstly, a literature review on WBFA in regards to its properties and up-to-date utilization approaches for the development of cementitious materials are conducted. Based on these knowledge, the research gaps are identified accordingly.

Three types of WBFA are initially collected and characterized. Following an assessment of their physicochemical properties, one specific type of WBFA, characterized with representative chemical and mineral compositions, and displaying the most promising potential, was selected for an in-depth study throughout this thesis.

Raw materials include WBFA, blast furnace slag (BFS), and Portland cement for binder development. The research is conducted at the paste level to facilitate an understanding of hydration kinetics and microstructure characterization. The effects of WBFA on hydration and microstructure evolution are comprehensively studied using multiple experimental techniques such as X-ray diffraction (XRD), mercury intrusion porosimetry (MIP), backscattered electron microscopy (BSE) etc. Based on the experimental results, the reaction kinetics of binders is calculated with the help of empirical equations. The phase evolutions during the reaction process are further calculated based on thermodynamic modelling, enabling a comprehensive understanding of the reaction mechanisms of these binders.

Accelerated carbonation with a CO₂ concentration of 3% and 20 °C, following the guidelines of EN 12390-12 [24], was conducted on the carbonation research. The research is conducted at the paste level to better compare the results of the carbonated sample with pastes hydrated for 28 days.

Based on the properties of the binders investigated, an upscale for product manufacturing is finally conducted. A cradle-to-gate life cycle analysis is conducted,

comparing market-available products with those produced using the studied binders in this thesis.

1.4 Outline of this thesis

The thesis comprises eight chapters in total and can be divided into five parts, as outlined in Figure 1.4.

The first two chapters provide the background information for this thesis. Specifically, Chapter 1 presents the research motivation, objectives, and scopes to convey the purpose, focus, and structure of the thesis. Chapter 2 provides a literature review of the most up-to-date research regarding the characteristics of WBFA and its application in the development of cementitious materials.

The second part is Chapter 3, which investigates the characteristics of wood biomass fly ash, pretreatment, and evaluating the potential to be used as a binder component. This serves as the fundamental basis for further studies in developing cementitious materials.

The third part includes Chapters 4 to 6, which are mainly focused on the binder formulation and extending the knowledge of cementitious materials in the carbonation aspect.

In Chapter 4, a clinker-free binary binder is formulated with wood biomass fly ash and blast furnace slag. The reaction mechanism, microstructure evolution, and mechanical properties of binders are comprehensively investigated, enabling an understanding of how wood biomass fly ash contributes to the reaction, providing suggestive information for mixture formulation.

Chapter 5 investigates the wood biomass fly ash in the blast furnace slag blended cement pastes as slag substitution. The experimental research covers reaction kinetics, microstructure development, and mechanical properties.

In the context of the inevitable carbonation process during the service life of materials, Chapter 6 studies the carbonation behaviour of the WBFA-containing cementitious materials from Chapters 4 and 5. The carbonation depth and strength evolution are measured, and their correlation to the microstructure alteration after carbonation is discussed.

The fourth part is Chapter 7, which quantifies the environmental benefits of utilizing wood biomass fly ash as construction materials by LCA. The mixtures studied in previous chapters are upscaled to mortars so as to prepare construction products. A cradle-to-gate LCA is conducted to compare these products with conventional products, highlighting the environmental benefits of the construction products with the integration of wood biomass fly ash.

The last part involves Chapter 8, which draws the conclusions and prospects of this work. Recommendations on the valorization of wood biomass fly ash in industrial applications are given.

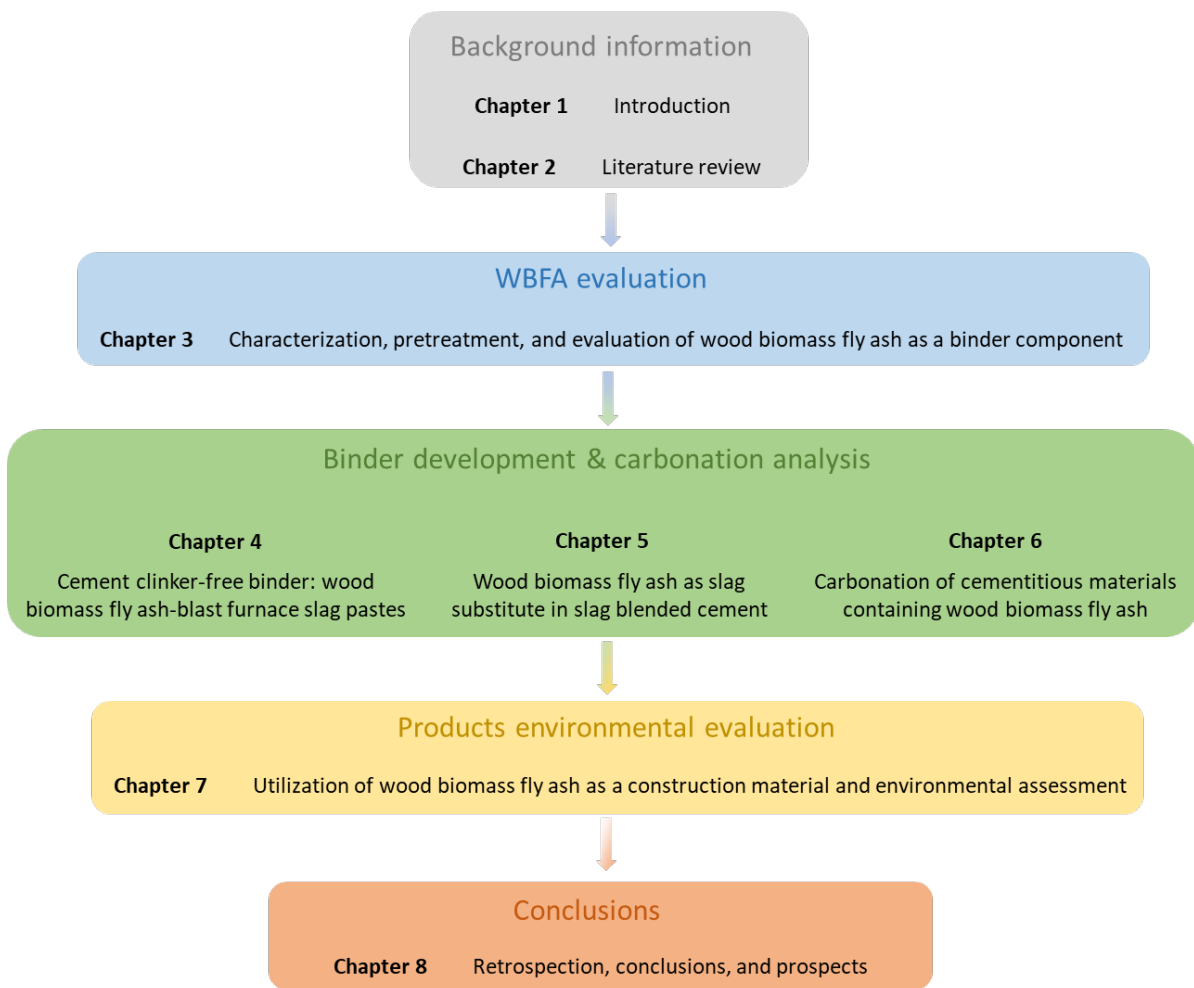


Figure 1.4 Outline of this thesis

Chapter 2

Literature review on the valorization of WBFA for the development of cementitious materials

2.1 Introduction

Chapter 1 clarifies the significant challenges and urgency of the management of wood biomass fly ash (WBFA). Additionally, the valorization of WBFA in construction material production holds substantial advantages due to the immense demand for raw materials in the construction sector, enabling significant ash consumption. This chapter aims to provide a comprehensive literature review of WBFA, with a specific focus on its physicochemical properties, pretreatment, and functional role in developing cementitious materials. This work serves as a foundational step to highlight the advancements made in the understanding of WBFA and to identify existing research gaps that warrant further investigation.

2.2 Fuels type, incineration techniques and ash collection

The variable properties of WBFA are dependent on multiple factors, including fuel feedstocks, incineration techniques, and ash collection methods [25]. This section provides information on these three aspects, associating these factors with the properties of WBFA. This information can facilitate the understanding of WBFA generation and how these factors can affect its valorization for developing cementitious materials.

The sources of wood biomass can be one of the main factors affecting the properties of WBFA, particularly in terms of chemical composition. For instance, WBFA derived from poplar and eucalyptus was normally reported to contain a high amount of calcium, while WBFA from spruce wood and wood residuals was found to contain a higher proportion of silica [26,27]. Vassilev et al. [27] compared the chemical compositions of wood ash from 28 types of wood resources. Despite the large variations in wood biomass sources, a general trend in element enrichment follows the orders: $\text{CaO} > \text{SiO}_2 > \text{K}_2\text{O} > \text{MgO} > \text{Al}_2\text{O}_3 > \text{P}_2\text{O}_5$. Still, conflicting reports on element distribution can be found in different research studies, indicating the diversity of wood biomass sources contributing to the complexity of WBFA chemical compositions.

In addition to the sources of wood biomass, combustion techniques can also influence the properties of WBFA. To date, there are mainly three types of incinerators used in electricity production, as summarized below:

- Grate furnace: This is one of the most commonly used combustors for biomass energy generation. It is feasible for small-scale biomass energy plants, showing high adaptability to a variety of biomass fuels in terms of size and moisture contents [28]. However, this combustion technique shows low burning efficiency, thus ashes generated from the grate furnace comes with high carbon contents [29]. In the context of by-products produced, bottom ash comprises a substantial portion,

ranging from 60% to 90% of the total weight fraction, while fly ash constitutes the minor by-products in this combustion technique [30].

- Fluidized bed incinerator: Compared with the grate furnace, the fluidized bed incinerator shows the advantage of high burning efficiency. As a result, ashes from the fluidized bed incinerator typically tend to have lower carbon contents in comparison to those from grate furnaces. In this type of combustor, fly ash becomes the main residual, in contrast to the dominance of bottom ash in a grate furnace [31,32]. Moreover, the fluidized bed incinerator is considered a more environmentally friendly option for biomass combustion compared to the grate furnace [33]. Therefore, the fluidized bed incinerator has become the more prevalent option for the newly developed biomass energy plants.
- Pulverized firing system: By pulverizing fuels into powders (typically with a size smaller than 0.1 mm [28]), this combustion method shows the advantages of having the highest burning efficiency among the three techniques. However, it is not applicable for the direct use of wood biomass as the main fuel, due to the challenges associated with fuel preparation and the potential corrosion of the combustor by inorganic salts from wood biomass [34,35]. Pulverized firing is typically used for the co-combustion process, where large proportions of coal are combusted alongside additional wood biomass (<20% wt.). The co-fired fly ash from a pulverized firing system is within the scope of fly ash used for concrete, with great similarity to coal fly ash [36]. Consequently, it is not further discussed in the following review.

During biomass combustion, fly ash particles are carried by the flue gas through ash collection devices before being released into the air, as depicted in Figure 1.3. Common devices for collecting WBFA include cyclones, bag filters, and electrostatic precipitators (ESP) [28]. Different ash collection methods initially determine the particle size of the WBFA. Among these systems, cyclones are normally used as the first step for ash filtering, and are reported to have the lowest ash collection capacity among the three [37]. WBFA collected from cyclones mostly consists of coarse fly ash, while WBFA collected from bag filters and ESP tends to have a relatively smaller particle size [38]. Additionally, the ash collection methods affect the carbon content. Since unburnt carbon normally presents in lightweights with large-size particles, WBFA with larger particle sizes is more likely to contain higher amounts of unburnt carbon. Cyclone WBFA is, therefore, observed to have higher carbon contents than those collected from ESP and bag filters [39].

2.3 Characteristics of WBFA

Despite the complicated influencing factors on the physicochemical properties of WBFA, as discussed in earlier sections, it remains feasible to deduce these properties from the available literature. Summarizing the physicochemical properties of WBFA is advantageous for better ash classification, which, in turn, aids in proposing a systematic valorization approach for WBFA in the development of cementitious materials.

2.3.1 Physical properties

The physical properties of WBFA include its particle size, morphology, texture, etc. The colour of WBFA can be an indicator of unburnt carbon content, as it turns darker with an increase in unburnt carbon contents. Relating the appearance of WBFA to the combustion techniques, it is normally reported that WBFA from a fluidized bed tends to show a lighter colour compared with the ones from grate [39], due to the normally higher contents of unburnt carbon in grate-fired WBFA.

The particle size of WBFA is largely dependent on the ash collection techniques, as previously illustrated in Section 2.2. Although the particle size of WBFA largely varied case by case, most of the particles maintain sizes within 300 μm [38,40,41], assuring the feasibility of WBFA being used as a binder component for developing cementitious materials. Figure 2.1 shows the representative scanning electron microscope (SEM) image of WBFA. Unlike coal fly ash (CFA) that is mostly spherical in shape, most of the WBFA particles are angular, with only a small fraction being spherical. This distinction arises from the lower burning temperature of wood biomass (normally below 1000 $^{\circ}\text{C}$) compared to coal combustion (above 1200 $^{\circ}\text{C}$). The low combustion temperature of wood biomass is less effective in melting the solids and subsequent condensation into spheres [42]. The lignocellulosic nature of wood biomass contributes to the formation of fibrous particles with large porous structures [43]. The heterogeneity and porous structure of WBFA particles lead to large variations in density and specific surface area ranges, with a range of 2.20-2.70 g/cm^3 [23,44] and 8-40 cm^2/g [41], respectively.

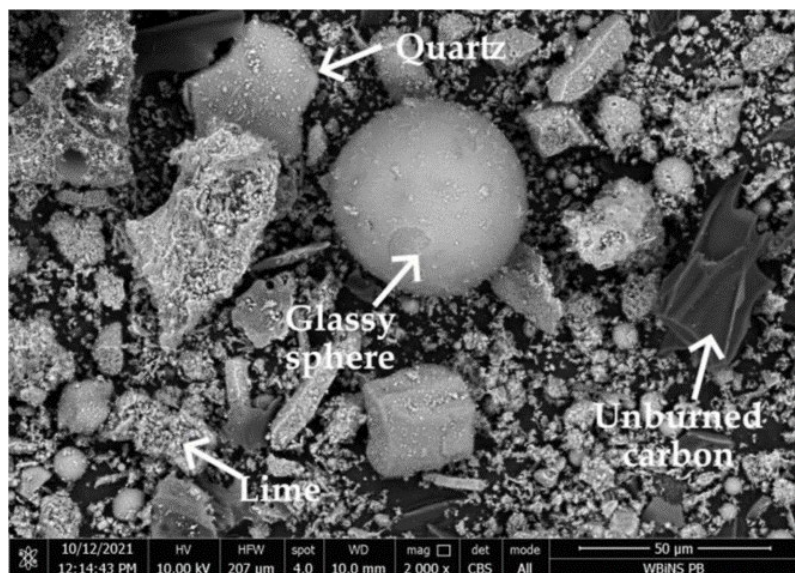


Figure 2.1 Morphology of WBFA determined by SEM (picture from [45])

2.3.2 Chemical compositions

2.3.2.1 Major elements

To date, the supply of forest residues (e.g., barks and branches), waste woods (e.g., discarded furniture and demolished wood constructions), as well as wood-based by-products from the pulp and paper industry, has become the main stream for wood biomass energy [46]. Thus, the diversified feedstocks of wood biomass contribute significantly to the considerable variation in the chemical compositions of the WBFA. Figure 2.2 presents the boxplots of the chemical compositions of WBFA from the literatures including 97 types of WBFA. Although wide variations are reported for these elements, a general trend for the major elements follows the order: $\text{CaO} > \text{SiO}_2 > \text{K}_2\text{O} > \text{MgO} \approx \text{Al}_2\text{O}_3 \approx \text{SO}_3 \approx \text{P}_2\text{O}_5 \approx \text{Fe}_2\text{O}_3$.

Despite coal being considered the fossilized form of biomass, this biological relationship between these two fuels does not translate into similarity in their ashes regarding chemical compositions. It is well known that CFA in cementitious materials is mainly rich in aluminosilicates. Even for high-calcium CFA, the sum of silica, alumina, and iron oxide is normally greater than 50% of the total weight [47]. Comparatively, as shown in Figure 2.2, WBFA contains a high amount of calcium and magnesium while having a relatively low content of aluminosilicates. The medium values of silica and alumina in WBFA are only 19.30% and 3.74%, respectively. This information suggests the possible latent hydraulic properties and low pozzolanic reactivity of WBFA. However, the high availability of calcium and magnesium also raises concerns about the cracking potential of cementitious materials if they are in the form of free lime or free MgO .

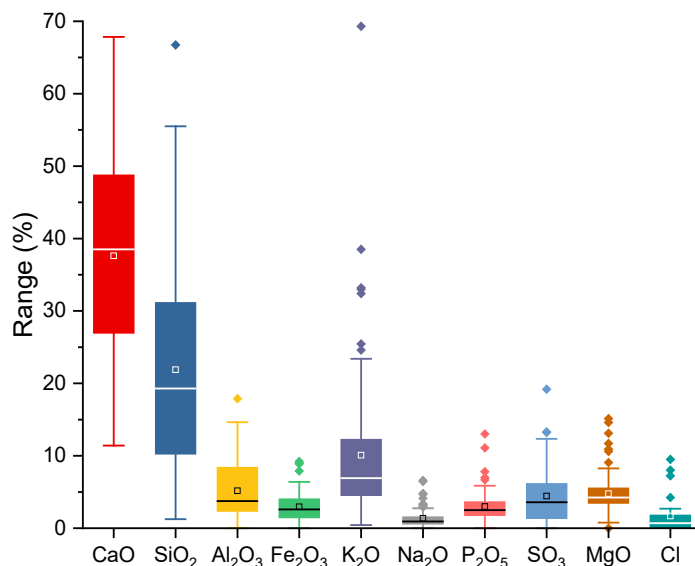


Figure 2.2 Boxplots of chemical compositions of 97 types of WBFA with data collected from literature [20–23,26,39,40,44,45,48–87]

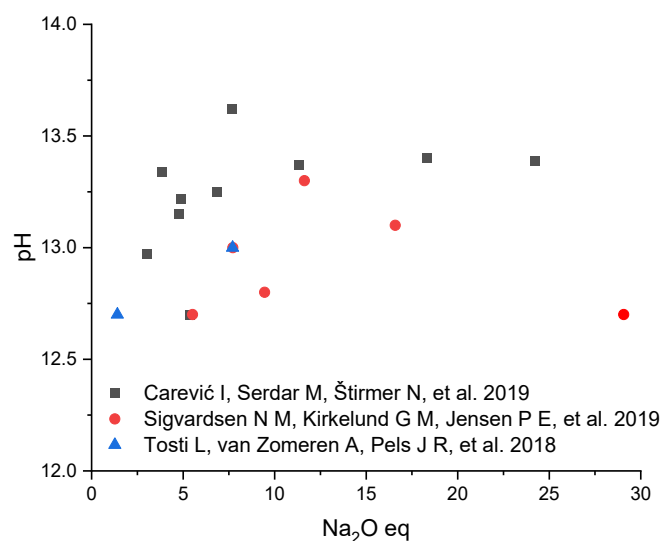


Figure 2.3 pH values of WBFA vs. their equivalent alkalis content
(data collected from [51,68,76], equivalent alkalis content = Na₂O wt.% + 0.658 K₂O wt.%)

Due to its high alkali content, WBFA is normally reported to be alkaline in nature, with a pH value ranging from 9 to 13.5 [88]. However, when measuring the pH value of WBFA, different water-to-ash ratios are normally employed in various studies. This renders it inappropriate to directly compare the pH values of WBFA across various studies. Figure 2.3 plots the measured pH values of WBFA from three research articles, along with their corresponding equivalent alkali contents. It is interesting to note that the pH values and equivalent alkali content in WBFA are not linearly correlated; WBFA with higher alkali contents may potentially display lower pH values. This phenomenon may be attributed to the presence of alkalis in the form of insoluble salts or in amorphous phases that are less susceptible to dissolve in water. Additionally, the elevated pH values in WBFA can also be influenced by the presence of free lime in the ashes, increasing the complexity of relating the alkalinity of WBFA to their chemical compositions.

Chloride is a potential threat to steel bar corrosion in reinforced concrete. Hence, the chloride content in cementitious materials must be strictly controlled. However, in WBFA, chloride content is typically reported to be high due to the wood feedstock. As indicated in Figure 2.2, the median chloride content is 0.70%, with the highest content reaching about 9.50%, which is much larger than the required maximum chloride content (0.40%) in cementitious materials [89]. This elevated chloride content would present a limiting factor for the use of WBFA in structural concrete.

To assimilate the chemical compositions of WBFA into cementitious materials, the classical normalized CaO-SiO₂-Al₂O₃ ternary diagram is employed to compare the composition of 97 types of WBFA (illustrated as black dots) with conventional cementitious materials, including Portland cement, BFS, class C (C) and class F (F) CFA, and natural pozzolans, as shown in Figure 2.4. The distribution of WBFA in the diagram is identical to the results found by Carević et al. [51]. It is evident that the representative area for WBFA covers a significant expanse, implying its inherent heterogeneity in chemical compositions. In addition, there are observable overlaps between WBFA and both Portland cement and BFS. This suggests that WBFA may possess latent hydraulic properties and possibly limited pozzolanic properties.

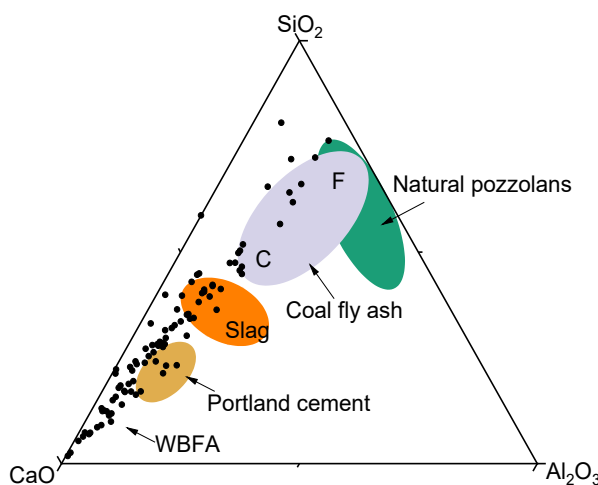


Figure 2.4 CaO-SiO₂-Al₂O₃ ternary diagram of WBFA (data collected from [21–23,39,40,44,45,48–62,64–68,70–87,90]) with comparison of conventional cementitious materials [91]

In summary, WBFA exhibits distinct major chemical compositions from CFA. It is, therefore, not applicable to directly adopt the valorization methodology of CFA in cementitious materials. Instead, new strategies are needed for the valorization of WBFA.

2.3.2.2 Heavy metals

The heavy metals in WBFA are largely influenced by the types and sources of wood biomass. As wood biomass grows, it absorbs heavy metals from the soil, which subsequently remain in the WBFA following wood combustion. In addition, heavy metals can also originate during the service life of wood. Demolition wood, for instance, is reported to contain high amounts of Pb and Cd due to its coating with paints [85,92].

Table 2.1 provides a concise overview of the findings from several studies regarding the measurement of heavy metals in WBFA. While the leaching results may vary depending on the experimental conditions and deviations in wood biomass, Cr, Cd, Pb, and Zn were consistently identified as the most commonly reported heavy metals in WBFA. It is essential to note that the evaluation criteria for heavy metals also differ in different countries. Currently, there is a lack of standardized requirements to evaluate the hazardous leaching potential of WBFA as a construction material. Nevertheless, it is encouraging that several studies have addressed the positive outcomes of using WBFA in cementitious materials in relation to heavy metal leaching [39,76,93,94]. This is because, on the one hand, the heavy metal leaching potential decreases with aging as a result of the formation of new mineral phases that reduce the mobility of heavy metals [95]. On the other hand, the implementation of WBFA in cementitious materials can significantly immobilize heavy metals through hydration products and a condensed microstructure [96]. Consequently, the monolithic leaching of cementitious materials containing WBFA has a limited leaching potential [76,94]. As such, further highlighting the use of WBFA in cementitious materials is advantageous from an environmental perspective.

Table 2.1 Main conclusions about heavy metals from WBFA

Ref	Measured heavy metals	Employed standards	Heavy metals beyond limit	Results remarks
[38]	Ti, Pb, Cr, Ni, Cd, As, Hg	Fertilizers Regulation Act in Japan	None	The heavy metal levels in WBFA met the regulatory standard, satisfying the requirements for fertilizer production
[39]	Sb, As, Ba, Cd, Cr, Hg, Pb, Mo, Ni, Se, Zn	Measured according to EN 12457; Evaluation based on SQD	Cr, Pb	Cannot be used for construction material due to the exceeded upper limits for Cr and Pb
[51]	Zn, Cd, Cr, Ni, Pb, Mn, Co, Ba, Bi, Sr, Cu, Hg	Measured according to EN ISO 16968:2015 and ASTM D 6722-11; Evaluation based on European Commission: Heavy metals and organic compounds from wastes used as organic fertilisers	Zn, Ni, Cd, Pb	The leaching of Cd surpassed the maximum allowable value in all 10 categories of WBFA.
[94]	Cd, Cr, Cu, Ni, Pb, Zn	Measured according to NEN 7345; Evaluation based on SQD	None	WBFA blended with cement showed good environmental stability
[95]	Cd, Cr, Cu, Ni, Pb, Zn	US EPA 3015A	n/a	Carbonation and hydration processes can reduce the leaching of heavy metals in WBFA

2.3.3 Mineral compositions

The mineral compositions in WBFA are closely relevant to its chemical compositions. Therefore, it can be anticipated that the major mineral phases are rich in calcium and alkalis, given the high content of these elements in WBFA, as indicated in Figure 2.2. Vassilev et al. [97] have provided a comprehensive list of minerals reported in biomass ash. However, the data encompasses a broad range of biomass sources without further distinguishing WBFA.

In light of the complexity of mineral compositions in WBFA due to the variation of wood sources as well as the limited availability of quantitative phase analysis in WBFA, it is unjustified to compare the abundance of minerals in WBFA. Nevertheless, a frequency analysis of different mineral phases reported in WBFA was conducted to better specify the most likely present mineral in WBFA. This was conducted by analysing the mineral phases in 70 types of WBFA from 27 research papers. The frequency was calculated according to Equation 2.1,

$$M_i(\%) = \frac{\text{Times of mineral } i \text{ being reported}}{\text{Numbers of WBFA samples}} \times 100\% \quad (2.1)$$

where M_i is the reported frequency of mineral phase i , and the numbers of WBFA samples are 70, which is collected from 27 research papers. The reporting frequencies of the prevalent phases in WBFA are presented in Figure 2.5.

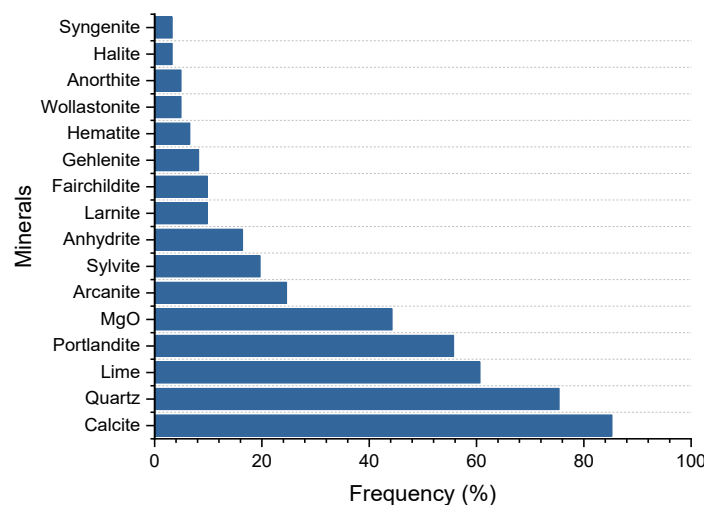


Figure 2.5 Minerals in WBFA reported from literature and their reported frequency (data collected from [20,22,39,45,48,50–55,57,59,60,63–65,67,68,72,74,78,81,83,86,87,98])

It is evident that calcium-bearing phases are frequently reported in WBFA, with calcite, portlandite, and lime being the most commonly observed. Additionally, quartz is the primary silicon crystalline phase in WBFA. Due to the abundance of sulfate, potassium, and chloride, minerals such as sylvite, anhydrite, and arcane are also commonly noted in the literature [68,74,87]. These phases contribute to the primary crystalline minerals in WBFA.

In addition to crystalline phases, the amorphous phase is another important component in WBFA. Amorphous phase is more prone to react in an alkaline environment compared to crystalline phases, thus indicating the reactivity of WBFA to a certain extent [99,100]. Since the combustion temperature of wood biomass is mostly within 1000 °C, which is insufficient for melting the ash particles to form a high content of amorphous phases, a generally low content of amorphous phases can be expected. This can be supported by the X-ray diffraction (XRD) patterns of WBFA, as shown in Figure 2.6. Materials with high amorphous content often exhibit a hump in their XRD patterns, whereas the XRD patterns of WBFA typically show highly crystalline features with flat patterns. Quantified phase analysis, although with limited data available from the literature, has shown a low amorphous content in WBFA. For instance, the amorphous content in WBFA was reported to be 27.6% in [101] and a range of 24-61% in [87] from QXRD analysis, and 11% from acid attack dissolution test [102].

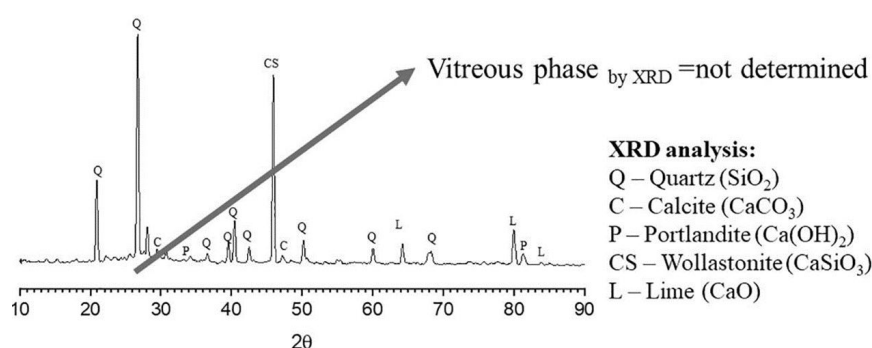


Figure 2.6 XRD patterns of WBFA (picture adopted from [102])

2.4 Pretreatment of WBFA

The purpose of pretreatment is to improve the feasibility of materials for developing cementitious materials, where sieving and washing were the most commonly adopted pretreatment techniques for WBFA.

Sieving is normally employed to remove coarse particles and especially unburnt carbon in WBFA [19,45,103]. Usually, particles above 300 μm are removed, and these particles constitute only a small weight proportion. As unburnt carbon with a great specific surface area would greatly increase the water demand in cementitious materials, this process can help with the workability when using WBFA in cementitious materials.

The purpose of washing is to eliminate soluble salts that could be detrimental to cementitious materials. Berra et al. [52] applied washing to remove alkalis, sulfate, and chloride in WBFA. Since these elements exist primarily as soluble salts, as previously demonstrated in Figure 2.5, such as sylvite and arcanite, washing is efficient in improving the quality of ash to meet the requirements of chemical compositions in fly ash used for concrete. Meanwhile, washing can also reduce the concentration of heavy metals [39]. However, it is important to note that washing only transfers the contaminating substances from WBFA into water. This means that further actions should be taken for waste water management; otherwise, secondary pollution may occur after the washing process, which is also unfavourable from an environmental perspective. However, there is limited information provided on wastewater management after washing WBFA.

2.5 Valorization of WBFA in cementitious materials

2.5.1 Clinker production

As presented in Figure 2.4, the normalized $\text{CaO-SiO}_2\text{-Al}_2\text{O}_3$ ternary chemical compositions of WBFA have a large overlap with Portland cement. This brings up the possibility of WBFA as one of the raw materials for cement clinker production. The benefits of applying WBFA as a raw material for clinker production can be concluded as follows:

- 1) Reducing the need for limestone quarrying, considering the abundance of calcium in WBFA;
- 2) Decreasing energy costs associated with raw material grinding, considering the particle size and grindability of WBFA compared to that of limestone;
- 3) Lowering the CO_2 emission during clinkering, given that portlandite and lime are part of the main calcium-bearing phases.

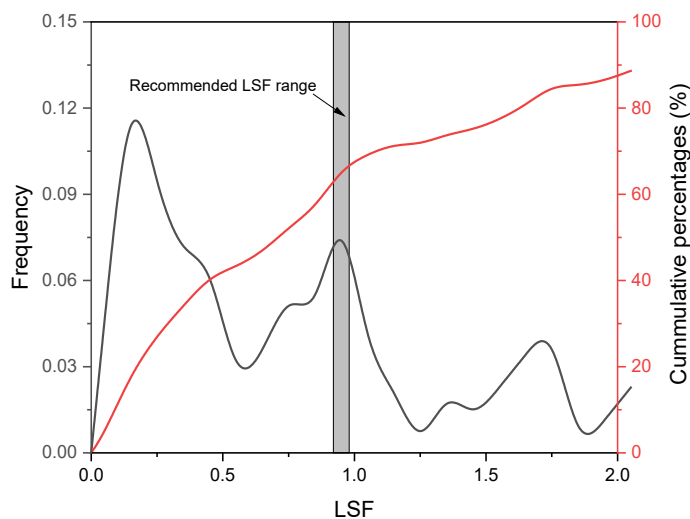


Figure 2.7 Distribution of LSF and their occurrence frequency in 88 types of WBFA from literature (data collected from [21–23,40,44,45,48–61,64–68,70–87,90])

To obtain high quality cement clinker, several factors should be considered when designing mixtures of raw materials. The lime saturating factor (LSF), as defined in equation 2.2, is one of the pivotal parameters. It is recommended to maintain a range of 0.92–0.98 in LSF for Portland cement to enlarge the amount of C_3S without yielding free lime [104]. Based on the chemical compositions of WBFA in the literature, the LSF of WBFA from 88 samples is calculated in this review. The distribution of LSF values and the frequency analysis are plotted in Figure 2.7. It can be seen that the LSF in WBFA exhibits a large variation. By comparing the recommended LSF values for Portland cement clinker production (plotted in grey area) with the distribution of LSF in WBFA, it is noticed that most of WBFA falls outside the recommended LSF range. Therefore, it is impractical to apply WBFA as the main component for Portland cement clinker production. Instead, it can only be used in a smaller quantity as a partial replacement for calcium and silicon sources, depending on the chemical compositions.

$$LSF = \frac{CaO}{2.8 \times SiO_2 + 1.2 \times Al_2O_3 + 0.65 \times Fe_2O_3} \quad (2.2)$$

Besides the major elements, the trace chemicals in WBFA should also be addressed. For instance, potassium, sulfur, and chloride, as indicated in Figure 2.2 with a moderate concentration in WBFA may lead to the corrosion of kilns [105] further negatively influencing the properties of clinker. It is, therefore, necessary to assess these elements before applying WBFA to clinker production.

Experimental research on the implementation of WBFA for clinker production is so far limited. Tosti et al. [106] conducted a feasibility analysis regarding WBFA for clinker production. They emphasized the significance of controlling the properties of biomass ash with desirable CaO/SiO_2 ratios to satisfy the requirements for clinker production. However, as shown in Figure 2.7, it is difficult to maintain the parameters in a stable condition. Instead of producing Portland cement, Carr [107] directly fired WBFA in order to obtain mineral phases with hydraulic properties. By subjecting WBFA to high temperatures at about 1200 °C, wollastonite and β - C_2S were formed, imparting hydraulic properties to the ash. The hydraulic property can be further enhanced by fixing the mixture designs to produce more hydraulic

phases. Carr extended this work by introducing pure chemicals to generate more alite and belite at the lab scale. Another study by Buruberri et al. [108] adopted other industrial wastes to fix the mixtures and produce belite clinker at about 1390 °C. Still, the compressive strength of the waste-derived cement was less satisfactory, reaching only about 10 MPa at 28 days.

To date, it is still challenging to apply WBFA to clinker production. One reason is attributed to the large variations in chemical compositions, and imbalanced chemical compositions from a raw material design perspective. There is a lack of research on the impact of unwanted chemicals in the WBFA on clinker formation and kiln corrosion. In addition, there is no quantified environmental analysis of the valorization of WBFA in clinker production. It is crucial to evaluate whether the environmental burden relief from employing WBFA in clinker production justifies the high-temperature process, especially considering the low-grade cement as reported in the literature.

2.5.2 Blended cement

Partially replacing cement with industrial by-products has become a well-established approach for waste recycling in the construction industry. A wide range of industrial by-products have been turned into valuable supplementary cementitious materials (SCMs) to partially replace cement, aiming at diminishing the carbon footprint of cement [109–111]. In this section, the implementation of WBFA in blend cement is discussed.

2.5.2.1 Roles of WBFA

Three aspects generally sum up the roles of most SCMs in blended cement:

- *Pozzolanic material*

The pozzolanic reaction primarily involves the interactions between portlandite, one of the primary hydrates in cement hydration, and reactive aluminosilicate phases in SCMs [112]. This reaction ultimately facilitates the formation of C-(A)-S-H gels, leading to a densification of the microstructure of the cement matrix [91]. The pozzolanic reactivity of the WBFA is therefore of great interest to evaluate the potential of WBFA in this regard.

The governing elements for pozzolanic reactivity are primarily aluminosilicates and iron [113]. To ensure the pozzolanic reactivity, the amount of those aforementioned elements shall be above certain criteria. For instance, it is suggested in coal fly ash with a lower limit of the sum of aluminosilicate and iron at 50% and 70% for C and N types, respectively [47]. In addition to the chemical compositions, it is preferable that these elements exist in an amorphous state rather than in an inert crystalline form like quartz, mullite etc., as amorphous phases are more conducive to reaction [99]. According to the chemical compositions provided in Figure 2.2, however, the mean value of the sum of silicon, alumina, and iron in WBFA is only about 29.77%, implying the possibly low pozzolanic reactivity of WBFA in general.

Besides the evaluation of WBFA in terms of pozzolanic reactivity from chemical and mineral compositions, direct experimental assessments of the pozzolanic reactivity of WBFA have been reported in a few papers. Among the available test methods [114], the saturation lime method (Frattini method) and the Chappelle test are seen as the most commonly adopted methods for measuring WBFA in the literature [52,72,75,115]. Nevertheless, it is

important to note that these methods may lead to an underestimation of the pozzolanic reactivity of WBFA, as the calcium leached from WBFA is overlooked. The example can be referred to in reference [102], where the Chappelle test result for WBFA shows a negative value.

When comparing different types of WBFA, it is normally found that WBFA with higher proportions of aluminosilicates tends to present greater pozzolanic reactivity [68,75]. However, compared to commonly used SCMs such as metakaolin and coal fly ash, WBFA demonstrates significantly lower pozzolanic reactivity [50,72]. Thus, less compelling properties are present in cement blended with WBFA compared with those blended with coal fly ash and slag.

- *Mineral with synergistic effect*

Even for WBFA with low pozzolanic reactivity, it is still possible to be used in blended cement as a mineral additive, provided it can positively contribute to the hydration of cement and/or other SCMs, instead of promoting pozzolanic reactions. This phenomenon is termed the "synergistic effect" in this thesis, a concept that has been extensively reported in the literature on other industrial by-products [116–118].

One representative case can be the limestone powder, which has been shown to react with aluminate and sulfate phases in blended cement, ultimately contributing to the increased monocarbonaluminate and stabilizing the presence of ettringite [119,120]. In this context, it is worth emphasizing that calcite is one of the main mineral phases in WBFA, as illustrated in Figure 2.4. The results in [19] found that when WBFA was blended with cement, there was an observed increase in the formation of ettringite content, accompanied by a decrease in calcite contents. The depletion of calcite in WBFA also led to the formation of mono/hemi-carbonaluminate. Consequently, in their research, WBFA was found to exhibit a similar function to limestone powder in reacting with the aluminate phase, suggesting its synergistic effects on cement hydration.

Considering the latent hydraulic property of WBFA in the presence of lime and periclase, a minor addition of WBFA can also positively contribute to the strength development of cement. Meanwhile, since WBFA is highly alkaline, the introduction of WBFA can increase the pH value of the pore solution, thereby promoting the hydration of cement and other components such as slag and coal fly ash [80,121,122]. However, it is necessary to note that the high alkali content might lead to side effects on the properties of cementitious materials, for instance, the deceased long-term strength [123], and possibly increased alkali-silica reaction potential [123].

- *Filler*

Filler is considered an inert component in blend cement, as it barely contributes to the formation of hydrates. Still, it can accelerate cement hydration by serving as a nucleation site for the growth of hydrates. For example, the addition of rutile [124] and quartz powder [125] has been shown to promote cement hydration through the nucleation effect. However, it is important to note that in order to achieve the quasi-chemical filler effect, it requires an extremely fine particle size. Until now, there has been limited research reporting the filler effects of WBFA in blended cement systems, mainly due to the typically large particle size of

WBFA. Bajto et al. [23] reported the possible nucleation effect of one type of WBFA in blended cement, observing an enhanced heat flow peak. In their research, WBFA presents a smaller particle size than cement, with the d_{50} of about 6.10 μm . Maschowski et al. [126] also reported that up to 5% of cement replacement by WBFA led to a significant strength increase due to the pore-filling effect. To improve the feasibility of non-reactive WBFA as a filler, grinding techniques can be recommended [22]. Still, an important consideration should be that when a large proportion of filler is added, the dilution effect would eventually lead to performance degradation [127,128]. Therefore, the amount of WBFA used for filler purposes should be carefully restrained.

2.5.2.2 WBFA on the fresh properties of blended cement

Regardless of the diverse properties of WBFA and its different functional roles in blended cement, it is interesting to observe that the results regarding the impact of WBFA on the fresh properties of cement concrete are largely consistent. It is generally acknowledged that WBFA can increase the water demand for cementitious materials [129]. Thus, the decrease in flowability is reported when WBFA is introduced as a partial cement replacement [52,80,101]. The reasons are attributed to water adsorption by unburnt carbon and particles with porous structures. The increased interparticle friction due to the angular WBFA particles is also one of the contributing factors [21].

The rheology properties influenced by WBFA are less investigated yet. One study [21] concluded that due to the water adsorption by WBFA particles and the agglomeration of WBFA particles, the yield stress of cement mortar was found to be largely increased with the addition of WBFA. The increased yield stress with WBFA could also be attributed to the potassium salts that led to the early precipitation of portlandite and gypsum [74]. In terms of setting time, an extend in both initial and final setting time is widely reported [21,23,78]. The phenomenon was explained from the physical perspectives: competition for water, reduced water for cement hydration [21], and chemically retarding effects: the high sulfate and phosphorus content-caused slower hydration of cement.

2.5.2.3 Hydration and microstructure alteration

Isothermal calorimetry test is normally used to investigate the hydration process of cementitious materials. When WBFA is introduced as a cement replacement, contrary results are reported. For instance, in [50,83], a decrease in the main hydration peak with the increment of WBFA was reported. This phenomenon was explained by the low reactivity of WBFA, which led to the dilution effect. However, in [23], when 15% of cement was replaced by different types of WBFA, it was found that all these mixtures showed a higher main exothermic peak than the reference mixture, despite that the occurrence of the main peak can be delayed or accelerated depending on the different ashes. By relating the chemical compositions of WBFA with the heat flow, it is seen that for WBFA with high calcium and alkali content, the exothermic peak tends to increase in isothermal calorimetry, and vice versa. The abundance of alkalis and calcium can help with the initial cement hydration to a certain extent, which can explain these results. The adiabatic calorimetry shows similar results. Rajamma et al. [21] measured the temperature evolution of cement pastes with two types of WBFA. They observed that pastes containing less than 20% of WBFA experienced an accelerated temperature rise during early hydration (before 10 hours). Furthermore, pastes with a higher

calcium content exhibited a more pronounced increase in temperature. Combining the information in short, the compositions of WBFA largely determines its effects on the hydration process when blended with cement. Higher calcium WBFA can slightly accelerate the early hydration process, while WBFA with high silicon tends to dilute the hydration intensity with its increased dosage.

As WBFA changes the hydration kinetics of cement, undoubtably the phase assemblages shall alter when WBFA is introduced. From a qualitative analysis point of view, cement blended with WBFA typically contains similar types of hydrates. The main distinction lies in the inert phases introduced by WBFA, such as quartz and calcite [22,67], present in the matrix. However, the introduction of WBFA can influence the quantity of hydrates. For example, considering the availability of sulfate in WBFA, an increased amount of ettringite might form when a large amount of WBFA is incorporated [67,75]. This could result from increased $\text{SO}_3/\text{Al}_2\text{O}_3$ ratios with WBFA, and the presence of calcite in WBFA can also help with the stabilization of ettringite. In addition, it had been reported that the content of portlandite generated in cement pastes increased with WBFA at early hydration [52,67], as the calcium-bearing phases in WBFA could lead to a higher accumulation of portlandite. However, this increment effect was found to decrease with hydration. Considering the limited pozzolanic activity in WBFA, its contribution to the formation of C-S-H gels was minor. In [67], pastes blended with WBFA were observed to contain a similar amount of bound water and portlandite content, but a higher amount of ettringite at later stages of hydration (> 28 days). Consequently, it was deduced that WBFA did not promote the formation of C-S-H gels. Fořt et al. [50] determined the content of amorphous phases in cement blended with WBFA using QXRD. They observed a linear decrease in the amorphous content with the increment of WBFA, which can be attributed to the decrement of C-S-H gels.

The phase assemblages influenced by WBFA in blended cement would eventually lead to changes in pore structure. Yet, only limited investigations have been conducted regarding the effects of WBFA on the pore structure of blended cement. Maschio et al. [74] observed a significant increase in water adsorption when cement was replaced by WBFA by greater than 5%, indicating the increase in open porosity with the increment of WBFA. Fořt et al. [50] applied the MIP technique to determine the cumulative pore volume and pore sizes of blended cement samples with WBFA. The results showed a gradual increase in total porosity with an increment in cement replacement level from 10% to 70% with WBFA. Particularly, capillary pores ranging from 10 nm to 1 μm showed the most significant increase in volume. Similar results were also reported in [130]. In all, due to the generally low reactivity of WBFA and coarse particle size, WBFA tends to cause a more porous microstructure in blended cement. This would be a significant factor affecting the mechanical properties and long-term performance of blended cement.

2.5.2.4 WBFA on the compressive strength of blended cement

Compressive strength of cementitious materials is a result of their phase assemblage and microstructure compactness. Given that in most cases WBFA leads to a reduction in hydrate phases and increased porosity, it can be anticipated, therefore, that WBFA may result in a negative impact on the compressive strength.

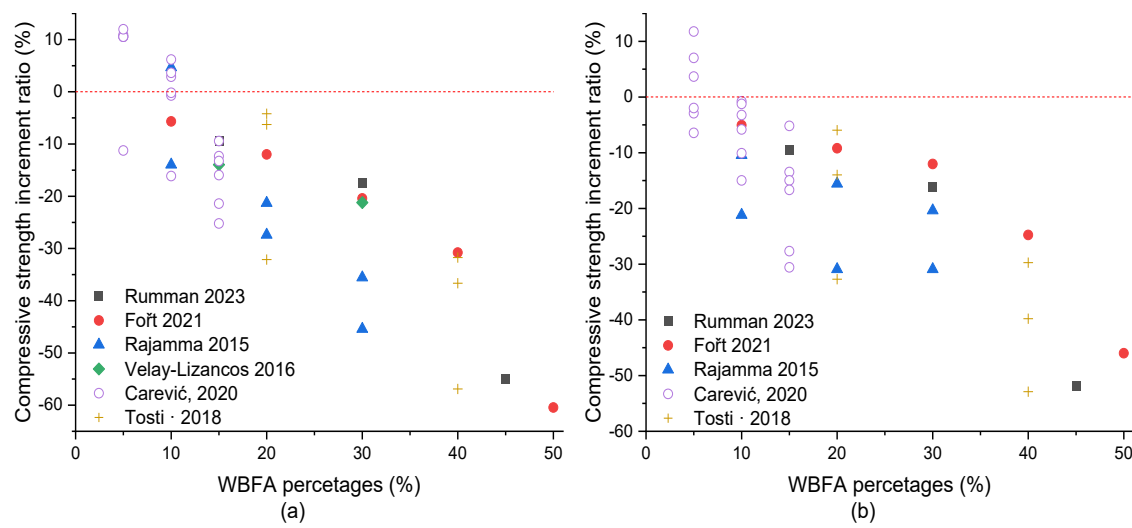


Figure 2.8 WBFA contents vs. compressive strength increment ratios
(a: 28-day specimens, b: 90-day specimens; data collected from [21,44,50,76,101,131])

Figure 2.8 summarizes the effects of different WBFA percentages on the compressive strength of blended cement. When more than 10% of cement is replaced by WBFA, in most research, a negative strength impact is observed [21,50,77,131]. Explanations for strength loss often point to the slow pozzolanic reaction of WBFA, which impedes strength development. Other factors such as the large WBFA particles with porous textures, and adverse effects on some alkali salts may also lead to a strength decrease, especially at a later stage. There are optimal dosages recommended for WBFA from the strength point in different studies, claiming that within these criteria, WBFA can positively contribute to strength development, or only lead to negligible strength compromise. Although the optimal dosages varied across different studies due to the variations of WBFA, a general 5-10% was suggested [21,44,62,83]. This is much lower than the upper limit criterion of conventional SCMs in blended cement [132]. The utilization efficiency of WBFA used in blended cement is relatively restrained.

2.5.2.5 Brief comments

To date, the integration of WBFA in blended cement remains one of the main approaches to its valorization. From the cement industry point of view, due to the scarcity of commonly used SCMs, there is an increasing demand to seek alternative raw materials, for the purpose of reducing the carbon footprint of cement. The substantial demand for alternative SCMs in cementitious materials can promote utilization efficiency in WBFA. These circumstances collectively build the foundation for the advantageous utilization of WBFA in blended cement.

The main challenge in this regard is mainly due to the low pozzolanic reactivity of WBFA. To avoid significant performance compromises in cement concrete, the amount of WBFA to be suggested in blended cement is restricted to 5-10%. Thus, the utilization of WBFA is relatively low.

Apart from the pozzolanic reactivity, it is noteworthy that there are valuable elements (calcium, sulfate, and alkalis) and phases (lime, portlandite, calcite etc.) in WBFA that can facilitate the reaction of cement and other SCMs. While it may be too ambitious to directly replace cement with WBFA, a more practical approach could involve using WBFA as a partial

replacement for common SCMs. This approach can yield synergistic effects, ultimately achieving satisfactory performance for cementitious materials. Unfortunately, there has been relatively little research and attention focused on this perspective.

2.5.3 Alkali-activated materials preparation

Alkali activation is another prevalent technique for waste recycling. In this technique, the reactions between precursors, contributing aluminosilicates and calcium species, and activators, providing a strong alkaline environment, lead to the formation of different hydrate gels like C-A-S-H, N-A-S-H, and C-(N)-A-S-H [133] and other secondary products. These hydrates ultimately confer mechanical properties on monolithic materials [134]. Any material capable of serving as either precursors or activators can be used for AAMs production. This versatility has led to the exploration of a wide range of industrial by-products for their potential use in AAMs production [135,136], including WBFA [60,137,138].

This section provides an overview of current research on the utilization of WBFA in AAMs production. Given the distinct characteristics of WBFA in chemical compositions and high alkalinity, studies have focused on both the precursor and activator perspectives.

2.5.3.1 WBFA as precursor

In the production of AAMs, the most commonly used precursors align with those frequently employed as SCMs in blended cement, such as slag, coal fly ash, metakaolin, etc [134]. This is because, for both alkaline activation and pozzolanic reactions, the reactive aluminosilicates are of great interest. Materials that present high pozzolanic reactivity can always be ideally used for AAMs preparation. Differently, materials with low or even poor pozzolanic reactivity, which may be considered less reactive in blended cement, could potentially be used for AAMs preparation. This is due to the fact that the highly alkaline environment can enhance the dissolution of the reactive phases [139]. Therefore, WBFA retains the feasibility of being used as one source of precursors in AAMs preparation, even though WBFA shows lower reactivity than those conventional precursors.

When WBFA is used as the singular precursor in AAMs, it is anticipated that a high activation energy, for instance, elevated alkalinity of activators, may be needed, considering the typically low reactivity of WBFA. Nevertheless, this assertion may not be consistently supported by the experimental findings. In [73], it was found that NaOH solution with a molarity of 10 M was optimal for alkali-activated WBFA mortar regarding compressive strength. Increasing the molarity to 18 M only led to a strength decrease. Similarly, in [64], the compressive strength of NaOH-activated WBFA pastes achieved its highest strength with a NaOH concentration at 2 M. Further increases in alkalinity barely promoted strength development but caused a slight reduction. These results can be explained from the dissolution point of view: Within a certain limit, a higher alkaline environment facilitates the dissolution of WBFA. However, as the alkalinity increases, the dissolution of calcium species is impeded. Thus, it is not feasible for the precipitation of C-A-S-H gels, ultimately resulting in a strength loss [140]. Therefore, an optimal mixture design is highly demanded to attain satisfactory performance without wasting extra activator. Still, it is essential to note that in general, the compressive strength of alkali-activated WBFA is relatively low (≤ 10 MPa)

[64,73,141]. This may restrain the application of alkali-activated WBFA from an engineering perspective.

Considering the limited strength of alkali-activated WBFA, it is viable to incorporate other highly reactive precursors, such as metakaolin[73,138,142–144], glass powder [64], and blast furnace slag [145] to create hybrid precursors. Partially replacing WBFA with reactive aluminosilicates has been reported to yield more reaction products, resulting in a denser microstructure and enhanced mechanical properties [73]. However, it is worth noting that in this context, the improved performance appears to be primarily due to the external reactive aluminosilicates. The addition of more reactive aluminosilicates materials results in superior performance. Thus, it is challenging to justify the contribution of WBFA to the AAMs. The practical significance of recycling WBFA would be largely diminished, even if a higher content of WBFA can be used in this scenario compared to its use in blended cement, as most of WBFA was only treated as inert aggregate instead of a value-added mineral in the binder system.

Instead of employing WBFA as the main precursor along with additional reactive aluminosilicates to prepare AAMs, a more practical strategy involves partially replacing the conventional precursors with WBFA in AAMs. The distinction between this strategy and the former one is that WBFA in this scenario is used as a mineral to tailor the reaction kinetics, influence the compositions of hydration products in AAMs, and subsequently improve their performance. There would be an optimal dosage for WBFA to justify its role in this system. For instance, in [146], when metakaolin was replaced by WBFA, the main reaction products evolved from N-A-S-H gels in the pure metakaolin system to the (N,C)-A-S-H gels in the blended mixture. A more compacted microstructure can be observed in SEM with the introduction of WBFA, and the compressive strength increased with the WBFA replacement ratio up to 50%. High calcium WBFA was also used to replace coal fly ash in AAMs, as reported in [147]. Due to the introduction of calcium from WBFA, the setting time of mixtures can be shortened. Besides, a strength improvement, especially at the early stage, was reported in the mixture with the optimal coal fly ash replacement dosage at 10% by WBFA. Similarly, the presence of C-A-S-H gels are evident as one of the main hydrates together with N-A-S-H gels, thus improved the mechanical properties.

2.5.3.2 WBFA as activator

Since WBFA is reported to have high alkalis salt contents, the anticipated high alkalinity of WBFA enables it to stimulate the alkaline activation process when blending WBFA with other precursors. Jurado-Contreras et al [146] investigated the soluble alkali salts from WBFA on the properties of alkali-activated WBFA-metakaolin mixtures. By comparing WBFA before and after washing, it was reported that AAMs with raw WBFA obtained a higher mechanical property than those prepared with washed WBFA. The alkalis were evident with great contribution to the reactions of AAMs.

Moreover, some research has attempted to directly employ WBFA as a solid activator for the preparation of one-part AAMs. In [148], the high calcium wood ash was used as a solid activator to activate coal fly ash. It was observed that by blending wood ash with water, the pastes had a pH value above 13, implying the feasibility of using wood ash as an activator. Meanwhile, due to the presence of high calcium, coal fly ash can be activated at ambient temperature, forming C-S-H gels as one of the main reaction products. In [149], WBFA was

used as a solid activator to activate silica fume. A mixture of 50% WBFA and 50% silica fume can obtain a compressive strength close to 30 MPa at 28 days. Additional studies exploring WBFA as an activator to combine with other aluminosilicate precursors have also been reported [54,150].

2.5.3.3 Brief comments

Alkali activation enhances the dissolution of precursors in a strongly alkaline environment. When used as precursors, WBFA can release more amounts of aluminosilicates compared to its dissolution in cement pore solutions [139]. However, if WBFA is used solely as a precursor, it may be difficult to achieve satisfactory performance due to its inherent reactivity limitations. Hence, it is more practical to introduce other precursors or replace traditional precursors by WBFA. Still, in the hybrid precursors, the recommended upper limit for WBFA is mostly larger than that reported in blended cement. This allows for a higher recovery efficiency when utilizing WBFA through alkali activation compared with blended cement.

Furthermore, considering their predominantly high alkalinity, it is of great interest in valorizing WBFA as an activator. On one hand, the implementation of WBFA as a solid activator enables the production of one-part AAMs, which solves the drawbacks of conventional AAMs with great difficulties in handling corrosive activators [151]. Additionally, since the primary carbon emissions of AAMs originate from activators [152], employing WBFA as an activator allows for the production of AAMs entirely derived from solid waste, resulting in significant environmental benefits. However, recent research on WBFA in AAMs still largely focuses on preparing conventional AAMs by adjusting the mixture designs (WBFA proportions in precursors, alkali contents, and modulus), further concluding an optimal mixture containing a certain amount of WBFA. There is a need for comprehensive research on studying WBFA as a solid activator, addressing aspects such as reaction kinetics, reaction mechanisms, microstructure evolution, and the eventual upscaling practice. Such research is essential to effectively take the use of the chemical compositions of WBFA in developing AAMs and enhance its valorization efficiency.

2.6 WBFA classification towards cementitious materials development

To date, research on the valorization of WBFA is primarily regional, often presented as case studies. Previous attempts to classify biomass ash have been conducted in a few studies. Vassilev et al. [97,153] proposed an initial classification of biomass and ashes based on chemical compositions. From a phylogenetic perspective, Zhai et al. [154] reviewed the chemical compositions of biomass ash from different sources. However, it is difficult to directly adopt these ash classifications to help the design of WBFA utilization methodologies in cementitious materials, as these classifications only aim to predict ash compositions based on the sources. To facilitate the valorization of WBFA in developing cementitious materials, therefore, it is essential develop ash classification methods from the cementitious materials perspective.

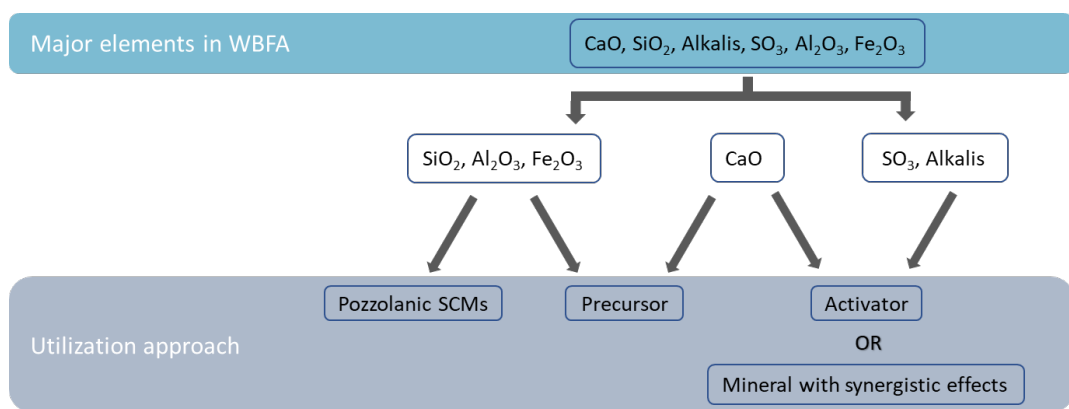


Figure 2.9 Elements of interest from WBFA used in blended cement and AAMs

In the current review, the primary roles of WBFA in cementitious materials may be categorized into four key aspects: functioning as pozzolanic materials, contributing to synergistic effects, acting as precursors, and serving as activators. The chemical compositions of WBFA are highly correlated with the functions of WBFA in the development of cementitious materials. Hence, it is possible to propose the WBFA classification method from an application-focused standpoint, linking the chemical compositions to the functions of WBFA. Figure 2.9 illustrates that the anticipated utilization methods for WBFA can be determined based on its primary chemical compositions. For example, in order to utilize WBFA as pozzolanic materials, a greater quantity of aluminosilicates is required. When adopting WBFA for precursors, in addition to aluminosilicates, calcium species are also preferred. Furthermore, if WBFA is to be utilized as activators, it is crucial to emphasize the presence of alkalis.

Figure 2.10 provides an application-oriented WBFA classification methods, derived from the modified ternary diagram, referring to the work from Vassilev et al. [97,153] and Zhai et al. [154]. The coloured areas in the figure represent the estimated distribution of WBFA, with the data plotted as a modified version of Figure 2.2. To further correlate the chemical compositions and their associated applications, the distribution of 20 types of WBFA from the literature identifying different roles in developing cementitious materials is specifically plotted. Thus, a simplified two types of WBFA are summarized. Type I WBFA primarily includes a high content of aluminosilicates and iron. The normalized weight proportions of these elements are above 50%. This makes it suitable for use as either pozzolanic material or precursors in AAMs production. Conversely, Type II WBFA primarily comprises a high content of calcium, alkalis, and sulfate, which make it a suitable activator or calcium source in AAMs production, or SCM with synergistic effects. Still, it is worth noting that this classification is limited to preliminary WBFA utilizing approaches. Further refinement should be considered once more detailed information on WBFA, for instance, mineral compositions, amorphous content, becomes available. Future refinement is necessary to provide a more precise ash classification.

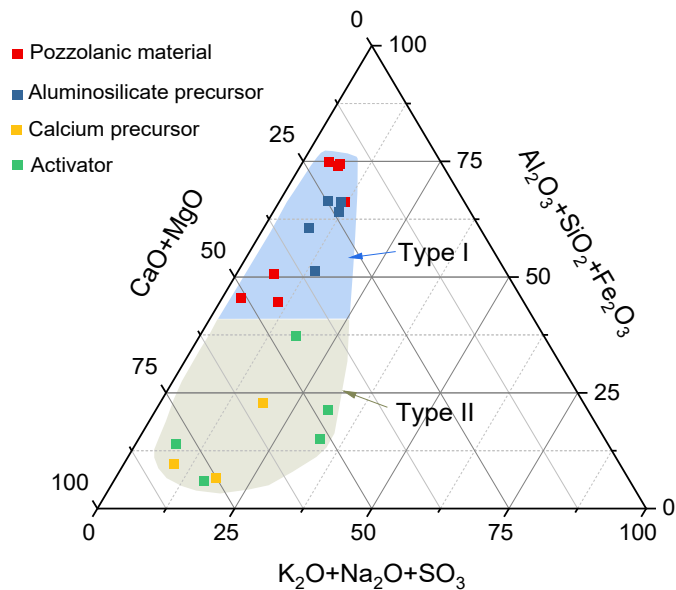


Figure 2.10 Application-oriented classifications of WBFA based on chemical compositions. (WBFA with pozzolanic activity in [63,65,72,77], WBFA used as aluminosilicate precursors in [73,138,142–144], used as calcium-based precursor in [64,147], used as activator in [54,146,150])

2.7 Research gap and problem definition

Based on the current review, the following aspects were summarized as the research gaps that are going to be investigated in this thesis.

- Low utilization efficiency of WBFA in cementitious materials

The low utilization efficiency of WBFA is mainly due to the improper methodology adopted. These methods often involve conventional approaches for aluminosilicate-rich industrial materials, such as directly substituting WBFA for cement or using it as a precursor. New strategies are needed to exploit the major components (alkalis, sulfate, and calcium-bearing phases) in WBFA for designing cementitious materials. One interesting example is leveraging the sulfate, alkalis, and calcium-bearing phases to promote the reaction of other aluminosilicates, thereby forming cement-free binders. This will be one of the binder systems investigated in this thesis.

- Reaction mechanisms of WBFA in cementitious materials remains unclear

Previous studies have widely investigated the performance of cementitious materials containing WBFA, while the reaction kinetics and microstructure evolution are not well understood. When WBFA is used for developing new types of cementitious materials, a more comprehensive investigation should be conducted to understand the role of WBFA and other components from the reaction mechanism perspective, which enables providing a fundamental basis for designing cementitious materials.

- Knowledge on durability aspects is limited

Besides fundamental research on reaction mechanisms, a broad knowledge of the new binders is needed, including their durability. Current research just simply compares the performance of cementitious materials before and after the introduction of WBFA in different durability performance, while the controlling factors influencing these durability performances is rarely discussed. This thesis aims to address this gap by focusing on

carbonation, an inevitable process during the service life of cementitious materials, with the investigation of the governing factors on carbonation in detail.

- Needs in the application-oriented research

Upon the development of cementitious materials based on the new methodologies, application-oriented research is necessary to verify the feasibility of producing construction products based on the materials developed in the thesis. Further, it is important to conduct an environmental impact assessment on the products to justify the benefits of utilizing WBFA in construction materials.

2.8 Summary

This chapter reviewed the current research on the physicochemical properties of WBFA and its utilization for the development of cementitious materials. Despite the considerable variability in the physicochemical properties of WBFA, the predominant chemical composition tends to follow the sequence: $\text{CaO} > \text{SiO}_2 > \text{K}_2\text{O} > \text{MgO} \approx \text{Al}_2\text{O}_3 \approx \text{SO}_3 \approx \text{P}_2\text{O}_5 \approx \text{Fe}_2\text{O}_3$. The crystalline phases predominantly consist of calcium-bearing phases, and the amorphous content in WBFA is generally lower than that in conventional materials employed in the cement concrete industry, resulting in limited pozzolanic reactivity.

Three main approaches for valorizing WBFA in cementitious materials, namely clinker production, cement substitution, and the development of AAMs, were reviewed. While clinker production demands high material stability and high energy costs in the clinkering process, which is not particularly advantageous for WBFA valorization, incorporating WBFA in blended cement and preparing AAMs remain the two most commonly used approaches. In blended cement, owing to the generally low pozzolanic reactivity of WBFA, it is recommended to use only 5-10% WBFA as a cement replacement, with an acceptable compromise on performance. In the production of AAMs, WBFA can be used as aluminosilicates and calcium sources depending on its chemical compositions. Besides, owing to the high alkalinity of WBFA, it is possible to use WBFA as a solid activator. Still, limited research has been conducted in this aspect.

To enhance the understanding of WBFA and facilitate its application, an application-oriented WBFA classification method is proposed, based on the chemical compositions and their correlation with their reported applications in the literature, aiming to provide guidance for WBFA valorization in construction materials. A further refinement of the ash classifications is suggested in future research when more information on WBFA, especially the quantification of mineral compositions, becomes available.

In light of the information from this review, it was concluded that the utilizing efficiency of WBFA in cementitious materials remains limited, necessitating the exploration of new methodologies. Consequently, this thesis is enclosed with comprehensive research that includes the investigation from raw materials to binder formulation, and extends to addressing carbonation, a significant durability concern in cementitious materials. Additionally, the research encompasses construction product development, with the overarching goal of enhancing our understanding of WBFA for more effective utilization in construction materials.

Chapter 3

Characterization, pretreatment, and evaluation of wood biomass fly ash as a binder component

3.1 Introduction

In the valorization of industrial by-products for construction applications, the first step is to determine the physicochemical properties of the materials. This information serves as the fundamental basis for identifying any necessary pretreatment process, and evaluating the feasibility of the materials for specific applications in construction.

This chapter includes the characterization, selection, pretreatment, and potential evaluation of wood biomass fly ash (WBFA) for construction purposes. Initially, three types of WBFA are collected and characterized. Subsequently, an initial screening process is conducted based on the physicochemical properties of WBFA, to identify the most promising ash for in-depth investigations. The selected ash is subjected to pretreatment processes, and its feasibility as a binder component is evaluated based on dissolution tests. These analyses provide valuable insights into the feasibility of WBFA as a binder component.

3.2 Materials and Methods

3.2.1 Raw materials

Three types of WBFA were collected from different bioenergy plants in the Netherlands. The detailed biomass input, combustion devices, burning temperature, and ash collection methods are provided in Table 3.1. Notably, due to the high carbon content in WBFA3, a preliminary sieving process was applied to remove particles above 256 µm, commonly referred to as unburned carbon [155].

Table 3.1 WBFA generations parameters

	Biomass type	Burning temperature	Incineration facility	Ash collection method
WBFA1	Wood chips, pruning wood, scrap wood, and paper sludge	900 °C	Bubbling Fluidized bed boiler	Bag filter
WBFA2	Demolition waste wood from municipal recycling center	900 °C	Bubbling Fluidized bed boiler	Bag filter
WBFA3	Waste contaminated wood	900 °C	Grate furnace	Bag filter

For comparative purposes, coal fly ash (CFA) and blast furnace slag (BFS), which are the most commonly used mineral additives in cementitious materials, were introduced as benchmarks alongside WBFA. CFA and BFS were supplied by VLLEGASUNIE B.V. (the Netherlands) and Ecocem B.V. (the Netherlands), respectively.

3.2.2 BFA characterization and screen-out

3.2.2.1 Ash characteristics

The particle size distribution (PSD) of WBFA, as measured by the laser diffraction analyzer (Mastersizer 2000), is shown in Figure 3.1. In general, the particles in all three types of WBFA are within 200 µm, consistent with the review in Chapter 2. Specifically, the particle sizes of both WBFA1 and WBFA2 fall within the range found in BFS and CFA. Conversely, WBFA3 shows the largest particle size among all of the materials. The variations in particle size among the three types of WBFA highlight their distinct characteristics. A possible explanation for this variation can be attributed to the combustion devices, with the grate furnace exhibiting a lower combustion efficiency compared to the fluidized bed [33]. Meanwhile, the differences in fuels in different plants can be another factor.

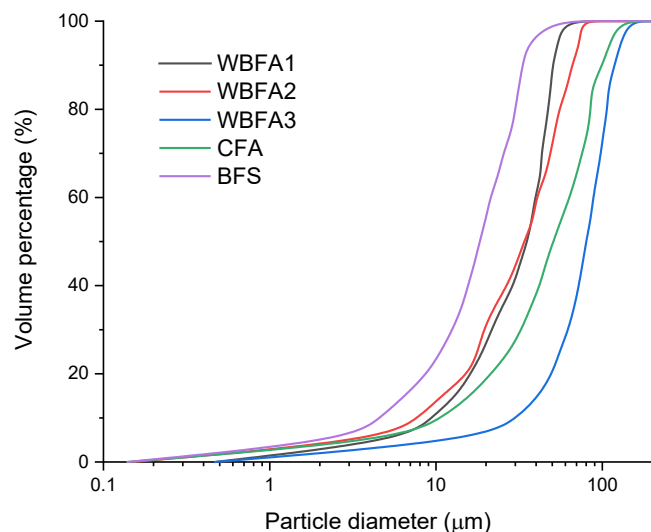


Figure 3.1 particle size distribution of WBFA, CFA, and BFS

Table 3.2 Chemical compositions (in wt.%) of WBFA, CFA, and BFS determined by XRF

	SiO ₂	Al ₂ O ₃	CaO	Fe ₂ O ₃	SO ₃	Na ₂ O	K ₂ O	Cl	MgO	PbO	LOI (550 °C)	LOI (1000 °C)
WBFA1	15.20	4.06	43.65	2.58	6.00	1.77	6.92	3.18	3.33	-	1.55	6.03
WBFA2	10.14	7.12	46.96	5.32	7.69	0.01	1.53	6.84	2.92	2.03	0.95	4.96
WBFA3	44.96	4.86	26.77	4.49	3.78	0.35	1.57	0.86	2.63	0.33	6.42	7.10
WBFA _{mean}	21.88	5.19	37.61	2.95	4.44	1.36	10.07	1.69	4.78	n/a	n/a	n/a
CFA	57.20	24.78	3.96	5.80	0.69	1.28	1.41	-	2.11	0.01	1.02	1.27
BFS	31.77	13.25	40.50	0.52	1.49	0.12	0.34	-	9.27	-	n/a	1.31

The chemical compositions of the three types of WBFA, as well as CFA and BFS, determined by the X-ray fluorescence (XRF) technique, are presented in Table 3.2. Additionally, $WBFA_{mean}$ represents the mean values of the chemical compositions of 97 types of WBFA from the literature, as previously presented in Figure 2.2 in Chapter 2. $WBFA_{mean}$ is utilized for comparison with the three types of studied WBFA to indicate their representativeness.

In general, the chemical compositions of WBFA1 and WBFA2 closely resemble those of $WBFA_{ave}$, indicating a high representativeness for a broad scope of WBFA. Specifically, WBFA1 and WBFA2 are predominantly composed of calcium, with relatively low amounts of aluminosilicates. In contrast, WBFA3 is silicon-rich, with calcium oxide accounting for only 26.77%. It is seen that the elements associated with pozzolanic reactivity (the sum of silicon, alumina, and iron) only account for 22.81% and 22.58% for WBFA1 and WBFA2, respectively, amounting to 54.31% for WBFA3. These values are considerably lower than the corresponding values in CFA at 87.78%. These findings suggest a potentially lower pozzolanic reactivity for all three types of WBFA.

The loss on ignition (LOI) at 550°C indicates the content of unburnt carbon, as suggested by EN 12880:2000 [156]. Since the grate furnace has a lower incineration efficiency compared with the fluidized bed incinerator, WBFA3 is found with a higher unburnt carbon content (6.42%) compared with WBFA1 (1.55%) and WBFA2 (0.95%). The continuous mass loss during ignition from 550°C to 1000°C is mainly attributed to the decomposition of carbonate-bearing phases. A detailed exploration of these phases can be found in the subsequent sections concerning mineral compositions.

The mineral compositions of three types of WBFA were measured by the X-ray diffraction (XRD) technique, and the corresponding patterns are present in Figure 3.2. For comparison, the diffraction patterns of BFS and CFA are also present.

The XRD pattern of WBFA1 is dominated by calcium-bearing phases, including calcite, lime, and anhydrite. Additionally, due to the relatively high alkali content in WBFA1, these elements exist in the forms of sylvite and aphthitalite. In WBFA 2, anhydrite is the major calcium-bearing phase, while other phases like calcite and lime are also present but with lower intensity. A noticeable hump between 25 and 35 degrees of 2 thetas is evident in both WBFA1 and WBFA2, indicating the presence of amorphous phases. In the case of WBFA3, quartz dominates in the diffraction pattern, which correlates well with the XRF results suggesting a high content of silicon. Other minerals with minor intensity e.g., anhydrite, lime, and rutile are observed. The XRD pattern of WBFA3 is flat without clear obvious of amorphous hump. Generally, the minerals observed in all three types of WBFA are consistent with those frequently reported in the literature, as shown in Figure 2.5.

In comparison, minerals present in CFA are mainly quartz, mullite, and hematite. A clear hump is identified in the pattern between 15 and 35 degrees of 2 thetas, implying the presence of amorphous phases. For BFS, on the other hand, no clear crystalline phase can be identified, and its diffraction pattern is seen as a hump across all diffraction ranges.

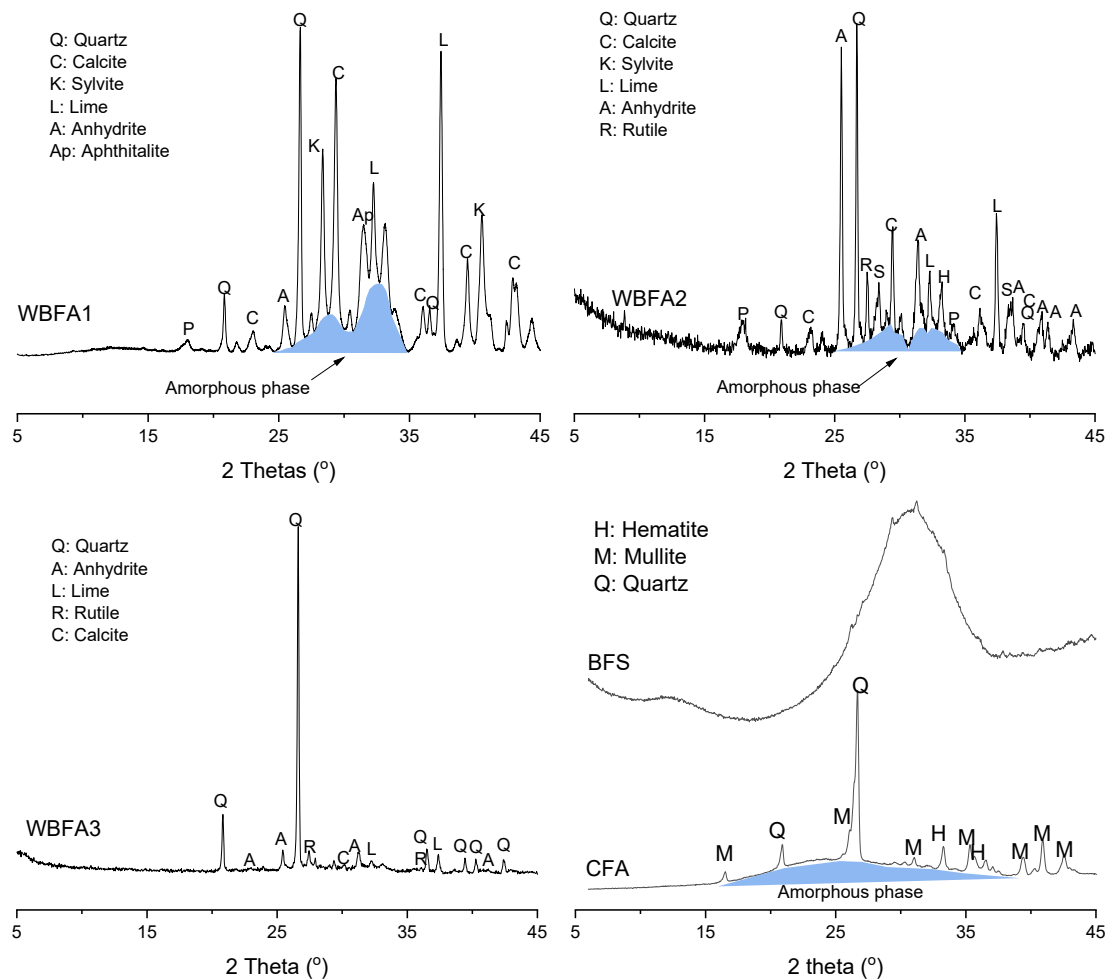
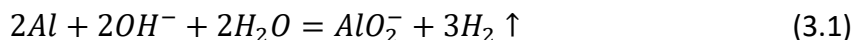


Figure 3.2 XRD patterns of raw WBFA, BFS, and CFA

The presence of free lime in cementitious materials can pose a potential threat to volume stability, as the slow generation of portlandite with a larger molar volume can lead to expansion in the solid matrix [157]. Since the diffraction peaks of lime are observed in all three WBFA patterns, the free lime content was further evaluated using a titration method according to EN 451-1:2017 [158]. Additionally, incineration ash from wastes has often been reported to contain metallic aluminum, which can lead to the generation of hydrogen gas and subsequent cracking in cementitious materials [159,160]. The metallic aluminum content of WBFA was therefore determined by a water displacement method with the setup depicted in Figure 3.3. For each test, 50 grams of WBFA were mixed with 200 ml of a 3 M NaOH solution for 24 hours. The suspensions were stirred automatically with a magnetic stirrer to accelerate the metallic oxidation reaction, and the volume of the hydrogen gas was recorded in the graduated cylinder. The metallic aluminum content in the WBFA was then calculated according to the chemical equation (3.1), as 1 gram of metallic aluminum could generate approximately 1.25 L of hydrogen gas. Three replicates are conducted for each test.



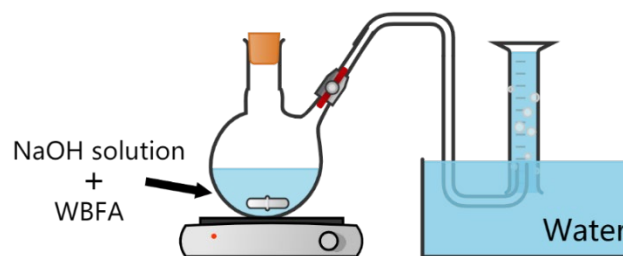


Figure 3.3 Schematic diagram of setup for determining metallic Al content

Table 3.3 Metallic aluminum and free lime content of WBFA

	WBFA1	WBFA2	WBFA3
Free lime (%)	8.56	11.02	1.47
Metallic aluminum (%)	0.13	0.71	0.45

The free lime and metallic aluminum contents are shown in Table 3.3. It is noted that the free lime content in fly ash is suggested to be restrained within 1.5% when used in cement [36]. The high content of free lime in WBFA shall be problematic in causing volume expansion. Therefore, it is strongly recommended to conduct treatment to reduce the free lime content in these ashes if they are intended to be used as construction material. As for metallic aluminum, on the other hand, all WBFA confirms the presence of metallic aluminum, which could originate from non-separable metal scraps in waste wood products. It is important to remind that metallic aluminum in WBFA should be strictly prohibited, as a great amount of hydrogen gas can be generated in an alkaline environment. This poses a substantial risk of expansion and cracking in cementitious materials. For instance, in the case of WBFA1, which has the lowest metallic aluminum content among the three, 1 gram of ash can already yield approximately 1.63 ml of hydrogen gas. Caution is needed when using metallic aluminum-bearing ash in concrete, especially when the ashes are used in large proportions. Therefore, it is suggested to implement a treatment process for the oxidation of metallic aluminum prior to utilizing the ashes in cementitious materials.

3.2.2.2 Ash screen-out

Before conducting further research, it is essential to select one type of most promising WBFA among the three for detailed investigation, aiming for a comprehensive study with representatives covering a broad spectrum of WBFA characteristics.

By associating the ash categorization according to Section 2.6, WBFA1 and WBFA2 should be classified as the type II WBFA while WBFA3 should be classified into type I WBFA. Considering the average chemical compositions from Table 3.2 and the mineral compositions from Figure 2.5, it can be concluded that WBFA1 and WBFA2 are more representative. To ensure the universality of the research results concerning WBFA materials, WBFA3 is excluded from further investigation.

As for WBFA1 and WBFA2, the first challenges for their utilizations are the presence of free lime and metallic aluminum. While free lime is commonly reported in WBFA, limited studies have explored the occurrence of metallic aluminum in WBFA, which may be linked to

the wood biomass resources in the Netherlands. From a pretreatment perspective, WBFA1 is more favourable as it contains a lower amount of metallic aluminum and free lime. Additionally, it is crucial to note that WBFA2 exhibits an exceptionally high lead content (2.03%) based on XRF results, raising significant safety concerns for subsequent studies. Therefore, in the following investigations, WBFA1 is chosen as the material of focus for a comprehensive investigation.

3.2.3 Ash pretreatment

The primary objective of pretreatment is to eliminate free lime and metallic aluminum in WBFA1, as these two substances pose significant threats of causing volume expansion and cracking in cementitious materials. Given that WBFA1 contains a high content of alkalis and free lime, its inherent alkalinity can be advantageous for eliminating metallic aluminum. Therefore, the proposed method involves water pretreatment, creating a moist environment to enable the hydration of lime, dissolving alkalis from WBFA1, and further facilitating the oxidation of metallic aluminum by the alkalis. To reduce costs during pretreatment, only a small amount of water is employed to achieve an earth-moisture state of ash particles, promoting the chemical reaction process.

The overview of pretreatment procedures is summarized in Figure 3.4. WBFA1 was mixed with water at a water-to-ash ratio of 0.2 in a Hobart mixer for 10 minutes, ensuring complete moistening of the particles. The ash was then sealed and stored in buckets, enabling the reactions to continuously occur. During this period, daily measurements were taken to track the amount of residual metallic aluminum until its complete oxidation was achieved. It was observed that after water pretreatment, particle agglomeration and the formation of hardened coarse particles occurred, as shown in Figure 3.5(b). Therefore, grinding was applied to pulverize these particles. The water-treated WBFA1 was first oven-dried at 105°C for one day and then pulverized using a tumbling ball milling machine with a rotation rate at 45 rpm. The treated WBFA1 underwent testing for its physicochemical properties and was used for further research.

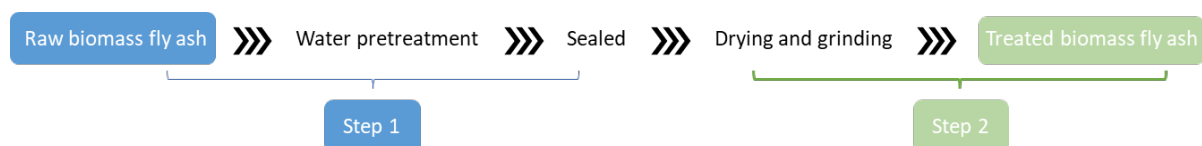


Fig 3.4 Flow chart of WBFA1 pretreatment process

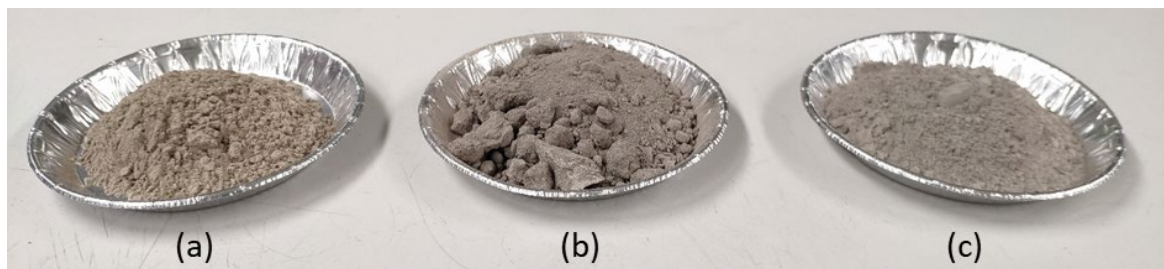


Figure 3.5 Appearances of WBFA1 through pretreatment process

(a: raw WBFA1, b: treated ash after step 1, c: treated ash after step 2)

3.2.4 Dissolution test

To evaluate the reactive potential of treated WBFA1, a dissolution test, one of the most commonly used methods for evaluating the reactivity of materials such as BFS and biomass ash etc. [139,161–164], was opted in this research. Three different media, namely deionized water and NaOH solutions with concentrations of 0.1 M and 3 M, were used for the dissolution tests. This allows the investigation of the potential contribution of treated WBFA1 as a self-hydraulic binder component, a SCM in blended cement systems (with the pore solution a pH around 13), and a precursor in alkali-activated materials, respectively.

The treated WBFA1 was mixed with different media at a mass ratio of 1:100 and horizontally shaken on the shaking table at 200 rpm to prevent precipitation. BFS and CFA were also tested as benchmarks. The suspensions were filtered after a designated period, and the supernatants were collected accordingly. Subsequently, the supernatants were acidified with nitric acid, diluted, and then subjected to the ion concentration test by Inductively Coupled Plasma Optical Emission spectroscopy (ICP-OES). The concentrations of Ca, Si, and Al were exclusively measured, as these elements are the main components present in the hydration products of cementitious materials. Meanwhile, the pH values of these materials were also measured by testing the concentrations of OH⁻ in the supernatants from water groups by the titration method with 0.1M hydrochloride acid, with phenolphthalein used as the indicator.

3.3 Results and discussion

3.3.1 Pretreatment of WBFA1

To assess the effectiveness of water pretreatment in depleting metallic aluminum, the changes in residual metallic aluminum content in WBFA1 over water pretreatment time were recorded, and the results are illustrated in Figure 3.6.

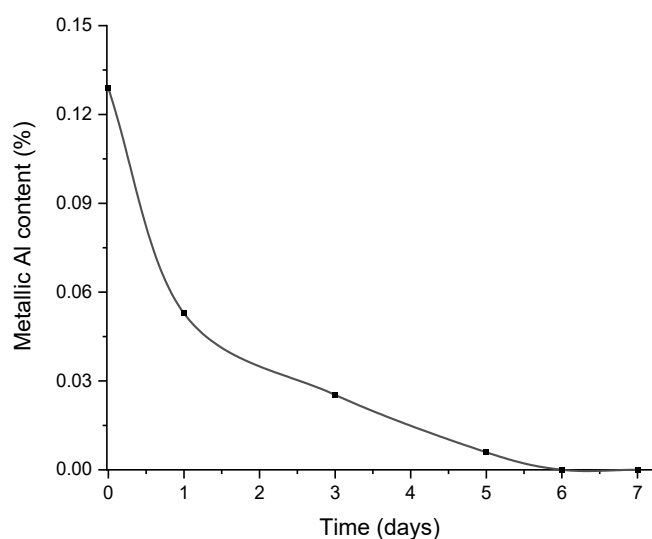


Figure 3.6 Correlation between residual metallic aluminum and water pretreatment durations

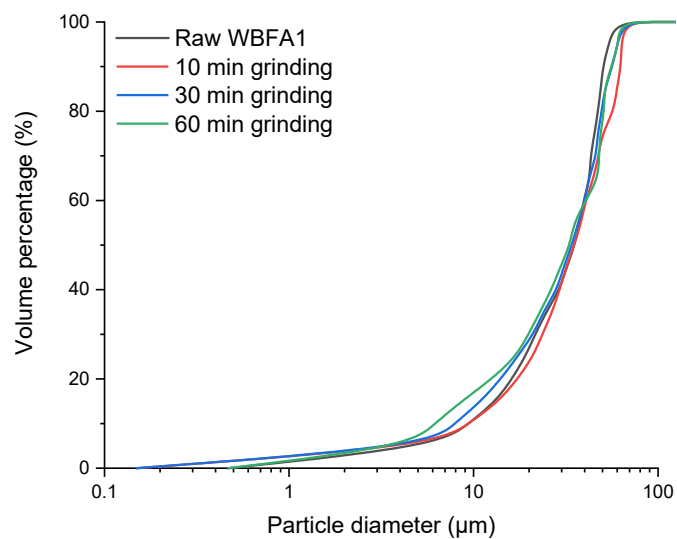


Figure 3.7 Particle size distribution of raw WBFA1 and treated WBFA1 after grinding

Table 3.4 Typical particle diameter of raw WBFA1 and treated WBFA1 after grinding

Raw WBFA1	Treated WBFA1		
	10 min grinding	30 min grinding	60 min grinding
D ₁₀ (μm)	9.41	9.47	7.91
D ₅₀ (μm)	35.33	34.97	34.12
D ₉₀ (μm)	50.26	62.98	56.53

The initial metallic aluminum content in WBFA1 is 0.13%, which decreases to 0.05% after 1 day of water pretreatment. Subsequently, the metallic aluminum depletion rate gradually slows down, taking a total of 6 days to complete its oxidation, reaching 0%. The observed metallic aluminum depletion rate generally aligns with the reaction kinetics of metallic aluminum suggested by Xuan et al. [165], who introduced alkaline solutions to accelerate the oxidation of metallic aluminum in municipal solid waste incineration (MSWI) ash. This evidence suggests that the alkalis in WBFA1 can function in promoting the depletion of metallic aluminum.

As indicated in Figure 3.5(b), treated WBFA1, after the drying process, is found to have agglomeration and the formation of hardened large particles. The grinding process is therefore necessary to break the agglomeration of water-treated WBFA1, ensuring a fine particle size of WBFA1 that is feasible as a binder component. The effect of grinding durations on the PSD of water-treated WBFA1 is studied, and the results are presented in Figure 3.7 and Table 3.4. A 10-minute grinding process already leads to a fine particle size in the treated WBFA1, with D₁₀ and D₅₀ values reaching 9.47 μm and 34.97 μm, respectively, which is comparable to that of raw WBFA1, and can be feasibly used as binder preparation. While longer grinding time could further reduce particle size, it is seen that the size reduction is less significant. As mentioned previously, the motivation for pretreatment is to improve the feasibility of WBFA as a construction material while minimizing costs. Given that grinding is

highly energy-demanding, it is therefore recommended to limit the grinding time to 10 minutes to reduce energy consumption while still achieving effective pretreatment.

3.3.2 Characteristics of treated WBFA1

Water pretreatment not only contributes to the oxidation of metallic aluminum, but other chemical reactions involving multiple phases may also occur simultaneously. Therefore, it is essential to characterize the physicochemical properties of treated WBFA1, providing precise information for further study.

3.3.2.1 Chemical compositions

Table 3.5 presents the chemical compositions of treated WBFA1, with raw WBFA1 as a comparison. The chemical compositions of treated WBFA1 remain rather stable in comparison to the raw ash, as the entire process is conducted in a sealed environment, preventing any leaching of elements. Furthermore, there is a marginal increase in LOI, which can only be ascribed to the increased bound water content in the ash after the pretreatment, as a consequence of reactions that occurred during the pretreatment.

3.3.2.2 Mineral compositions

Figure 3.8(a) presents the XRD patterns of WBFA1 before and after pretreatment. To quantitatively analyze the phase alterations in WBFA1 after pretreatment, the Rietveld method was employed. For this analysis, 10% of an internal standard (Si, PDF# 01-086-4266) was homogenously mixed with 90% of ash by weight, and the samples were subjected to XRD testing. The Rietveld analysis was carried out using the BGMIN-based program Profex [166], with results shown in Figure 3.8(b). To validate the accuracy of the quantification results, the amount of portlandite and calcite in WBFA1 before and after pretreatment is also determined by the TGA test (Figure A3.1). The consistent results, as shown in Table A3.2, for portlandite and calcite content from QXRD and TGA indicate good reliability of the QXRD results.

The XRD patterns indicate that quartz and calcite are the two most stable crystalline minerals dominant in both raw and treated WBFA1. When comparing WBFA1 before and after treatment, one notable observation is the disappearance of the diffraction peaks of lime in raw WBFA1, while the intensity of the diffraction peaks of portlandite in treated WBFA1 increases significantly. During the water pretreatment process, lime is hydrated into portlandite (as elaborated in equation 3.2) and possibly other calcium-bearing phases. The QXRD results show that the lime content decreases from 7.31% in raw WBFA1, which is slightly lower than the results from Table 3.3, possibly due to the overestimation of free lime contributed by other calcium-bearing phases during the boiling process, to 0.27% in treated WBFA1. This depletion of lime is particularly favoured, as it suggests that besides metallic aluminum, the other volume stability-threatening factor in cementitious materials has also been removed.

Furthermore, another new phase, Friedel's salt ($\text{Ca}_2\text{Al}(\text{OH})_6(\text{Cl}, \text{OH}) \cdot 2\text{H}_2\text{O}$ PDF #01-078-1219), is formed after pretreatment. This phase is typically reported in cementitious materials exposed to a chloride-rich environment, such as those serving in marine environments [167]. The precipitation of Friedel's salt can be elaborated by equation 3.3. It can be seen that this reaction involves multiple minerals containing calcium (can be possibly from lime, anhydrite,

and portlandite etc.), sulfate, aluminum (can be possibly from oxidized metallic aluminum and aluminum-containing glass phases), and chloride (mainly sylvite).

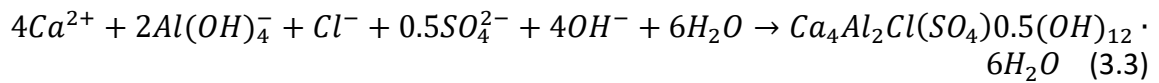


Table 3.5 Chemical compositions of BFA1 before and after pretreatment

	SiO ₂	Al ₂ O ₃	CaO	Fe ₂ O ₃	SO ₃	Na ₂ O	K ₂ O	Cl	MgO	LOI 550 °C	LOI 1000 °C
Raw WBFA1	15.20	4.06	43.65	2.58	6.00	1.77	6.92	3.18	3.33	1.55	6.03
Treated WBFA1	14.98	4.02	41.77	2.32	6.12	1.68	6.53	3.27	2.92	2.67	7.05

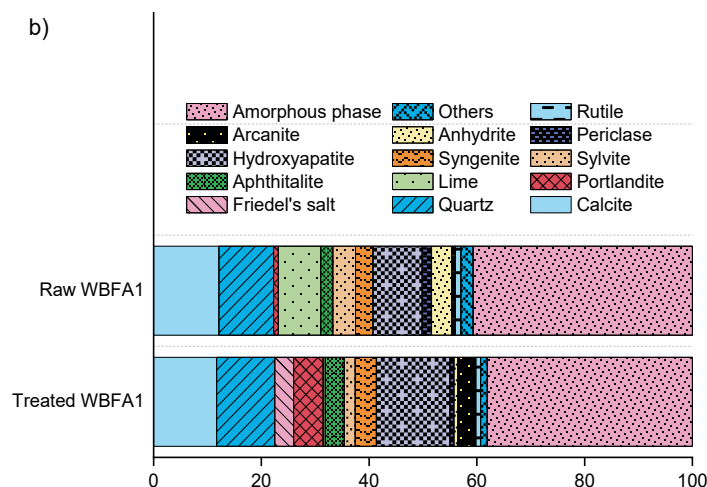
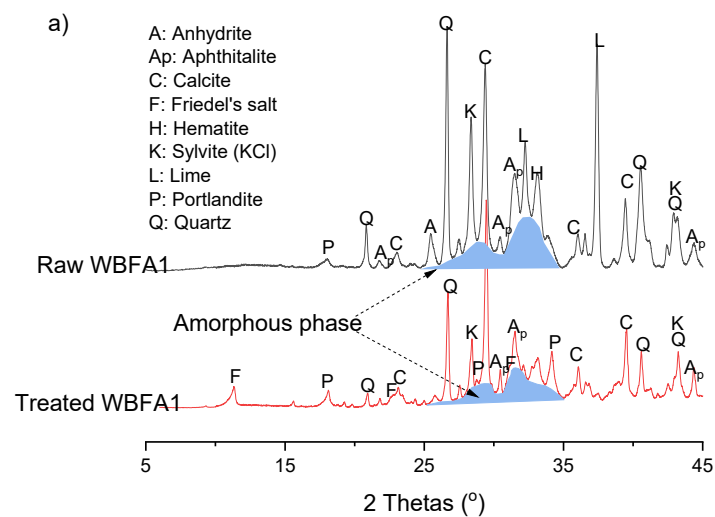


Figure 3.8 Comparison of XRD patterns of WBFA1 before and after pretreatment (a) and their mineral compositions in quantity from QXRD (b)

Table 3.6 Main chemical compositions of amorphous phase in WBFA1 before and after pretreatment

	SiO ₂	Al ₂ O ₃	CaO	Fe ₂ O ₃	SO ₃	MgO	K ₂ O	Others
Raw WBFA1	5.05	4.06	20.73	0.63	1.35	1.42	1.93	3.52
Treated WBFA1	4.18	3.40	20.15	1.06	1.20	2.01	0.55	5.51

The amorphous contents in raw WBFA and treated WBFA are 40.69% and 38.06%, respectively, aligning with previous research indicating a low quantity of amorphous phases in WBFA in the literature. By subtracting the elemental content of WBFA from crystalline phases based on QXRD results, it is possible to obtain the chemical compositions of WBFA in the amorphous phases, as presented in Table 3.6.

It is evident that calcium is the dominant element in the amorphous phase of WBFA1, irrespective of the pretreatment process. This suggests that the primary reactions during pretreatment mainly involve crystalline minerals. To validate the chemical composition of amorphous phase of treated WBFA, a dissolution test according to EN 196-2 was also conducted for the determination of reactive silica content, with results shown in Table A3.3. In general, the reactive silica content from dissolution test is similar to, although slightly higher than, the amorphous silica content obtained from QXRD. This difference may arise because, in the dissolution test, WBFA1 was continuously crushed manually, facilitating the dissolution of a small quantity of quartz during the test.

3.3.2.3 Chemical bonds

The Fourier-transform infrared spectroscopy (FT-IR) technique is used to further investigate the change in molecular structure of WBFA1 before and after pretreatment. The corresponding spectra are displayed in Figure 3.9, and the main band assignments are listed in Table 3.7.

In general, the IR bands in WBFA1 remain almost constant regardless of the pretreatment process. The spectrum of treated WBFA1 is nearly identical to that of raw WBFA1, with three main bands at 875 cm⁻¹, 1105 cm⁻¹, and 1415 cm⁻¹. Specifically, bands at 875 cm⁻¹ and 1415 cm⁻¹ should be assigned to the bending and stretching of CO₃, respectively [168,169]. Based on the mineral phases, these bands should be attributed to the presence of calcite. The band at 1106 cm⁻¹ could be linked to the overlapping of S-O and Si-O bands [170–172]. Besides, reactive silicate phases with different polymerized degrees are shown in the range of 900-1150 cm⁻¹ with several adsorption humps [172–174]. All of this information is well correlated to the previous analysis, showing that WBFA1 is rich in carbonate, silicate, and sulfate minerals.

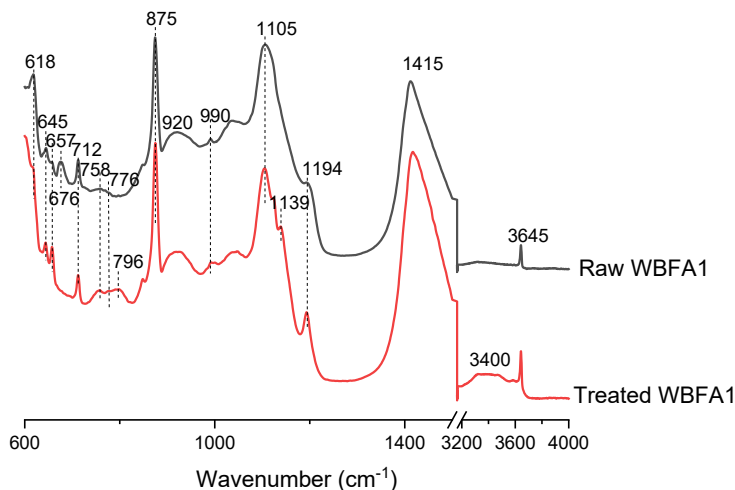


Figure 3.9 FT-IR spectra of BFA before and after pretreatment

Table 3.7 Assignment of the major IR bands in WBFA1

Spectral position (cm ⁻¹)	Assigned to	Reference
3645	OH (Portlandite)	[175]
3400	OH (water molecules)	[129,142,176]
712, 875, 1410	CO ₃	[168,169]
618, 657, 676, 1139, 1194	SO ₃	[170,171]
796	Al-OH	[129,142,176]
900-1150	(Si, Al ^{IV})-O-(Si, M), M refers to alkali-earth metals;	[172-174]

By comparing the WBFA1 before and after pretreatment, a clear difference is the stretching of O-H at 3400 cm⁻¹, which is not clearly observed in raw WBFA1 but is present in treated WBFA1. This band is associated with the chemical water generated during the water pretreatment process [129,142,176]. In addition, the peak at 3645 cm⁻¹, representative of portlandite [175], shows a significant increase after pretreatment, indicating a higher amount of portlandite, which is consistent with the XRD results. A new peak at 796 cm⁻¹, corresponding to the vibration of Al-OH, is seen in the treated WBFA1, which should be due to the formation of Friedel's salt [175,177]. Still, it is important to note that no C-S-H gel-like phases are formed during the pretreatment of WBFA1, as the typical Si-O vibration band for C-S-H gels at 950 cm⁻¹ is not observed.

3.3.2.4 Morphology

The morphology of WBFA1 before and after pretreatment, measured by scanning electron microscopy (SEM), is illustrated in Figure 3.10.

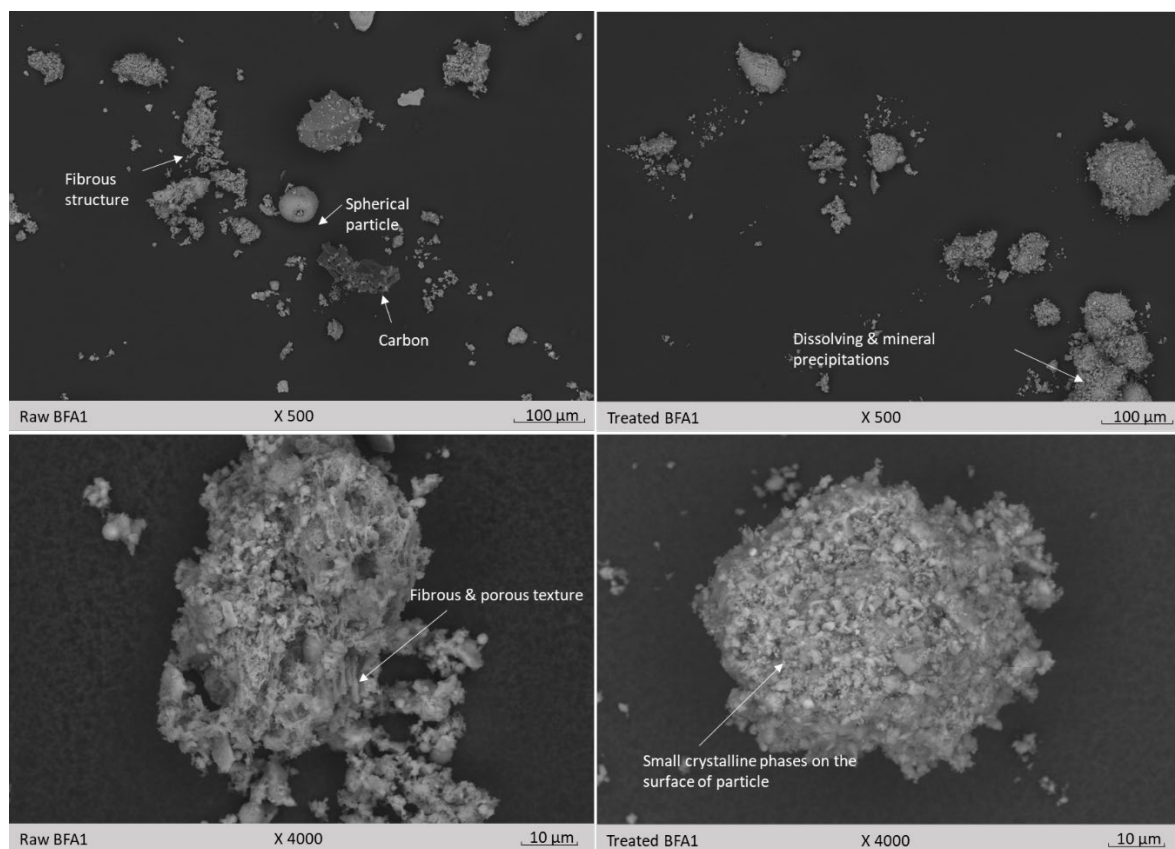


Figure 3.10 Morphology of raw WBFA1 and treated WBFA1

Unlike CFA particles, which are mainly composed of spherical particles as reported in the literature [178], WBFA1 particles exhibit mostly irregular shapes. Additionally, some particles still present a fibrous structure, with substances displaying a flocculence texture on the particle surface. Unburnt porous carbons are also clearly visible in the image, consistent with previous findings in the literature [50,51].

After pretreatment, the treated WBFA1 particles exhibit fewer instances of fibrous texture, possibly due to the grinding process that crushes those particles. Moreover, tiny crystals are observed on the surface of most particles, likely the result of the chemical reaction remnants and erosion observed during the pretreatment process.

3.3.3 Ash dissolution

Dissolution is an important process in the hydration of binders. Both crystalline and amorphous phases undergo dissolution in an aqueous solution, releasing ions that contribute to the formation of reaction products. In this section, the dissolution behaviour of treated WBFA1 in solutions with different alkalinity levels is investigated, aiming to assess the potential of treated WBFA1 in terms of its hydraulic properties, pozzolanic activity, and/or reactivity for alkaline activation.

3.3.3.1 Dissolution in water

The concentrations of Ca, Si, and Al in the leachates of treated WBFA1, BFS, and CFA are plotted as a function of time in Figure 3.11.

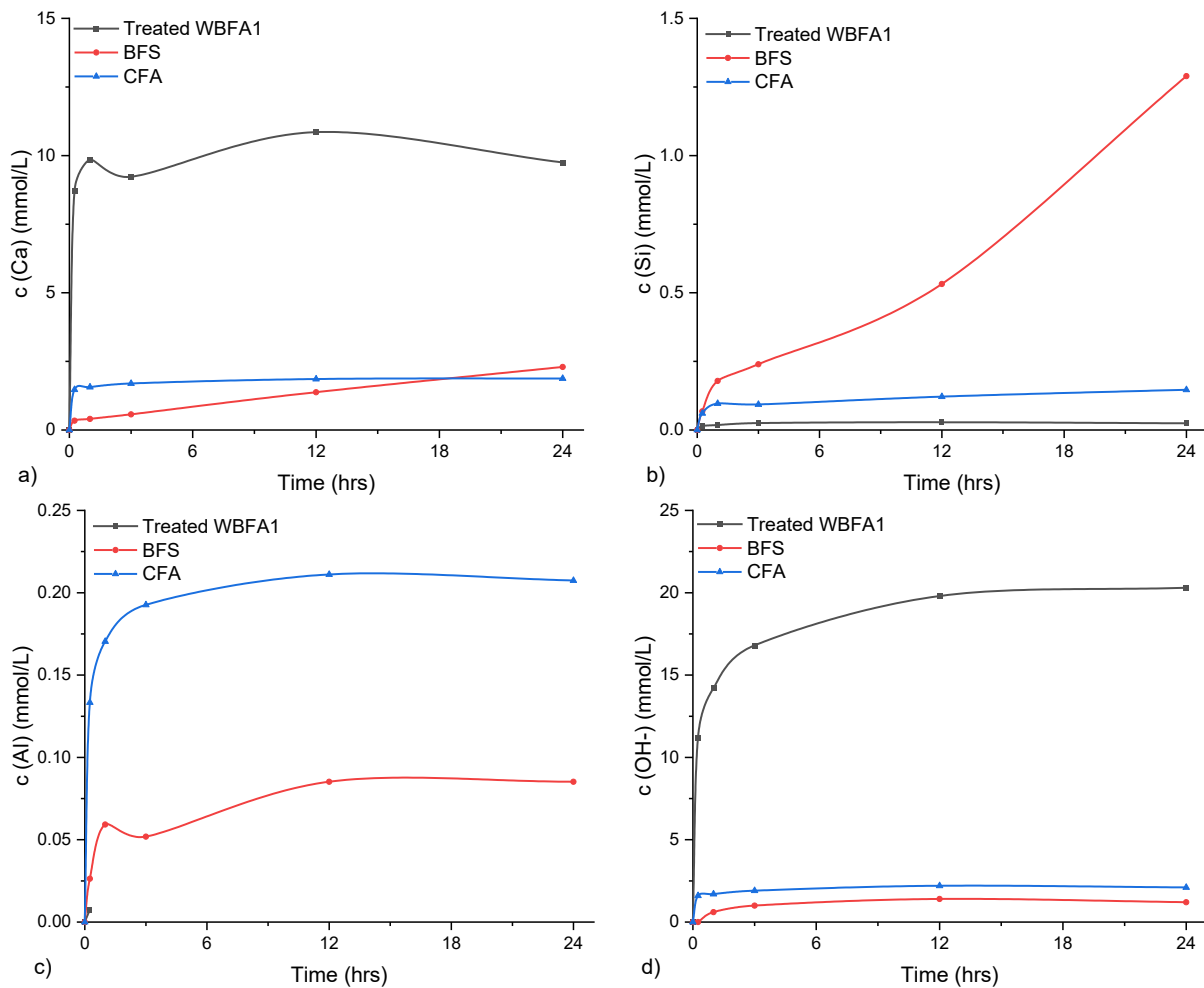


Figure 3.11 Dissolution of treated WBFA1, BFS, and CFA in deionized water

In the leachates of treated WBFA1, the concentrations of Ca exhibit a significant increase within the first 30 minutes, followed by minor fluctuations over the subsequent hours, stabilizing at around 10 mmol/L. It is important to note that the concentrations of Ca in the leachates of treated WBFA1 consistently surpass those in BFS and CFA at any given time. This can be attributed to the high content of portlandite and the availability of Ca in the amorphous phases of treated WBFA1. In the case of CFA leachates, the concentration of Ca experiences a rapid increase within the first 15 minutes, primarily due to the dissolution of free lime. Once the lime is depleted, the concentration of Ca remains relatively constant. On the other hand, the initial concentration of Ca in BFS leachates is the lowest among the three materials. However, it gradually increases over time through a hydrolysis process, facilitated by the dissolution of a substantial amount of Ca from the amorphous phases.

In regards to the dissolution of aluminosilicates, it is found that the concentrations of Si in treated WBFA1 leachates are plainly low, with a minor increase over time. Furthermore, the concentrations of Al fall below the detection limit. The results are consistent with the limited presence of aluminosilicates in WBFA1, as indicated by its chemical compositions. In contrast, in the BFS and CFA leachates, a higher amount of Al and Si can be dissolved compared with those in treated WBFA1 leachates, as a consequence of the significant

presence of amorphous aluminosilicates in these two materials that are more susceptible to be dissolved.

Figure 3.11 (d) illustrates the concentration of hydroxyl ions in leachates during the dissolution process. A small amount of hydroxyl ions can be released from BFS through the hydrolysis process, with a gradual increase over time [179]. The concentration of hydroxyl ions in CFA leachates increases initially in the first 15 minutes due to the presence of lime, and it remains constant afterwards. Notably, the concentration of hydroxyl ions in leachates from treated WBFA1 is significantly higher than BFS and CFA throughout all stages. This discrepancy can be attributed to the substantial amount of portlandite and alkaline minerals in treated WBFA1. After continuous dissolution for 24 hours, the concentration of hydroxyl remains at 20.30 mmol/L in treated WBFA1, resulting in a pH value of the leachates reaching 12.31. The highly alkaline nature of treated WBFA1 is identified.

3.3.3.2 Dissolution in alkaline solutions

Figures 3.12 and 3.13 present the concentrations of Ca, Si, and Al in leachates of treated WBFA1, BFS, and CFA dissolved from NaOH solutions with molarities of 0.1M and 3M, respectively.

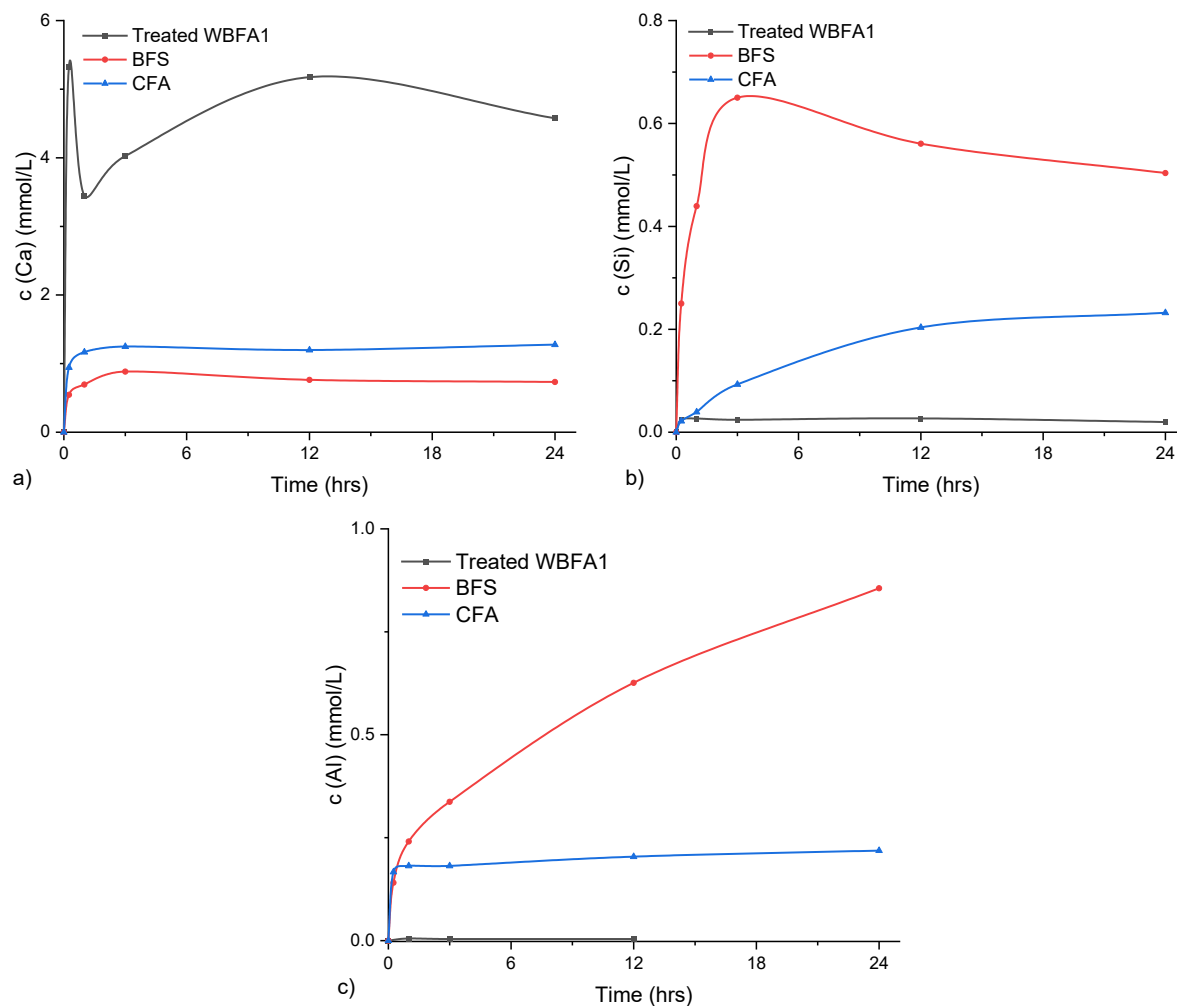


Figure 3.12 Dissolution of treated WBFA1, BFS and, CFA in 0.1 M NaOH solution

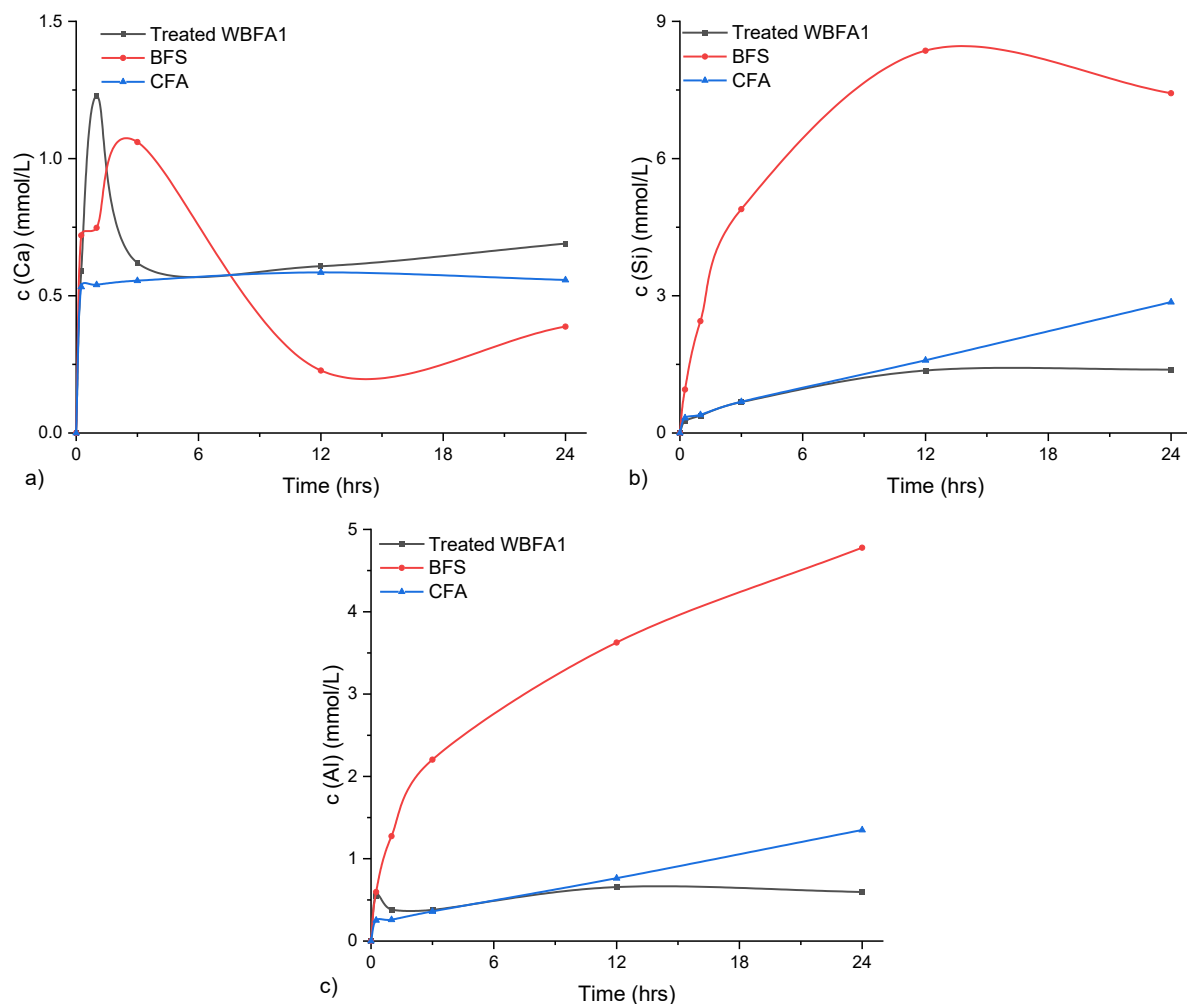


Figure 3.13 Dissolution of treated WBFA1, BFS, and CFA in 3 M NaOH solution

With the increment in alkalinity of the solutions, the concentration of Ca in the leachates decreases in all three materials. This can be attributed to the lower equilibrium aqueous solubility of Ca species in solutions with higher alkalinity [180]. In both 0.1M and 3M NaOH solutions, the concentration of Ca leached from treated WBFA1 and BFS increases initially and subsequently decreases. This reduction could be ascribed to the precipitates, including portlandite and possibly other Ca-bearing phases [164]. With continuous dissolution, the concentration of Ca would increase further.

The high alkalinity of solutions could promote the initial dissolution of aluminosilicates. As depicted in Figures 3.12 (b) (c) and 3.13 (b) (c), the concentrations of Al and Si in the leachates increase exponentially with the increase in the alkalinity of the solutions. This is in agreement with previous research as the high alkaline solution could accelerate the dissolution of amorphous aluminosilicates [164,180,181]. Although more Al and Si were dissolved from the treated WBFA1 in contact with 3M NaOH solution, it should be noted that due to the low content of amorphous aluminosilicates, the concentrations of Al and Si in WBFA1 leachates are still the lowest among the three materials. Unlike BFS and CFA from which the dissolved Al and Si increased over time, the concentrations of Al and Si in the

treated WBFA1 leachates remained steady after 12 hours of dissolution test, which is due to the completion of the depletion of the amorphous aluminosilicates.

3.3.4 Comments on the utilization approaches for treated WBFA1

Considering the characteristics of treated WBFA1, its potential as a binder component can be discussed in the following aspects:

1) *Self-hardening (latent hydraulic) material.*

Self-hardening properties encompass the ability of materials to react with water and solidify with certain mechanical strength. These reactions typically involve the formation of hydrates, such as C-S-H gels, portlandite, and/or ettringite, as reported in previous research [182,183]. However, it is unlikely that treated WBFA1 will exhibit further self-hardening properties. The limited dissolution of Al and Si from treated WBFA1 in water suggests that no additional hydrates are expected to precipitate.

2) *SCMs in blended cement or precursors in alkali-activation*

For both SCMs and precursors, a large content of dissolvable aluminosilicates is demanding. The presence of Al and Si is crucial for promoting the formation of C-(A)-S-H gels in blended cement and calcium-rich geopolymers, or N-A-S-H gels in aluminosilicate-based geopolymers [184–187]. However, when exposed to mimicked cement pore solutions (0.1M NaOH solutions), the amount of dissolved Si and Al from treated WBFA1 is considerably lower than those from BFS and CFA. The dissolution can be enhanced in highly alkaline solutions. Although a higher amount of Al and Si can be dissolved from treated WBFA1 in a 3M NaOH solution, the concentrations of Al and Si remain relatively constant after about 12 hours due to the limited amount of dissolvable components. Therefore, it can be concluded that treated WBFA1 is not suitable as a new source for SCMs or precursors.

3) *Minerals with synergistic effect*

It is interesting to highlight the high alkalinity of treated WBFA1, as well as the large presence of calcium and sulfate-bearing minerals. It is seen that the leachates of treated WBFA1 in water exhibit a pH value above 12 after 3 hours, with a water to solid ratio at 100. In binder preparation, a much lower water to solid ratio would be applied, thus a higher pH value in the pore solution can be obtained. The high alkalinity can be beneficial for the dissolution of pozzolanic materials. Moreover, the calcium and sulfate-bearing phases in treated WBFA1 can react with aluminate phases to generate ettringite. In general, these features of WBFA1 can promote the dissolution of pozzolanic materials, leading to the generation of hydrates. Therefore, it can be deduced that the combination of treated WBFA1 and pozzolanic materials can be promising to formulate cement-free binders. Since neither treated WBFA1 nor the pozzolanic materials alone can achieve significant hydration and mechanical strength in water, it is anticipated that these materials will function synergistically as a mineral for hydration. Detailed research on the binary pastes is subsequently conducted in Chapter 4 with an investigation of reaction mechanisms and microstructure evolution.

3.4 Conclusion

In this chapter, three types of WBFA were collected and subjected to initial analysis. Among them, the most promising candidate was selected for comprehensive pretreatment, characterization, and evaluation of potential utilization approaches. The primary conclusions drawn are as follows.

- 1) The as-received three types of WBFA are characterized and screened based on their physicochemical properties. WBFA1 was selected as the most feasible candidate for construction purpose. WBFA2 was excluded mainly due to its high content of lead, while WBFA3 was excluded for its low representativeness in the chemical compositions.
- 2) The proposed pretreatment process for WBFA1 involves water pretreatment followed by drying and grinding. After 6 days of water pretreatment, metallic aluminum is fully oxidized, and free lime contents decrease to 0.27%, effectively eliminating factors that threaten the volume stability of cementitious materials. The subsequent drying and 10-minute grinding of water-treated WBFA1 help to pulverize agglomerated particles, producing fine particles suitable for use as a binder component.
- 3) The physicochemical properties of treated WBFA1 are thoroughly analyzed. A specific focus on the functional elements, Ca, Si, and Al, involved in the reaction of cementitious materials is studied through the dissolution tests. The results show that only limited amounts of Al and Si can be dissolved from treated WBFA1, while a high amount of Ca can be extracted. Due to the high availability of calcium and its elevated alkalinity in treated WBFA1, it is not recommended to utilize treated WBFA1 as a conventional SCM. Instead, it is advised to valorize it as a synergistic mineral to enhance the hydration of pozzolanic materials.

Appendix

The heavy metal leaching of treated WBFA1 was determined according to EN 12457, where ash was mixed with deionized water with a liquid to solid ratio at 10. The sample was kept shaking on the shaking table with a speed of 200 rpm for 24 hours, and eluate was collected for measuring the concentration of heavy metals using ICP-MS. The results are provided in Table A3.1.

Chromium (Cr) is found as the only element that exceeds the requirement of un-moulded building materials according to the Dutch Soil Quality Decree (SQD) [188]. Still, the treated WBFA1 can comply with the requirement of IBC (Isolatie, Beheer en Controle) building materials. This means that WBFA can be directly used as construction material under proper conditions, for instance, avoid direct contact with underground water.

Figure A3.1 shows the TGA-DTG curves of WBFA1 before and after pretreatment. The test is conducted at argon atmosphere, from 40 °C to 1000 °C with a temperature rising rate of 10 °C/min, aiming to quantify mineral phases such as calcite and portlandite.

Table A3.1 Heavy metal leaching (mg/kg) from treated WBFA1 and comparison with Dutch regulation

	As	Ba	Cd	Cr	Cu	Ni	Pb	Zn
Measured	0.04	7.60	-	4.80	-	0.03	0.60	2.90
Un-moulded building materials	0.90	22	0.04	0.63	0.90	0.44	2.30	4.50
IBC building materials	2	100	0.06	7	10	2.10	8.30	14

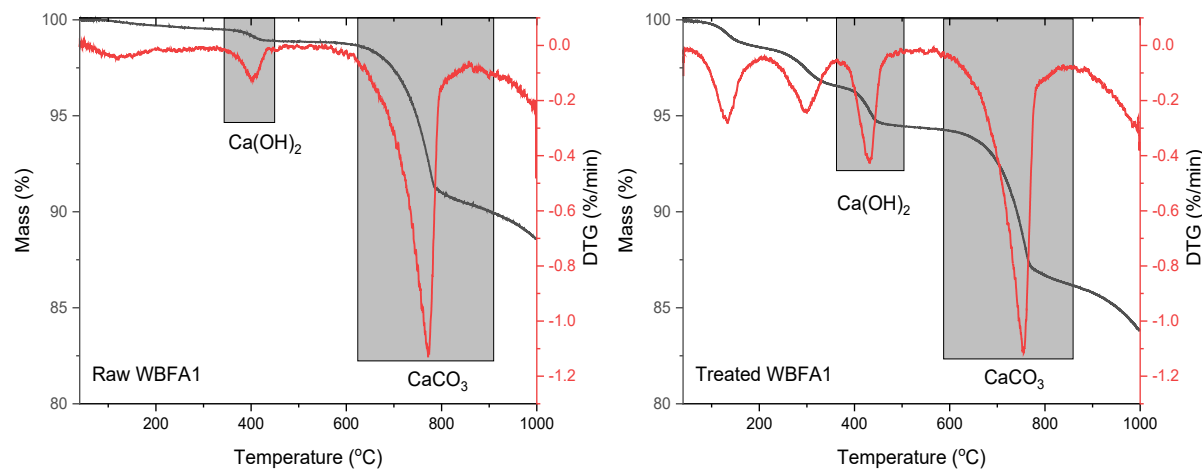


Figure A3.1 TGA-DTG curves of WBFA1 before and after pretreatment

Table A3.2 Comparison of the quantifications results of portlandite and calcite in WBFA1 before and after pretreatment using TGA and QXRD analysis

	Portlandite		Calcite	
	TGA	QXRD	TGA	QXRD
Raw WBFA1	1.12	0.88	12.13	12.01
Treated WBFA1	5.92	5.51	11.32	11.7

Table A3.3 Reactive silica content determined by dissolution test according to EN 196-2

Raw WBFA1	Treated WBFA1
5.97	5.35

The reactive silica content of WBFA1 before and after pretreatment is determined by the dissolution test according to EN 196-2. WBFA1 was dissolved in dilute hydrochloric acid and further treated in a boiling sodium carbonate solution. The chemical compositions of the insoluble residual can be then determined by XRF technique, and the reactive silica can be calculated by subtracting the insoluble silica from the total silica content in WBFA1.

Chapter 4

Cement clinker-free binder: wood biomass fly ash-blast furnace slag binary material

4.1 Introduction

The results in Chapter 3 suggest integrating treated WBFA1 with pozzolanic materials to develop a new binder system. To validate this hypothesis, this chapter steps into the formulation a clinker-free binder with treated WBFA1 and pozzolanic materials, where blast furnace slag (BFS) is selected as the pozzolanic material due to its high reactivity.

The objective of this chapter is to design a cement-free binder with treated WBFA1 and BFS. Through the investigation of the reaction process and the microstructure development of the binder, the mechanism of how treated WBFA1 impacts the reaction process can be revealed. This knowledge would serve as a basis for tailoring the performance of WBFA-BFS binary binder.

4.2 Materials and experiments

4.2.1 Materials and mixtures

The raw materials include treated WBFA1 and BFS. For clarity, in the following thesis, the abbreviation WBFA refers to the treated WBFA1. The chemical compositions, mineral compositions, and physical properties of WBFA and BFS can be found in Section 3.2.2. The particle size distribution of BFS and WBFA can be found in Figure 3.1 and Figure 3.7, respectively.

Table 4.1 Mixture proportions of pastes

Groups	WBFA (wt. %)	BFS (wt. %)	Water to binder ratio (W/B)
B0S100	0	100	
B30S70	30	70	
B50S50	50	50	0.40
B70S30	70	30	
B100S0	100	0	

Table 4.1 shows the mixture proportions of WBFA-BFS binary pastes. Pastes with varying WBFA to BFS ratios, namely B30S70, B50S50, and B70S30, were used for investigations of the reaction kinetics, microstructure evolution, and compressive strength. Singular pastes with pure WBFA (B100S0) and pure BFS (B0S100) cannot generate strength for demoulding, thus were only introduced as reference samples in the isothermal calorimetry test to compare with the three binary mixtures. The water to binder ratio (W/B) of pastes was kept at 0.40 to ensure a satisfactory workability for sample casting.

4.2.2 Experimental methods

4.2.2.1 Isothermal calorimetry

An isothermal calorimetry test was conducted to investigate the reaction kinetics of the pastes. The experiments were carried out using a TAM-Air-314 isothermal conduction calorimeter. A calibration program was executed at a temperature of 20°C for at least 24 hours before the experiments. During the test, pastes were prepared by hand-mixing, and approximately 7 grams of fresh paste were used for the tests. A fixed amount of sand with a heat capacity equivalent to that of the pastes, was used as reference material. Given the slow reaction of WBFA-BFS pastes, the test was carried out for 14 days.

4.2.2.2 Pore solution

The ion concentration in the pore solutions was measured to study the reaction process of binary pastes. To prepare the samples for pore solution analysis, fresh pastes were firstly cast into cylindrical polyethylene bottles with a diameter of 35 mm and a height of 70 mm. Samples were well sealed and cured at 20 °C for 1 day, 7 days, 14 days, and 28 days until pore solution extraction.

The extraction of pore solutions from pastes was performed using the steel-die method [189]. Specimens were subjected to a gradually increasing load by a high-pressure device up to 250 MPa, and the pore solutions would be gradually extracted. After collection, the pore solutions were vacuum filtered to remove the retained particles. The concentrations of OH⁻ were determined by titration against hydrochloric acid (0.1 M) with a phenolphthalein indicator. The concentration of chloride was determined by Mohr's method [190,191]. The remaining pore solutions were acidified by HNO₃ solutions, diluted, and then analysed for the concentrations of Ca, Si, Al, K, S, Na by Inductively Coupled Plasma Optical Emission Spectroscopy (ICP-OES).

4.2.2.3 Reaction products characterization

- Sample preparation

Before test, samples should undergo a hydration stoppage program to ensure that they retain the hydration at a designated time. The hydration stoppage of specimens was carried out by solvent change methods as suggested by Snelling et al. [192]. The samples were immersed in isopropanol and manually crushed into fines in the mortar with a pestle. Afterwards, the crushed samples were immersed in isopropanol for 15 minutes and then filtered. Residuals were rinsed with diethyl ether, followed by oven drying at 40 °C for about 8 minutes to facilitate the evaporation of the organic solvents. The dried samples were then collected and subjected to characterization.

- X-ray diffraction (XRD) test

XRD was conducted to identify the crystalline phases in the binary pastes. A Bruker D8 Advance diffractometer with Cu $\text{K}\alpha$ radiation was used for this experiment. The operating voltage and current were set at 45 kV and 40 mA, respectively. The diffraction scanning of 2θ ranges from 5-70° with a counting speed of 0.01 °/s.

- Fourier-transform infrared spectroscopy (FTIR)

FTIR was applied to investigate the evolution of the chemical bonds of pastes during the hydration process. The test was performed with a Spectrum TM 100 Optical ATR-FTIR spectrometer. The scanning range is between 600-4000 cm^{-1} with a resolution of 4 cm^{-1} . An average of 20 scans were applied to obtain reliable spectra.

- Thermogravimetric analysis (TGA)

TGA was used as a semi-quantification tool for analysing the contents of hydrates in the pastes. The test was operated with a NETZSCH STA 449 F3 Jupiter instrument. An argon atmosphere was employed with a temperature range from 40 to 1000 °C and a heating rate of 10 °C/min. Approximately 30 mg of powder samples were used in each test.

4.2.2.4 Microstructure characterization

- Mercury Intrusion Porosimetry (MIP)

The MIP test was performed to determine the pore structure of pastes. Initially, specimens were sawed into small pieces and immersed in the isopropanol for approximately 5 days, with the solvent being renewed every day. Afterwards, samples were freeze-dried to allow the evaporation of isopropanol until a constant weight was reached. An AutoPore IV mercury porosimeter was used with a mercury contact angle of 141° and a surface tension of 480 mN/m. The intrusion process includes a low-pressure program ranging from 0 to 0.14 MPa and a high-pressure program ranging from 0.14 to 210 MPa. Pore diameter can thus be determined by the Washburn equation, which correlates pore diameter with pressure [193].

- Scanning electron microscopy (SEM) coupled with electron dispersive spectroscopy (EDS)

Backscattered electron (BSE) is one of the electrons used in SEM for better identifying phases through a distinguished grey scale variation, mainly influenced by the atomic number [194]. Hence, BSE was used for microstructure characterization. Before experiments, the freeze-dried samples, as illustrated in MIP sample preparation, were impregnated with a low viscosity epoxy resin, then subjected to a grinding and polishing process down to 0.25 μm . Finally, the well-polished samples were carbon-coated and prepared for test.

A FEI QUANTA FEG 650 ESEM (Thermo Fisher Scientific), equipped with a solid-state EDS detector, was used under a high vacuum mode. The working voltage was kept at 15 kV and the working distance was 10 mm [195].

Owing to the complexity of the mineral compositions of the WBFA, the selective dissolution method [196] commonly used for measuring the reaction degree of BFS is not applicable for determining the reaction degrees of BFS in the WBFA-BFS binary pastes. Instead, the image analysis technique can be employed. However, it is challenging to directly use

greyscale to distinguish the area of BFS and WBFA, as the complexity of WBFA leads to it covering a wide range of greyscales. Therefore, a modified image analysis technique was adopted, which incorporates EDS mapping, analyzing the average elemental ratios in each particle, and greyscales analysis. For each picture, 50 frames of mapping were captured to ensure reliable results.

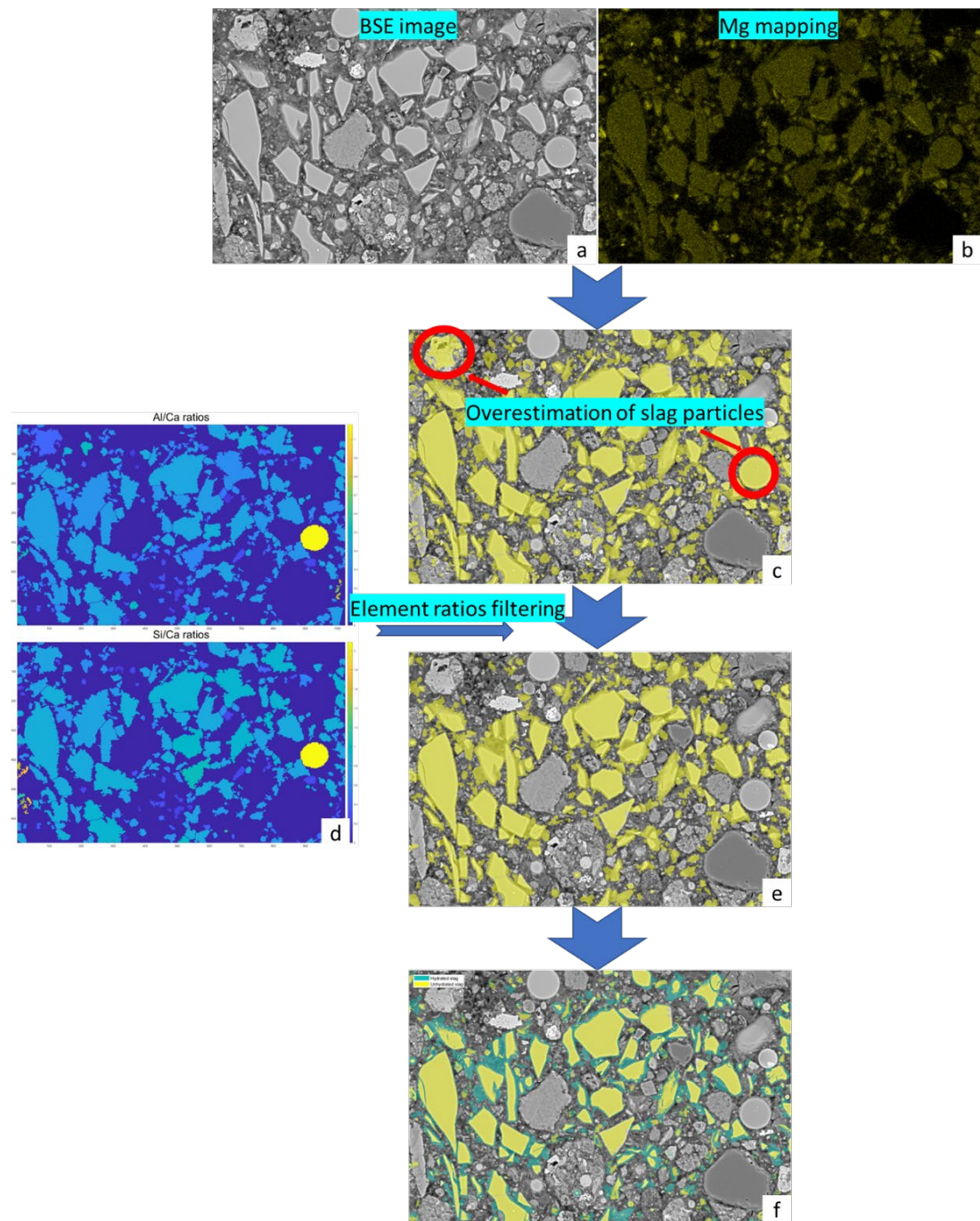


Figure 4.1 Schematic diagrams of analyzing the reaction degree of BFS by BSE-EDS mapping

The schematic for determining the reaction degree of BFS is present in Figure 4.1. Firstly, Mg mapping (Figure 4.1 (b)) was used to define the original boundary of BFS grains, as Mg is believed to remain stable during the reaction of BFS [197,198]. By overlapping the Mg mapping onto the BSE image, an overestimation of BFS particles was observed (Figure 4.1(c)), owing to the heterogeneous distribution of Mg in WBFA particles. To screen out the Mg-containing WBFA particles, an elemental ratio evaluation method was individually conducted for each particle. Within individual particle boundaries, the total atomic weight of specific elements can be summed up. Thus, the elemental ratio evaluation can be conducted for each Mg-containing particle, as indicated in the heatmap (Figure 4.1 (d)). It was observed that Mg-containing WBFA particles exhibited extremely low or high values in Si/Ca and Al/Ca ratios compared to BFS particles. Consequently, WBFA particles can be eliminated by setting filters based on the elemental ratios (Figure 4.1 (e)). Subsequently, a clear BFS boundary was established. Hydrated areas were then segmented based on grayscale variations in the selected particles, with hydrated areas typically appearing as dark grey [199]. The reaction degree of BFS could then be calculated with equation 4.1. The resolution of the mapping was 203.32 nm/pixel, with a domain size of 628×1024 pixels. It is suggested that a surface area of $4.0\text{--}5.0 \times 10^5 \mu\text{m}^2$ should be acquired for BSE image analysis to ensure representativeness [200]. Therefore, about 15 EDS mappings were conducted for each sample to ensure the representativeness of the results. This requires a total of 8 hours for each sample.

$$DoH \text{ Slag} = \frac{\text{Hydrated slag area}}{\text{Total slag area}} \times 100\% \quad (4.1)$$

4.2.2.5 Compressive strength

The compressive strength of binary pastes was measured using cubic specimens with a dimension of 4 cm. The fresh pastes were firstly sealed cured for 3 days before demoulding, subsequently cured in the fog room at a temperature of 20 °C and RH above 95%. The compressive strength of binary pastes at age of 7 days, 28 days, and 60 days was measured. The average compressive strength of six samples was reported.

4.3 Results

4.3.1 Heat evolution

Figure 4.2 plots the normalized heat flow of pastes with varying WBFA to BFS ratios. The first exothermal peak is identified once the pastes are placed in the calorimeter chamber (Figure 4.2 (a)). It is believed that this peak is mainly due to the wetting and dissolution of raw materials [201,202]. Besides this exothermal peak, no clear peak could be further found in the singular pastes (BOS100 and B100SO). On the contrary, binary pastes present additional exothermic peaks later on. These results imply that while the reactions in the singular pastes are limited, more intensive reactions occur in the binary pastes, leading to the generation of a substantial amount of reaction products.

The heat flow curves of the binary pastes, in general, are similar to those reported for cement hydration [203]. To clarify the reaction process, besides the wetting and dissolution-introduced thermal peak, three other distinguishable stages could be observed in the binary pastes:

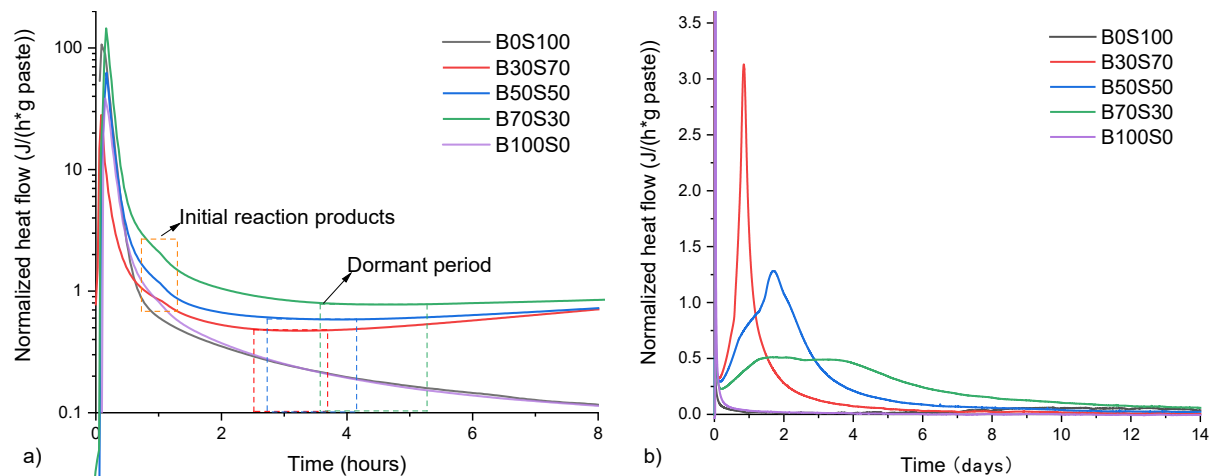


Figure 4.2 Normalized heat flow of pastes (a) at first 8 hours; (b) until 14 days

- **Dormant period**

The dormant period follows the end of the first main peak. It is seen that during this period, the heat flow of pastes remains low for a short period. By amplifying the exothermal heat flow curves of binary pastes in the first 8 hours, it is observed that the dormant period comes earlier with a shorter duration in pastes with a lower WBFA/BFS ratio. Therefore, it can be deduced that pastes with a lower amount of WBFA tend to have a more intensive reaction in the initial reactions.

- **Acceleration and deceleration periods**

Following the dormant period, the main exothermal peaks (acceleration and deceleration stages) are observed in binary mixtures, and should correspond to the large amounts of hydrates formation. It is interesting to note that with the increasing WBFA/BFS ratios, pastes are found with a clear second wave or shoulder close to the main peak, which is similar to the hydration characteristics of cement [204]. Given the high amount of sulfate in WBFA, it can be deduced that the wave is associated with the precipitation of ettringite [205,206]. Increasing WBFA/BFS ratios results in a larger amount of sulfate in the pastes, promoting the formation of ettringite and therefore, a broader second main peak is observed in pastes with a larger proportion of WBFA.

- **Steady period**

The steady stage follows the end of the deceleration period, during which the reaction rate of pastes gradually decreases to a low extent while maintaining a mild reaction. Mixtures with a higher WBFA/BFS ratio are detected with a higher heat release, indicating a more severe reaction. This can be attributed to the continuous supply of alkalis, sulfate, and portlandite from WBFA, which promotes the reaction of BFS during the later hydration stages.

4.3.2 Pore solution chemistry

4.3.2.1 Ion concentrations

The ion concentrations in binary pastes at 1 day, 7 days, 14 days, and 28 days are present in Figure 4.3. The reasonable charge balance between major positive ions and negative anions, as illustrated in Figure 4.3 (a), implies an overall satisfactory result.

The concentration of Ca (Figure 4.3 (b)) undergoes a significant decrease from 1 day to 7 days in both B50S50 and B70S30. Changes after 7 days are not significant. In contrast, in B30S70, the concentration of Ca slightly increases from 1 day to 7 days, followed by a marginal decrease at 14 days and a marginal increase at 28 days. The overall concentration changes in B30S70 regarding [Ca] are relatively low.

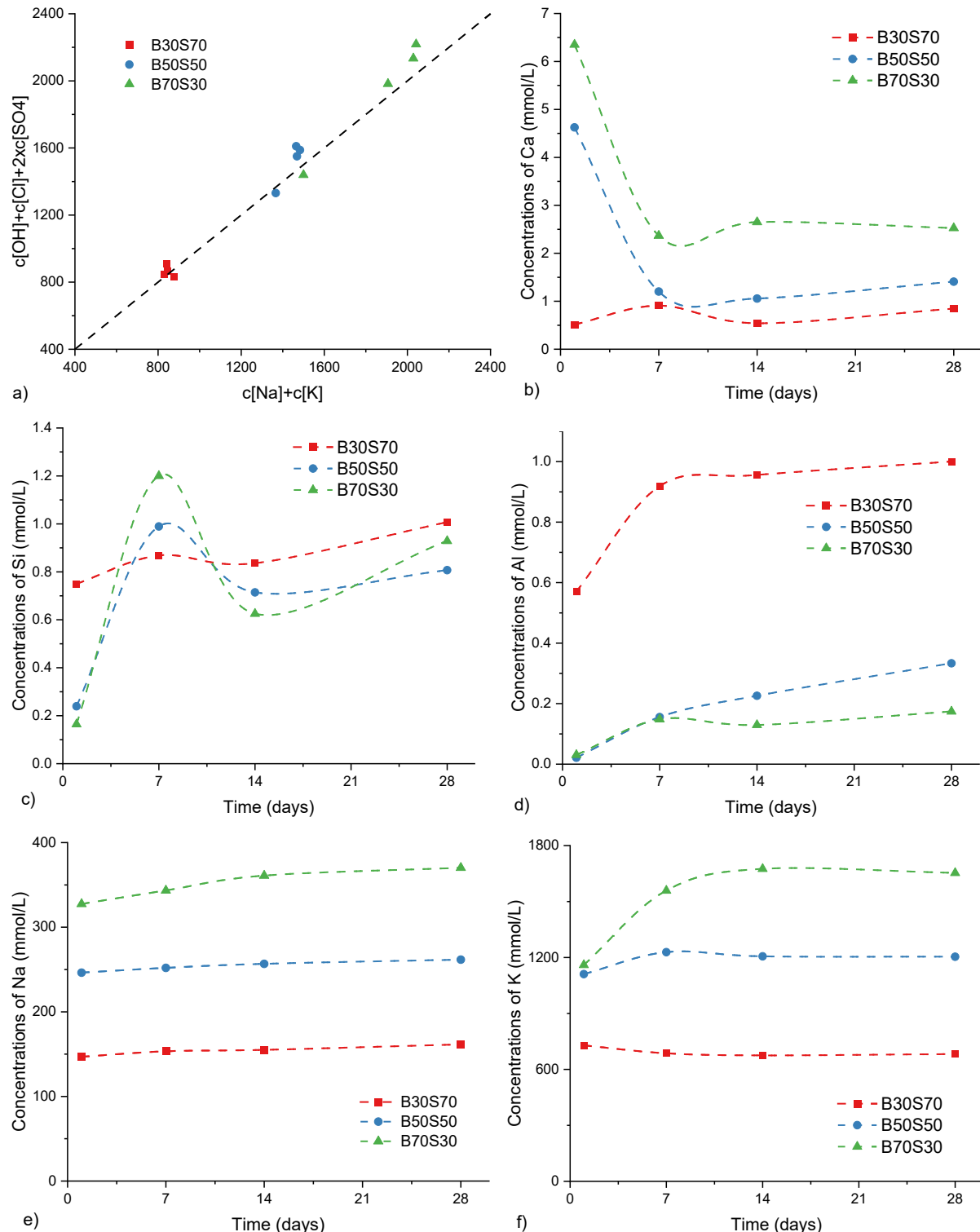


Figure 4.3 ion concentration in the pore solutions of pastes at 1 day, 7 days, 14 days, and 28 days

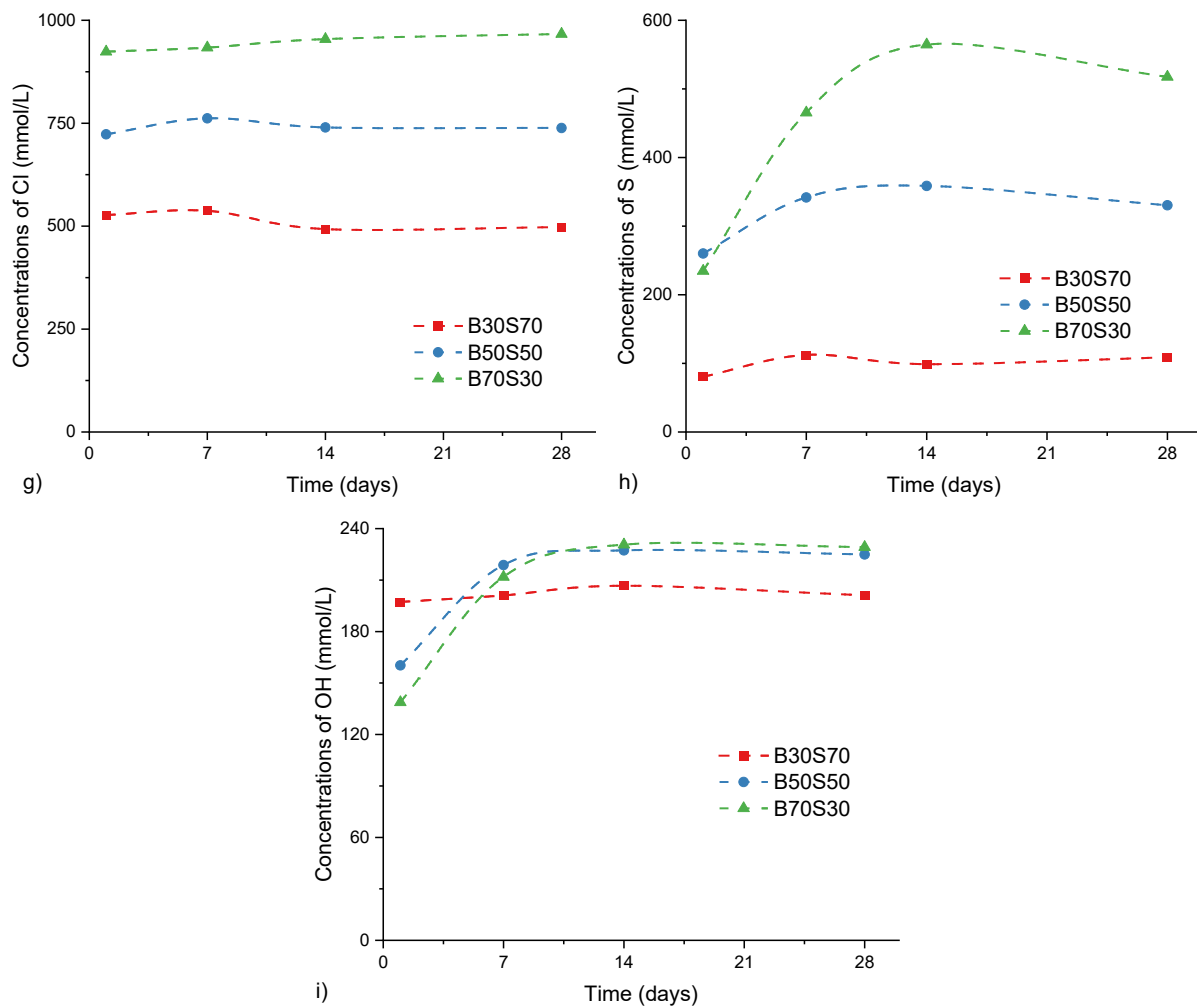


Figure 4.3 ion concentration in the pore solutions of pastes at 1 day, 7 days, 14 days, and 28 days (Continued)

While the content of calcium in both WBFA and BFS is relatively high (about 40% w.t%), which may lead to debateable arguments for the variation of Ca concentrations, the [Si] and [Al] in the pore solutions should mainly come from the dissolution of BFS. It is interesting to point out that the concentrations of [Si] and [Al] do not decrease proportionally with the decrease in BFS. The concentrations of [Si] in B50S50 and B70S30 are comparable at 1 day, which is much lower than that in B30S70. The same trends are also seen for [Al]. Therefore, it can be deduced that the dissolution of BFS is initially suppressed in samples with more WBFA. This also agrees with the results in isothermal calorimetry, where pastes with a larger amount of BFS exhibit slower initial reactions.

The alkalis (Na, K) in pore solutions mainly result from the dissolution of alkaline minerals, primarily originating from WBFA based on its chemical compositions as outlined in Table 3.2. An intriguing observation can be seen in the concentrations of [K], where B70S30 contains a much higher amount of bulk potassium found with similar concentration of [K] to that of B50S50 at 1 day. Pastes with more WBFA is seen with a more pronounced increment in the concentrations of [K] from 1 day to 7 days. This indicates that the initial dissolution of potassium salt in WBFA is to some extent restrained in pastes with a higher amount of WBFA.

For anions, chloride is primarily dissolved from sylvite (KCl) in WBFA as the main highly soluble chloride-bearing phase. The concentrations of [Cl] are proportional to the amount of WBFA in the pastes. In B30S70 and B50S50, the concentration of [Cl] slightly decreases over time, while it remains comparable in B70S30. Considering the gradual reduction of pore solutions through hydration, it can be expected that chloride is gradually immobilized due to the formation of chloride-bearing hydrates. The concentration of [S], on the other hand, exhibits an identical time-dependent trend to that of [K]. For instance, B70S30 contains a comparable concentration of both [S] and [K] to those in B50S50 at 1 day. The concentrations of these two elements show a similar increment with time until 28 days. Therefore, it can be deduced that pastes with more WBFA might exhibit a restrained initial dissolution of minerals containing these two elements, such as arcanite (K_2SO_4) and syngenite ($K_2Ca(SO_4)_2 \cdot H_2O$).

The concentration of [OH] is present in Figure 4.3 (i). Despite the fact that WBFA is the main alkaline resource in the pastes, it is surprising to find that samples with a higher WBFA/BFS ratio have a lower concentration of [OH] at 1 day, indicating that B30S70 has the highest alkalinity whereas B70S30 has the lowest alkalinity at 1 day. The concentrations of [OH] in B50S50 and B70S30 increase rapidly from 1 day to 7 days, then remains almost constant until 28 days. In contrast, the concentrations of [OH] in B30S70 is rather stable from 1 day to 28 days. Based on the development of alkalinity of pore solutions, together with the concentrations of [K] and [S] from WBFA, and [Si] and [Al] from BFS, it can be further convinced that the initial dissolution of both WBFA and BFS is restrained in pastes with a higher proportion of WBFA. Still, it is important to note that this does not indicate that WBFA only presents a side effect in the hydration of binary pastes. With the increment of WBFA, the significant increase in alkalinity in later hydration promotes the dissolution of aluminosilicates from BFS, which can be convinced by the increased concentrations of [Al] and [Si] at later hydration.

4.3.2.2 Effective saturation indices (ESI)

Based on the compositions of pore solutions, it is possible to predict the potential hydrates through thermodynamics. To conduct this, a Gibbs Energy Minimization Software (GEMS) [207,208] with the CEMDATA18 database [209] was applied, with the ion concentration of pore solutions in Section 4.3.2.1 used as input. This enables the calculation of ESI for specific hydrates, providing an expectation for the possible hydrates. A positive value of ESI indicates the potential precipitation of a specific phase, while a negative value means the phase is undersaturated and thus cannot be generated. An error and uncertainty range of ± 0.20 is suggested considering the error of the solubility products [210]. Based on the ions available, the ESI of C-S-H gels, ettringite, portlandite, and chloride bearing hydrates Friedel's salt are calculated, enabling an initial estimate of possible hydrates and exploring the reasons for the evolution of ion concentration with time.

As shown in Figure 4.4, C-S-H gels and ettringite are the most probable hydrates to be generated in the binary pastes, which are also widely reported as the main hydrates in cement [211,212]. For portlandite, its negative ESI is observed in all mixtures from 1 day to 28 days. Since portlandite is one of the minerals in WBFA (5.56% wt.), its continuous consumption is expected with the hydration of the binary pastes

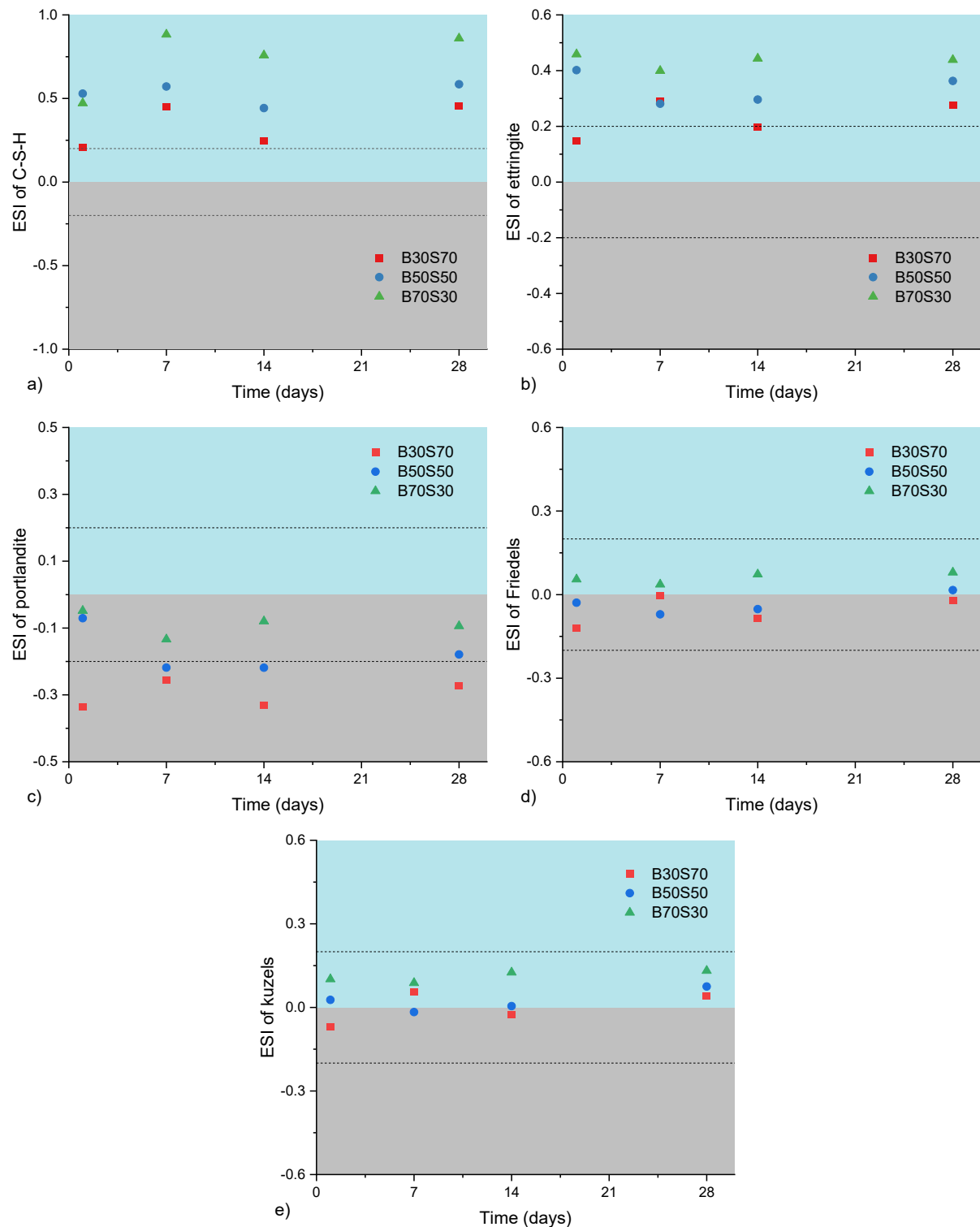


Figure 4.4 ESI of phases with interests

The chloride is assumed to be encapsulated in the hydrates due to the general decrease in concentrations over time. Hence, the ESI of the two commonly formed chloride-containing hydrates in cementitious materials, namely Kuzel's salt and Friedel's salt, are calculated. Although some negative values are obtained in mixtures with a low WBFA/BFS ratio (especially for Friedel's salt), it should be noted that these values are still greater than the

thresholds of uncertainty (-0.2). Therefore, it is still possible for the precipitation of these two phases from a thermodynamic standpoint. A detailed characterization of reaction products using XRD shall be provided in the following sections to confirm the actual formed hydrates.

4.3.3 Solid phases

4.3.3.1 XRD analysis

The XRD patterns of binary pastes at 7 days and 60 days are plotted in Figure 4.5. Generally, the phase compositions in the three mixtures are consistent. The primary crystalline phases observed include ettringite, Friedel's salt, portlandite, quartz, and calcite in all mixtures, irrespective of curing ages.

Quartz and calcite are two stable phases that originate from WBFA according to Section 3.3.2.2. Ettringite can be seen as one of the main crystalline hydrates, with strong diffraction peaks identified in all binary pastes. This is in line with the ESI calculations suggesting the precipitation of ettringite during the hydration of binary pastes. For portlandite, the intensity of its diffraction peaks can be seen to have decreased from 7 days to 60 days, which should be associated with its reaction with BFS during hydration, and is well correlated to the ESI results. On the other hand, Friedel's salt is the only chloride-bearing phase being identified in the pastes, while no Kuzel's salt is observed, despite its possible precipitation suggested by the ESI results. This can be resulted from the displacement of sulfate by chloride, leading to the conversion of Kuzel's salt into the more stable Friedel's salt [167,213,214].

A weak hydrotalcite diffraction peak is detected in B30S70 at 7 days. The intensity of the hydrotalcite diffraction peak becomes notably stronger in B30S70 at 60 days, and it is also observable in B50S50 at 60 days. No clear hydrotalcite diffraction peak is seen in B70S30. It is noteworthy that the strong diffraction peak of Friedel's salt can overlap with that of hydrotalcite, complicating their differentiation. Since the concentration of Mg is too low to reach the detection limit in the pore solution, the ESI of hydrotalcite cannot be provided. Still, the formation of hydrotalcite in the binary pastes can be evidenced by EDS analysis and thermodynamic modelling in the following sections.

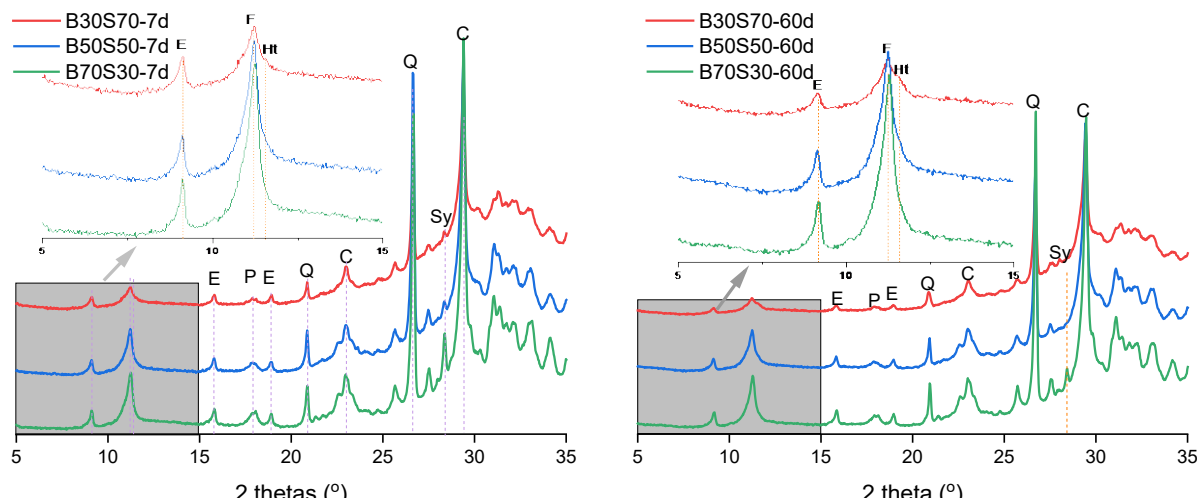


Figure 4.5 XRD patterns of binary pastes at 7 days (left) and 60 days (right)
(E: ettringite, F: Friedel's salt, Ht: hydrotalcite, P: portlandite, Q: quartz, C: calcite, Sy: sylvite)

Besides crystalline hydrates, the other main hydrate, C-S-H gels can only introduce a broad diffraction hump in the XRD pattern at around 29° due to the semi-crystallization characteristic [215]. However, with the presence of unreacted BFS and calcite, the diffraction hump of C-S-H might be obscured. Therefore, FTIR is further applied to identified the chemical bonds reflecting the existence of C-S-H gels.

4.3.3.2 FTIR analysis

The FTIR spectra of pastes at 7 days and 60 days are plotted in Figure 4.6, with the adsorption bands being accordingly marked. The main bands of all samples are located at approximately 950 cm^{-1} , which is associated with the stretching vibration of Si-O bonds (Q2). This is a typical signal for the presence of C-S-H gels as previously reported in the literatures [216,217]. This validates the presence of the C-S-H gels as the reaction products in the binary pastes. Other Si-O bonds that relate to C-S-H gels with lower intensities are at 815 cm^{-1} and 1037 cm^{-1} , and should be assigned to Q1 and Q2 silicate species, respectively [216]. These bands become more pronounced over time as the fact of the continuous formation of C-S-H gels with the extend of curing ages.

The band at 3640 cm^{-1} is the O-H strength vibration and should be assigned to the portlandite [217]. The intensity of the portlandite band increases in samples with higher WBFA/BFS ratios and decreases as hydration progresses. This is in line with the ESI calculations indicating the depletion of portlandite during the hydration process. Bands at 3400 and 1640 cm^{-1} can be attributed to the asymmetric stretching and bending of O-H, respectively [142]. These bands exist in the hydration products as chemically bonded water. Bands at 796 cm^{-1} should be attributed to the Al-OH, and could be assigned to the ettringite [218]. These results are in line with ESI and XRD results in general, evidencing the formation of C-S-H gels, ettringite, and consumption of portlandite.

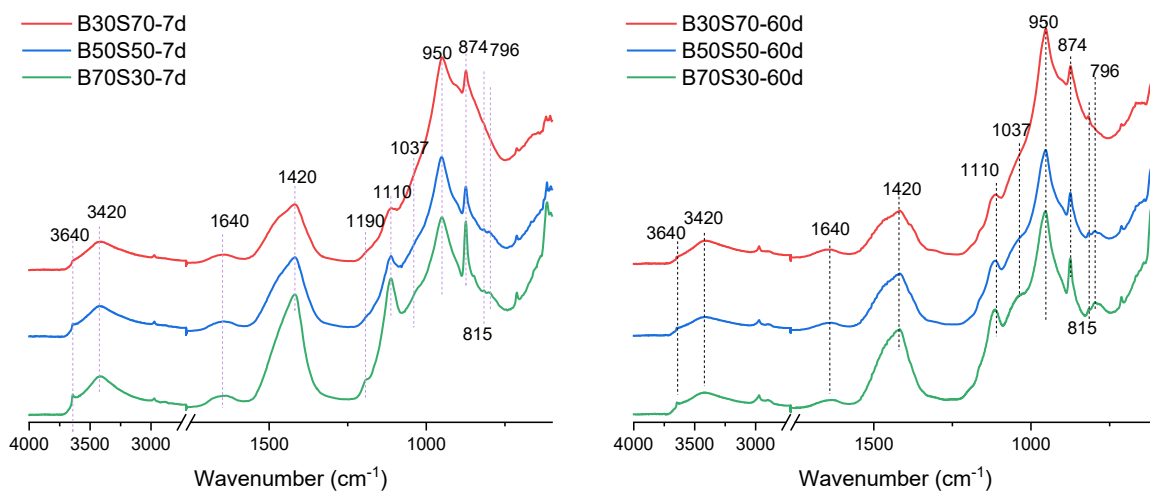


Figure 4.6 FTIR spectra of WBFA-BFS pastes at 7 days (left) and 60 days (right)

4.3.3.3 TG/DTG analysis

The TG and DTG curves of the binary pastes are shown in Figure 4.7. The main DTG peak is located at approximately 110 °C. Based on the hydrate components, it can be inferred that this peak should be attributed to the loss of the physically bound water in C-S-H gels pores [195], and the decomposition of ettringite [219]. These two phases are reported with an overlapped decomposition temperature range [220]. The double-layered hydrates (Friedel's salt and hydrotalcite) have been reported to have doublet decomposition peaks in DTG curves with similar decomposition temperatures [213]. They are identified with the first shoulder occurring at approximately 170 °C, followed by a second peak around 320°C. Additionally, a small DTG peak between 400 and 500 °C should be correlated to the decomposition of portlandite. Decarbonation occurs predominantly above 600 °C, mainly as the decomposition of calcite that originates from WBFA.

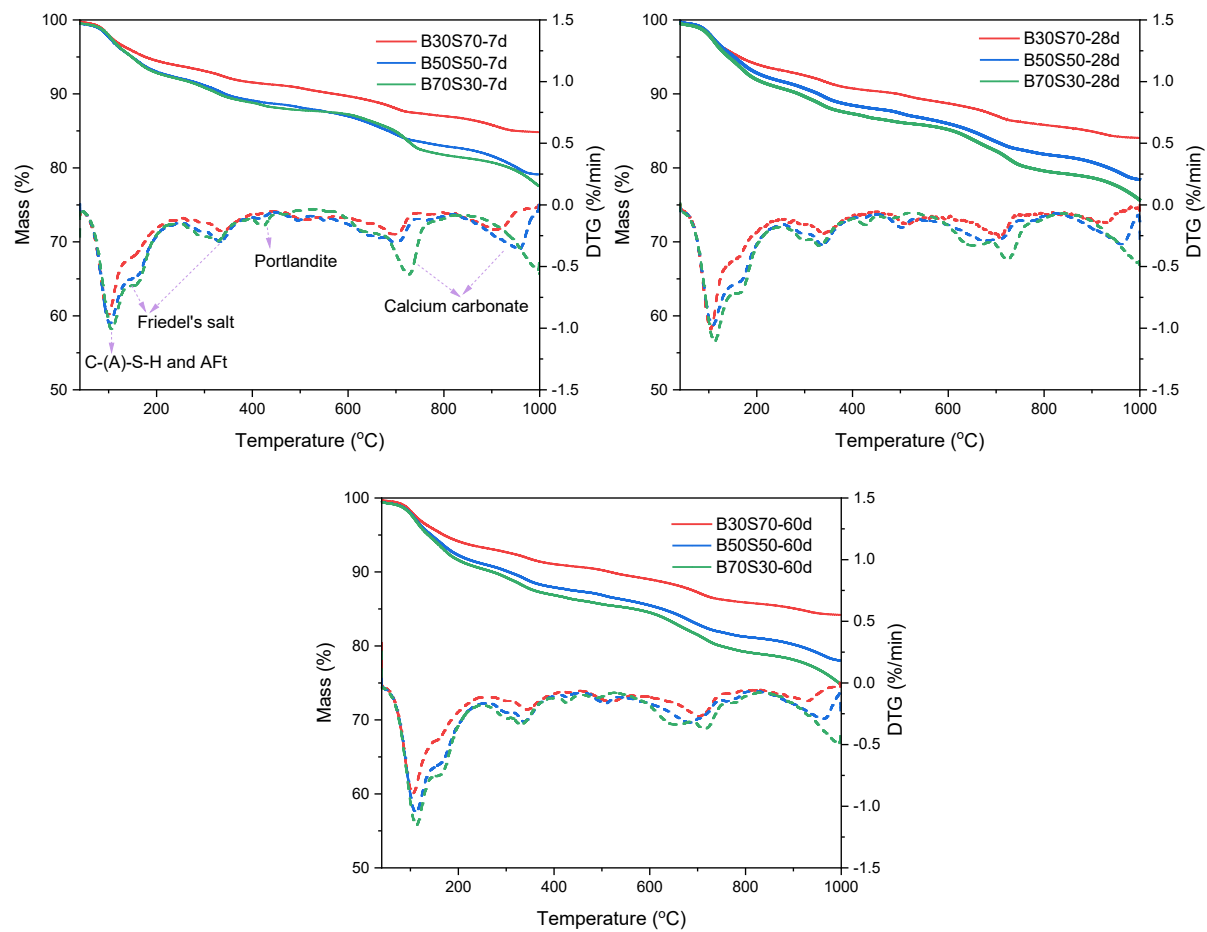


Figure 4.7 TG/DTG curves of WBFA-BFS pastes at 7days, 28 days, and 60 days
(Solid lines refer to the TG results and dash lines refer to DTG results)

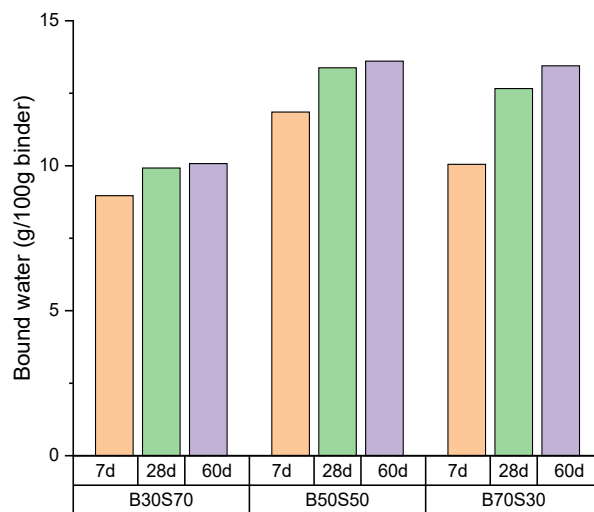


Figure 4.8 Evolution of bound water in binary pastes

The dehydration and dehydroxylation of hydrates result in mass loss, which is normally referred to as bound water content, and is directly proportional to the contents of hydrates. Figure 4.8 shows the content of bound water in different mixtures at 7 days, 28 days, and 60 days. The bound water content is calculated by the mass loss within the temperature range of 40-550 °C [195]. The increase in mass loss over time suggests the continuous hydration of pastes. Since the compositions of hydrates in pastes differ with varying WBFA/BFS ratios, it is irrelevant to directly compare the absolute values of mass loss among different mixtures for indexing the overall reaction degrees of the binder. However, the changes in mass loss with time for an individual mixture can be indicative of its own reaction development. Overall, it can be seen that the rate of bound water increase follows the trend B30S70 < B50S50 < B70S30. Mixtures with higher WBFA/BFS ratios can have a faster development of bound water, suggesting more precipitation of hydrates. This result also agrees with the results in previous sections that larger WBFA/BFS ratios proportionally promote the hydration of binary pastes at a later stage.

4.3.4 Microstructure development

4.3.4.1 Pore volume and size

The MIP results for binary pastes are presented in Figure 4.9. The binary pastes show a highly porous microstructure. The total intrusion porosity of pastes ranges between 30-45%, which is generally higher than that reported for cement pastes with a similar water-to-binder ratio [212,221].

The total intrusion porosity of paste decreases with time, which can be attributed to continuous hydrate precipitation filling pore spaces and densifying the microstructure. Notably, regardless of curing age, B50S50 exhibits the lowest porosity among the mixtures. Moreover, an interesting observation is the more pronounced reduction in intrusion porosity from 7 days to 60 days in B50S50 and B70S30 compared to B30S70. This phenomenon can be associated with the reaction rate from a long-term perspective. As indicated by the development of bound water, mixtures with a larger WBFA/BFS tend to show a more pronounced bound water increment, facilitating the generation of more hydrates and subsequently reducing porosity.

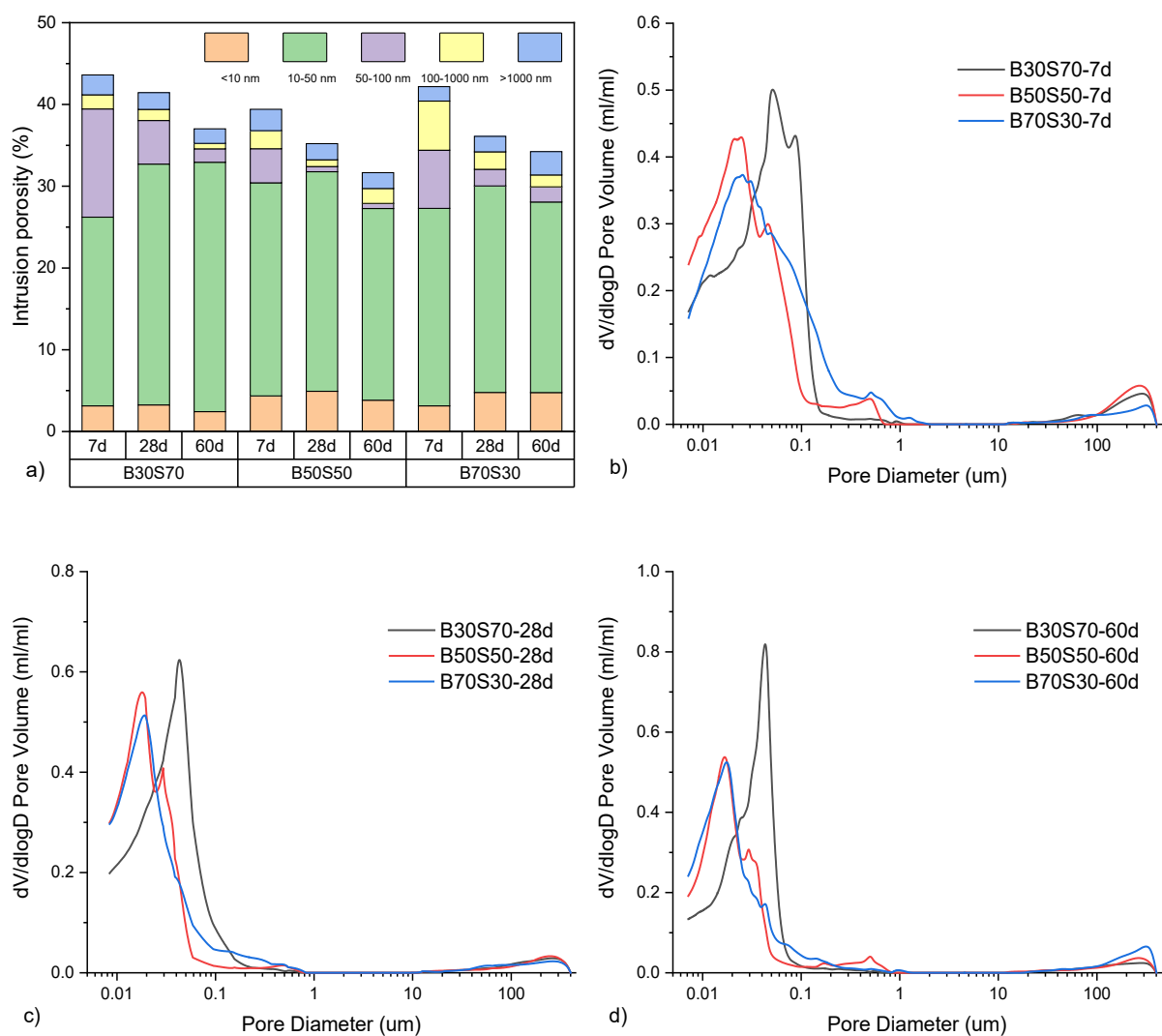


Figure 4.9 Pore proportions (a) and differential pore size distribution (b, c, d) of binary pastes

The pore proportions of pastes are divided into 5 categories, namely gel pores ($<10\text{ nm}$), micro capillary pores ($10\text{--}50\text{ nm}$), medium capillary pores ($50\text{--}100\text{ nm}$), large capillary pores ($100\text{--}1000\text{ nm}$), and air voids ($>1000\text{ nm}$) as shown in Figure 4.9(a) [221–223]. Capillary pores are dominant pores that account for more than 75 % of the intrusion pore volumes regardless of mixture proportions and ages. It is evident that pastes with higher WBFA/BFS ratios exhibit a higher volume fraction of large and medium capillary pores at 7 days, which can be interpreted from the aspect of the initial particle packing. As WBFA particles have a larger size compared to BFS particles, an increase in WBFA ratios will lead to an increase in larger particles packing together to form large pores, which cannot be adequately compacted with insufficient numbers of small particles.

The refinement of pore structures through hydrates filling pore spaces leads to an increase in the proportions of micro capillary pores. A noticeable reduction in pore size is indicated by the shift of the differential pore size distribution curves (Figure 4.9 b), c), and d)) towards lower values over time. The critical pore, which corresponds to the point of steepest increase in pore volume and is closely related to the transport properties and strength of the pastes, is used as the parameter to compare the pore structures among the three groups.

B30S70 shows the largest critical pore size at all ages, and its reduction in size is less pronounced compared to the other two groups. Larger WBFA/BFS ratios benefit more hydrates precipitation, especially at later hydration, leading to a more significant effect on the pore refinement.

4.3.4.2 Microscopy analysis

Figure 4.10 shows a representative BSE image of B50S50 at 60 days, with a brief illustration of the WBFA and BFS particles. Owing to the variation of the average atomic number in different phases, it is practical to identify the remaining BFS and WBFA particles from their grayscale. Anhydrous BFS particles are represented by bright areas. WBFA particles show both angular and spherical geometries represented by a broad range of grayscale values from a relative dark area (mainly quartz) as well as bright particles, indicating the heterogeneous nature of WBFA. The black region represents epoxy-immobilized pores. The hydrates appear to be dark grey, with a grey scale between those for the pores and anhydrous particles.

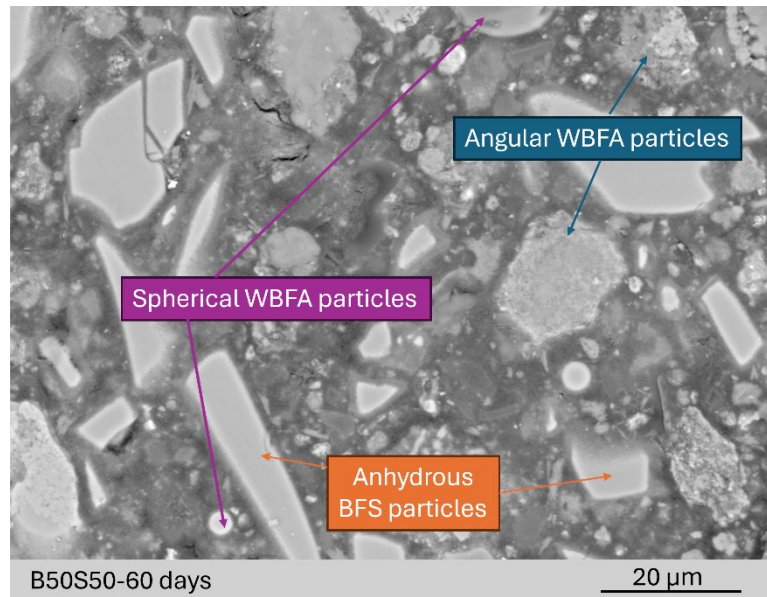


Figure 4.10 Representative BSE images of B50S50 at 60 days

Figure 4.11 compares the BSE images of WBFA-BFS binary pastes with varying WBFA/BFS ratios at 7 days and 60 days. It can be observed that anhydrous particles are adhered to the hydration products to form the microstructure of the pastes. In general, porous microstructure can be seen in pastes since a generally looser microstructure can be found for all pastes when compared with those reported in cement matrix [198,224,225]. The microstructure of pastes becomes denser with longer curing ages, as a result of the continuous generation of reaction products filling the pore spaces. However, it can be seen that the improvement regarding microstructure refinement for B30S70 is less significant than that of the other groups. This result is well correlated with the previous result in 4.3.3.3. Mixtures B50S50 and B70S30 can generate more reaction products from 7 days to 60 days, therefore, the densification of the microstructure is more noticeable.

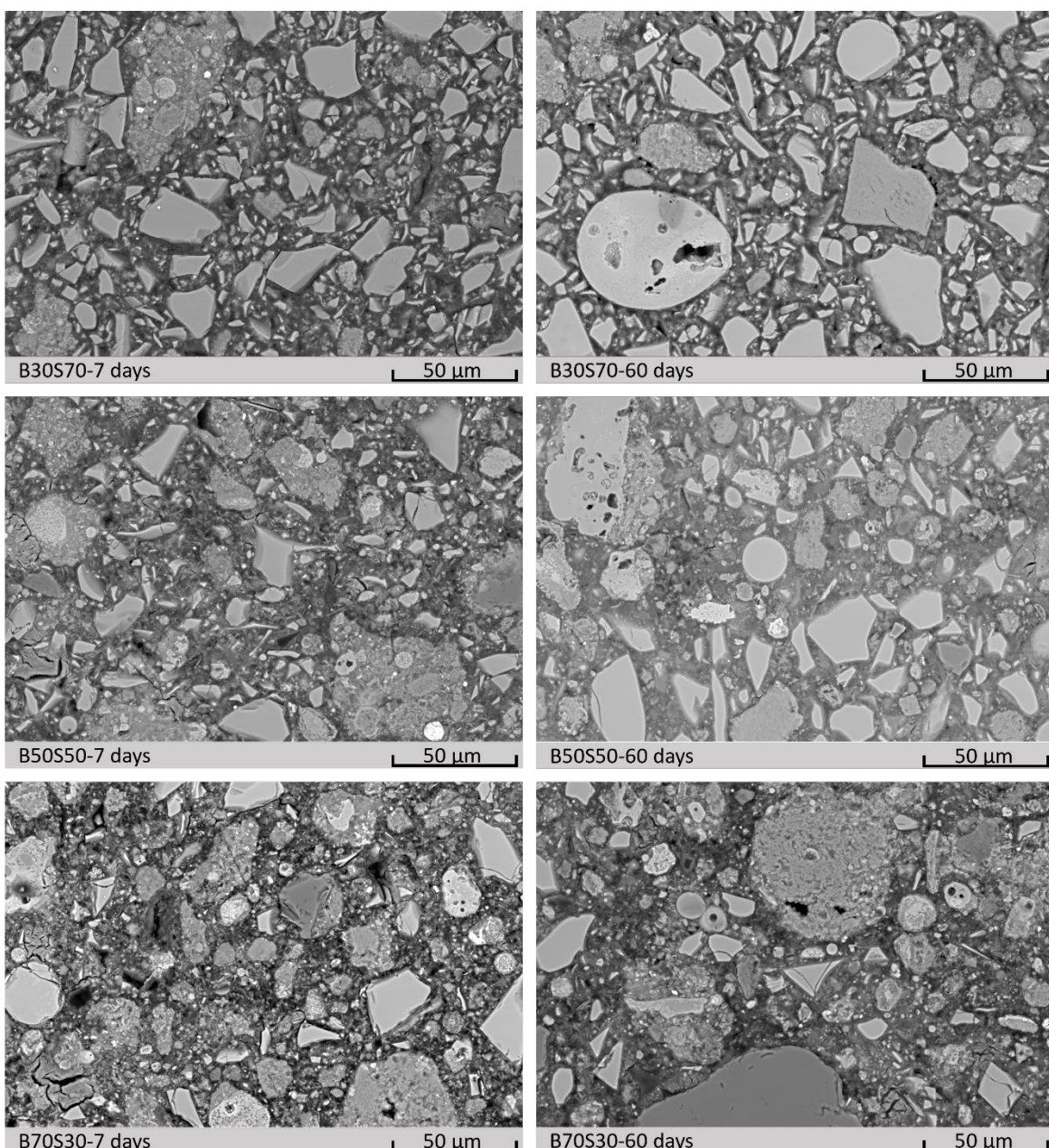


Figure 4.11 BSE images of binary pastes

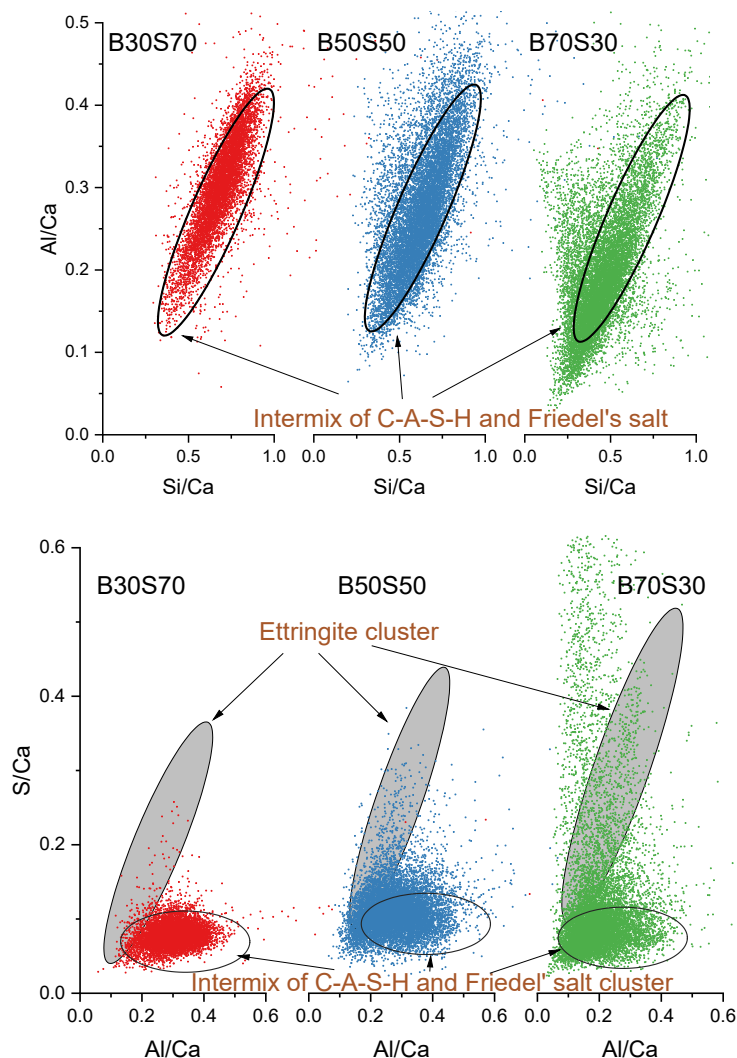


Figure 4.12 EDS scatters of hydration products

To further analyse the difference in chemical compositions of the reaction products with different mixture proportions, the EDS hypermaps of samples at 60 days are segmented into three parts, namely, pores, anhydrous particles, and hydrates, by Edxia method [226]. The example of phase segmentations is provided in Figure A4.1. The EDS data regarding the reaction products is then plotted in Figure 4.12. As illustrated, the main hydration products are simply separated based on their characteristic element ratios. The main clusters in the hydrates are the intermix of C-A-S-H gels, Friedel's salt, and ettringite. A higher WBFA/BFS ratio is clearly associated with an increased presence of scattered points in the ettringite region. The density of these points indirectly reflects the weight proportion, indicating that a higher WBFA/BFS ratio corresponds to a larger amount of ettringite as a reaction product.

4.3.5 Compressive strength development

Figure 4.13 shows the compressive strength of binary pastes.

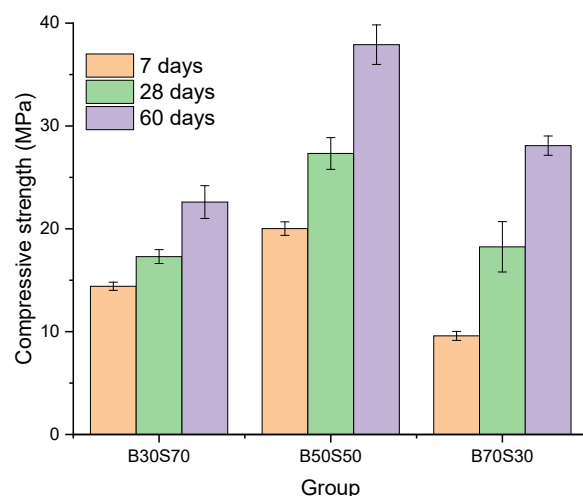


Figure 4.13 Compressive strength of binary pastes

Due to the high porosity of these pastes, the compressive strength of the binary pastes is relatively low compared to cement pastes or water glass-activated slag [227,228]. However, it is comparable to sodium salt and lime-activated slag [229,230]. The compressive strength of pastes increases with time, as a consequence of continuous hydrate generation densifying the microstructure. B50S50 shows the highest compressive strength at all ages. B30S70 shows the least strength improvement from 7 days to 60 days, while B70S30 is found with a significant strength increase. A higher WBFA/BFS ratio is facilitating the strength development of pastes at a later stage, which agrees with previous discussions on the reaction process and bound water content evolution.

4.4 Discussions

4.4.1 Reaction kinetics of binary pastes

4.4.1.1 General comments

Based on the isothermal calorimetry with ion concentration, it can be deduced that the initial dissolution of WBFA can be suppressed with the increment of WBFA contents. While WBFA is the primary alkalis source to promote the reaction of BFS, pastes with more WBFA present a decreased initial hydration rate, as seen in Figure 4.2, showing a retarding occurrences of acceleration period in mixtures with a higher content of WBFA. Restraint in the initial dissolution of WBFA is also found in ion concentration, typically for sulfur and potassium. Still, it is challenging to illustrate the reasons for this initial retarding effects. One possible hypothesis can be attributed to the membrane effect. In the amplified heat flow curves in Figure 4.2, it can be seen that within the first 2 hours, mixtures with a higher WBFA content present a higher heat flow, and the initial shoulder representing the formation of initial hydrates is more intensive in pastes with a higher WBFA, potentially indicating a higher content of initial hydrates formed. These hydrates may act as the membrane to impede the dissolution of mineral salts from WBFA and aluminosilicate glass from BFS. While the discussion of the membrane effect in cement hydration has been extensively debated with limited supporting evidence [231], there is corroborating information regarding the

membrane effect in the incongruent dissolution and reaction of poorly reactive glass materials, which include the materials (WBFA and BFS) used in this research [139,161,232].

Furthermore, considering the particle size of raw materials, fine BFS particles can possibly serve as the nucleation sites for hydrates growth. Therefore, mixtures with a higher WBFA/BFS ratio tend to have a decreasing quantity of fine BFS particles, this can also lead to a delayed occurrence of the main hydration peaks in their heat flow.

Nevertheless, WBFA in the binary paste overall only presents a slightly restrained early hydration but exhibits a more pronounced effect in the later hydration of binary pastes. The kinetics of binary reactions will be discussed in the following sections.

4.4.1.2 Reaction degrees of BFS

The hydration degrees of BFS are calculated based on the BSE-EDS mapping as described in Section 4.2.2.4, and the results are present in Figure 4.14. Comparable reaction degrees of BFS are observed at 7 days for all mixtures. However, a high WBFA/BFS ratio is found to significantly promote BFS hydration in the long term. For instance, the reaction degrees of BFS increase from 31.41% to 42.22% from 7 days to 60 days in B70S30. In contrast, for B30S70, the increase is relatively smaller, from 25.68% to 28.78% over the same period. This result directly validates the discussions in previous sections that larger WBFA/BFS ratios can facilitate the long-term hydration of BFS.

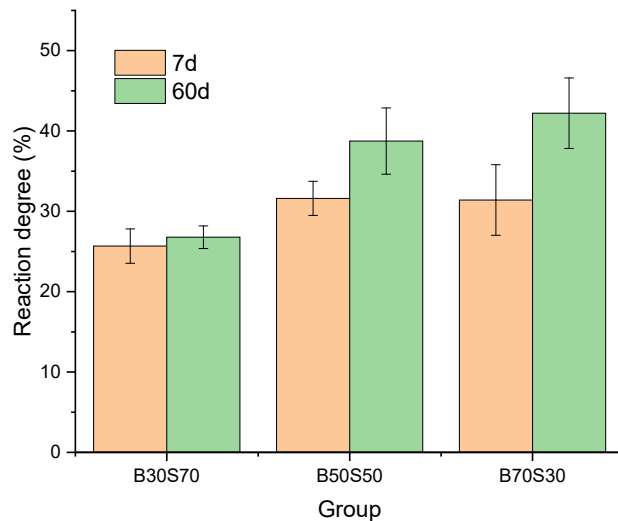


Figure 4.14 Hydration degrees of BFS determined by BSE-EDS mapping analysis

Table 4.2 Amount of reacted BFS in pastes (g/100g binder)

	B30S70	B50S50	B70S30
7 days	17.97	15.81	9.42
60 days	18.74	19.38	12.67

Based on the reaction degrees of BFS, the reacted amount of BFS in binders can be calculated and the results are listed in Table 4.2. It is interesting to note that although the reaction degrees of BFS in B70S30 can reach up to about 40%, the amount of reacted BFS is still relatively low, especially compared to that of B30S70. To comprehensively illustrate the reaction kinetics of the binary pastes, the contribution of WBFA in the reaction is of great interest.

4.4.1.3 Reaction contribution by WBFA

Owing to the complexity of WBFA, it is difficult to determine the reaction degrees of WBFA based on the experimental techniques. Still, one approach to investigate the contribution of WBFA in the reaction can be performed from the perspective of reaction enthalpy, which is largely dependent on the reaction degrees of binders.

The exponential equation as presented in equation 4.2 has been widely reported to be one of the best mathematical functions to fit the reaction enthalpy of cementitious materials [233],

$$Q(t) = Q \times \exp \left(-\frac{\tau}{t} \right)^\beta \quad (4.2)$$

where $Q(t)$ is the cumulative heat of binder (J/g) released at time t (hours), Q is the heat that can be generated by the final reaction degree, τ is hydration time parameter, β is the shape parameter.

The fitted normalized total heat, as shown in Figure 4.15, aligns well with the experimental data. As the reaction degrees of BFS have been obtained by image analysis, the enthalpy of BFS at 7 days and 60 days can be calculated according to Equation 4.3,

$$Q_i(t) = Q_{max,i} \times \alpha_i(t) \quad (4.3)$$

where $Q_i(t)$ is the heat released by the reactive component I (BFS) at time t ; $Q_{max,i}$ is the maximum enthalpy of the component (with 100% of reaction degrees); $\alpha_i(t)$ is the reaction degrees of the reactive component at time t .

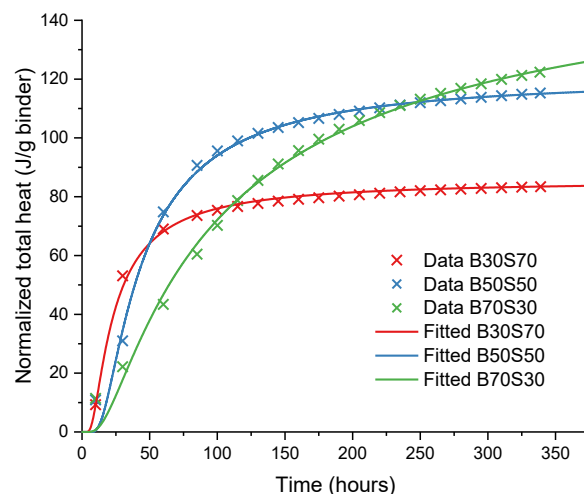


Figure 4.15 Calculated normalized total heat of binary pastes

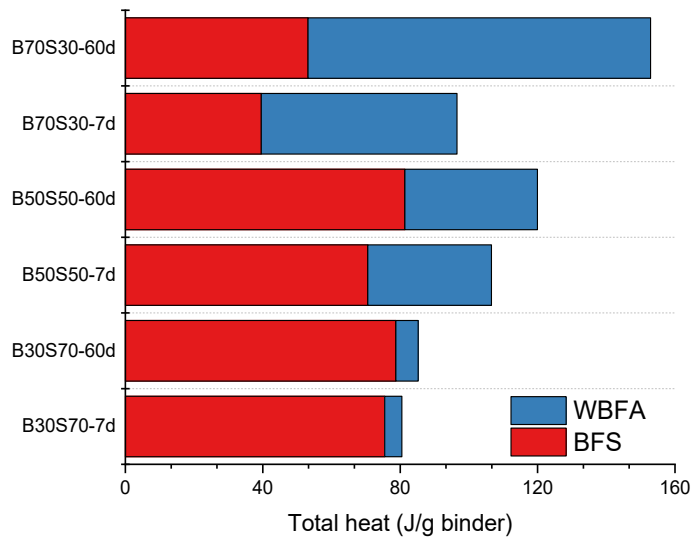


Figure 4.16 Calculated total heat of binder contributed from BFS and WBFA

To calculate the heat release from BFS, it is essential to know the maximum enthalpy for the BFS reaction ($Q_{\max, \text{slag}}$). According to the literature [199,234], it is found that the enthalpy of BFS is mainly about 400 J/g. Thus, this value is adopted for further analysis. Although this is an estimation of $Q_{\max, \text{slag}}$, the results can still be informative for further analysis of the contribution of WBFA. By subtracting the enthalpy from BFS, the released heat contributed by WBFA can therefore be obtained. The reaction contributions of BFS and WBFA in the form of heat are shown in Figure 4.16. It is seen that WBFA can greatly contribute to the heat release in binary pastes, especially in mixtures with a higher content of WBFA.

4.4.1.4 Reaction kinetics

Based on the released heat of BFS and WBFA at 7 days and 60 days, it is, however, challenging to present a time-dependent reaction kinetics model for each component, unless at least one parameter (Q , τ , β) in the exponential equation can be defined. Besides the exponential equation, there is another empirical equation, Knudsen's equation (shown in Equation 4.4) [235,236], has also been widely used for the determination of the parameter Q in cementitious materials:

$$\frac{1}{Q(t)} = \frac{1}{Q} \left(1 + \frac{t_{50}}{t - t_0} \right) \quad (4.4)$$

where $Q(t)$ is the cumulative total heat of binder (J/g) at time t , t_0 is the end of the induction period, t_{50} is the time needed to reach 50% reaction degree for cementitious materials.

This equation implies a linear relationship between $1/Q(t)$ and $1/(t - t_0)$. It has been confirmed that this equation can accurately calculate the value Q with a longer measuring time (more than 3 days) [235]. To validate the feasibility of Knudsen's equation in the binary pastes, a comparison of the value Q of the pastes from both the exponential equation and Knudsen's equation has been conducted, with the results presented in Table A4.1. The Q values show good agreement between these two methods. Based on the released heat from WBFA and BFS at 7 days and 60 days (Section 4.4.1.3), therefore, it is applicable to apply Knudsen's equation to calculate the value of Q of WBFA and BFS individually. The calculated Q of WBFA and BFS in different mixtures are presented in Table A4.2.

To further establish the reaction kinetics of these two components, their reaction degrees should be calculated. It is important to note that the Q is different from the Q_{max} . Q_{max} is assumed to be the enthalpy with 100% of reaction degrees, while Q is the eventual heat can be released from one component with its ultimate reaction degree (<100%). Therefore, it is applicable to calculate the maximum reaction degrees of each component by using Equation 4.5, and further establish the time-dependent reaction equation with Equation 4.6:

$$\alpha_{ut,i} = \frac{Q_i}{Q_{max,i} \times W_i} \times 100\% \quad (4.5)$$

$$\alpha(t) = \alpha_{ut,i} \times \exp\left(-\frac{t}{\tau}\right)^\beta \quad (4.6)$$

where W_i is the weight ratios (wt. %) of one component in the binder.

With the current data, it is sufficient to establish the reaction kinetics equation for BFS. However, to further depict the reaction kinetics equation for WBFA, the Q_{max} of WBFA is needed. For now, there is limited information available on the Q_{max} of WBFA. One possible approach is to refer to the Q_{max} of high calcium coal fly ash. Schindler et al [233] found that for high calcium coal fly ash, its Q_{max} can be defined by Equation 4.7:

$$Q_{max,FA} = 1800 \times P_{FA,CaO} \quad (4.7)$$

where $P_{FA,CaO}$ is the weight proportion (wt. %) of calcium oxide in fly ash.

It is essential to note that the calcium oxide in equation 4.6 mainly refers to the reactive calcium content. While in WBFA, we assume that this should mainly be contributed from the reactive calcium oxide from the amorphous phases. The other calcium salts mainly influence the heat release at the very beginning of hydration, which is already excluded when fitting the cumulative curves. From Chapter 3, the amorphous calcium oxide content in WBFA is 20.15%, thus the $Q_{max,FA}$ is 362.7 J/g.

Following the approach, the reaction kinetics of BFS and amorphous phase in WBFA in the binary mixtures can be established, as shown in Figure 4.17. It is important to note that for the reaction degree of WBFA, there are certain assumptions made in the calculation. Since the $Q_{max,FA}$ is obtained by considering the amorphous phase in WBFA, the reaction degree of WBFA in Figure 4.16 should only be considered as the reaction degrees of the amorphous component in WBFA (38.5% wt.). Still, it is noteworthy that this calculation can only be used for informative analysis, instead of quantitative analysis due to the assumption of $Q_{max,slag}$ and $Q_{max,WBFA}$. The changes of these values would affect the final maximum reaction degrees of WBFA and BFS, respectively.

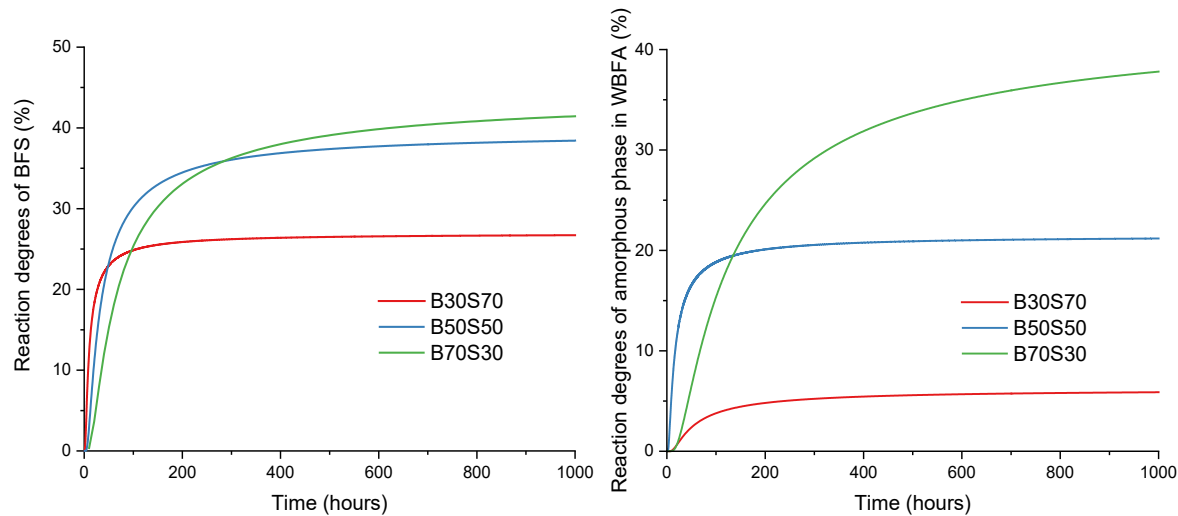


Figure 4.17 Calculated reaction degrees evolution of BFS and amorphous phase in WBFA

4.4.2 Thermodynamics modelling

With the information in Figure 4.17, it is possible to predict the phase evolution of the binary pastes with the help of thermodynamic modelling, by using GEMs software coupling with CEMDATA18 database.

Figure 4.18 provides the time-dependent phase evolution of binary pastes. It is noteworthy that the (partial) reactive phases originated from WBFA, for instance, calcite, portlandite, syngenite, sylvite etc. are directly used as inputs in the modelling based on the QXRD results. Based on the modelling, it is seen that the main reaction products are C-S-H gels, ettringite, Fridel's salt, and hydrotalcite. These results are well aligned with the experimental findings. Meanwhile, the time-dependent modelling shows that mixtures with a higher amount of WBFA exhibit a slower initial hydrates formation, which is also in line with the experimental data showing a restrained initial reaction with more WBFA.

As illustrated earlier, considering the assumptions made in the kinetics calculation, it is challenging to quantitatively analyse the reaction products. Still, the changes in hydrates among the mixtures with different WBFA/BFS ratios can provide insightful information on the phase evolutions with mixtures. As it can be seen, a higher amount of WBFA can eventually lead to an increased amount of Friedel's salt, as chloride originated from WBFA largely being bound in the hydrates. Meanwhile, it is seen that B50S50 contains the largest amount of ettringite, C-S-H gels, and hydrotalcite. These hydrates can largely contribute to its strength development, which can be partial supporting evidence for the highest compressive strength. By further increasing the amount of WBFA to B70S30, however, the amount of hydrates shall be reduced due to the limited amount of reacted BFS. A synergistic effect between WBFA and BFS is, therefore, presented.

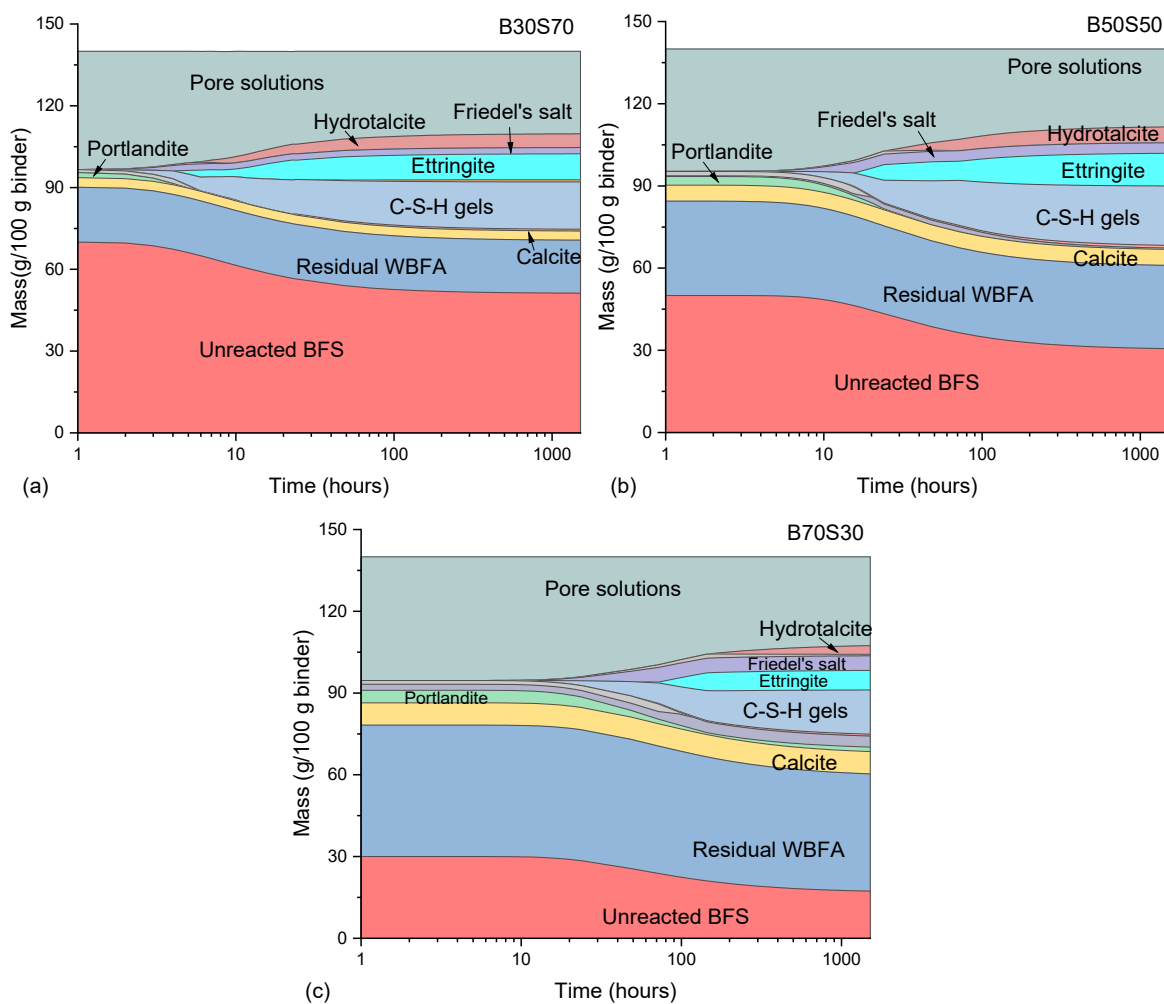


Figure 4.18 Thermodynamics modelling of phase evolution of binary pastes with time
 (a: B30S70; b: B50S50; c: B70S30)

4.5 Conclusion

This chapter investigated the reaction kinetics and microstructure development of WBFA-BFS binary pastes, validating the hypothesis in Chapter 3 that WBFA can be implemented to enhance the reaction of pozzolanic materials, demonstrating a synergistic effect with BFS during hydration. Based on the results, the following conclusions can be drawn:

- 1) The combination of BFS, WBFA, and water leads to an intense 'cement hydration-like' exothermic reaction, implying the precipitation of reaction products. Mixture with a lower WBFA/BFS ratio is found with more intensive hydrations during the early hydration. Increasing the amount of WBFA is beneficial for BFS hydration in the long term.
- 2) The primary hydration products in the binary pastes are C-S-H gels, ettringite, Friedel's salt, and hydrotalcite. The hydrate compositions are influenced by WBFA/BFS ratios, with hydrotalcite preferably forming in mixtures with lower WBFA/BFS ratios, and ettringite preferably forming in mixtures with higher WBFA/BFS ratios.

- 3) From the reaction and compressive strength point of views, B50S50 is the optimal mixture among the three mixtures, with the lowest porosities as well as the highest compressive strength at all ages.
- 4) The binary pastes have a highly porous microstructure, with porosities ranging from 30% to 45%. Longer curing leads to a reduction of porosities. The volume of medium and large capillary pores decreases while the volume of micro capillary pores increases with the refinement of the pore structure.

Due to the intrinsic reaction process and slow strength development, it can be expected that the application of WBFA-BFS binary pastes should be used for low-strength demanding products. To further extend the utilization approach and improve the utilization efficiency of WBFA, integrating WBFA into blended cement can be applied, which will be discussed in the next chapter.

Appendix

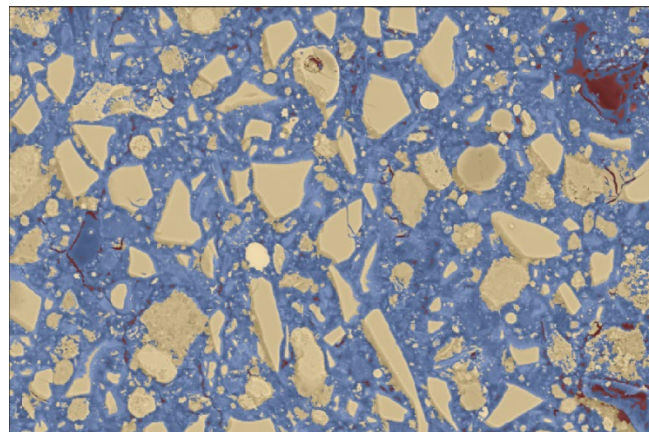


Figure A4.1 Phase segmentation of B50S50 at 60 days (The red area indicates the pores and cracks, yellow area indicates the anhydrous particles, blue area indicates the reaction products in the matrix)

Table A4.1 Comparison of values Q in binary pastes from Exponential equation and Knudsen's equation

	Exponential equation	Knudsen's equation
B30S70	85.57 J/g	86.81 J/g
B50S50	120.8 J/g	126.29 J/g
B70S30	168.55 J/g	164.83 J/g

Table A4.2 Calculated value Q for BFS and WBFA in binary pastes by Knudsen's equation

	Q _{BFS}	Q _{WBFA}	Q _{Binder}
B30S70	79.17	6.76	85.93
B50S50	82.98	38.94	121.92
B70S30	55.65	110.31	165.96

In Table A4.2, the enthalpy of binder can be calculated by equation A4.1

$$Q_{\text{binder}} = Q_{\text{BFS}} + Q_{\text{WBFA}} \quad (\text{A 4.1})$$

It is seen that the calculated Q_{binder} is comparable to that calculated directly from the Knudsen's equation calculated from the total heat from the isothermal calorimetry results. This indicates a well-satisfied result for determining the value of Q_{BFS} and Q_{WBFA} .

Chapter 5

Wood biomass fly ash as slag substitute in slag blended cement

5.1 Introduction

Chapter 4 presents one promising approach for the valorisation of wood biomass fly ash (WBFA) as a valuable mineral in a cement clinker-free binary binder formulation. While this binder exhibits a great advantage from an environmental perspective, its application shall only be restricted to moderate strength grades. To promote the utilization efficiency of WBFA in binder formulation, it is essential to integrate WBFA into the preparation of binders with enhanced strength, expanding its use for various strength demands. One option is to introduce WBFA as a mineral additive into cement, considering its wide applications in both low-strength and high-strength scenarios.

As discussed in the literature review (Chapter 2), a wide range of supplementary cementitious materials (SCMs) have been intensively used as a partial substitution for cement, aiming at reducing both the environmental and economic cost of cement concrete [237]. However, the insufficient resources of conventional SCMs persist as a challenge in executing this approach. Therefore, it would be of great interest if WBFA could be used in blended cement to replace conventional SCMs. The primary challenge of the utilization of WBFA in cement is attributed to its low reactivity. Studies indicate that directly replacing cement with WBFA results in unsatisfactory mechanical properties [44]. Nevertheless, as investigated in Chapter 4, the addition of WBFA facilitates the enhancement of blast furnace slag (BFS) reactions. This brings a new solution for utilizing WBFA as a mineral additive to partially replace BFS in BFS-blended cement. By promoting the reaction of BFS, pastes with a reduced amount of BFS can potentially attain comparable strength. Given the diminishing availability of BFS, this approach offers a practical solution to utilize WBFA and expands the options for mineral additives in blended cement.

In this chapter, WBFA is employed as a partial replacement for BFS in BFS-blended cement. The investigation delves into the reaction process, microstructure evolution, and mechanical properties of the pastes to elucidate the functional role of WBFA in BFS-blended cement. The objective is to integrate WBFA into the formulation of ternary paste systems, thereby advancing the application of WBFA in construction materials.

5.2 Materials and methods

5.2.1 Materials

The materials used in this chapter include WBFA, BFS and Portland cement.

Table 5.1 Chemical compositions of raw materials (wt. %)

	SiO ₂	Al ₂ O ₃	CaO	Fe ₂ O ₃	SO ₃	Na ₂ O	K ₂ O	Cl	MgO	LOI (550 °C)	LOI (1000 °C)
Cement	20.17	3.22	64.17	5.01	2.93	0.16	0.82	-	1.33	n/a	0.37

Table 5.2 Mineral compositions of cement by QXRD

Alite	Belite	Ferrite	Aluminate	Gypsum	Anhydrite	Bassanite	Quartz	Calcite	Others
64.97	9.32	9.12	8.17	2.88	0.73	1.41	0.81	0.90	1.69

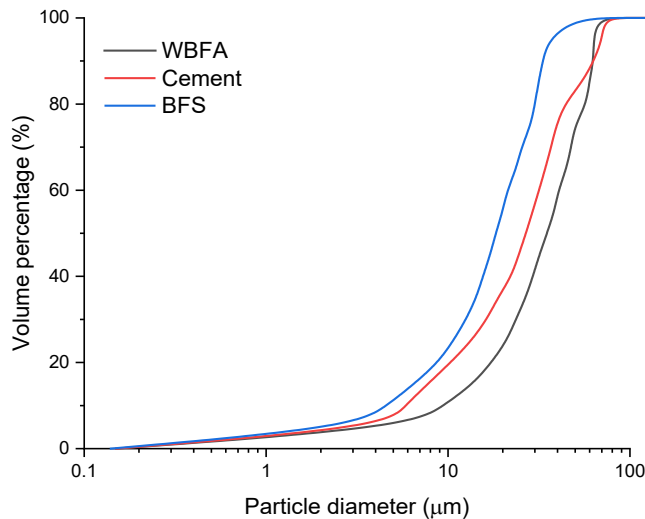


Figure 5.1 Particle size distribution of WBFA, cement and BFS measured by laser diffraction method

BFS and WBFA are the same as the ones in previous chapters. ENCI CEM I 42.5N Portland cement (in short 'cement') was used, considering its simple constituent (clinker with minor additives). The chemical compositions of BFS and WBFA can be found in Table 3.2 and 3.5, respectively. The chemical compositions (measured by XRF) and phase compositions (measured by QXRD) of cement are detailed in Table 5.1 and 5.2, respectively.

The particle size distribution of raw materials was determined by laser diffraction (Mastersizer 2000), and the results are depicted in Figure 5.1. BFS is observed to have the smallest particle size with a d_{50} of 18.31 μm , while WBFA exhibits the largest particle size with a d_{50} of 34.97 μm . The particle size of cement falls between those of BFS and WBFA, with its d_{50} at 26.81 μm .

5.2.2 Experiments

5.2.2.1 Mixture design

The mixture compositions of pastes are given in Table 5.3.

Table 5.3 Mixture proportions of pastes

Group	Cement (wt. %)	WBFA (wt.%)	BFS (wt.%)	w/b
C1	40	0	60	
C2	40	15	45	0.35
C3	40	30	30	

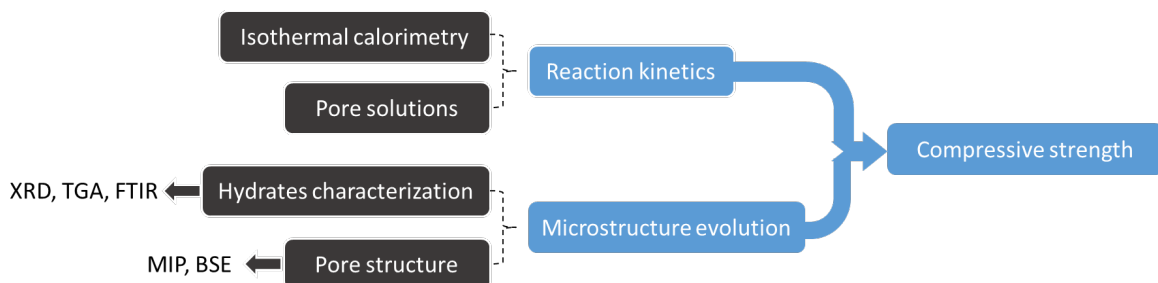


Figure 5.2 Schematic of experimental programs

The reference mixture C1 was composed of 40% cement and 60% BFS, which was a typical composition of CEMIII/A according to EN 197-1. 15% and 30% of WBFA by the total mass of the binder were introduced to replace BFS, as referred to C2 and C3, respectively. The upper limit of 30% of WBFA by total weight is set considering the amount of chloride content in WBFA (3.27%). This ensures the accumulated chloride content is below the upper limit (1%) of chloride content in concrete for non-structural application (EN 206), guaranteeing the practical execution of the binder from an engineering perspective. The water to binder ratio (w/b) was kept at 0.35 to ensure the good consistency of all mixtures.

5.2.2.2 Experimental program

The overall experimental program is depicted in Figure 5.2. The experiments are designed to investigate the impact of WBFA on the reaction of BFS blended cement. This includes studying the hydration process (through isothermal calorimetry and pore solutions), microstructure evolution (characterization by XRD, TGA, and FTIR), and mechanical properties (specifically compressive strength). The aim is to provide fundamental knowledge for the mixture design when using WBFA in BFS blended cement binders. The detailed test methods for examining reaction kinetics, characterizing microstructure evolution, and compressive strength can be found in Section 4.2.2.2. In addition, QXRD was performed to quantify the clinker phases throughout hydration. The method for QXRD can be found in Section 3.3.2.2.

5.3 Results

5.3.1 Heat evolution measured by isothermal calorimeter

Since the dissolution of raw materials and precipitation of hydrates are accompanied by heat release, the normalized heat flow can be indicative of the reaction rate of pastes. In the amplified curves for the first 4 hours of reaction in Figure 5.3 (a), it can be seen that pastes

with WBFA (C2 and C3) have a greater initial exothermic peak compared to the reference (C1). Given that the initial peak is associated with wetting and dissolving of the raw materials [238], it infers that the introduction of WBFA leads to an enhanced dissolution of the raw materials. Meanwhile, it is observed that mixtures with larger proportions of WBFA tend to have shorter durations of the dormant period. As indicated in Figure 5.3(a), the end of the dormant period is 2.96 hours, 2.68 hours, and 2.16 hours for C1, C2, and C3, respectively. Pastes with WBFA exhibit a faster initial reaction. This phenomenon can be attributed to the significant dissolution that occurs when WBFA is introduced. The enhanced dissolution in C2 and C3 leads to the faster accumulation of ion concentrations in the pore solution, resulting in an accelerated oversaturation of hydrates. As a result, hydrates precipitation occurs faster [239].

After the dormant period, there is a notable increase in heat flow for all pastes, achieving their main hydration peaks at approximately 12 hours, as shown in Figure 5.3(b). This stage is commonly known as the acceleration period, which is believed to be associated with the generation of a substantial amount of hydrates [239]. Similar to that in the initial peak, pastes with WBFA (C2 and C3) show a higher main peak than C1, suggesting that WBFA promotes early hydrates formation. An advancement in hydration is caused by addition of WBFA.

The deceleration period follows the acceleration period, where the heat flow gradually decreases with time. During this stage, a distinctive secondary reaction peak can be observed in all mixtures. The peak is typically associated with the formation of ettringite [104,240]. In the case of C1, this peak is right next to the main hydration peak, with almost identical intensity to the main peak. The introduction of WBFA leads to a delayed and broader secondary reaction peak. The onset of the secondary reaction peak is observed after 15 hours in C1 and is delayed to 23.94 hours in C3. Similar phenomena have also been observed in cement pastes with the addition of sulfate, as previously reported in literature [241,242]. Based on the chemical compositions of WBFA in Section 2.3.3, a higher amount of sulfate can be expected in mixtures with more WBFA. Still, all the mixtures are in the scenario as properly sulphated condition, consistent with previous research [241,243,244]. In the case of an oversulfated condition, the aluminate peak is typically observed much later [204,241]. Oversulfated condition can cause significant retardation effects on cement, and is negative for the mechanical strength [245]. Therefore, careful attention should be paid if the addition of WBFA is more than 30%.

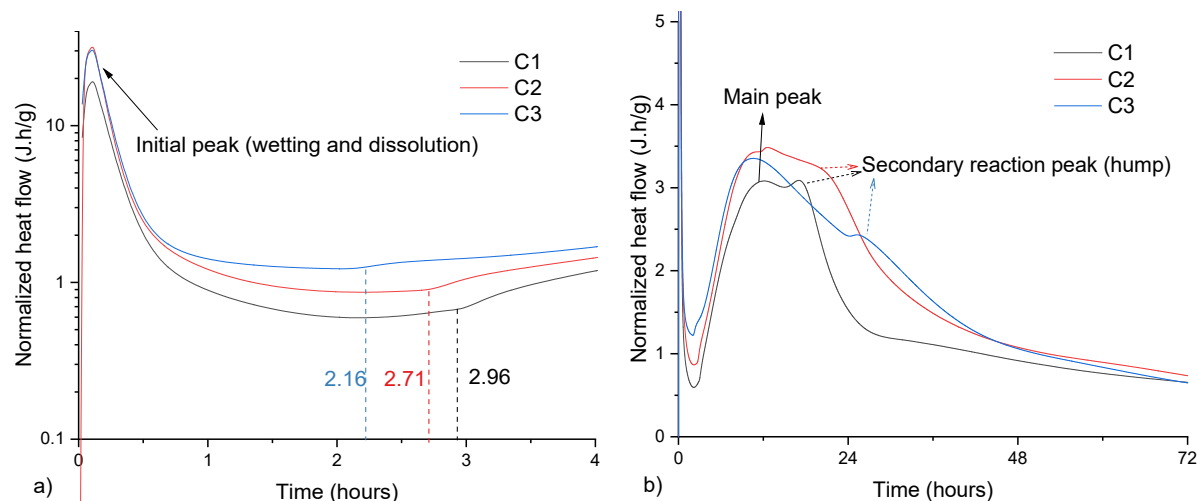


Figure 5.3 Normalized heat flow of pastes (a) within first 4 hours; (b) until 72 hours

5.3.2 Pore solutions

5.3.2.1 Ion concentration

To further study the effect of WBFA on the hydration of BFS blended cement, the evolution of ion concentration in the pore solution is measured. Figure 5.4 shows the pore solution compositions of pastes at 1 day, 7 days, 14 days, and 28 days. As the concentrations of Mg and Fe are below the detection limit of ICP-OES, the results are not included. The ion concentrations demonstrate a balanced charge relationship between anions and cations (Fig 5.4 (a)), affirming the reliability of the pore solution compositions.

Due to the high alkalis content in WBFA, the introduction of WBFA leads to increased concentrations of Na (Figure 5.4 (b)) and K (Figure 5.4 (c)) at all ages. Thus, a higher alkalinity of the pore solution can be expected in pastes with WBFA, as evident by the increasing concentration of OH in the pore solutions of C2 and C3 compared to the reference sample C1 (Figure 5.4 (d)). Still, it is interesting to note that the concentration of OH is not linearly dependent on the concentration of alkalis. C2 shows a higher concentration of OH than C3 at 1 day and 7 days, indicating a higher alkalinity in C2. Meanwhile, the concentration of sulfate (Figure 5.4 (e)) does not proportionally increase with WBFA. The concentration of sulfate in paste with 15% of WBFA (C2) is only 39.28 mM while paste with 30% of WBFA (C3) contains 221 mM sulfate at 1 day. The lower initial alkalinity in C3 may be ascribed to the slower depletion of sulfate in C3 compared to C2, as indicated by the isothermal calorimetry showing a later occurrence of the aluminate peak in C3. Thus, a lower concentration of OH should be achieved in C3 compared to C2 to meet the charge balance.

The rise in alkalinity in pore solutions can promote the dissolution of clinker phases and BFS [123]. As suggested by the calorimetry results, pastes containing WBFA present higher wetting and dissolution peaks. Evidences can be observed in the concentration of Al and Si (Fig 5.4 (f), (g)). For three mixtures, the concentration of Al and Si increases over time, which is consistent with previous research [246,247]. As WBFA contains a lower content of amorphous aluminosilicates than BFS, the dissolvable aluminum and silicon in pastes containing WBFA are, therefore, expected to be lower. However, it is seen that the concentration of Si increases with the increase of WBFA, inferring that WBFA promotes the dissolution of aluminosilicate phases in cement and BFS.

In a pure cement system, the concentration of Ca is largely influenced by the solubility of portlandite [246]. Normally, a higher alkalinity in pore solution leads to a decreased concentration of Ca. This trend is also observed in the current research, as seen in the evolution of the concentration of Ca in controversy with that of OH over time. However, it is noted that the concentration of Ca increases with the increased WBFA, despite the fact that C2 and C3 have higher alkalinity in pore solutions. One reason can be the dissolution of the calcium-bearing crystalline phase, for instance, syngernite, from WBFA. Besides, the promoted dissolution of BFS and cement can affect the dissolution of calcium species. A sulfate-rich environment in C2 and C3 is also believed to be the reason for their high concentration of Ca, as these elements are expected to form aqueous $CaSO_4^0$ complexes [246].

Free chloride is detected in the pore solutions in C2 and C3, as the high availability of chloride originates from WBFA ((Fig 5.4 (i)). It is interesting to note that the concentrations of

chloride decrease with time, which implies that the chloride is bound in the hydrates of the blended cement pastes. The reduced chloride concentration can be attributed to chemical binding by the generation of chloride-bearing hydrates, and physical sorption by hydrates [190,214]. The chloride-bearing phases will be further discussed in the following sections.

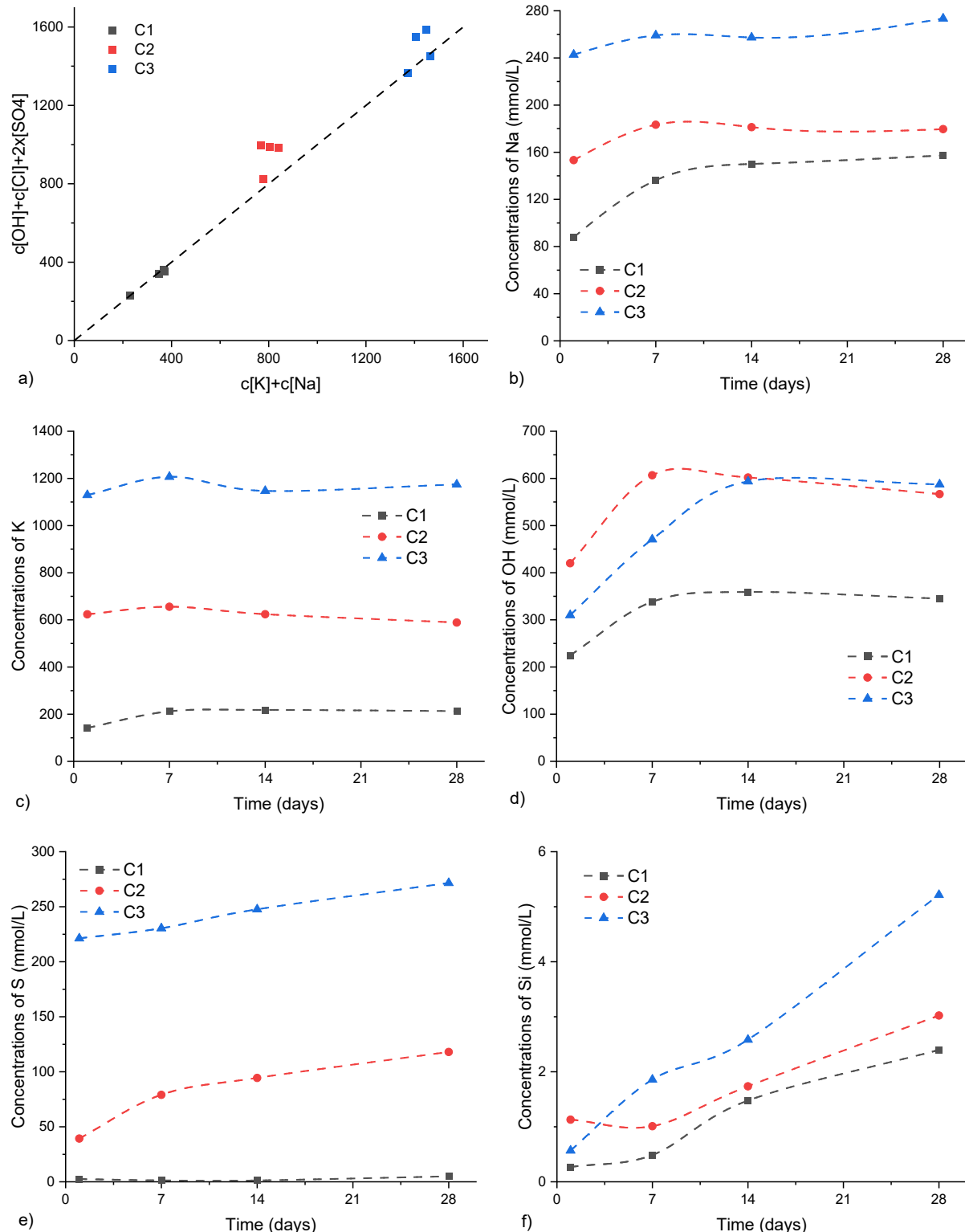


Figure 5.4 The charge comparison (a) and ions concentration (b)-(i) in pore solutions

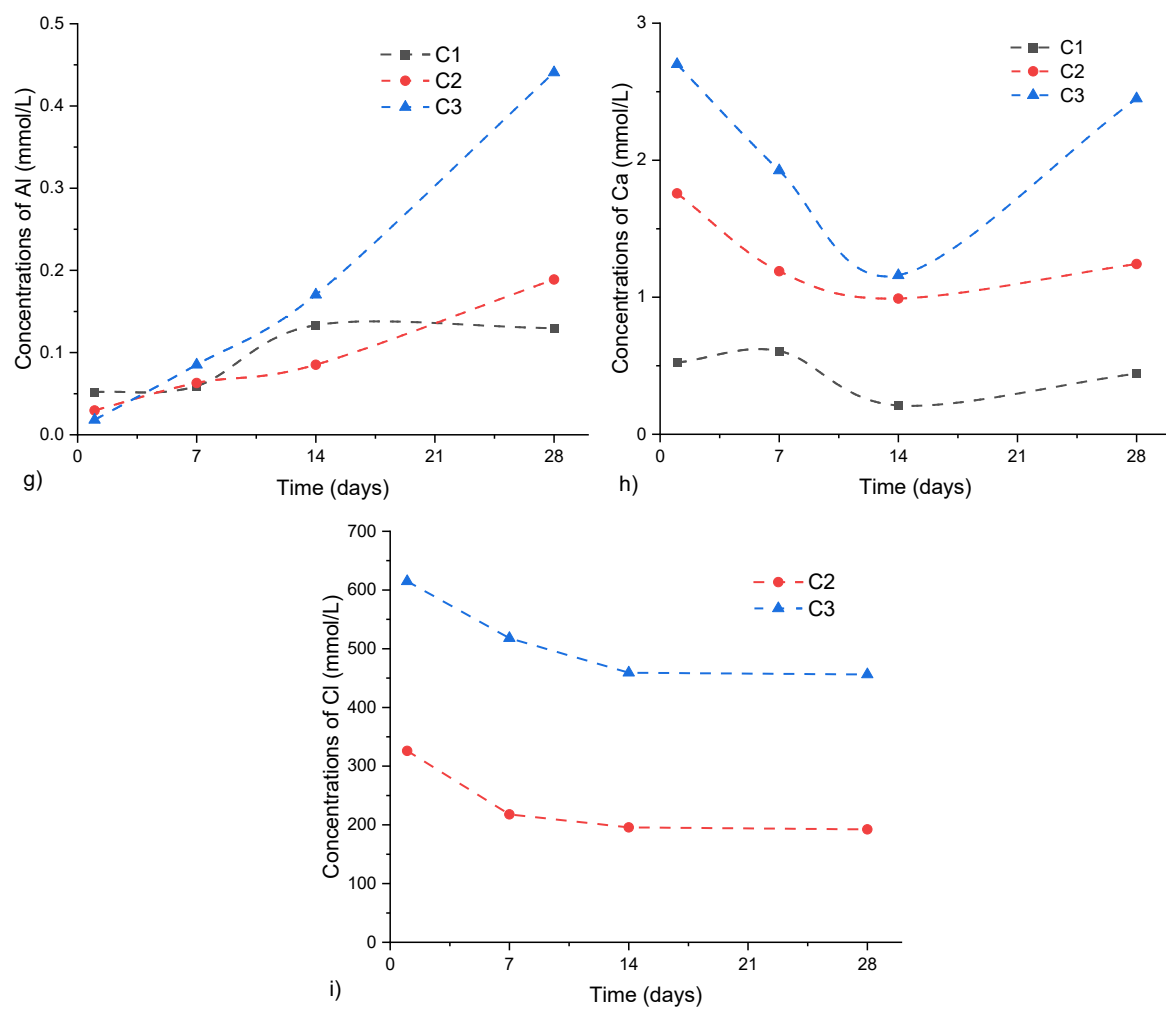


Figure 5.4 The charge comparison (a) and ions concentration (b)-(i) in pore solutions (continued)

5.3.2.2 Effective saturation index (ESI)

With the ion concentration, the ESI of suspected hydrates is calculated following the methodology described previously in Section 4.3.2. A positive ESI value indicates the potential generation of phases due to oversaturation, whereas a negative value indicates undersaturation and the inability to form those phases. The tolerance area within the dashed lines represents the uncertainty range of the solubility products [210].

C-S-H gels are the most likely hydrates to be precipitated, as indicated by the highest ESI values among the other hydration phases. The ESI values of ettringite in C2 and C3 are consistently positive throughout the measured hydration durations, whereas the ESI value of ettringite in C1 at 1 day is close to 0, and further falls outside the tolerance area at later stages of hydration. This indicates that ettringite is expected to be one of the primary hydrates in C2 and C3. In C1, on the other hand, it is deduced that ettringite would decompose into other phases. Further XRD analysis would confirm this argument.

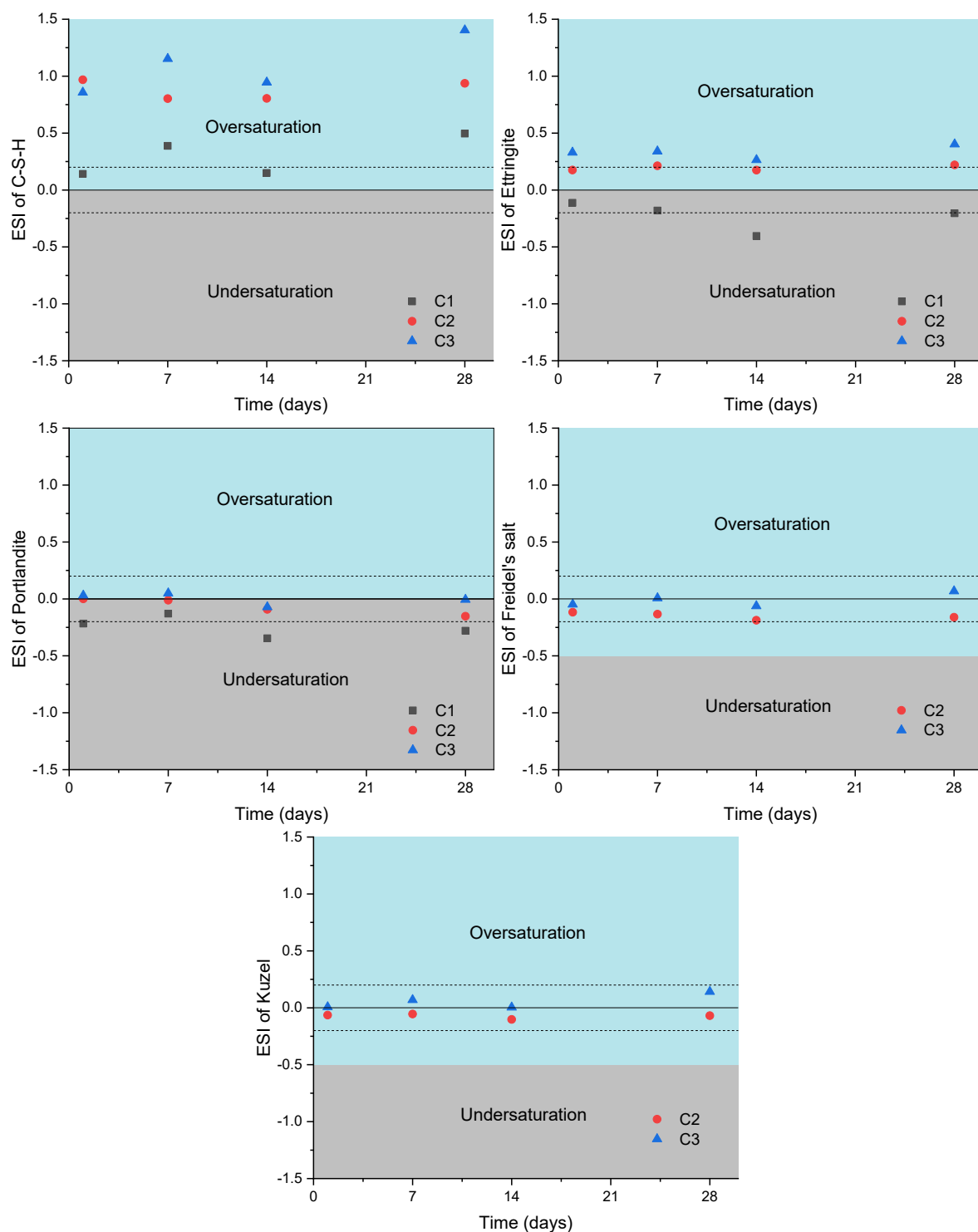


Figure 5.5 ESI of calculated from pore solutions

The ESI of portlandite in C1 is seen to be negative at 1 day, further decreasing to fall outside the tolerance area afterwards. Comparatively, the ESI of portlandite in C2 and C3 remains around 0 during the measured period, with a generally slight decreasing trend over time. The decrease in ESI of portlandite with time in all samples should be the result of pozzolanic reaction between BFS and portlandite, which is consistent with other studies [248,249]. The negative ESI of portlandite in C1 starting from 1 day implies that the

portlandite consumption rate due to the pozzolanic reaction is faster than the portlandite precipitation rate from the clinker hydration. However, this does not necessarily indicate that C1 exhibits a faster pozzolanic reaction compared with C2 and C3, especially considering that pastes containing WBFA have been found with a promoted BFS dissolution as indicated in Figure 5.4. The higher ESI values in C2 and C3 should mainly be attributed to the initial presence of a certain amount of portlandite (5.51% wt.) in WBFA, which maintains the ESI of portlandite at a relatively higher value.

For the chloride-bearing hydrates, similar to the results in Chapter 4, the ESI values of both Kuzel's salt and Friedel's salt are located above the lower limit of the tolerance area for both C2 and C3. This indicates that from the thermodynamic perspective, both two phases can possibly be generated, which explains the decrease in chloride concentration over time. Still, further XRD test shall be implemented to determine the actual chloride-bearing hydrate formation.

5.3.3 Solid phases

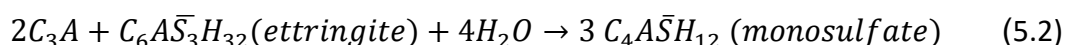
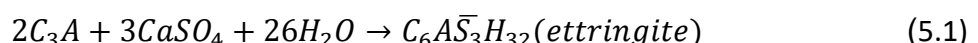
5.3.3.1 XRD analysis

- *Phase identification*

Figure 5.6 displays the XRD patterns of the pastes, and the minerals are correspondingly marked.

For samples at 1 day, it is seen that ettringite and portlandite are the primary hydrates in all pastes. While ettringite remains the main hydrate in C2 and C3 at later hydration, it is noteworthy that the diffraction peaks of ettringite in C1 become less visible with time. For samples at 28 days and 90 days, another sulfate-bearing phase, monosulfate, becomes significant in C1. This aligns with the ESI calculation on ettringite, where an undersaturation condition of ettringite is found in C1 after 1 day, while the oversaturated condition is observed in C2 and C3 throughout the measurement.

Equations 5.1 and 5.2 illustrate the formation of ettringite (AFt) and its conversion into monosulfate (AFm), respectively, with C₃A as the example for the aluminate-bearing phases:



From these chemical reactions, it can be informed that the conversion of ettringite into monosulfate is the result of the complete consumption of sulfate. In this scenario, ettringite would further react with the remaining aluminate phases to form monosulfate [104]. By replacing BFS with WBFA, the aluminate phases in pastes decrease while the sulfate content increases. Therefore, the sulfate-rich systems in C2 and C3 are more favourable for the precipitation of ettringite.

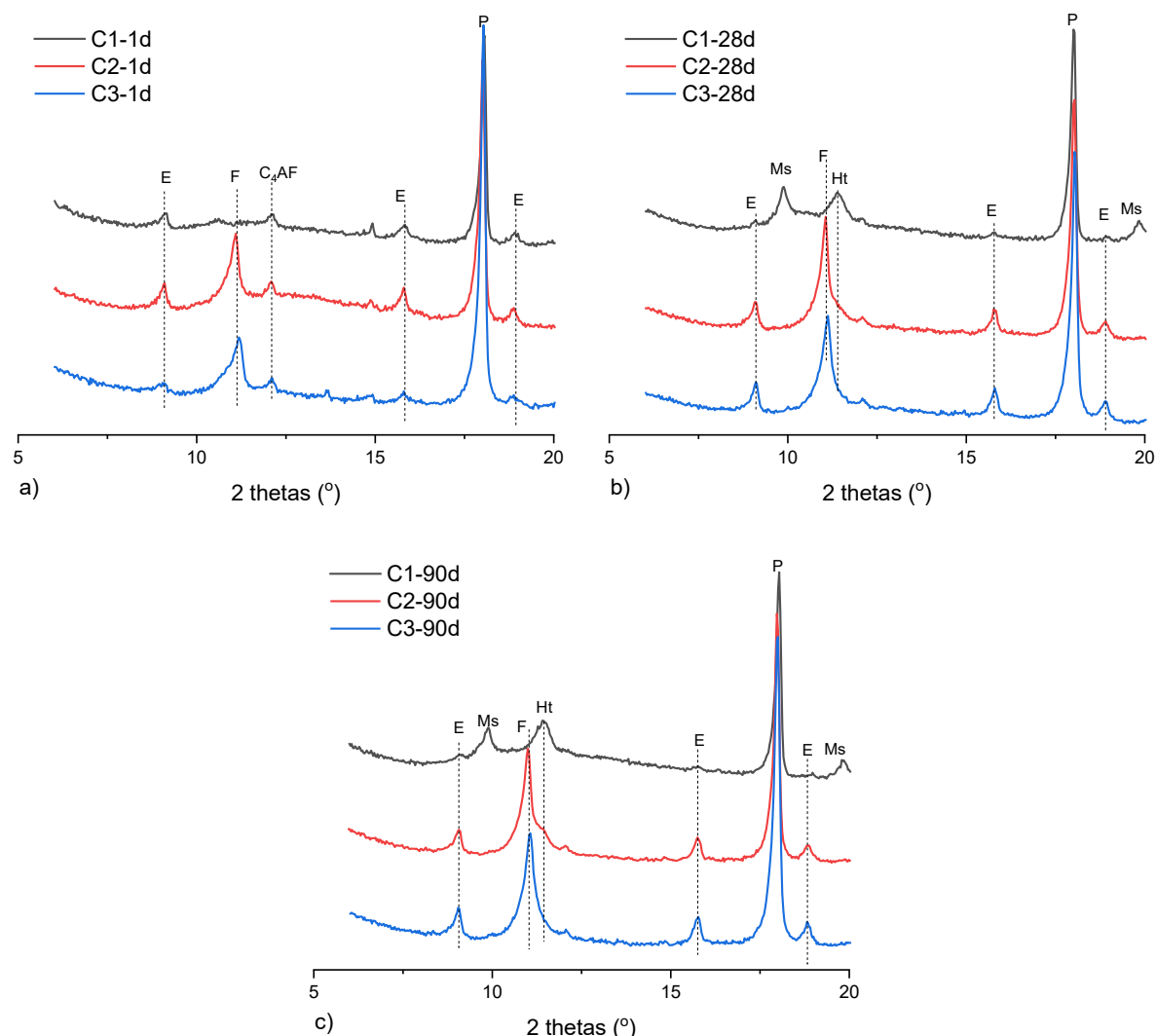


Figure 5.6 XRD patterns of the pastes at 1 day (a), 28 days (b), and 90 days (c)
(E: ettringite, Ms: monosulfate, F: Friedel's salt, Ht: hydrotalcite, P: portlandite)

For the chloride-bearing hydrates observed in XRD patterns, unlike the ESI calculations indicating the possible formation of Kuzel's salt, only Friedel's salt is actually detected at 11.20° of 2 thetas in the C2 and C3. The intensity of the diffraction peaks of Friedel's salt increases over time due to its ongoing precipitation. The reason for the absence of Kuzel's salt can be attributed to the substitution of sulfate by chloride in Kuzel's salt in the chloride-rich environment, leading to its conversion into a more stable Friedel's salt [250]. Moreover, hydrotalcite, one of the primary secondary hydrates in BFS blended cement, is observed at 11.36° of 2 thetas in C1 at 28 days and 90 days (Figure 5.6 (b), (c)). The diffraction peak for hydrotalcite is less observable in pastes with more WBFA. Although no clear hydrotalcite diffraction peak can be found in C2 and C3 at 28 days, it becomes visible at 90 days in C2. However, hydrotalcite can be rarely found in the XRD pattern of C3. The decrease in hydrotalcite can be attributed to the reduced magnesium content in mixtures with the increase in the replacement of BFS by WBFA.

- *Quantitative analysis*

QXRD is carried out to quantify the remaining anhydrous clinker phases in the hydrates, further can be implemented to determine the reaction degrees of individual clinker phases of cement, with results presented in Figure 5.7. Additionally, the hydration degrees of cement can be calculated accordingly based on Equation 5.3, and the results are plotted in Figure 5.8.

From Figure 5.7, it is clear that all of the clinker phases exhibit enhanced hydration at 1 day in the pastes containing WBFA. The accelerated hydration can be attributed to, on the one hand, the increasing alkalinity in the pore solutions (seen from Figure 5.4(d)) that facilitates the dissolution of clinker phases. Meanwhile, as stated in [240,242], sulfate can accelerate the early hydration of alite. The increasing amount of sulfate in blends containing WBFA can therefore facilitate the early hydration of cement. As a result, the hydration degree of cement at 1 day increases with the increment of WBFA. The hydration degrees of cement at 1 day are 49.25%, 59.69%, and 60.14% in C1, C2, and C3, respectively.

$$DoH_{cement} = \left(1 - \frac{\sum(C_3S + C_2S + C_3A + C_4AF)_{residuals}}{\sum(C_3S + C_2S + C_3A + C_4AF)_{raw}} \right) \times 100\% \quad (5.3)$$

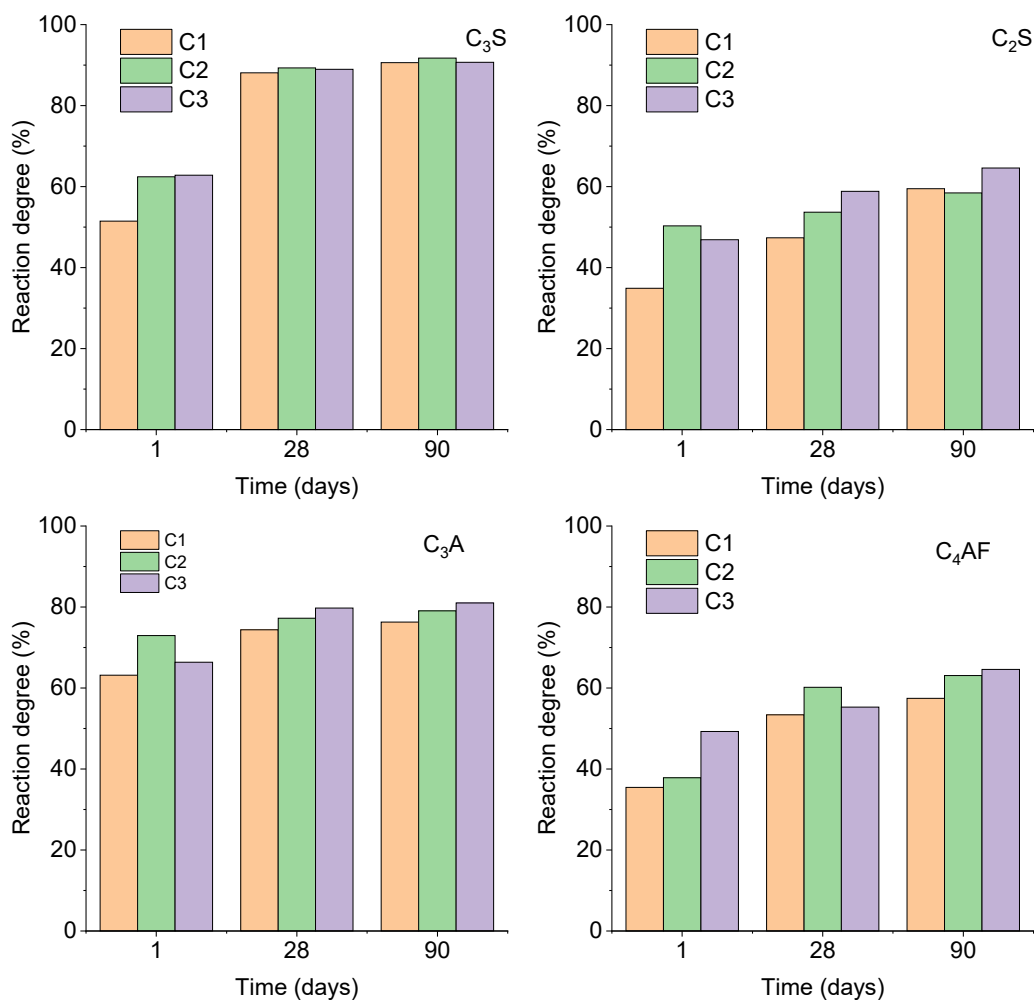


Figure 5.7 Reaction degrees of individual clinker phase by QXRD

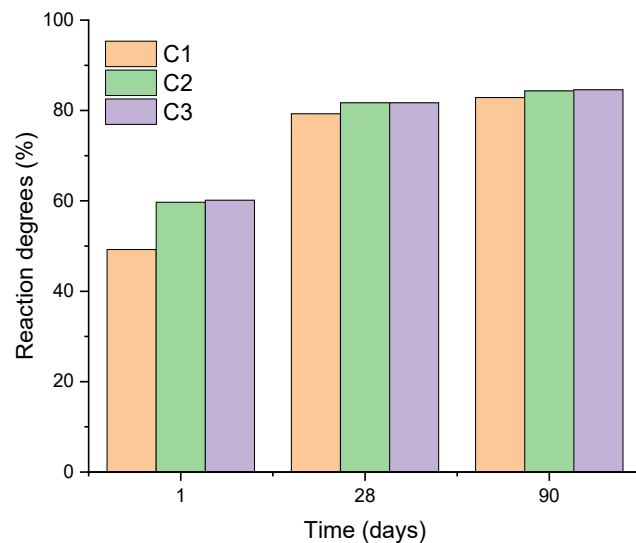


Figure 5.8 Reaction degrees of cement

The reaction degrees of individual phases increase with time as a consequence of continuous hydration. However, it seems that the effect of WBFA on the hydration degree of the clinker phase is less noticeable at later stages. Concerns about alkalis negatively affecting cement hydration from a long-term perspective have been reported elsewhere [251,252]. Still, in the current research, it is clear that the WBFA shows no negative impact on cement hydration in the BFS blended cement at a later stage. The reaction degrees of cement among these three mixtures are generally comparable at 90 days.

5.3.3.2 FTIR analysis

Figure 5.9 presents the FTIR spectra of pastes at 1 day, 28 days, and 90 days. The main band for all pastes is located at approximately 950 cm^{-1} . This band is associated with the adsorption of Si-O (Q2), and is the typical signal for the presence of C-S-H gels [216,217]. The other Si-O bands at 820 cm^{-1} are reported to be the Q1 species in C-S-H gels [253]. The identical location of the main band in the samples indicates that the introduction of WBFA does not significantly affect the polymerization of Si in C-S-H gels. The shift of main bands from a lower wavenumber (947 cm^{-1} at 1 day) to a higher wavenumber (954 cm^{-1} at 90 days) is the result of the gradual decalcification and polymerization of silica, which has been widely reported in the literature [217] as the consequence of long-term hydration.

The bands at 1115 cm^{-1} are identified in all three groups at 1 day, and correspond to the presence of sulfate in the form of ettringite [253,254]. With the hydration process, the S-O band in the spectra of C1 at 28 days and 90 days has shifted to 1160 cm^{-1} , which should be attributed to the sulfate in monosulfate. This is consistent with the XRD results indicating the conversion from ettringite to monosulfate. In terms of the OH bands, three bands are identified at 1650 , 3420 , and 3640 cm^{-1} . The first two bands are associated with the chemical water in the hydration products. The band at 3640 cm^{-1} corresponds to portlandite, which is more pronounced in samples of the same age as the amount of WBFA increases. One explanation for this is that WBFA has a stimulating effect on the hydration of cement, especially at early age. Additionally, WBFA is composed of 5.51% of portlandite, which enhances the band intensity. However, the portlandite band gradually loses its visibility in all samples over time, as a result of its depletion during the hydration process of BFS.

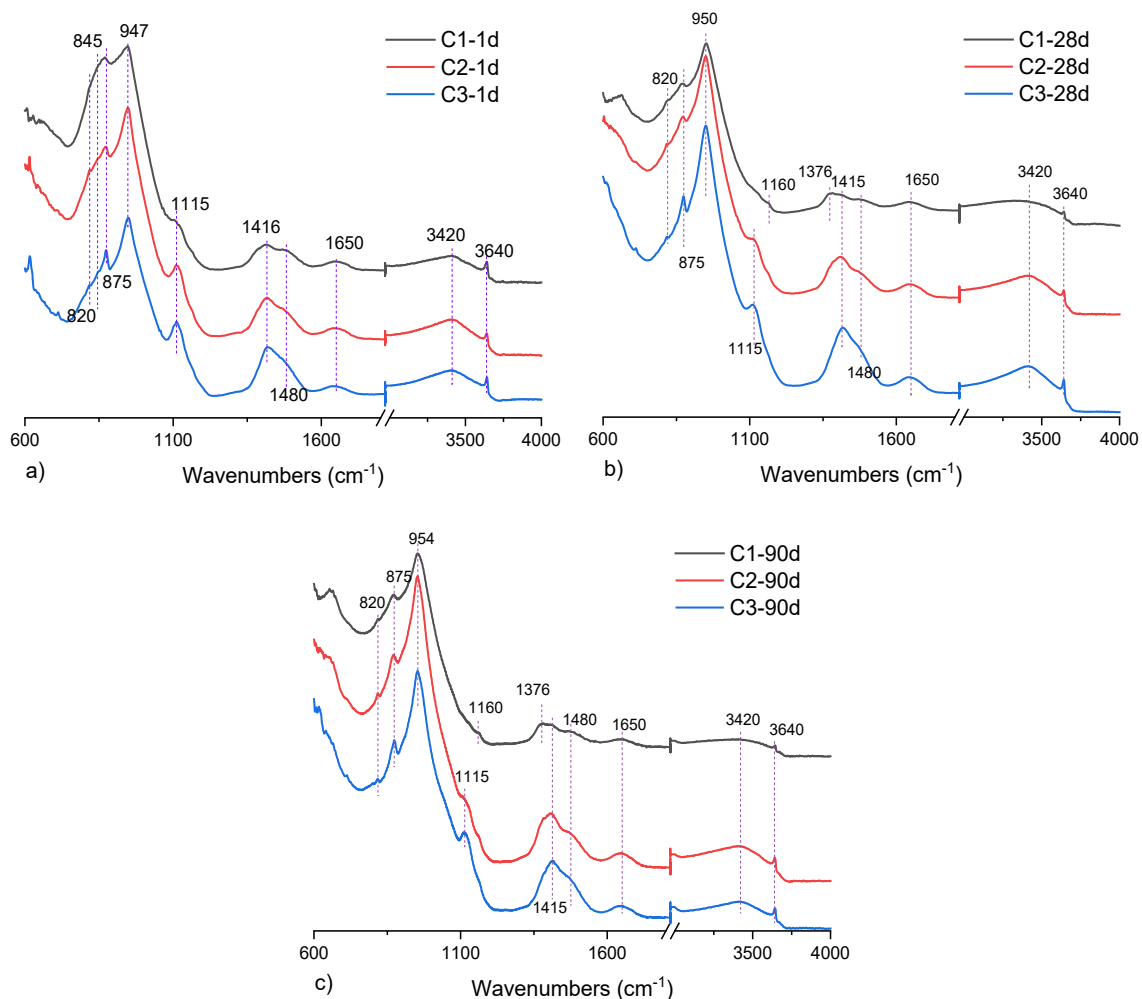


Figure 5.9 FTIR spectra of the pastes at 1 day (a), 28 days (b), and 90 days (c)

5.3.3.3 TGA-DTG analysis

Figure 5.10 illustrates the TGA-DTG curves of the pastes. Based on the DTG curves, the decomposition of hydrates can be broadly categorized into three regions: Region I occurs within about 400°C and is characterized by the dehydration and dihydroxylation of various hydrates, with several peaks observed. Specifically, for samples at 1 day, the main peak at around 110°C is attributed to the dehydration of C-S-H gels and ettringite [255,256]. Due to the similar decomposition temperatures of these two phases, the main peak represents the overlap of the two phases decomposition. The small shoulder at about 160°C in C2 and C3 is likely the decomposition of Friedel's salt, which has a doublet decomposition peak, with the second peak at around 320°C [213]. The decomposition peak of the pastes is similar to that of the cement-free binder reported in Chapter 4, as these binders contain similar types of hydrates in general. The only difference is in C1 at 28 and 90 days, where monosulfate contributes to a small decomposition shoulder at around 170°C. Additionally, several minor peaks between 250-400 °C are found for samples at 28 and 90 days, which can be attributed to the decomposition of hydrotalcite phases. Besides, Region II between about 400-500°C corresponds to the decomposition of portlandite, and region III is associated with decarbonation above 600°C.

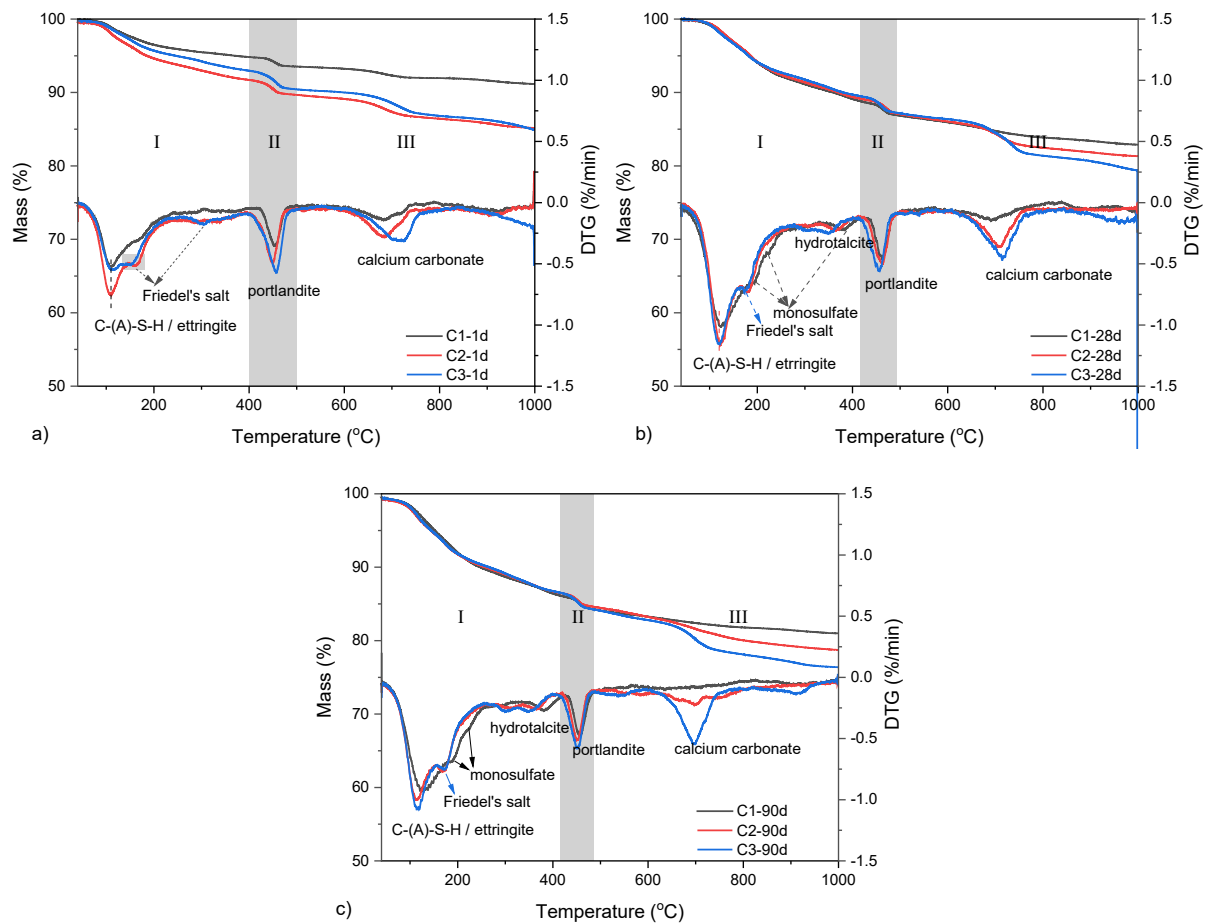


Figure 5.10 TG-DTG curves of pastes at 1 day (a), 28 days (b), and 90 days(c)

- *Portlandite content*

The portlandite content calculated according to the TGA results with the tangential method [195] is shown in Figure 5.11.

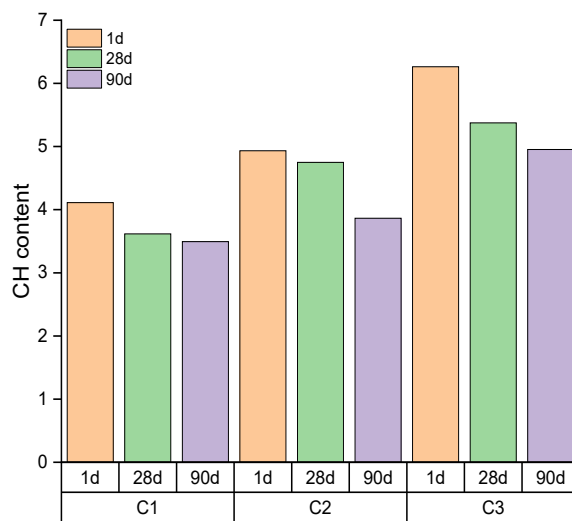


Figure 5.11 Portlandite content from TGA

Portlandite is one of the main hydrates of cement, and is also the reactant for the pozzolanic reaction that reacts with BFS. There is a gradual increase in portlandite content with the increment of WBFA, while a general decrease of portlandite content over time. These trends are in agreement with the ESI results on portlandite, as well as the IR bands of portlandite observing a decreased intensity with time.

- *Bound water content*

With the accumulation of hydrates, an increasing amount of water becomes part of the hydrates, which can be referred to as bound water. Therefore, the amount of bound water can, to a certain extent, be used as an indirect index for the reaction degrees of cementitious materials. The bound water was calculated by the weight loss of pastes below 550 °C, as illustrated in Figure 5.12. An increasing amount of bound water with time is observed for all mixtures, as the consequence of the continuous generation of reaction products. It is worth noting that mixtures containing WBFA are found with a large increase in bound water at 1 day, indicating that at 1 day, pastes containing WBFA generate more reaction products than the reference sample. This result is in line with the results obtained from the calorimetry test and QXRD, which show that WBFA accelerates the hydration of cement, leading to a larger quantity of hydrates formation (see Figures 5.2 and 5.8). A minor difference in the amount of bound water can be found for mixtures at 28 and 90 days among the three pastes, as the reaction degrees of cement are less different at later stages (seen in Figure. 5.8).

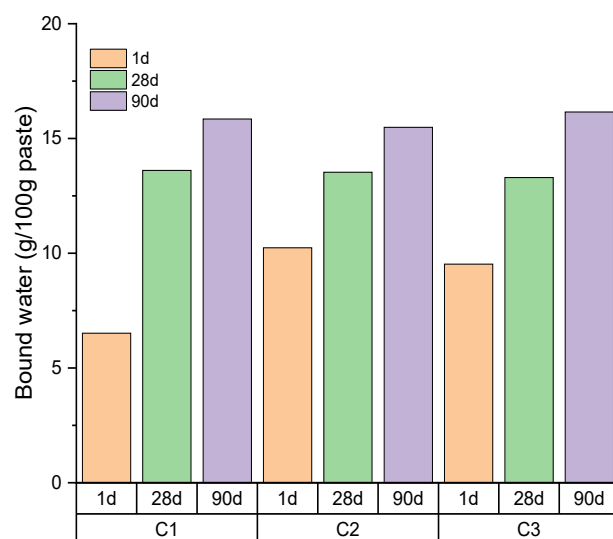


Figure 5.12 Bound water content in pastes

5.3.4 Microstructure analysis

5.3.4.1 BSE-EDS

Figure 5.13 displays the micro-morphology of blended cement pastes. The black area represents the pores immobilized by epoxy. The brightness of the particles reflects the atomic numbers of phases that enable the identification of anhydrous grains. Due to the presence of the ferrite phase, cement particles with ferrite can be brighter than the other particles. BFS grains are irregularly shaped with a uniform grey level. The WBFA particles, however, are challenging to distinguish since they exhibit a broad range of grey levels and consist of both spherical and angular particles.

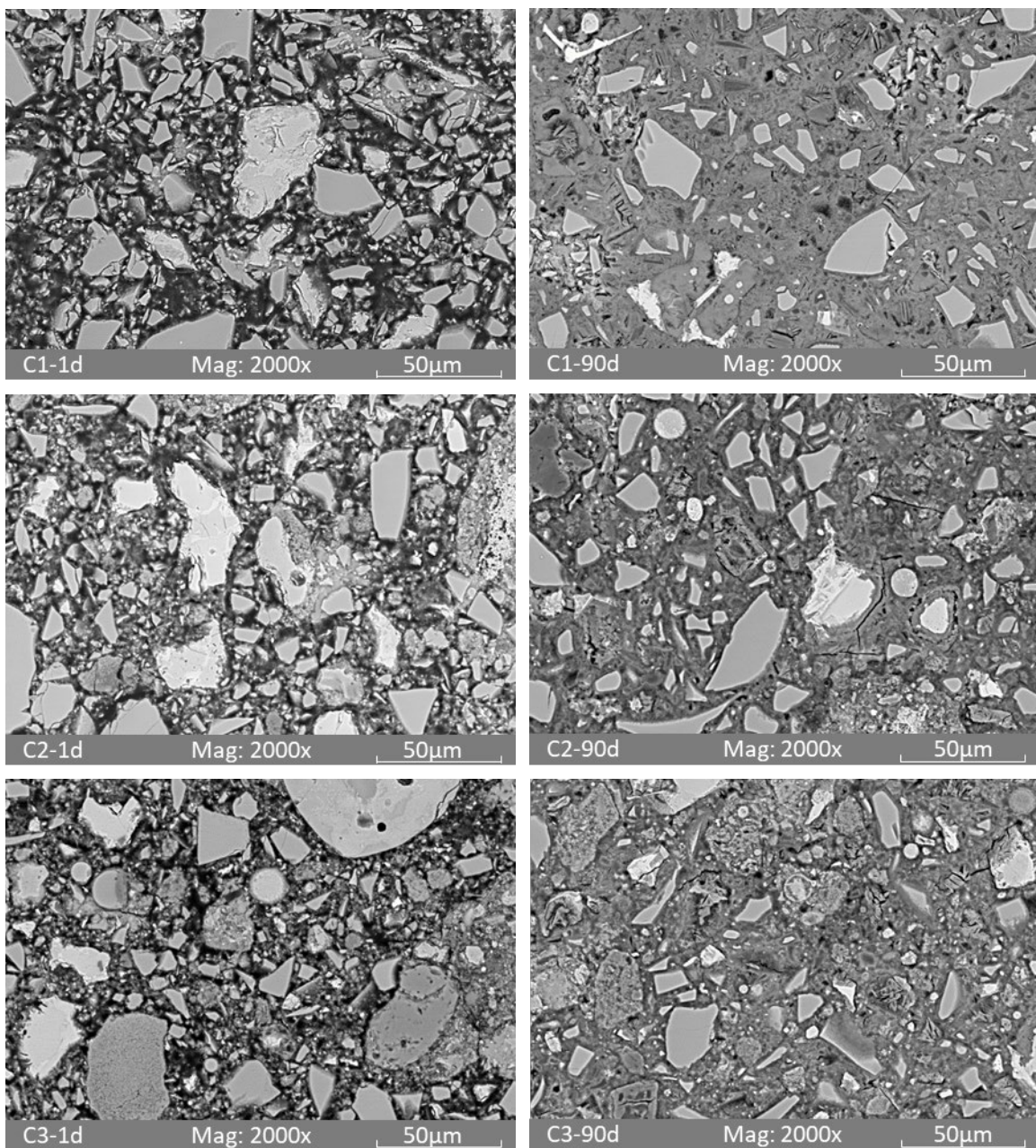


Figure 5.13 BSE images of pastes at 1 d and 90 d

For samples at 1 day, it is clear that the microstructure of C1 is highly porous, while C2 and C3 are more compacted and denser. As discussed in previous sections, WBFA accelerates the hydration of cement and BFS, promoting the formation of hydration products. A higher amount of hydrates in C2 and C3 can be expected to fill the pore spaces to densify the microstructure of pastes. The pore size distribution in Section 5.3.4.2 would further provide detailed information on these aspects. With hydration, the microstructure of pastes is further densified. The continuous generation of hydrates is found among the anhydrous particles, leading to the formulation of a dense microstructure.

The reaction degrees of BFS in the pastes can be determined by image analysis coupled with BSE-EDS mapping, as previously discussed in Section 4.2.6. As seen in Figure 5.14, the calculated reaction degrees of BFS are within the similar ranges as reported elsewhere [120,199]. A general increase in reaction degrees can be observed in mixtures with WBFA compared with the reference sample at all ages. This can be correlated to the increased alkalinity in the pore solutions with the addition of WBFA that promotes the dissolution of BFS.

The EDS mapping of cement pastes was further utilized to analyse the chemical compositions of hydration products. Since the grey scale for hydrates is generally lower compared to anhydrous particles, it is possible to screen out the hydrates through image analysis. For samples with WBFA, a preset elemental ratio restriction [226] is additionally applied to remove the anhydrous particles, as mentioned in Section 4.2.2.4. Consequently, EDS mapping on hydrates can be obtained.

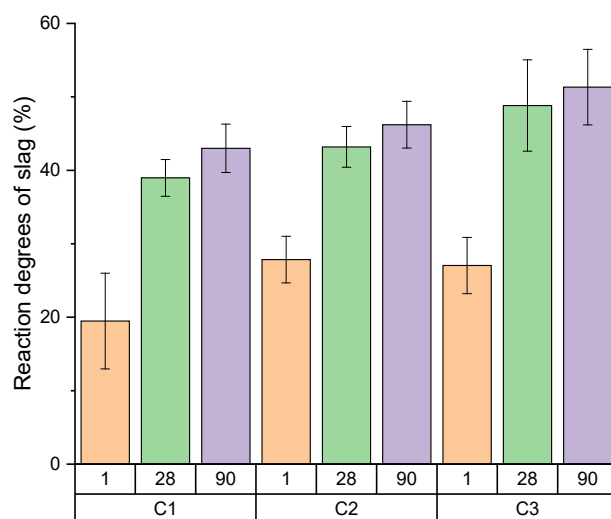


Figure 5.14 Reaction degrees of slag determined by EDS mapping

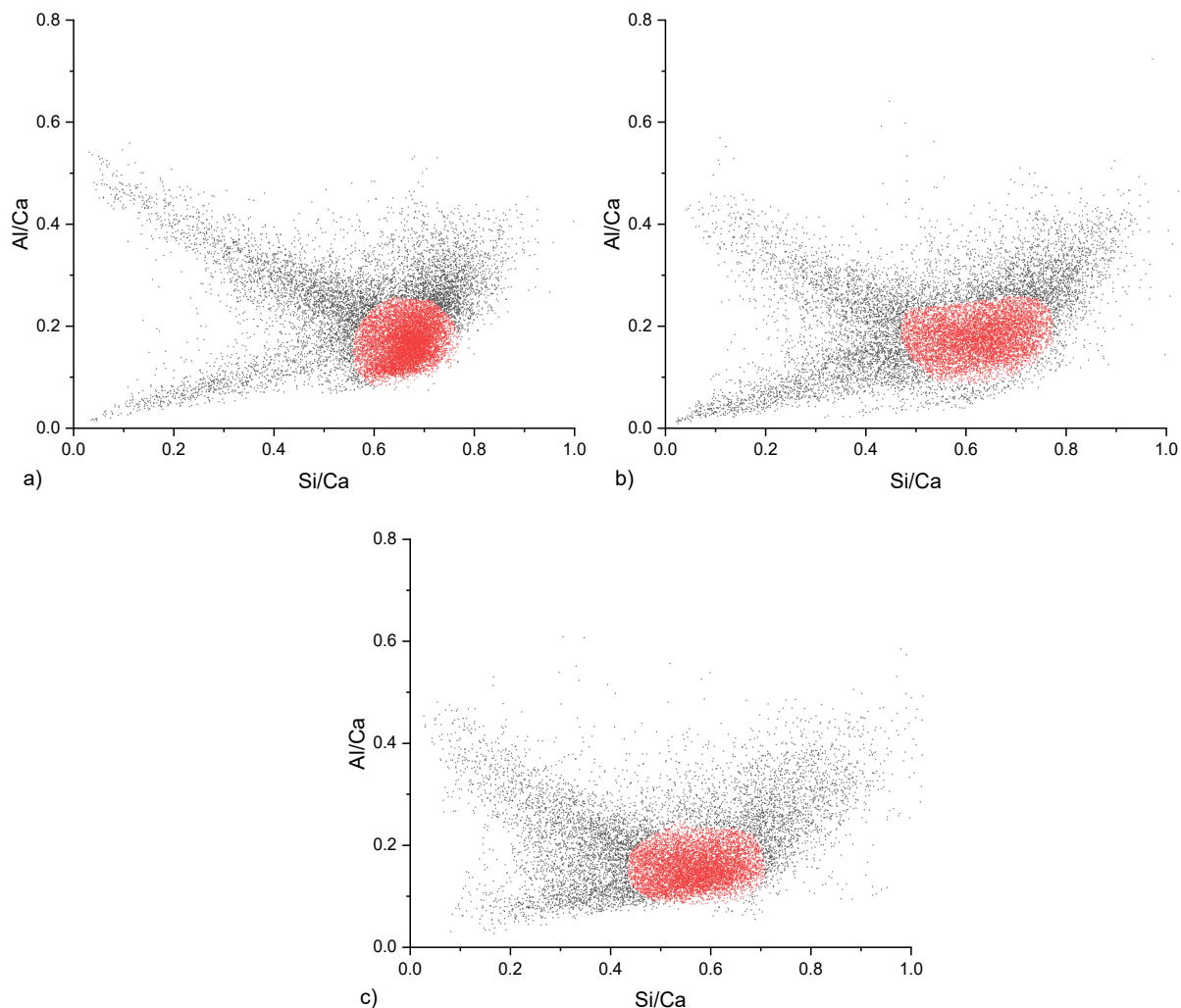


Figure 5.15 2D scatter plots of the hydration products in the pastes at 90 days (a: C1, b: C2, c: C3.)

The chemical compositions of hydration products are plotted in Figure 5.15 in terms of Si/Ca verse Al/Ca. As it is known that C-S-H gels remains its chemical compositions with a Si/Ca between 0.5 and 1. While C-S-H gels are the primary hydrate in cementitious materials, the most concentrated area in the figure is therefore identified as an intermix of C-S-H gels marked with red scatters. A slight decrease in Si/Ca ratio is observed with the addition of WBFA. The Si/Ca ratios gradually drop from 0.66 in C1 to 0.57 in C3. This is because calcium is the primary element in WBFA, while there is a significant reduction in reactive Si content in WBFA compared to BFS. Although it is agreed that the Si/Ca ratios can affect the properties of C-S-H gels, especially the micromechanical properties, the results are still debatable [257–260]. Therefore, the results here only to unveil the gels chemical compositions.

5.3.4.2 Pore structure evolution

Figure 5.16 shows the pore size distribution of pastes at 1 day, 28 days, and 90 days, determined by mercury intrusion porosimetry (MIP).

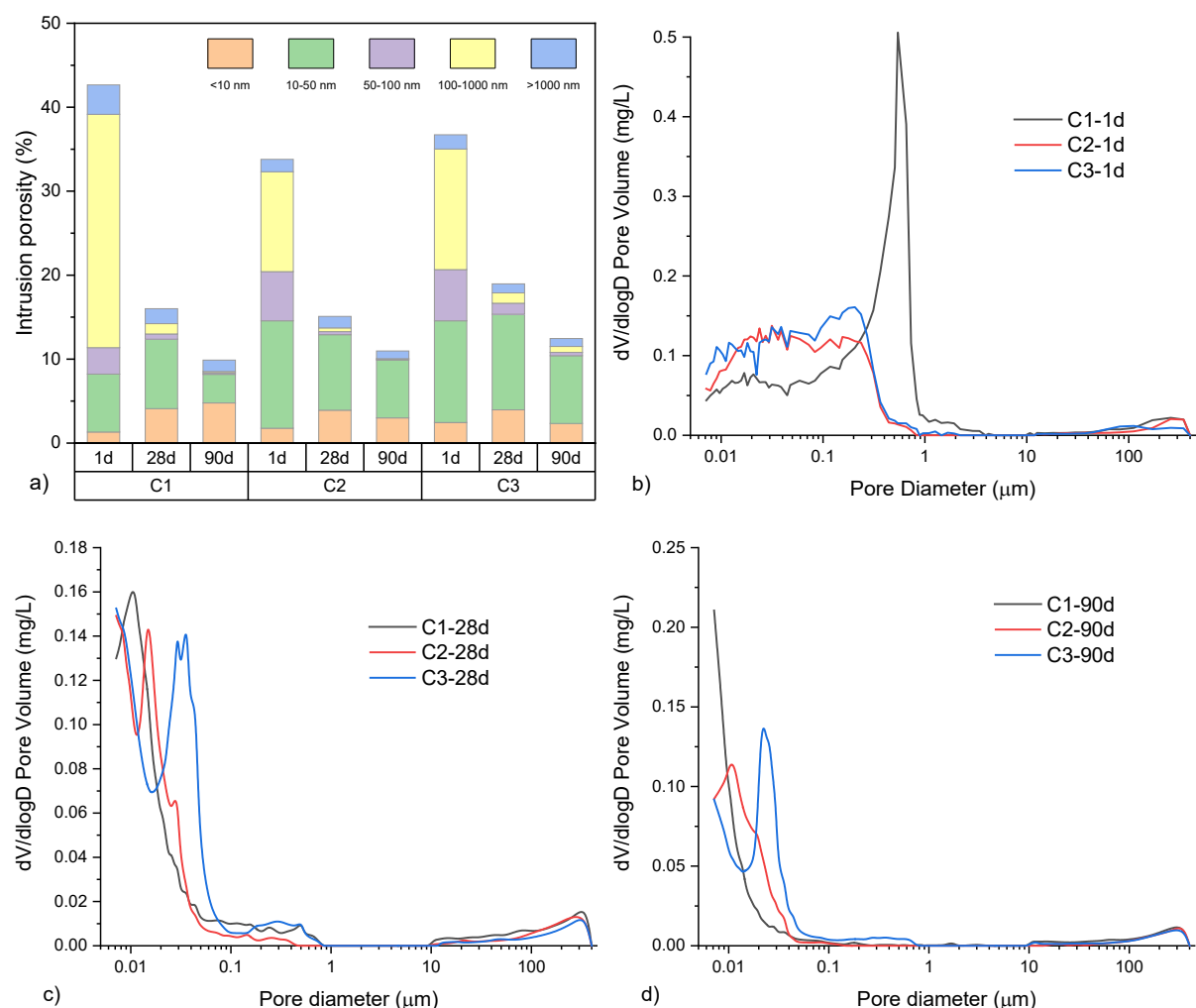


Figure 5.16 Pore proportions (a) and differential pore size distribution (b, c, d) of pastes

To better identify the pore distribution in the pastes, the pores are classified into five categories: gel pores (<10 nm), micro capillary pores (10-50 nm), medium capillary pores (50-100 nm), large capillary pores (100-1000 nm), and air voids (>1000 nm) [221-223]. For C1 at 1 day, the highest proportion of pores is attributed to large capillary pores (approximately 65%). In comparison, C2 and C3 exhibit lower proportions of large capillary pores at 1 day, more than half of the pores in C2 and C3 are under 100 nm. Additionally, a remarkable reduction in porosity is observed with the addition of WBFA. The total porosity of pastes at 1 day follows the order: C1 (42.66%) > C3 (36.72%) > C2 (33.80%). These results are consistent with the BSE image at 1 day, showing a clear improvement in microstructure in pastes with WBFA.

As the hydration process continues, both the porosity and pore size of the pastes gradually decrease. By 28 days, the total porosity of C1 decreases to 16.01%, which is comparable to that of C2 (15.09%) and lower than that of C3 (18.96%). The porosity of the pastes continues to decrease further by 90 days, with C1 having porosity of 9.88% that is comparable to C2 (10.98%), and still lower than that of C3 (12.45%). In terms of pore size, while a larger pore size is seen in C1 at 1 day compared to those in C2 and C3, it is seen that there is more significant pore refinement in C1 during hydration. The critical pore size, which

is identified by the pore size associated with the steepest peak in the differential pore volume, is found to be smaller in C1 than those in C2 and C3 after 28 days. With a larger amount of WBFA replacement, although higher reaction degrees can be achieved for both cement and BFS, the reactive component reduces in quantity given the lower reactive component in WBFA than that in BFS. Therefore, a coarser microstructure and lower strength can be foreseen with a large proportion of WBFA. Besides, as the particle size of WBFA is much larger than that of BFS and cement, the particle packing can be another reason for the porous microstructure. Further grinding can be applied to improve the microstructure and therefore, enlarge the proportion of WBFA.

5.3.5 Compressive strength

Figure 5.17 presents the compressive strength evolution of pastes. Unlike previous studies [21,76] reporting the reduction of compressive strength when WBFA is used as a cement substitute, it is seen that WBFA poses a positive impact on compressive strength in BFS blended cement pastes as a partial BFS substitution. A remarkable improvement in compressive strength is found for pastes containing WBFA at early ages. Specifically, when 15% of WBFA is introduced, the compressive strength of pastes is 75.97% and 44.05% higher than the reference group at 1 day and 7 days, respectively. Moreover, samples can still show comparable strength to the reference at 28 days and 90 days. By increasing the amount of WBFA to 30%, a noticeable but inferior early-age strength improvement is found compared to the mixture with 15% WBFA, and the compressive strength at 28 days and 90 days is slightly lower than that of reference specimens. Thus, it can be concluded that within a certain dosage, the incorporation of WBFA as BFS replacement is beneficial for the strength development of slag blended cement pastes.

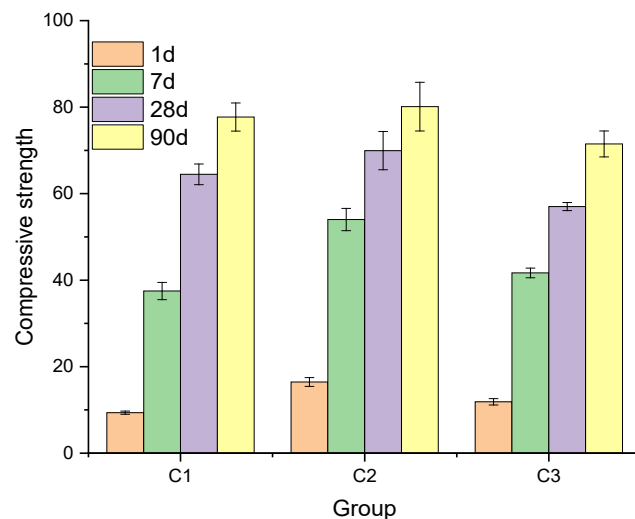


Figure 5.17 Effect of WBFA on the compressive strength of slag cement pastes

As elaborated in previous sections, WBFA can promote the reaction degrees of BFS and the early hydration of cement. This leads to the accumulation of a larger content of hydrates in C2 and C3 compared with C1, leading to the densification of pore structures. The evolution of porosity generally correlates well with strength development. However, as the decrease of BFS with the incorporation of WBFA, the reactive components decrease accordingly. Fewer hydrates can be obtained even though a higher reaction degree of BFS can be achieved, and this eventually causes the reduction in strength. This explains the marginal decrease in strength observed in C3 compared to that in C1 at 28 days and 90 days. Therefore, more attention should be paid if the content of WBFA were planned to be higher than 30%, as a more significant decrease in strength could occur.

5.4 Discussions

5.4.1 Reaction contribution from WBFA

As previously discussed in Section 4.4, it is challenging to experimentally investigate the reaction degrees of WBFA. As reaction enthalpy correlates to the hydration process of cementitious materials, it is applicable to investigate the enthalpy contributed by WBFA as an indicator to evaluate its reaction degrees.

The exponential equation in equation 5.4 has been verified as a reliable tool to fit the cumulative curves of cementitious materials [233,235]:

$$Q(t) = Q \times \exp \left(-\frac{\tau}{t} \right)^\beta \quad (5.4)$$

where $Q(t)$ is the cumulative heat of pastes (J/g) released at time t (hours), Q is the heat can be generated by the final reaction degree, and τ is hydration time parameter, β is the shape parameter.

The cumulative heat curves of C2 and C3 are fitted following this approach, as shown in Figure 5.18, with parameters present accordingly. The fitted curves show good agreement with the experimental results, indicating their applicability in predicting the heat release evolution for long-term reactions.

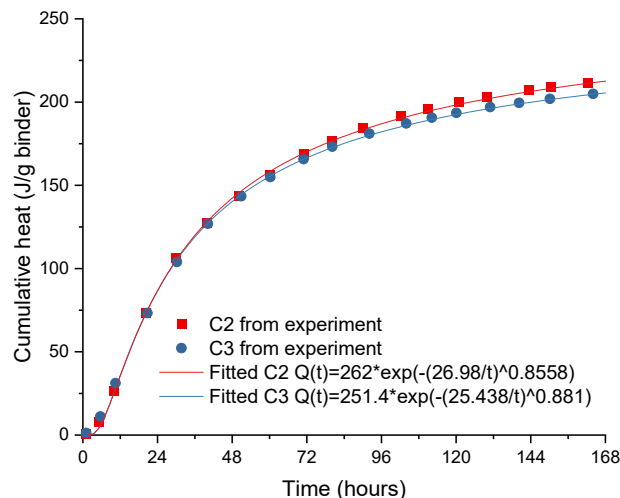


Figure 5.18 Fitted cumulative heat curves of C2 and C3 comparing with experimental data

Table 5.3 Enthalpy of complete hydration of clinker phases (J/g)

C ₃ S	C ₂ S	C ₃ A	C ₄ AF
517	262	1144, 1672	418

Table 5.4 Comparison of reaction enthalpy from cumulative fitting and from reaction degrees by QXRD and BSE-EDS mapping

	Calculated from cumulative heat (J/g binder)	Calculated from cement and BFS reaction degrees (J/g binder)		
		Clinker	BFS	Sum
C2	28 days	245.80	175.69	77.74
	90 days	255.91	181.73	83.17
C3	28 days	237.73	177.25	58.59
	90 days	246.43	182.29	61.60

As the reaction degrees of BFS and cement have been obtained from BSE and QXRD, their reaction enthalpy can be estimated by equation 5.5:

$$H_i(t) = m_i(t) \times H_i(\infty) \quad (5.5)$$

where $H_i(t)$ is the released heat (J/g binder) by component i at time t . $m_i(t)$ is the weight proportion of component i being reacted at time t . $H_i(\infty)$ is the theoretical heat of component i after hydration completion.

The $H_{BFS}(\infty)$ is set as 400 J/g, in accordance with Chapter 4. For cement, $H_i(\infty)$ for each clinker phases are adopted from the work by Copeland et al. [261], with detailed information shown Table 5.3. It is noted that for reaction of C₃A, 1144 J/g is assigned to the formation of monosulfate, while 1672 J/g is used for ettringite formation.

The enthalpy calculated from clinker phases (obtained by QXRD) and BFS (obtained from BSE-EDS image analysis) is compared with that from the predicted cumulative heat in Figure 5.18. As shown in Table 5.4, it is interesting to note that the predicted cumulative heat is almost comparable to that of the reaction contributed by BFS and cement. Hence, it can be assumed that the enthalpy contribution from the amorphous phase of WBFA is negligible. In other words, WBFA primarily provides mineral salts such as portlandite, sylvite, aphthitalite, etc., influencing the reaction of pastes, while the amorphous phase of WBFA undergoes no significant reaction.

5.4.2 Phase evolution prediction of BFS blended cement containing WBFA

Experimental results on the reaction degrees of different components enable the establishment of kinetic relationships. This facilitates the execution of modelling the reaction

process using thermodynamics, which can provide informative insights into phase evolution and their related properties.

Since the amorphous phases in WBFA are excluded from consideration, for BFS and cement, the exponential equation (5.6) is believed to be one of the most acceptable empirical equations for a simple representation of the hydration process:

$$\alpha_i(t) = \alpha_{ut,i} \times \exp\left(-\frac{\tau}{t}\right)^\beta \quad (5.6)$$

where $\alpha(t)$ is the reaction degree of one component i at time t (hours), α_{ut} is the ultimate reaction degree that can be achieved.

With the reaction degrees of BFS and cement at 1 day, 28 days, and 90 days, the unknown three parameters $\alpha_{ut,i}$, τ , and β can be calculated. The detailed parameters are provided in Table 5.5. Thus, their kinetic equations can be established, with the results shown in Figure 5.19. The thermodynamic modelling is further introduced to provide insights regarding the time-dependent phase evolution as shown in Figure 5.20.

The results from the thermodynamic modelling generally align well with experimental findings. C-S-H gels are predicted to be the most dominant hydrates in all mixtures. The addition of WBFA leads to a faster generation of C-S-H gels at early hydration, which can contribute to strength development. A minor decrease in C-S-H gels is predicted with the increment of WBFA at later hydration, which is mainly because of the reduced content of reactive aluminosilicates when BFS is replaced with WBFA. On the other hand, in C1, the transformation of ettringite to monosulfate is seen, which agrees with the experimental results. By introducing WBFA, the ettringite remains stable. A greater amount of ettringite can be generated in pastes with more WBFA due to the high content of sulfate in WBFA. This can be helpful for the densification of the microstructure, further contribute to the strength development.

Table 5.5 Parameters in equation 5.6 for the expression of reaction degrees of cement and BFS

Group	Component	α_{ut}	τ	β
C1	BFS	51.41	22.15	0.3762
	Cement	87.20	8.46	0.5367
C2	BFS	52.96	6.66	0.3446
	Cement	87.71	3.66	0.5081
C3	BFS	54.11	12.68	0.5730
	Cement	88.75	3.15	0.4648

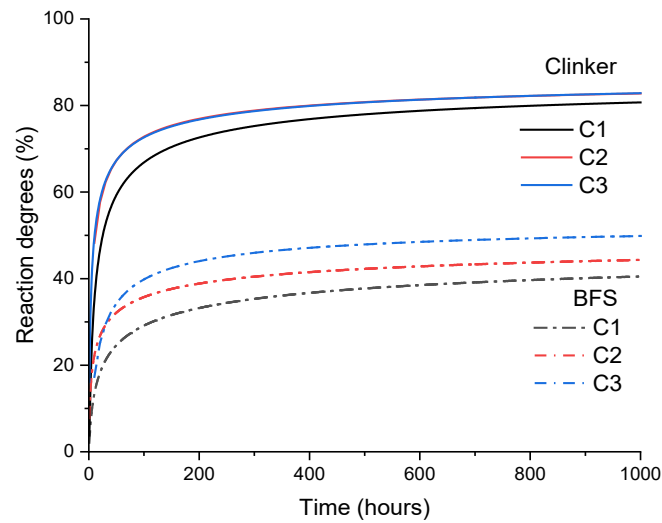


Figure 5.19 Calculated reaction degrees of cement and BFS as a function of time

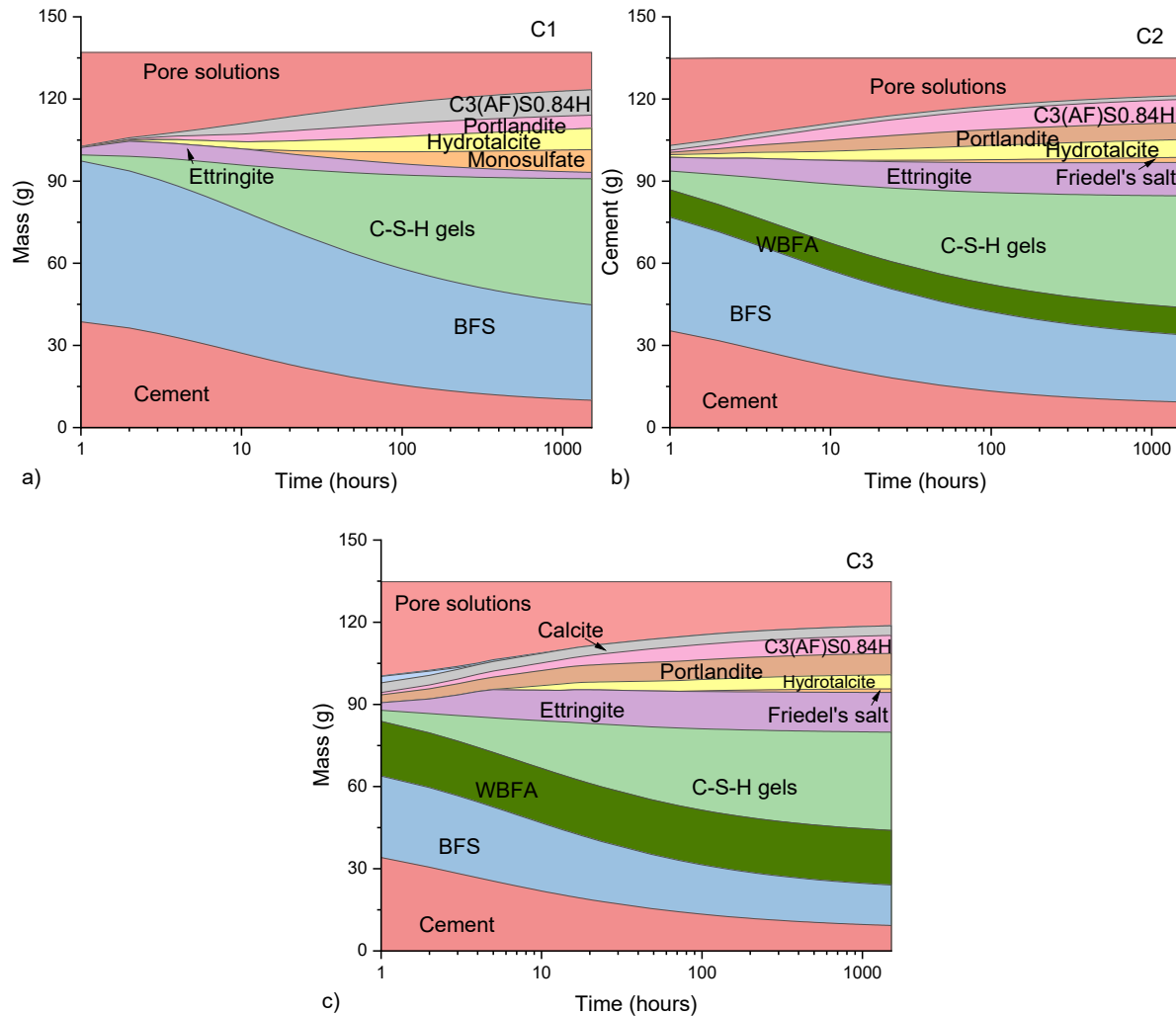


Figure 5.20 Thermodynamics modelling of phase evolution in pastes (a: C1; b: C2; c: C3)

5.5 Conclusions

This chapter uses WBFA as a partial BFS replacement in BFS blended cement pastes, aiming at integrating WBFA as a new mineral additive for blended cements. WBFA up to 30% of total binder by weight was introduced, and the impacts of WBFA on reaction kinetics, microstructure formation, and compressive strength on BFS blended cement were comprehensively investigated. The following conclusions can be drawn:

- 1) WBFA can promote the early hydration of BFS and cement. The QXRD results confirm the accelerated hydration of cement during the early stages while maintaining a comparable reaction degree in the later stages. Additionally, the reaction degrees of BFS, as determined by BSE-EDS analysis, prove that a higher degree of BFS can be achieved in pastes with a larger proportion of WBFA.
- 2) The addition of WBFA induces alterations in the composition of hydrates. In reference mixture C1 (BFS blended cement pastes), the primary hydration products are C-S-H gels, monosulfate, hydrotalcite, and portlandite at later hydration. By incorporating WBFA, ettringite maintains stability and is seen as the main sulfate-bearing hydrate, attributed to the high sulfate content in WBFA. The chloride salt in WBFA prompts the precipitation of Friedel's salt as well. C-S-H gels are found to have an increased Ca/Si ratio with the addition of WBFA.
- 3) The microstructure evolution of pastes correlates to the reaction of binders as well as particle packing. The promoted hydration of cement and BFS by WBFA significantly reduces the porosity and pore size at early age. However, the reactive component in WBFA is lower compared with BFS, and the particle size of WBFA is larger than BFS. Substituting a large proportion of BFS with WBFA would lead to a coarser microstructure of pastes at later ages.
- 4) From the strength development perspective, adding WBFA can significantly increase the early strength of BFS-blended cement. Incorporating 15% of WBFA brings no negative impact on compressive strength at later hydration. This has significant implications for industrial applications.

In this chapter, WBFA has been approved as a promising mineral in BFS blended cement. Apart from the technical properties of WBFA contained BFS blended cement, further investigations on environmental perspectives should be conducted, which will be addressed in Chapter 7.

Chapter 6

Carbonation of cementitious materials containing wood biomass fly ash

6.1 Introduction

Carbonation of cementitious materials includes both physical diffusion processes where CO_2 permeates into the matrix through pores [262], and chemical reactions between the dissolved CO_2 and the cementitious matrix (both hydrates and anhydrous phases) [263]. These reactions will cause alterations of the microstructure in cementitious materials, which have profound implications on the functional properties of cementitious materials [263–265]. Although specifying intended use conditions can mitigate exposure to severe conditions, contacting with air, where carbonation occurs, is hardly evitable during the service life of cementitious materials.

Cementitious materials with low clinker contents are typically more vulnerable to carbonation, as seen in alkali-activated materials and blended cement systems compared to Portland cement [266,267]. In the case of the WBFA-BFS binary binder, the absence of clinker raises concerns and sparks research interest regarding its carbonation resistance. Conversely, in blended cement with WBFA, the introduction of WBFA actually increases the content of portlandite, which is assumed to act as a carbonation buffer, potentially benefiting carbonation resistance. Therefore, it is of interest to investigate whether WBFA can improve the carbonation resistance of BFS blended cement.

In light of previous chapters with the results of the reaction mechanism and microstructure evolution of both WBFA-BFS binary pastes and BFS blended cement pastes containing WBFA, this chapter is dedicated to study the carbonation effects on phase compositions, microstructure alteration, and strength evolution of the pastes examined earlier. These outcomes contribute to a deeper understanding of these binders, in terms of their long-term performance, particularly emphasizing their resistance to carbonation.

6.2 Materials and experiments

6.2.1 Materials and mixtures

Raw materials include treated WBFA, BFS, and cement. They are the same as those used in previous chapters. Two binder systems investigated in Chapters 4 and 5 are studied in this chapter for the investigation of the impact of carbonation on these pastes. The binary pastes include B30S70, B50S50, and B70S30, where B refers to WBFA and S refers to BFS, with the number indicating the weight percentage of individual components in the binders. The BFS blended cement includes C1, C2, and C3, where C1 is the reference mixture containing 40% cement and 60% BFS, similar in composition to CEM III/A. C2 and C3 contain 15% and 30% of WBFA, respectively, of the total mass in the binder, as a replacement of BFS. Detailed mixture

proportions can be found in Sections 4.2.2 and 5.2.2 for these two binder systems, respectively.

6.2.2 Experimental methods

The overall experimental program is illustrated in Figure 6.1. Specifically, the experimental program includes the following three parts:

6.2.2.1 Accelerated carbonation

Cubic samples with a dimension of 4 cm were initially cast and cured for 28 days under the standard curing condition (relative humidity above 95% and temperature at 20°C). Following this, the specimens underwent a preconditioning program in a climate chamber at $55\pm 5\%$ relative humidity and 20°C for 14 days before being placed in the carbonation chamber, enabling samples to attain an equilibrium similar to the carbonation condition. Accelerated carbonation experiment was conducted to investigate the carbonation process of pastes, following EN 12390-12 with CO₂ concentration set at 3% and RH at $55\pm 5\%$.

6.2.2.2 Carbonation depth and compressive strength measurements

Carbonation depth of samples was determined by the phenolphthalein method. Specimens were split into halves after being carbonated for a certain period, and the cross sections were sprayed with phenolphthalein solution. As indicated in Figure 6.1, based on the colour change of specimens, the colourless area is considered as fully carbonated area, and the carbonation depth was measured accordingly. For binary pastes, due to the fast carbonation rate, the carbonated samples were measured at carbonation durations of 1 day, 3 days, 7 days, and 14 days. For pastes containing cement (C1, C2, and C3), samples after carbonation periods of 7 days, 28 days, and 70 days were measured. The carbonation depth results represent an average measurement of three specimens.

The compressive strength of the carbonated pastes was monitored simultaneously with the carbonation depth measurement. The average compressive strength of five specimens was used as the final result.

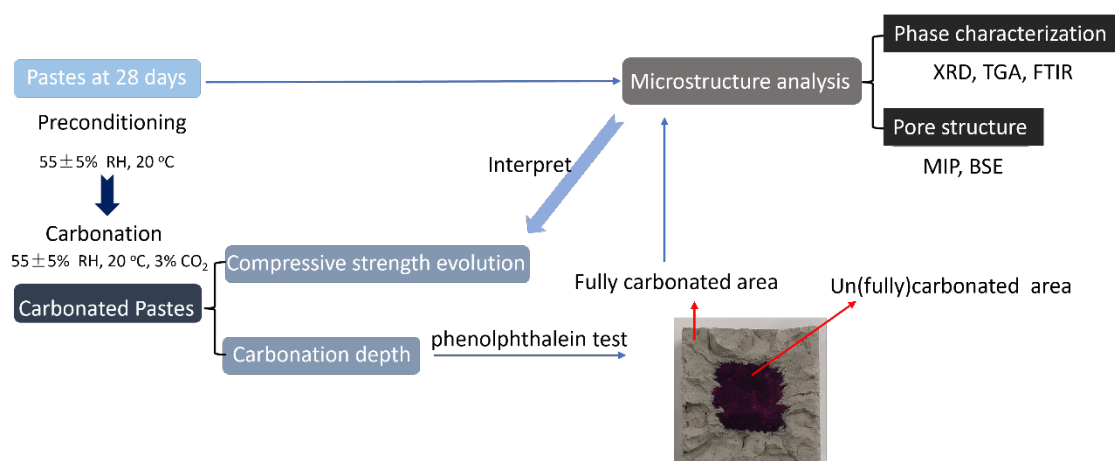


Figure 6.1 Schematic of experimental program

6.2.2.3 Microstructure analysis

After the carbonation program (B30S70, B50S50, B70S30 carbonated after 14 days and C1, C2, C3 carbonated after 70 days), the fully carbonated areas as indicated in Figure 6.1 were sawed apart and collected. Part of the samples were prepared for the characterization of carbonated products by using XRD, TGA, and FTIR techniques. Another part of the samples was prepared for pore structure analysis by using MIP test and BSE analysis. Detailed sample preparations for different experiments and the related test procedures can be found in Sections 4.2.2.3 and 4.2.2.4.

6.3 Results

6.3.1 Carbonation Rate

As the carbonation of cementitious materials follows Fick's first law of diffusion [268,269], a linear relationship can be established between the carbonation depth of pastes and the square root of carbonation time as shown in equation 6.1:

$$d = K \times \sqrt{t} \quad (6.1)$$

where d (mm) is the carbonation depth of samples at time t (days), and K (mm/days $^{1/2}$) is the carbonation coefficient, representing the carbonation rate of samples. A smaller carbonation coefficient implies a slower carbonation progress while a larger one indicates a faster carbonation.

A detailed comparison of the carbonation coefficient of the binder in the current study with other cementitious materials from the literature is provided in Table 6.1. Since the carbonation concentrations vary in different research, the carbonation coefficient can be recalculated to a fixed concentration of 3% to provide a reasonable comparison. The calculation can be conducted based on equation 6.2 [270]:

$$K_a = K_b \sqrt{\frac{C_a}{C_b}} \quad (6.2)$$

where K_a represents the calculated carbonation coefficient under a CO₂ concentration at 3% (C_a), K_b is the measured carbonation coefficient under their experimental CO₂ concentration (C_b).

This equation is normally used for predicting the natural carbonation resistance of cementitious materials based on their accelerated carbonation results [271]. It is important to note that this equation is only validated when the other carbonation conditions are similar, for instance, the relative humidity. The comparison in Table 6.1 aims to provide a brief overview of the carbonation resistance between WBFA-containing cementitious materials and other common materials.

Table 6.1 Carbonation coefficient of pastes in the current study comparing with literature

Binder components	CO ₂ concentration	Carbonation coefficient	Calculated Carbonation coefficient at 3%	Ref
WBFA-BFS binary pastes	3%	3.68-4.97	Current study	
WBFA in BFS-Cement pastes		0.18-0.70		
Portland cement	2%	1.05	1.29	[270]
BFS blended cement		1.43-2.11	1.75-2.58	
Cement paste	10%	2.83	1.55	[272]
BFS blended cement	3%	0.90	-	[273]
Coal fly ash blended cement		0.93	-	
Alkali-activated slag and fly ash pastes (S50)	1%	1.58-2.65	2.74-4.59	[274]

- *WBFA-BFS binary pastes*

The carbonation depth of binary pastes over the square root of carbonation time is shown in Figure 6.2, with all fitting parameters being presented accordingly.

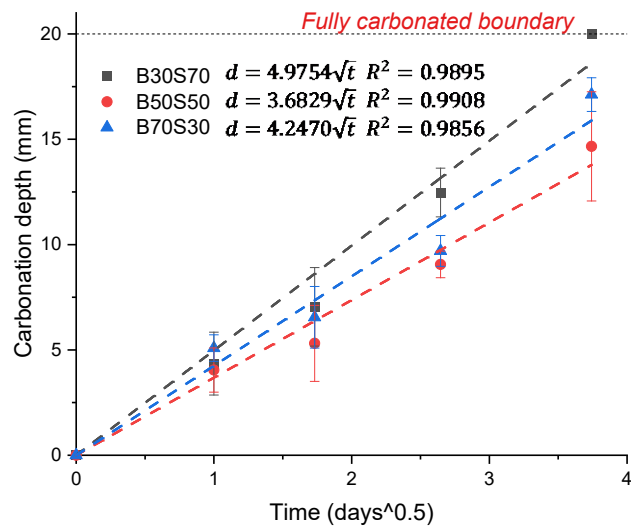


Figure 6.2 Carbonation depth of binary pastes as the function of square root of carbonation time

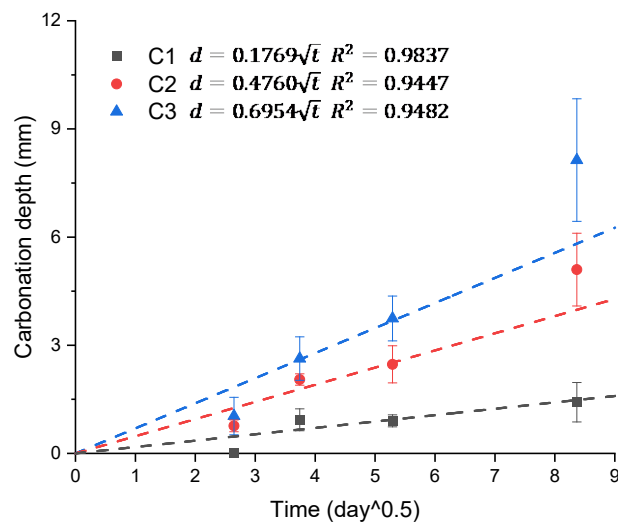


Figure 6.3 Carbonation depth of pastes C1, C2, and C3 as a function of square root of carbonation time

In general, binary pastes show a fast carbonation process. B30S70 reaches its full carbonation after 14 days (carbonation depth ≥ 20 mm). The carbonation coefficients of the three mixtures are 4.97, 3.68, and 4.25 for B30S70, B50S50, and B70S30, respectively. Although these values vary with different WBFA/BFS ratios, it is noticed that they are much higher than those reported for cement-based materials carbonated at the same conditions [273] but comparable with those in alkali-activated materials [271,274]. The high carbonation rate of binary pastes can be attributed to the limited amount of portlandite, which acts as a buffer for carbonation in the pastes [275]. Additionally, the high porosity discussed in Section 4.5 can also contribute to the fast carbonation. Detailed discussions will be presented in the following sections.

- *BFS blended cement pastes with WBFA*

Figure 6.3 shows the impact of WBFA on the carbonation rate of BFS blended cement pastes. The carbonation coefficients for C1, C2, and C3 are 0.18, 0.48, and 0.69, respectively. These values align with the results reported in the literature for BFS blended cement [273,276]. As discussed in Section 5.3.3.3, pastes containing WBFA contain a higher amount of portlandite, which is considered the carbonation buffer. Still, a clearly diminished carbonation resistance in pastes is observed with the increment of WBFA. The reasons for this phenomenon will be discussed in the following sections.

6.3.2 Phases alteration via carbonation

6.3.2.1 Mineral phases

- *WBFA-BFS binary pastes*

Figure 6.4 compares the XRD patterns of WBFA-BFS binary pastes at their 28-day hydration (solid line) and after full carbonation (the colourless parts of samples after the phenolphthalein test, dash line). The XRD analysis of binary pastes at their 28-day hydration have been discussed in Section 4.3.4, with clear presence of Fridel's salt, ettringite, and hydrotalcite as the crystalline hydrates in all mixtures. The diffraction peak of portlandite is also seen as unreacted phase from WBFA.

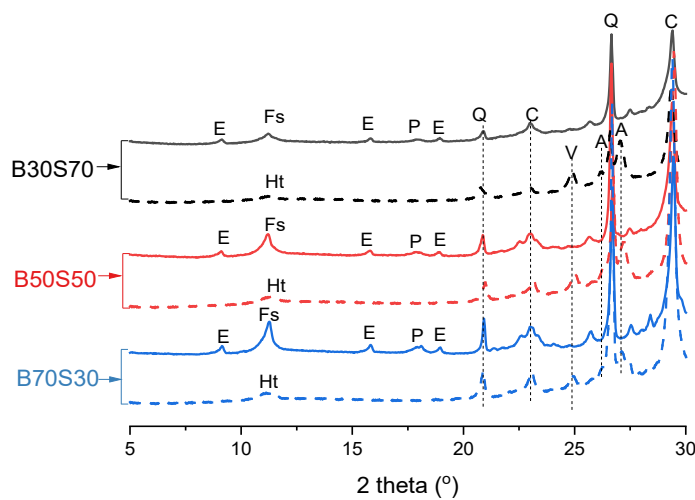


Figure 6.4 XRD patterns of WBFA-BFS pastes at 28 days (solid lines) and after carbonation (dash lines). (Phases are denoted as, E: ettringite, Fs: Friedel's salt, P: Portlandite, V: vaterite, A: aragonite, C: calcite, Q: quartz, Ht: hydrotalcite)

Carbonation leads to significant phase alterations. In the carbonated samples, ettringite, Friedel's salt, and portlandite are absent, while hydrotalcite is the only remaining crystalline hydrate after carbonation. It is noted that there is a sharp increase in the diffraction peak of calcite, indicating the continuous precipitation of calcite in pastes after carbonation. Other calcium carbonate polymorphs, i.e., aragonite and vaterite, are also identified. No significant difference can be observed among the carbonated samples with different WBFA/BFS ratios, as all these mixtures are comprised of similar hydration phases.

- BFS blended cement pastes with WBFA

Figure 6.5 presents the XRD patterns of C1, C2, and C3 at their 28-day hydration and after carbonation.

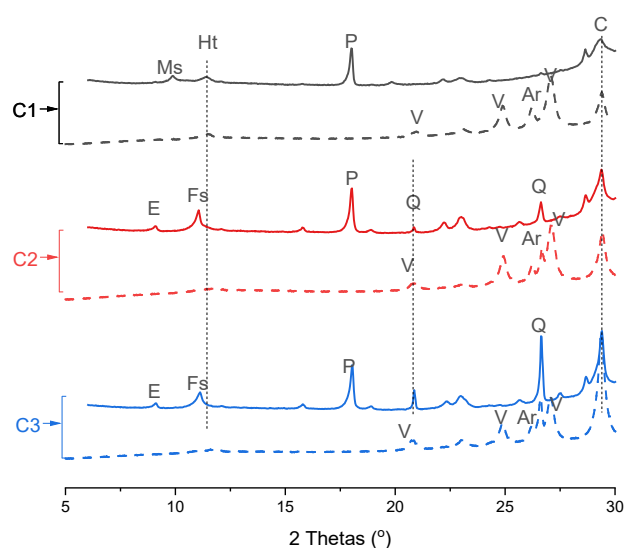
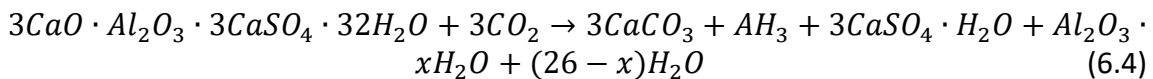
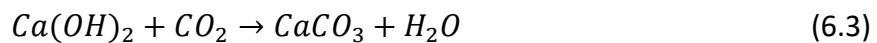


Figure 6.5 XRD patterns of C1, C2, and C3 at 28 days (solid lines) and after carbonation (dash lines) (Phases are denoted as, E: ettringite, Fs: Friedel's salt, P: Portlandite, Ms: monosulfate, V: vaterite, A: aragonite, C: calcite, Q: quartz, Ht: hydrotalcite)

As discussed in Section 5.3.4.1, the main hydration products of these pastes at 28 days include C-S-H gels, portlandite, hydrotalcite, monosulfate (only in C1), ettringite, and Friedel's salt (only in C2 and C3). All of the hydrates are well identified in the patterns except for C-S-H gels due to their amorphous structure. Carbonation induces significant phase changes. The diffraction patterns of carbonated cement pastes are identical to those found in Figure 6.4, all of the crystalline phases lose their presence in the carbonated samples, except for hydrotalcite with a minor diffraction peak observed at 2 thetas around 11.7°. Calcium carbonate in different polymorphs (calcite, vaterite, aragonite) is present. The carbonated samples show minor differences in their diffraction patterns, due to their similar phase compositions undergoing identical phase alterations during carbonation.

- *Overview of crystalline phase alteration*

Calcium-bearing hydrates are the most susceptible phases during carbonation. Among these phases, portlandite shall convert into calcium carbonate during its carbonation (equation 6.3). Ettringite shall eventually transform into gypsum, alumina gels, and calcium carbonate (equation 6.4) [277,278].



Notably, aluminate gels are amorphous, thus they can hardly be observed in the XRD patterns. The absence of the diffraction peaks of gypsum, on the other hand, may also be attributed to its formation in a poor crystallinity or amorphous state [279]. In addition, sulfate may also be absorbed in silica and aluminate gel, thus gypsum is less likely to precipitate in large quantities in this scenario.

Both monosulfate and Friedel's salt are typical Ca-Al AFm phases with a doubled-layered structure. Carbonate can preferentially occupy the interlayer space by replacing their original anions (sulfate and chloride) [280]. With the introduction of excess CO₂, the decreasing pH in pore solution would eventually lead to phase decomposition into calcium carbonate, aluminate gels, gypsum (for monosulfate), and calcium chloride (for Friedel's salt) [281–283].

Similarly, hydrotalcite with doubled-layered structure is capable of capturing carbonate into its interlayer structure, replacing hydroxide to form the stabilized Mg-Al-CO₃ hydrotalcite phase after carbonation [280,284,285]. Compared to Ca-Al AFm phases, hydrotalcite can remain stable at a lower pH [286]. Meanwhile, hydrotalcite remains constant in diffraction peaks before and after carbonation, allowing for its identification in the carbonated samples.

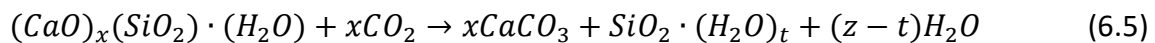
6.3.2.2 Chemical bonds

As XRD can only provide information on crystalline phases, the carbonation of C-S-H gels can hardly be distinguished. Therefore, FTIR analysis was implemented to investigate the alteration of silicate species in C-S-H gels during carbonation.

- WBFA-BFS binary pastes

As discussed in Section 4.3.3.2, the variations in WBFA/BFS ratios bring a minor impact on the IR bands of binary pastes. Thus, only B50S50 was presented in this regard to illustrate carbonation on the binary pastes, as presented in Figure 6.6.

The main band of B50S50 before carbonation is located at 950 cm^{-1} , representing the Q2 species of Si-O bonds, which is the signal of C-S-H gels [216]. This Si-O bond shifts when there is a significant change in the Ca/Si ratios within C-S-H gels, with the band moving to a higher wavenumber when C-S-H gels change to a lower Ca/Si ratio [169,216,287]. It is evident that the main Si-O bonds move from 950 cm^{-1} in uncarbonated samples to 1018 cm^{-1} in carbonated paste, implying the decalcification of C-S-H gels during the carbonation of pastes. This will eventually lead to the formation of amorphous silica gels and calcium carbonate, as shown in equation 6.5.



Besides the silicate species, carbonation induces a significant change in C-O bands. In B50S50 at 28 days, calcite originating from WBFA can be found by C-O bands at 1415 cm^{-1} , 875 cm^{-1} , and 710 cm^{-1} with sharp peaks [288]. In carbonated samples, the relative intensity of these bands significantly increases, indicating a higher amount of calcite due to the carbonation of hydrates. Furthermore, unlike the uncarbonated spectrum, which only shows a sharp band at 1420 cm^{-1} due to the presence of calcite alone, the carbonated samples exhibit a broader feature in this band. This broader feature is attributed to the intermixing of amorphous calcium carbonate and aragonite [169,289]. Moreover, band at 855 cm^{-1} is particularly observed in the carbonated samples, and is the typical signal for the presence of vaterite [290]. These findings align with the XRD results, which confirm the coexistence of multiple polymorphs of calcium carbonate in the carbonated samples.

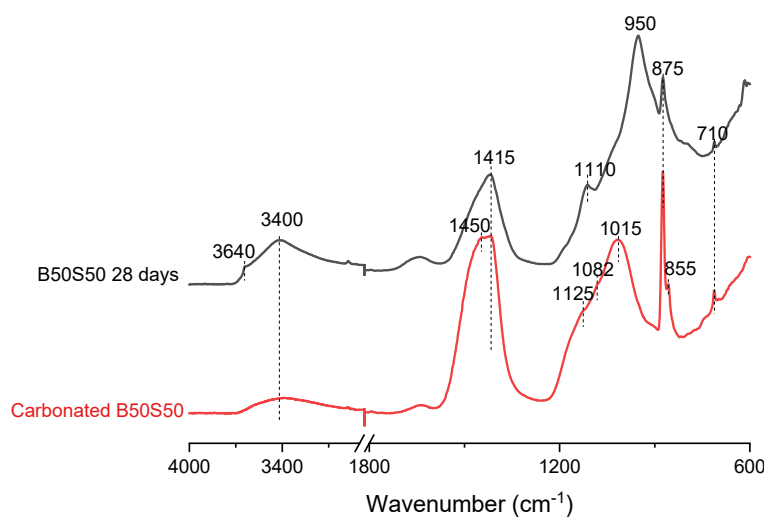


Figure 6.6 FTIR spectra of B50S50 at 28-day hydration and after carbonation

The band at 1115 cm^{-1} should be assigned to the vibration of sulfate. Previous results indicate that the sulfate band at this position is a specific signal of ettringite [253], and this sulfate band is unseen in the carbonated sample, implying the decomposition of ettringite, which is aligned with the XRD results. The presence of OH bonds at 3640 cm^{-1} in B50S50, with low intensity before carbonation, provides evidence of a small amount of portlandite. This band disappears in the carbonated spectra, as a consequence of the conversion into calcium carbonate. Other bands at 3400 cm^{-1} should be the free water of pastes. The weakened intensity might be the consequence of free water loss during carbonation at a low RH.

- BFS blended cement pastes with WBFA

Figure 6.7 compares the chemical bonds of BFS blended cement pastes with WBFA before and after carbonation. Discussions on the chemical bonds in hydrates have been presented in Section 5.3.4.2.

The carbonated samples, in general, exhibit identical carbonated IR spectra. Similar to the ones of carbonated binary pastes shown in Figure 6.6, the representative bands for portlandite (OH bond at 3640 cm^{-1}) and ettringite (S-O bond at 1115 cm^{-1}) disappear after carbonation, which is in line with the XRD results indicating their full carbonation. All mixtures show the shift of Si-O bands to a higher wavenumber, as a consequence of the decalcification of C-S-H gels with the formation of silica gels [291]. Compared to mixtures containing WBFA that shift the main Si-O bands to 1026 cm^{-1} , the reference mixture C1 exhibits the main Si-O band at 1009 cm^{-1} . WBFA leads to more vulnerable C-S-H gels under carbonation. This can be attributed to different Si/Ca ratios as reported in Section 5.3.4.1 where WBFA leads to an increase in Ca/Si ratios in general. As C-S-H gels with lower Ca/Si ratios are more polymerized with a stronger interaction of siloxane with calcium, better carbonation resistance should be attained for C-S-H gels with lower Ca/Si ratios [292].

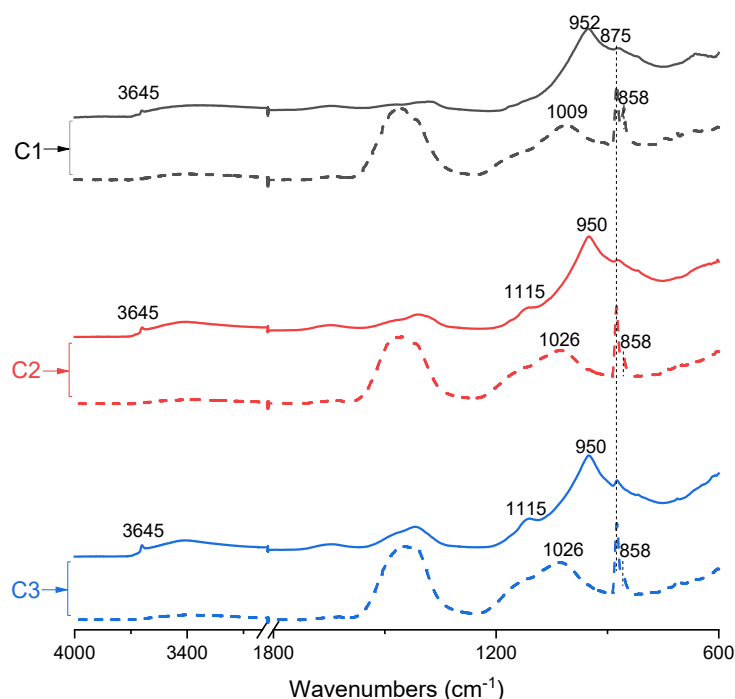


Figure 6.7 FTIR spectra of C1, C2, and C3 after 28-day hydration (solid lines) and after carbonation (dash lines)

Regarding the C-O bands, similar to the findings in binary pastes, the intensity of C-O bands largely increases after carbonation, revealing the increasing amount of carbonate in the samples. The C-O bands representing calcite at 875 cm^{-1} and 1420 cm^{-1} become the main peak, thus calcite should be the main carbonate phase among the three polymorphs. A slight shift of the C-O band from approximately 1466 cm^{-1} to 1452 cm^{-1} with the increment of WBFA, due to the increased proportion of calcite compared to the amorphous calcium carbonate.

6.3.2.3 CO_2 binding

TGA-MS was further applied to study the CO_2 binding capacity in different mixtures.

- *DTG analysis*

The DTG curves of pastes at their 28-day hydration have been previously discussed in Section 4.3.3.3 (WBFA-BFS binary pastes) and Section 5.3.3.3 (WBFA in BFS blended cement pastes). The DTG profiles of pastes are illustrated in Figures 6.8 and 6.9, respectively, with a comparison to their carbonated samples.

As discussed in previous sections, most hydrates eventually transfer into calcium carbonate, gypsum, and silica-aluminate gels. Therefore, the DTG curves for all carbonated samples are identical in shape with similar decomposition temperatures.

The first decomposition peak in carbonated samples is found to shift to around $160\text{ }^\circ\text{C}$, compared to the uncarbonated one at about $110\text{ }^\circ\text{C}$. This peak should mainly correspond to the free water loss of silica-aluminate gels [291], and the possible dehydration of gypsum (conversion into hemihydrate) and hemihydrate (conversion into anhydrite III) [293]. The peak at around $380\text{ }^\circ\text{C}$ in uncarbonated pastes remains present in the carbonated pastes, which should be related to the decomposition of carbonated hydrotalcite phases, consistent with XRD results.

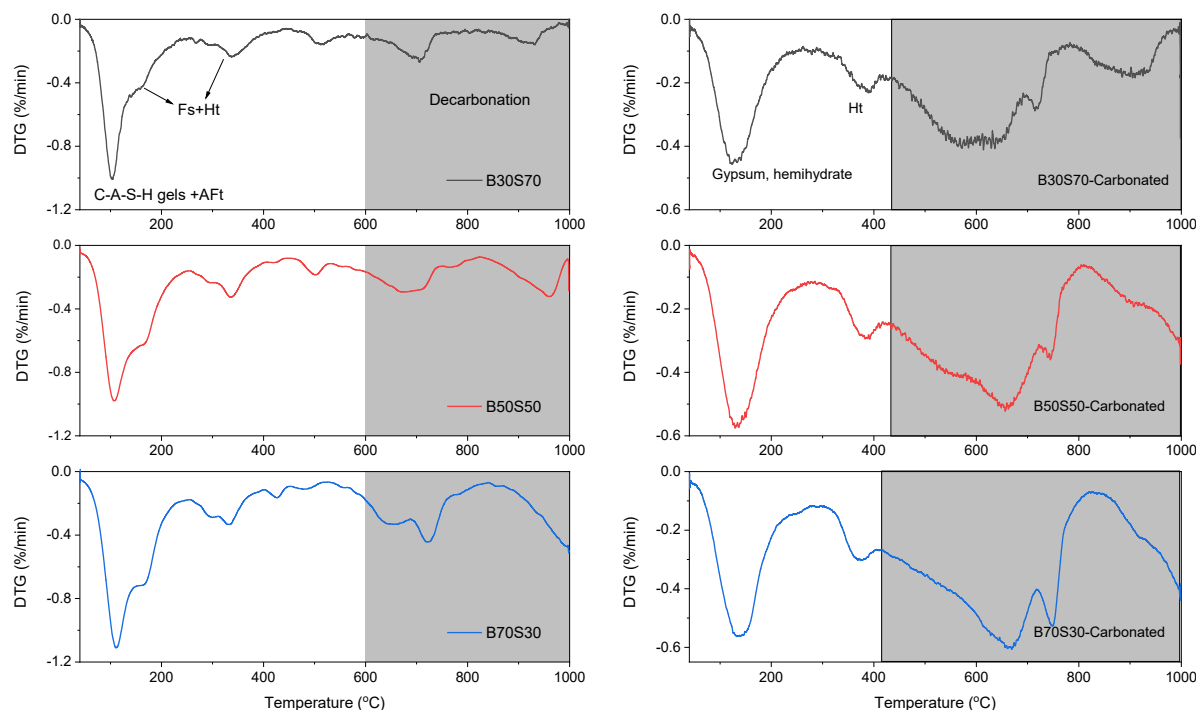


Figure 6.8 TG and DTG curves of WBFA-BFS binary pastes at 28 days (left) and after carbonation (right)

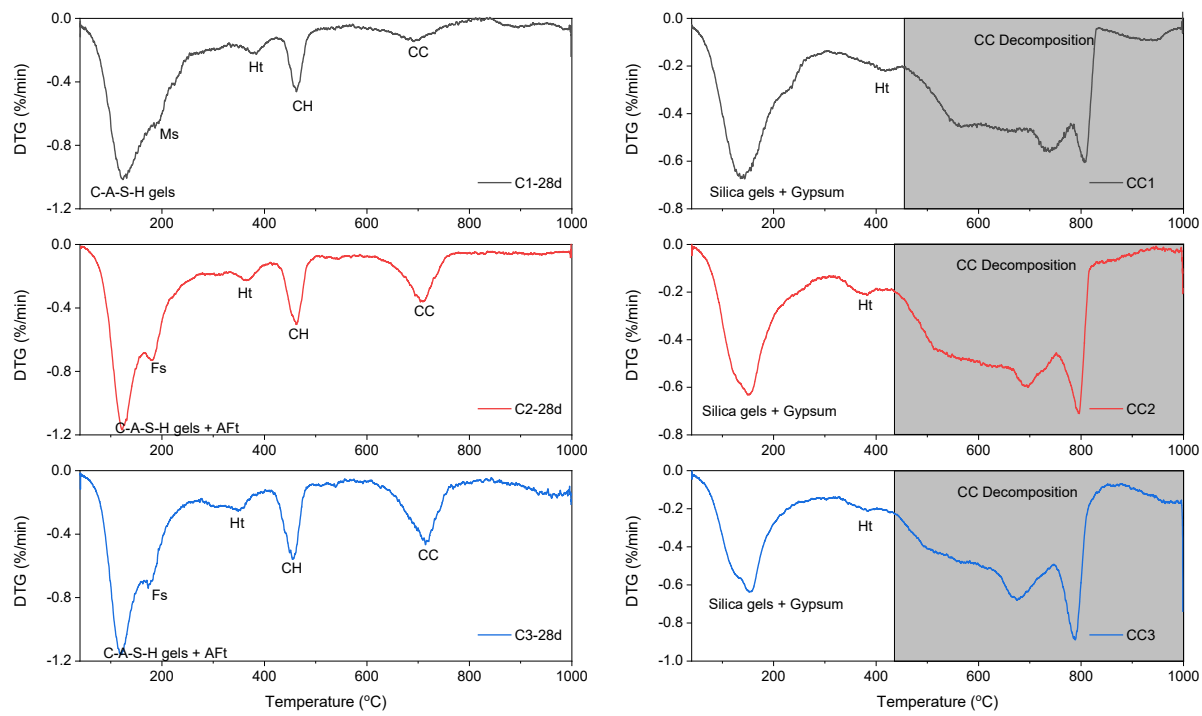


Figure 6.9 DTG curves of BFS blended cement with WBFA at 28 days (left) and after carbonation (right)

The decarbonation process is seen in uncarbonated samples from around 600 °C, which is mainly due to the presence of calcite introduced by WBFA. In carbonated samples, however, the decarbonation is identified starting at around 420 °C. The lower decarbonation temperature in carbonated samples has also been reported elsewhere [272,294], which is mainly due to the precipitation of poor-crystallized calcium carbonate (amorphous calcium carbonate), vaterite, and aragonite, which are reported to have lower decomposition temperatures compared with calcite [295].

- CO₂ Mass spectroscopy (MS) analysis

To further quantify the CO₂ binding capacity in different mixtures, mass spectrometry was applied to identify the CO₂ emission during the thermogravimetric analysis of carbonated specimens.

Different from DTG curves showing a clear decarbonization process in carbonated samples at 420 °C, the occurrence of decarbonization in carbonated samples actually begins much earlier, as shown in the MS curves in Figure 6.11. A weak CO₂ signal is observed in carbonated pastes between 100-300°C. Similar findings have also been reported by other researchers [267,272,286]. The early CO₂ signal should be attributed to the desorption of carbonate from hydrotalcite and also the decomposition of amorphous calcium carbonate [296]. Still, the main decarbonization process occurs above 420°C, which is consistent with the DTG curves, as the results of the decomposition of calcium carbonate in different polymorphs. Due to the complexity of these phases with overlapping decomposition temperatures, it is not applicable to distinguish these phases individually.

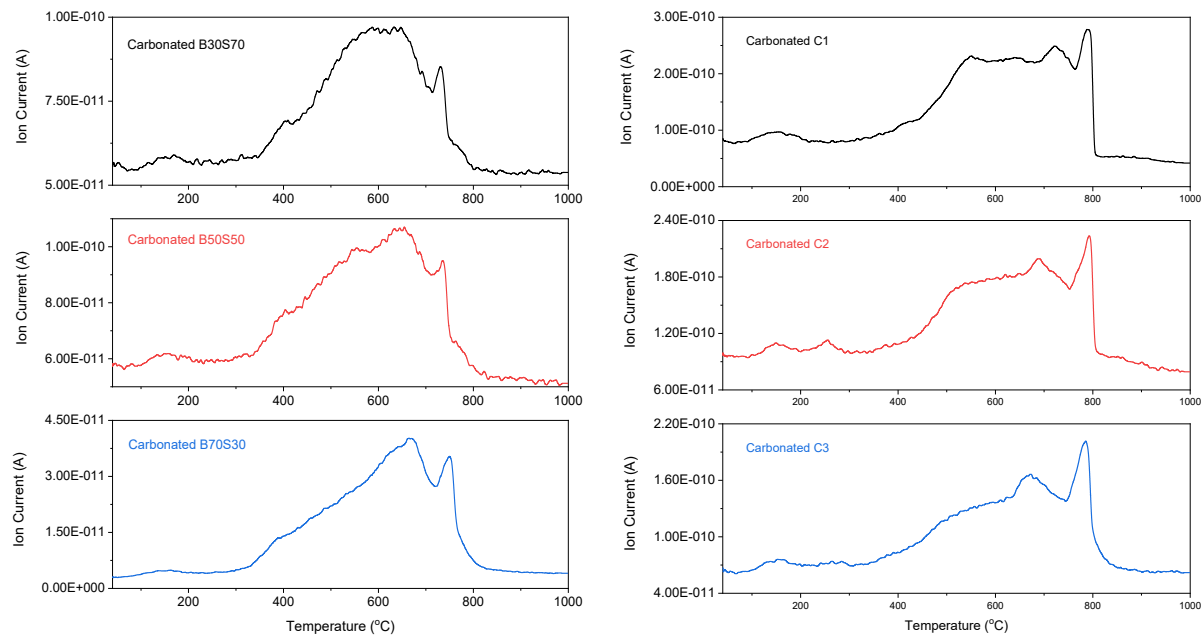
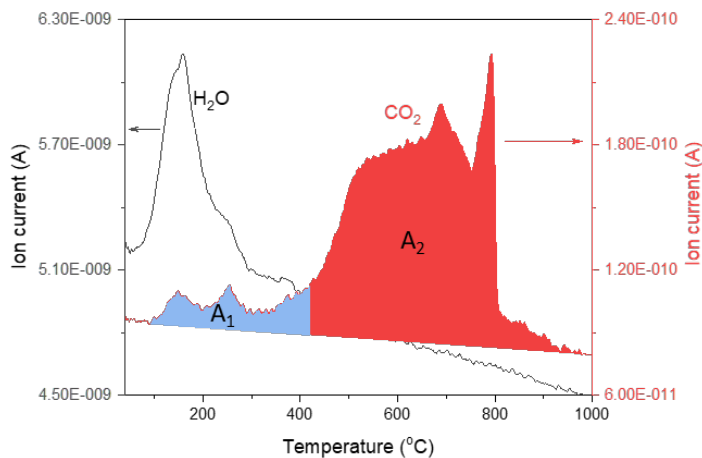
Figure 6.10 CO₂ MS curves of pastes after carbonation

Figure 6.11 Example of C2 for calculating the mass loss due to decarbonation in carbonated samples

To better determine the mass loss corresponding to decarbonation in carbonated samples, an analogy approach can be applied. From the H₂O MS curves in Figure 6.11, it is confirmed that the water-related mass loss occurs before 400 °C. The major decarbonation region from 420°C above as indicated by both DTG and CO₂ MS curves should only be assigned to decarbonation. Therefore, the integrated area of CO₂ MS curves above 420°C (shown as A₂ in Figure 6.11) can be inferred to the mass loss above 420°C from the TGA results. The total decarbonation-related mass loss can be calculated by equation 6.7:

$$M_{CO_2 total} = \frac{\Delta M_2 \times (A_1 + A_2)}{A_2} \quad (6.7)$$

where $M_{CO_2 total}$ is the total CO₂ contents in the pastes. ΔM_2 is the mass loss in carbonated pastes between 420°C to 1000°C from TGA. A₁ and A₂ are the integrated area of the CO₂ MS curves between before and after 420°C, respectively.

Table 6.2 Comparison of decarbonation-related mass loss in uncarbonated samples and carbonated samples (g/g paste)

	B30S70	B50S50	B70S30	C1	C2	C3
Uncarbonated sample	0.04	0.08	0.11	0.01	0.05	0.07
Carbonated sample	0.15	0.21	0.21	0.20	0.22	0.25

For uncarbonated samples, owing to their well-crystalline calcite phases in the mixtures, the mass loss above 600 °C is considered the decarbonation range. The comparison of decarbonation related mass loss is provided in Table 6.2.

When discussing carbonation resistance, the evolution of pH values in the pore solutions of cementitious materials during carbonation is one of the most commonly used parameters, as it is closely associated with engineering practices concerning steel bar corrosion. From the reaction perspective, on the other hand, the CO₂ binding capacity should be highlighted, as this determines the amount of CO₂ that can be captured in the matrix of cementitious materials. Without considering the kinetics of carbonation, a higher CO₂ binding capacity of the cementitious materials should be associated with better resistance to the carbonation reaction, as more CO₂ is required to cause the degradation of hydrates.

Calcium is regarded as one of the most important elements that determines the CO₂ binding capacity of cementitious materials [297]. In WBFA-BFS binary pastes, the CO₂ binding capacity follows the order B50S50 > B30S70 > B70S30. As previously discussed in Chapter 4, B50S50 is found with a highest amount of reacted BFS, followed by B30S70 and B70S30. While WBFA can contribute to the calcium sources to a certain extent, the content of reacted BFS dominates the overall reacted calcium content in the binder. This explains the higher CO₂ binding capacity of B50S50. In BFS blended cement pastes, as discussed in Section 5.4.1, the amorphous phases in WBFA do not contribute much to hydration, thus an increasing WBFA content would lead to a reduced amount of calcium, eventually affecting the CO₂ binding capacity.

6.3.3 Microstructure alteration via carbonation

6.3.3.1 MIP analysis

- WBFA-BFS binary pastes

Figure 6.12 compares the total pore volume and pore size distribution of WBFA-BFS binary pastes before and after carbonation. Similar to Section 4.3.4.1, pores from MIP results are divided into 5 categories to better identify the pore volume in different sizes, as shown in Figure 6.12 (a). The total intrusion porosity slightly decreases after carbonation for all three groups. Similar trends have also been reported in both cement and alkali-activated slag under carbonation [298]. One explanation of porosity reduction can be attributed to the carbonation of portlandite, although in small quantity in the binary pastes as indicated in TGA and FTIR results, leading to the formation of calcium carbonate with increasing molar volume [263]. Besides, the carbonation of C-S-H gels can also be one of the factors contributing to the porosity reduction. Castellote et, al [299] found that the reduction in porosity in cement pastes during carbonation is not mainly governed by the content of portlandite but is positively proportional to the fraction of C-S-H gels. From mathematical calculation, it is

deduced that C-S-H gels with Ca/Si ratios over 1.5 present the possibility of porosity reduction after carbonation [272,300]. The Ca/Si ratios of C-S-H gels in the WBFA-BFS binary pastes in the current research cover a wide range mainly between 1.25-1.80 (presented in the following content), thus this can also be part of the supportive argument for porosity reduction.

The pore size distribution reveals notable changes for pastes after carbonation. For uncarbonated pastes, the majority of pores are smaller than 50 nm (Figure 6.12 (a)). However, the carbonated samples exhibit that more than 50% of pores are larger than 50 nm. This pore coarsening effect is more pronounced in B30S70, showing that more than half of the pores are larger than 100 nm. The noticeable shift towards larger pore sizes can also be seen from the differential pore volume in Figure 6.12 (b), (c), and (d). While a clear and sharp peak can be distinguished from the differential pore volume curves of uncarbonated samples (identifying as the critical pore size), the carbonated samples, especially carbonated B50S50 and carbonated B70S30, are found with a broader hump in their differential pore volume curves. Similar coarsening of capillary pores has been previously reported in both (blended) cements and alkali-activated materials [270,300,301]. This redistribution of pores to a larger size is the consequence of the decomposition of hydrates, especially the decalcification of C-A-S-H gels and the formation of highly porous silica (alumina) gels.

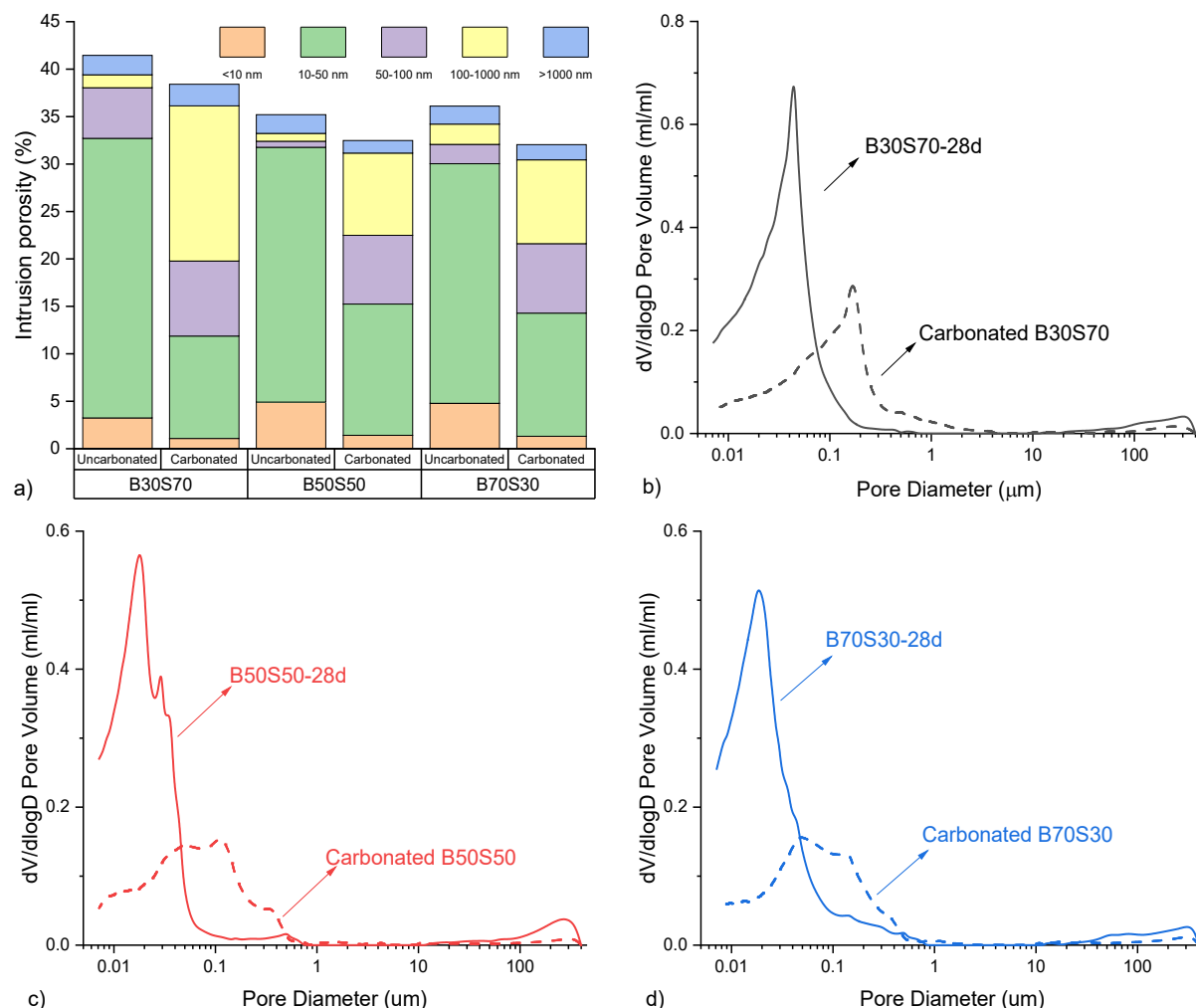


Figure 6.12 Pore volume fractions (a) and pore size distribution WBFA-BFS binary pastes at 28-day of hydration (solid lines) and after carbonation (dash lines)

- *BFS blended cement pastes with WBFA*

Figure 6.13 presents the pore parameters of BFS blended cement with WBFA before and after carbonation. Similar to the findings in WBFA-BFS binary pastes, a significant porosity reduction is observed in the BFS blended cement pastes with WBFA. With the increment of WBFA, the porosity reduction is more pronounced. In light of the increasing amount of portlandite in the pastes with more WBFA, the porosity reduction in the slag blended cement pastes should be, therefore, largely ascribed to the contribution of the carbonation of portlandite, with the volume increasing when it converts into calcium carbonate.

Despite the significant porosity reduction, the pore coarsening effect is also observed in the carbonated samples. The differential pore volume curves shift to the larger pore diameter for all mixtures after carbonation. No clear critical pore size can be distinguished in the differential pore volume curves, as the curves are seen with a broad hump. By comparing the fractions of pores in different sizes, it is seen that samples after carbonation have reduced pore volume in gel pores and micro capillary pores but increased medium and large capillary pores, irrespective of the mixtures.

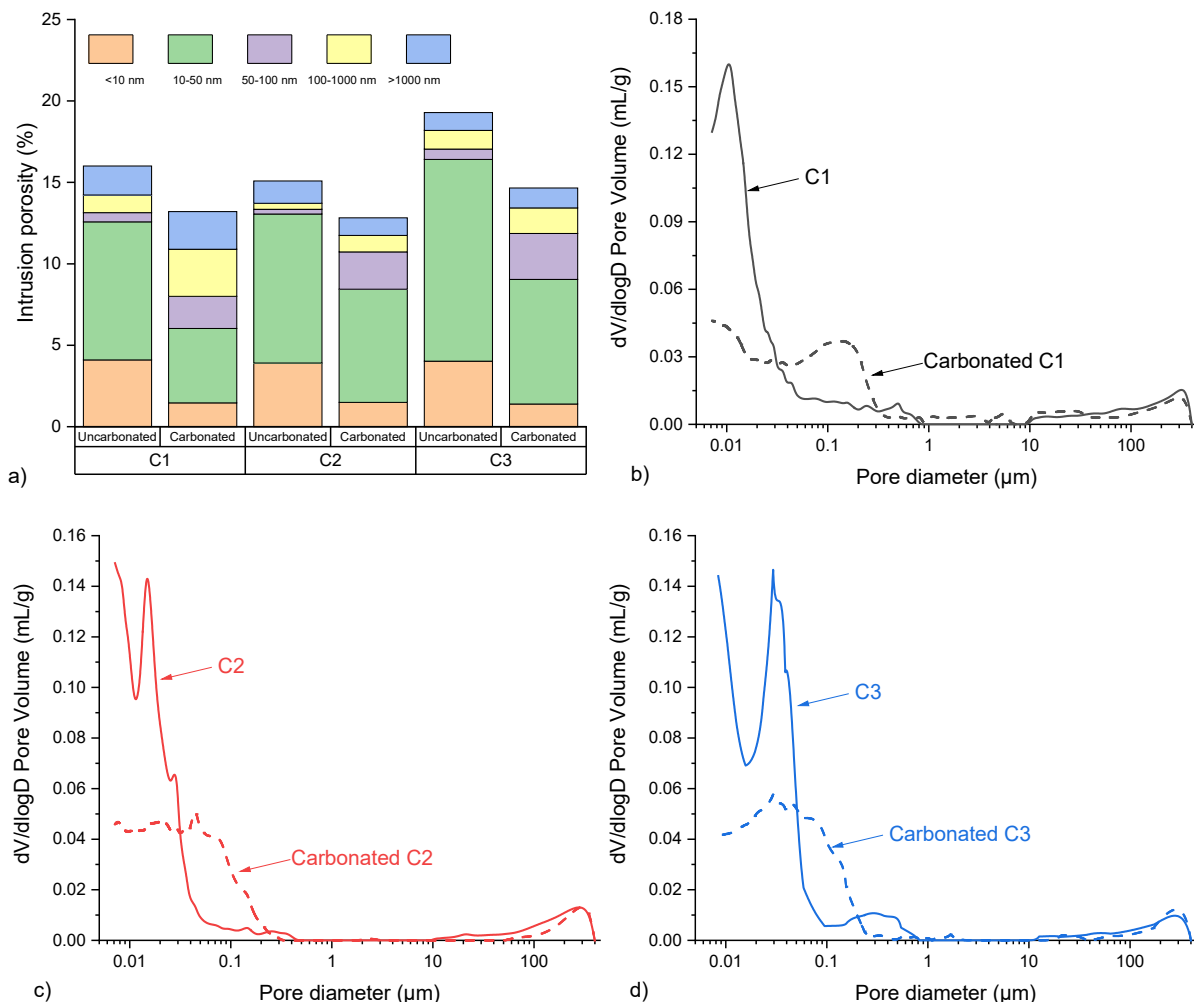


Figure 6.13 Pore volume (a), and pore size distribution (b), (c), (d) of pastes C1, C2, and C3 before (solid line) and after carbonation (dash line).

6.3.3.2 BSE analysis

- WBFA-BFS binary pastes

B50S50 is presented as the representative of WBFA-BFS binary pastes, illustrating the deterioration of microstructure after carbonation, as depicted in Figure 6.14. A distinct microstructure change can be observed for binary pastes before and after carbonation. For the non-carbonated sample, a compact microstructure is clearly observed, and the anhydrous particles are firmly bonded in the matrix by hydration products. The distinguishable grey level of different phases is seen in the matrix. In contrast, the microstructure of the sample after carbonation becomes highly porous. Microcracks can be observed in the matrix, which are mainly located around the anhydrous particle grains, as marked in the figure. This indicates a poor bond between the matrix and the anhydrous particles, due to the deterioration of the hydrates.

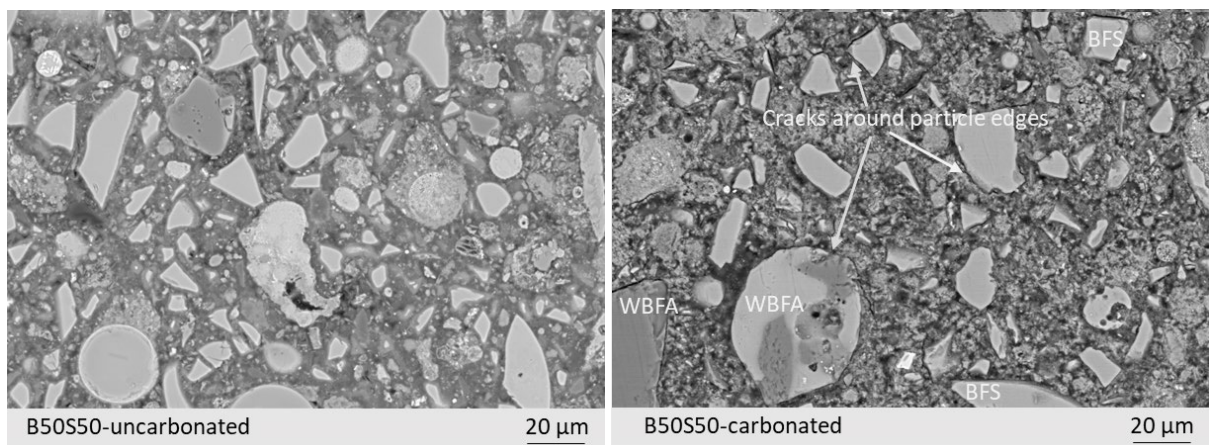


Figure 6.14 BSE images of B50S50 before (left) and after (right) carbonation

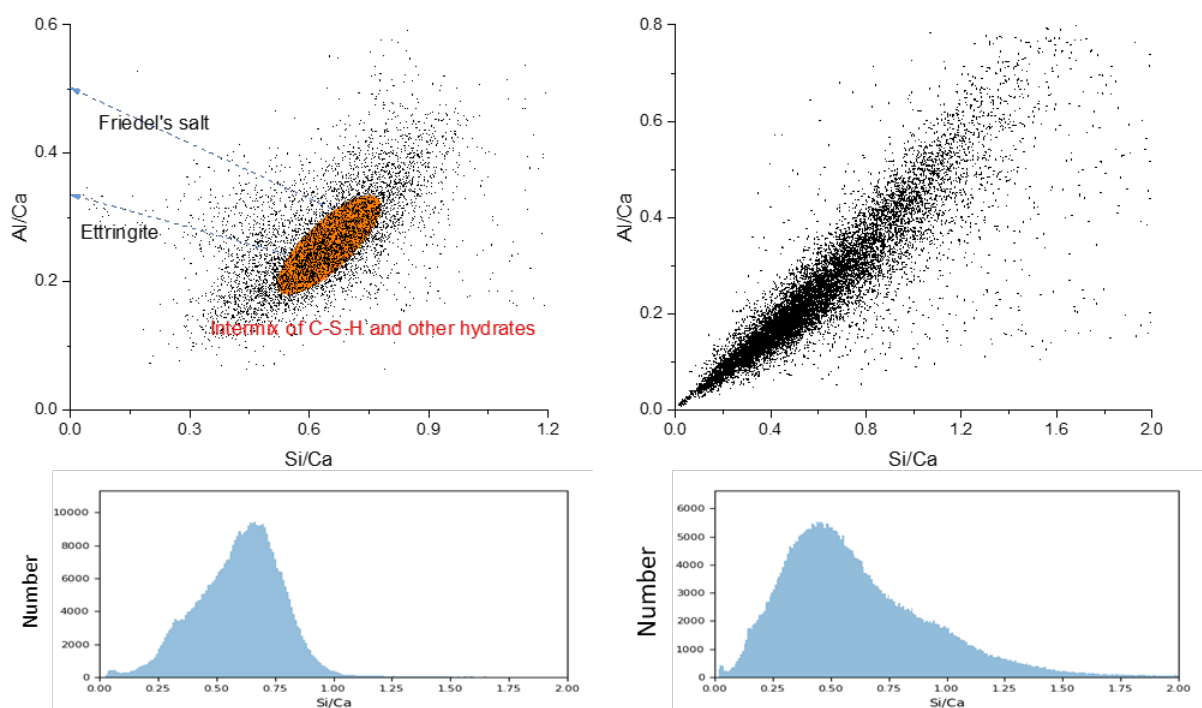


Figure 6.15 EDS scatters of B50S50 at 28-day hydration (left) and after carbonation area (right)

EDS mapping analysis was carried out to compare the chemical compositions of hydrates and their alteration after carbonation. The EDXIA program through the Glueviz interface [226,302] was used to link the BSE images with the EDS mapping data. A simple phase segmentation was conducted for BSE images, dividing them into pores, anhydrous particles, and reaction products by processing images with filters such as greyscale, RGB, and PCA modes. The segmented images are provided in Figure A6.1. By masking out the reaction products, the chemical compositions can be obtained accordingly, with the results being presented in Figure 6.15.

The elemental ratios of reaction products of B50S50 at 28-day hydration have been discussed in Section 4.4.5. Due to the compact nature of hydrates, isolating C-S-H gels along with other phases is not practical from the EDS mapping. However, since C-S-H gels are expected to be the primary hydrates in the pastes, clusters with the highest concentration are identified as the main domain of C-S-H gel, as indicated in the figure. Besides, ettringite is also clearly observed. The dashed lines represent 'tie-lines' connecting pure phases (ettringite and Friedel's salt) with the C-S-H gels cluster, suggesting that dots along this line may represent the intermixing of specific phases with C-S-H gels [195]. These observations are consistent with previous findings in the literature, which are commonly observed in cementitious materials [303,304].

For carbonated B50S50, on the other hand, it seems that there is a more random distribution of elements. There is no clear identification of ettringite and other hydrates in the carbonated samples, which corroborates previous results indicating the decomposition of ettringite during carbonation. From the histogram of Si/Ca ratios of the reaction products, it can be seen that clusters shift to lower Si/Ca ratios in general, as a result of the increasing amount of calcium carbonate in the matrix. Additionally, scatters in the matrix exhibit extended Si/Ca and Al/Ca ratios reaching about 2. This extension suggests the formation of amorphous (aluminate) silica gels as a consequence of the decalcification of C-S-H gels and the decompositions of aluminate containing phases.

- BFS blended cement pastes with WBFA

The BSE images of C1, C2, and C3 before and after carbonation are shown in Figure 6.16. Similar to the findings in the binary pastes, microcracks are largely seen in the carbonated samples. These cracks should mainly come from the decomposition of hydrates due to carbonation [305]. In addition, the microstructure becomes highly porous and less compacted. The cracks together with the decomposed hydrates form the overall degradation of the microstructure after carbonation.

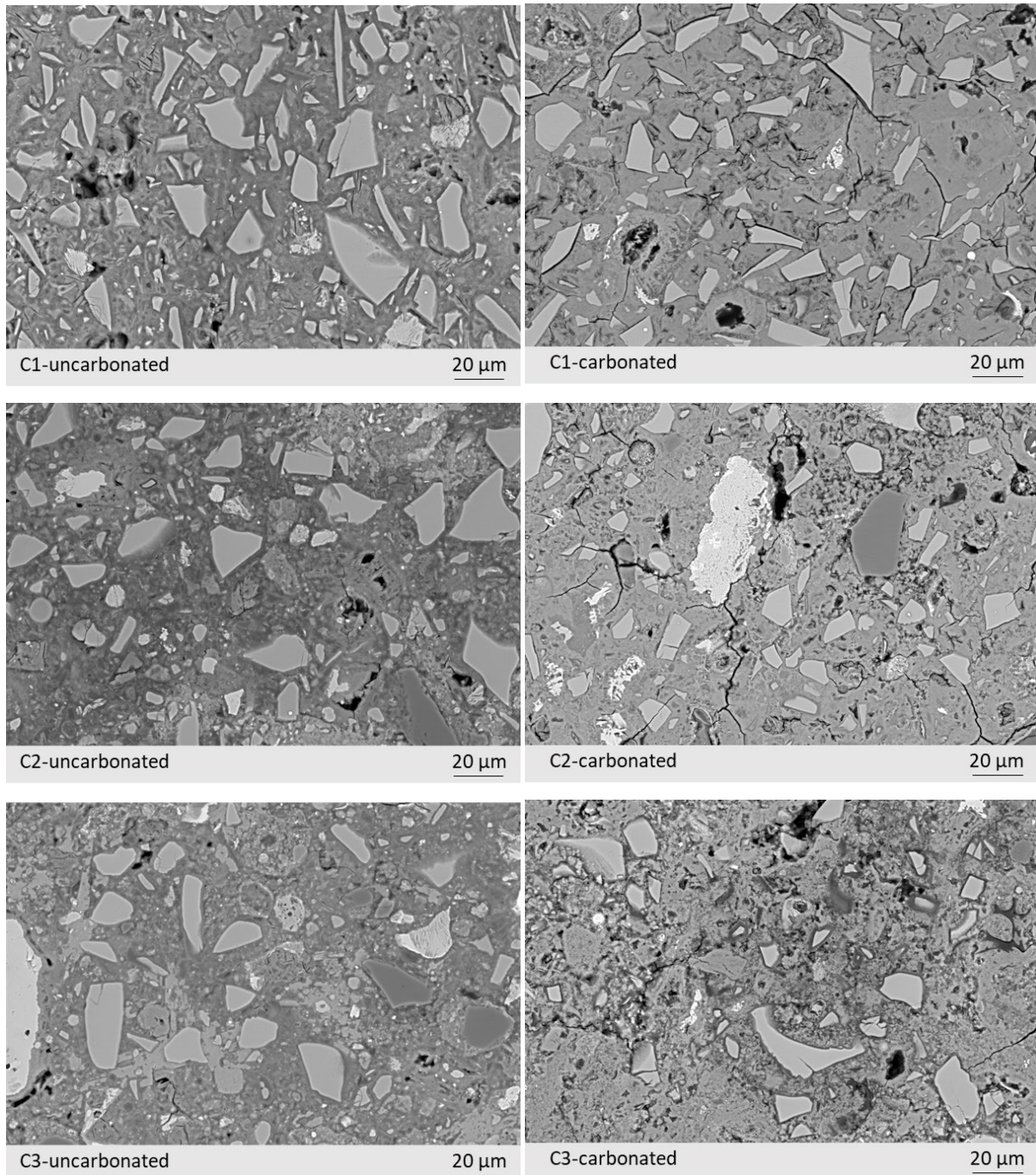


Figure 6.16 BSE images of slag blended cement pastes with/without biomass fly ash before and after carbonation

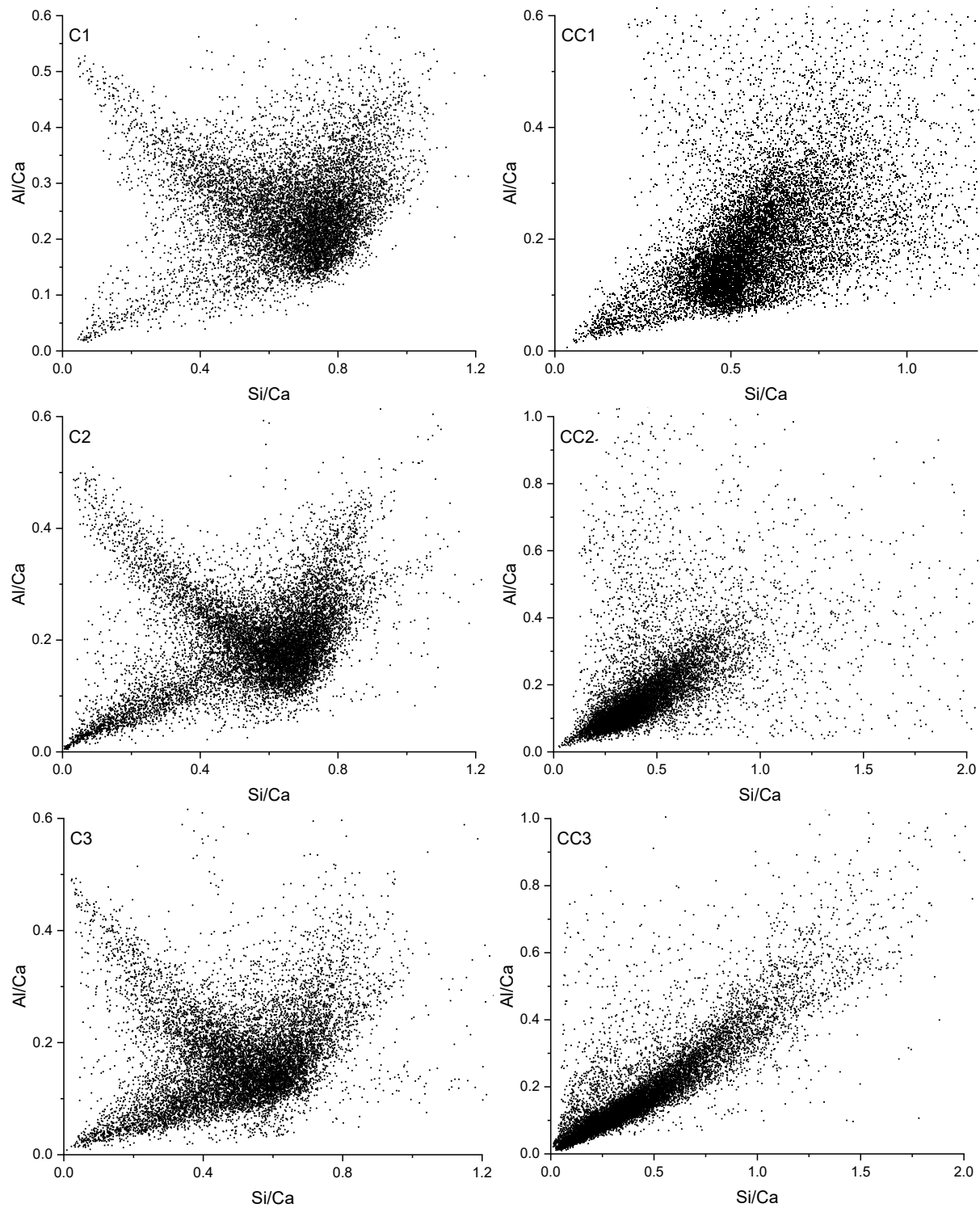


Figure 6.17 EDS scatters of hydration products of pastes (left) and the corresponded carbonated matrix (right)

Phase segmentation was conducted to study the chemical compositions of reaction products. The images of segmentation can be found in Figure A6.2. The 2D scatters of hydration products and carbonated matrix are plotted in Figure 6.17. In uncarbonated samples, the clusters representing hydration products are located within Si/Ca ratios of approximately 1. The characteristic hydration products such as ettringite, monosulfate,

Friedel's salt, and intermix hydrates containing C-S-H gels and other hydrates can be clearly identified. Similar to the previous results in Section 5.3.5, the scatters for C-S-H gels demonstrate a decreasing trend in Si/Ca ratios as the amount of WBFA increases. This trend is a consequence of the reduction in the bulk content of aluminosilicates in the mixtures due to the replacement of BFS with WBFA. After carbonation, the scatters undergo significant changes, and the representative hydrates can no longer be distinguished. The major clusters shift to a lower Si/Ca ratio as the result of the formation of a large quantity of calcium carbonate. Other carbonated phases are present with clusters locating in high Al/Ca or Si/Ca ratio regions, implying the formation of silica (alumina) gels.

6.3.4 Compressive strength

The compressive strength of WBFA-BFS binary pastes over carbonation is shown in Figure 6.18. A gradual loss in strength is seen with the extend of carbonation duration. With the increment of carbonation time, the decomposition of hydrates leads to form a large amount of aluminate silica gels, contributing to the porous microstructure. In addition, the hydrates decomposition leads to the weakened bond between the carbonated products and anhydrous particles, eventually causing strength loss. Still, all of the pastes show a compressive strength higher than 10 MPa, and B50S50 has the highest compressive strength of about 15 MPa. With this strength it is still possible to use this mixture to develop construction products with low strength demands, such as low-strength cementitious materials (LSCM) and bricks.

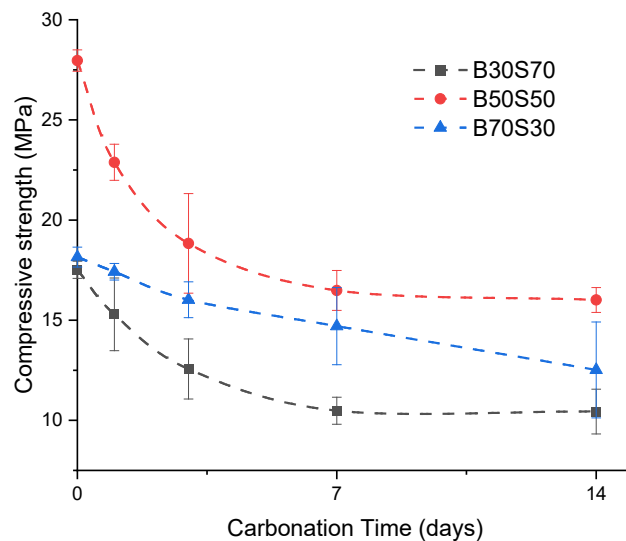


Figure 6.18 Compressive strength evolution of binary pastes with carbonation time

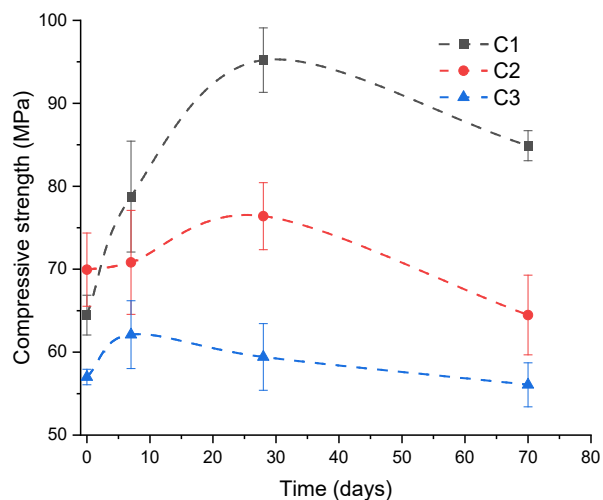


Figure 6.19 Compressive strength evolution of C1, C2, and C3 with carbonation time

Figure 6.19 shows the strength evolution of BFS blended cement with or without WBFA during carbonation. Unlike the strength evolution observed in binary pastes, where there is a direct decrease in strength throughout carbonation, it is observed that during the initial period of carbonation, the compressive strength of pastes increases with time. This initial strength increase is mainly attributed to the carbonation of portlandite, which converts into calcium carbonate with an increased volume. This densification eventually leads to the strength increment. Similar results have been reported previously [306]. However, with continuous carbonation, the compressive strength of the pastes decreases. This is due to the degradation of hydrates, such as C-S-H gels, ettringite, and LDH phases, resulting in a highly porous microstructure. As WBFA leads to a faster carbonation process in BFS blended cement, pastes with more WBFA experience a faster hydrate decomposition process. The positive effect of portlandite carbonation on compressive strength dominates in pastes with lower WBFA content (C1 and C2) until 28 days of carbonation, while in C3, a decrease in strength is already observed after 7 days. Nevertheless, the compressive strength of both carbonated C2 and C3 after 70 days of carbonation remains comparable to that of non-carbonated samples, indicating satisfactory strength maintenance and resistance during carbonation.

6.4 Discussions

6.4.1 Hydrates vs. carbonation

To better illustrate the phase evolution in the pastes during carbonation, the process calculation with a stepwise increase of CO_2 content of 0.5 g was conducted through thermodynamic modelling using GEMs.

Figure 6.20 shows the evolution of phases and pH values in binary pastes during carbonation, with B50S50 as a representative example. As previously discussed, C-S-H gels, ettringite, hydrotalcite, and Friedel's salt are the primary hydrates in the binary pastes. Once contacting with CO_2 , C-S-H gels and ettringite are found to undergo direct decomposition, indicating their vulnerability to carbonation from the thermodynamic perspective. Hydrotalcite, on the other hand, remains stable until more than 5 grams of CO_2 is introduced. This is because carbonate initially binds as anions in the interlayer structure of hydrotalcite.

As the CO_2 content increases, representing higher degrees of carbonation, hydrotalcite gradually decomposes.

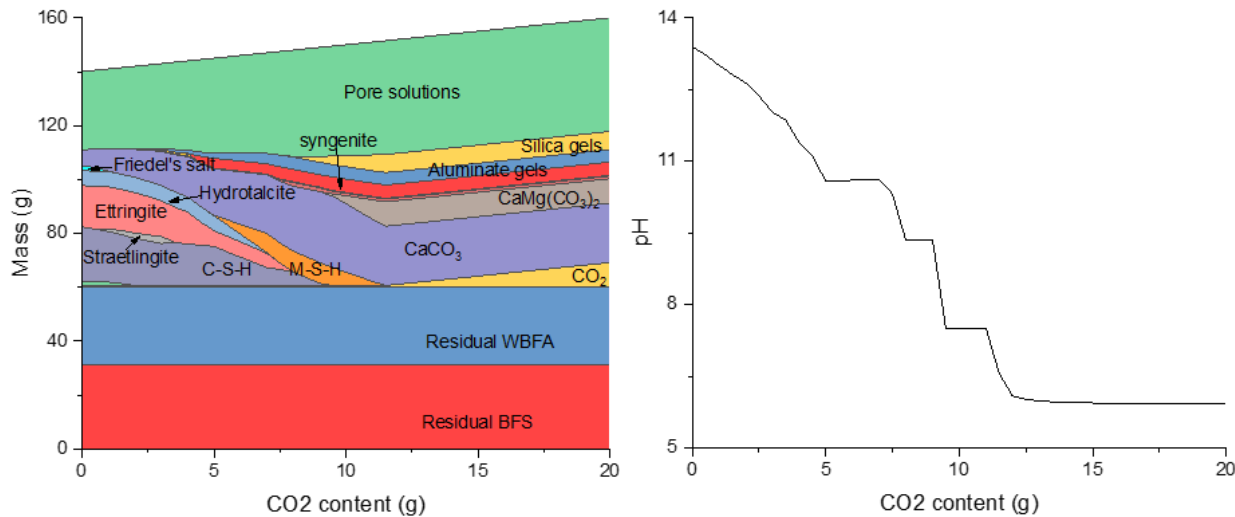


Figure 6.20 Thermodynamics modelling of B50S50 through carbonation

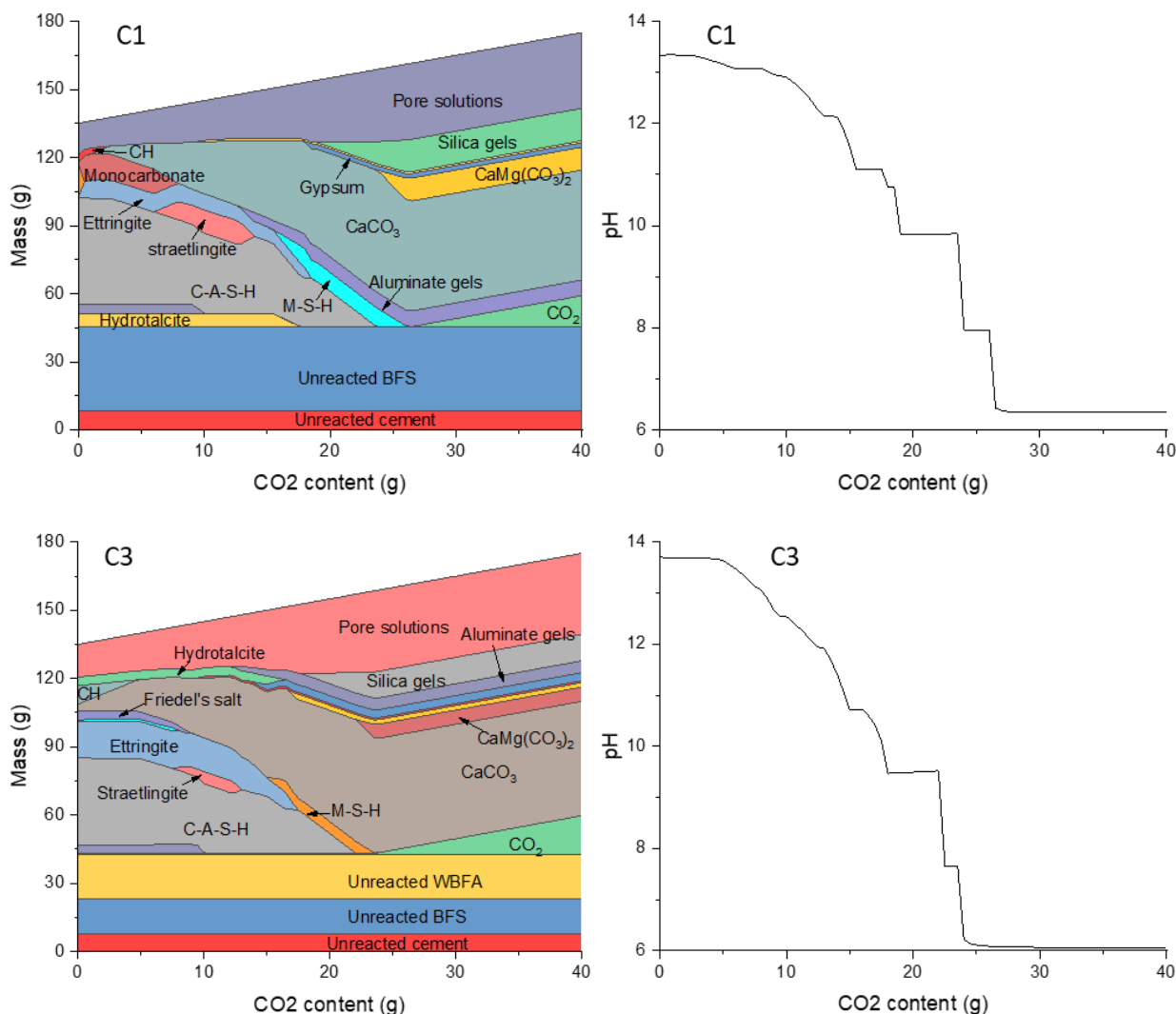


Figure 6.21 Thermodynamics modelling of C1 and C3 through carbonation

Similar phase transformation is also observed in the carbonated BFS blended cement. Figure 6.21 presents the carbonation evolution C1 and C3 to compare WBFA on the carbonation of BFS blended cement. The phase evolution is in general similar to that found in the binary pastes. The final carbonation products are aluminate silica gels, calcium carbonate, dolomite, and gypsum. In C3, the syngenite forms as the major sulfate-bearing salt due to its rich in potassium. During the carbonation process, the Ca-Al AFm phases (monosulfate in C1 and Friedel's salt in C3) serve similarly to hydrotalcite in absorbing carbonate as anions in their structure to form monocarbonate. The presence of these hydrates with layered double hydroxide (LDH) structure is beneficial in improving carbonation resistance.

The evolution of pH values during carbonation reveals a decreasing ladder-shaped trend in all mixtures. It is observed that the pH begins to decrease noticeably after the complete carbonation of portlandite. In B50S50, where portlandite is absent, there is a direct reduction in pH, whereas C1 and C3 exhibit a steady stage period initially. The significance of portlandite in controlling the carbonation process in cementitious materials is widely acknowledged [263,307]. The conversion of portlandite to calcium carbonate leads to volume expansion, which contributes to matrix densification in cementitious materials. It is necessary to note that in real situations, the carbonation of hydrates should occur simultaneously. However, the more interesting finding from the pH evolution is that carbonation resistance is not directly correlated to the portlandite content. If we regard pH values as the indicator of carbonation resistance, when comparing C3 and C1, the pH values drop from 13.70 to about 9.50 in C3, compared to a drop from 13.33 to 9.83 in C1 when 15 grams of CO₂ are introduced. In other words, the mixture with higher portlandite content (C3) is less capable in CO₂ binding. The CO₂ binding capacity is, therefore, more related to the overall compositions of hydrates other than the pure portlandite content.

To improve the carbonation resistance, from the perspective of hydration products, a higher amount of LDH hydrates, such as Fridel's salt and hydrotalcite, can benefit carbonation resistance. These phases can 'store' CO₂ during early carbonation, slowing down the rapid carbonation of other vulnerable phases. However, it may be challenging to demand a higher amount of Fridel's salt and achieve better carbonation resistance simultaneously. This is because WBFA is the main source of chloride in the WBFA-containing binders suggested in this thesis. Adding more chloride would lower the amount of BFS while increasing the amount of WBFA in the mixtures, which would then affect the amount of other hydrate phases as well. Instead, a practical approach would be to introduce extra magnesium minerals into the binders to increase the content of hydrotalcite. Additionally, introducing extra lime or portlandite in the binder can be an option to enable longer carbonation buffer effects.

6.4.2 Pore structure vs. carbonation

The microstructure of pastes consists of hydrates, anhydrous particles, and pores. These pores act as pathways for mass migration, enabling CO₂ gas to infiltrate, dissolve in the pore solutions, and react with hydrates. To evaluate the pathways, two parameters are considered of great importance, i.e., the critical pore size and pore connectivity. The former one indicates the size of the majority of pores, and the latter one determines the accessible routes for mass movement within the microstructure.

Table 6.3 Pore parameters of pastes at 28-day hydration obtained by MIP

Groups	B30S70	B50S50	B70S30	C1	C2	C3
Critical pore size (nm)	47.87	16.68	19.42	11.13	14.70	29.46
Pore connectivity (%)	32.90	35.95	39.80	31.04	43.81	46.67
Effective porosity (%)	13.64	12.65	14.37	4.97	6.61	9.00

Based on the MIP results, the pore connectivity of pastes before carbonation can be calculated according to the volume percentages of pores subtracted by inkbottle porosity [200], and the results are present in Table 6.1. A detailed pore structure calculation is illustrated in Figure A6.3. It is interesting to note that the pores parameter correlates well with the carbonation rate of pastes. B50S50 that has the smallest effective porosity and critical pore size exhibits the lowest carbonation coefficient in binary pastes. Besides, in BFS blended cement pastes, an increase in critical pore size and effective porosity is found for pastes with increased WBFA, which is in line with the trend of the carbonation coefficient.

The increased pore connectivity with the increased amount of WBFA is seen in all pastes, which can be explained by the porous structure of WBFA particles. Unlike BFS particles as solid grains, WBFA particles are heterogeneous and part of them are porous, as seen in Figures 6.14 and 6.16. These anhydrous WBFA particles remain in the matrix and connect with the capillary pores formed during hydration, enabling the formation of more pathways. To improve the carbonation resistance of cementitious materials containing a high volume of WBFA, a more sophisticated mixture design is suggested from the particle packing perspective to increase the packing density of matrix. Besides, it is advisable to reduce the water-to-binder ratios with the help of superplasticizers when use the WBFA-containing binders. Grinding can be also an effective option to reduce the porous WBFA particles, further reducing the pore connectivity in the pastes with WBFA.

6.5 Conclusions

- 1) WBFA-BFS binary pastes show a faster carbonation rate compared to cement pastes reported in the literature, which is due to the lack of buffering hydrates and porous microstructure. In BFS blended cement pastes, replacing BFS with WBFA leads to a faster carbonation rate. Still, the carbonation coefficient is comparable to that of cement pastes in the literature.
- 2) Degradation of hydrates under carbonation is observed in two binder systems. The primary carbonated products for the pastes are identical, including calcium carbonate, silica aluminate gels, and gypsum,
- 3) In both system, carbonation causes the porosity decrease, and this is more pronounced in BFS blended cement pastes due to the higher amount of portlandite. Pore coarsening is found in all mixtures after carbonation, which should be due to the degradation of hydration products, deterioration of microstructure with the formation of carbonated products.

- 4) By comparing the phases composition and microstructure of pastes before carbonation, it is seen that portlandite content is not determinative for the carbonation kinetics of pastes. Instead, pore structure such as the critical pore size and pore connectivity is more critical governing the carbonation resistance of two types of pastes.
- 5) To improve the carbonation resistance, from the reaction perspective, it is applicable to increase the content of hydrotalcite in hydrates by adding extra magnesium; from the pore structure point, a compacted microstructure is suggested by reducing the water-to-binder ratios and reducing the pores in WBFA.

Appendix

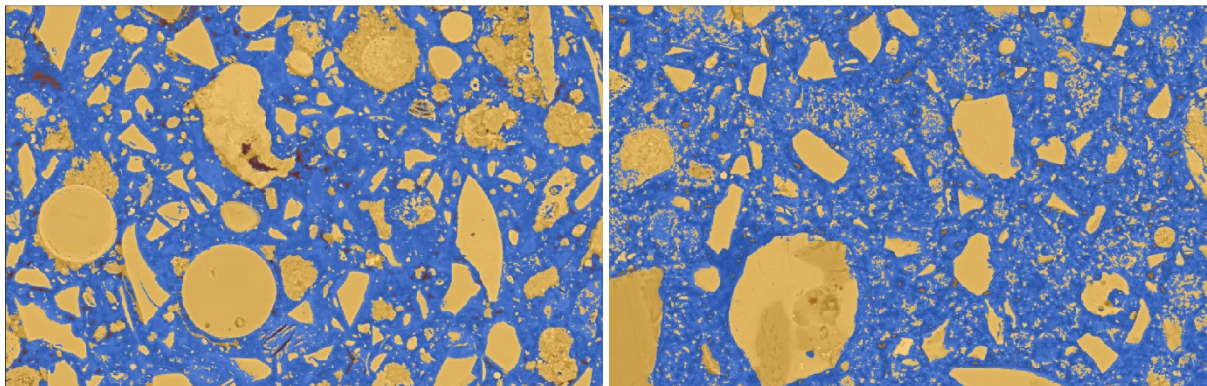


Figure A6.1 Phase segmentation of B50S50 before (left) and after carbonation (right) (The red area indicates the pores, yellow area indicates the anhydrous particles, blue area indicates the reaction products)

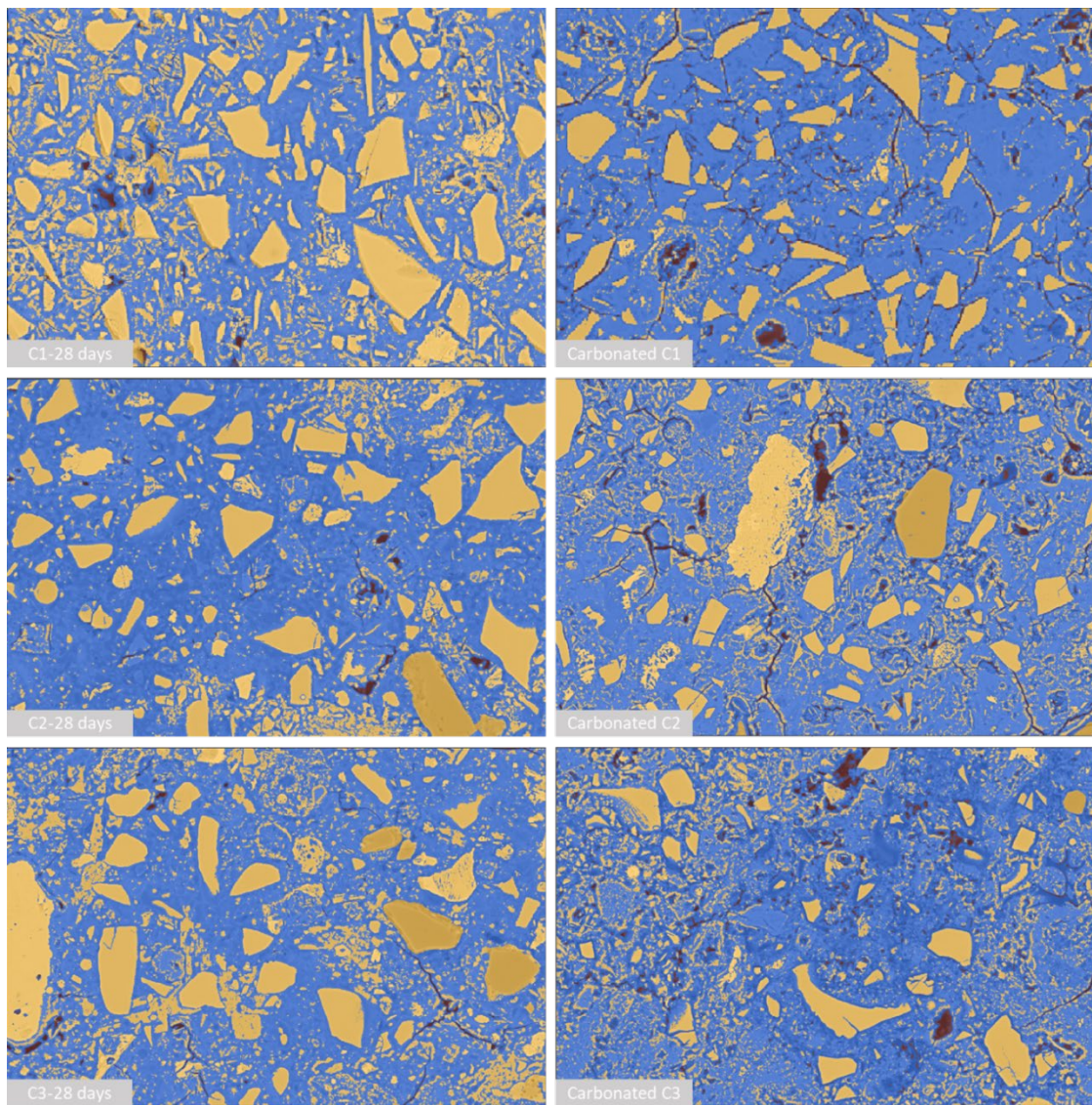


Figure A6.2 Phase segmentation of C1, C2 and C3 before and after carbonation (The red area indicates the pores and cracks, yellow area indicates the anhydrous particles, blue area indicates the reaction products in the matrix)

Figure A6.3 shows the MIP results of intrusion and extrusion process. The mercury captured in the matrix after extrusion process is assumed to be retained in the ink bottles. The ink bottles are considered as blocked path in the microstructure of cementitious materials. The effective porosity φ_e and pore connectivity \emptyset can be calculated based on equation A6.1 and A6.2, respectively.

$$\varphi_e = \varphi_1 - \varphi_2 \quad (A6.1)$$

$$\emptyset = \frac{\varphi_1 - \varphi_2}{\varphi_1} \quad (A6.2)$$

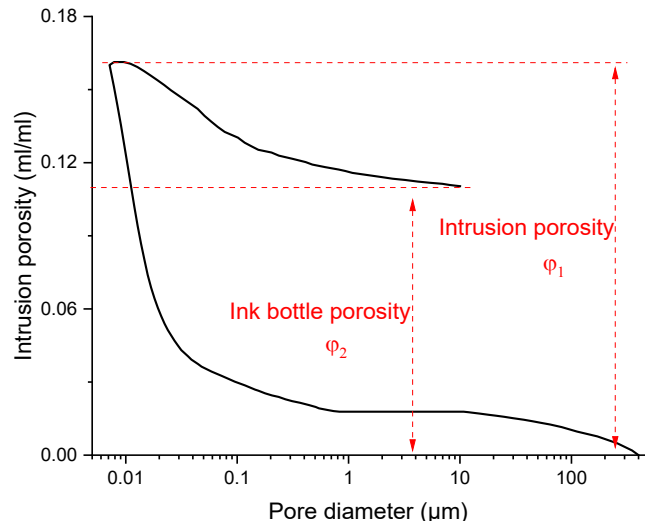


Figure A6.3 Example of MIP results interpretation for pore connectivity and effective porosity

Chapter 7

Utilization of wood biomass fly ash as a construction material and environmental assessment - Case studies in brick and cement production

7.1 Introduction

Previous chapters have presented validated evidence supporting the feasibility of utilizing WBFA as a valuable component in binder formulation. To demonstrate the applicability of WBFA in developing sustainable construction materials from an industrial perspective, manufacturing construction products using WBFA is of great interest.

Based on the results in Chapters 4 and 5, two products are proposed as potential applications. For WBFA-BFS binary binder, the proposed product is non-fired brick. The moderate compressive strength of the binary binder shall meet the requirement for bricks. Considering the long setting time and low initial strength of the binary pastes, it is inapplicable to apply vibrating and demoulding methods for brick manufacturing. Instead, the compression moulding method, one of the most common methods in brick manufacturing [6], is adopted to guarantee a fast brick production process. This can help to avoid the limitations associated with traditional demoulding techniques and is aligned with the demand in engineering practice. These bricks are denoted as "bio-ash bricks" within the context of this research. Besides, in BFS blended cement system, the introduction of WBFA for BFS replacement leads to the formulation of a new type of cement. For clarity, the term 'bio-ash composite cement' is employed in this research to refer to this specific cement.

While it is widely acknowledged that employing industrial by-products for cementitious materials is environmentally advantageous [308], it remains imperative to conduct quantitative research to verify the environmental benefit, and explore further improvement. Life cycle assessment (LCA) is a pivotal tool for assessing the environmental impact of specific products and activities [309], and has been widely used in the construction industry [310–312]. The valorization of WBFA for construction product manufacturing should be addressed from the environmental perspective to better highlight the value of WBFA for the construction industry.

This chapter is dedicated to upscaling the WBFA-involved binders for construction product manufacturing. The technical properties of the construction products are firstly examined. Furthermore, the environmental impact analysis of these products is studied. A cradle-to-gate LCA is carried out for the construction products made with WBFA, and results are compared with conventional products with similar physical properties, aiming at highlighting the environmental benefits of using WBFA in developing construction products and proposing possible improvements.

7.2 Products development and technical properties

7.2.1 Materials and products development

Raw materials include WBFA, BFS, and Portland cement (CEM I 42.5 N ENCI Heidelberg). Detailed material properties can be found in Section 3.3.2.

Two products were developed with the integration of WBFA.

- Bio-ash bricks

As discussed in Chapter 4, the WBFA-BFS binary binder exhibits moderate compressive strength at the paste scale, enabling it suitable for low-strength demanding products. Therefore, brick is considered to be an appropriate product for upscaling WBFA-BFS binary binder. The mixture composition of 1 litter of bricks is provided in Table 7.1. The brick manufacturing process is illustrated in Figure 7.1.

Initially, a mixture of BFS, WBFA, and sand is premixed for 5 minutes to ensure homogeneity. Water is then added, followed by an additional 5 minutes of mixing. The binder to sand ratio is maintained at 1:2, and the water to solid (binder and sand) ratio is fixed at 0.1 to obtain an earth moisture state mortar. The mortar is cast into steel moulds with dimensions of 240×115×53 mm and subjected to a compression force of 10 MPa for 30 seconds. Subsequently, the bricks are demoulded and cured in a fog room with a relative humidity above 95% and a temperature of 20°C for 28 days before being tested on the technical properties.

- Bio-ash composite cement (BCC)

The research findings in Chapter 5 convey the feasibility of incorporating WBFA as a valuable mineral additive in BFS blended cement, up to 30% by weight of the binder. This enables the development of a new type of cement, named as bio-ash composite cement (BCC), as the final product. It is important to note that BCC is currently excluded in the type of cement according to EN 197-1:2018 [132], as WBFA is not included as the mineral in cement industry. BCC proposed in the current research aims at promoting WBFA as a potential constituent for cement production.

Two types of cement, CEM I 42.5 N and CEM I 52.5 R, were employed for BCC formulation, in order to attain a strength class of 42.5 MPa for BCC. Mixtures formulated with CEM I 42.5 N and CEM I 52.5 R are referred to as the N-series group (NC1, NC2, and NC3) and R-series group (RC1, RC2, and RC3), respectively. According to EN 197-1: 2018 [132], the reference mixture (NC1 and RC1) consists of 40% CEM I cement and 60% BFS, which can be classified as CEM III/A cement based on its composition. Upon incorporating WBFA at 15% and 30%, the newly formulated BCC exhibits compositions similar to CEM V Slag-pozzolanic cement. The detailed cement classifications and their compositions are listed in Table 7.2.

Table 7.1 Mixtures of 1L of Bio-ash Bricks

	BFS (g)	WBFA (g)	Sand (g)	Water (g)
Bio-ash Brick	318.20	318.20	1272.70	190.90

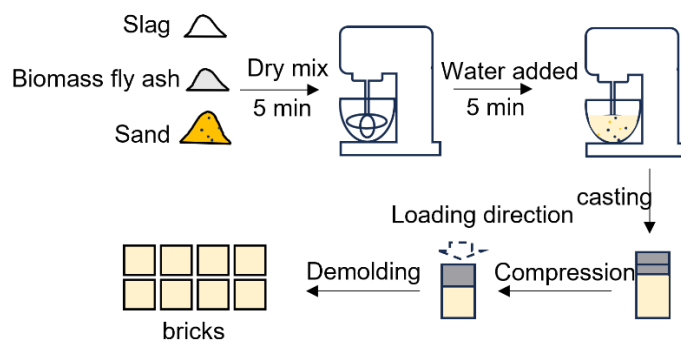


Figure 7.1 Schematic of bio-ash bricks manufacturing process

Table 7.2 Compositions of BCC (%) and comparison with common cement defined in EN 197-1

Group	Main constituents (wt. %)			Minor additional constituents (wt. %)	Refer to types of cement (EN 197-1:2018)
	Clinker ^a	BFS	WBFA		
NC1	38-40	60	-	0-2	CEM III/A
NC2	38-40	45	15	0-2	CEM V/B
NC3	38-40	30	30	0-2	CEM V/A
RC1	38-40	60	-	0-2	CEM III/A
RC2	38-40	45	15	0-2	CEM V/B
RC3	38-40	30	30	0-2	CEM V/A

(a: The clinker content is calculated EN 197-1, which requires the clinker content in CEM I should be higher than 95%. N-series used CEM I 42.5N cement and R-series used CEM I 52.5R cement)

7.2.2 Products testing methods

- Bio-ash brick

The tested properties of bio-ash brick include compressive strength, cold water absorption, and 5-hour boiling water absorption, which are the general physical requirements for bricks from ASTM standards. The test methods follow ASTM C67. The compressive strength of bricks was directly measured after 28 days of curing. For water absorption, specimens cured after 28 days were firstly oven-dried at 105 °C for 24 hours. Afterwards, samples were naturally cooled to room temperature for the water absorption test. The saturation coefficient is the ratio of 24-hour cold water adsorption to 5-hour boiling adsorption. All brick properties were determined from the average of three specimens.

- Bio-ash composite cement (BCC)

The properties of BCC include the setting time, flexural strength, and compressive strength of standard mortar at curing ages of 2 days and 28 days.

The setting time of cement follows the procedures outlined in EN 196-3 [313]. Pastes with standard consistency were cast into the Vicat mould, and the setting time was

automatically measured using a digital Vicat apparatus. The strength of cement is measured according to EN 196-1 [314] by testing standard mortar samples. Mortars were prepared with one portion of cement to three portions of standard sand by weight, with a water-to-binder ratio maintained at 0.5. After mixing, the mortars were cast into the prism moulds with dimensions of 40×40×160 mm. The top surface of the specimens was sealed with plastic films to avoid moisture loss after casting. Mortars were demoulded after 24 hours and then cured in the standard curing room until strength test.

7.2.3 Technical properties of construction products

Product 1: Bio-ash brick

Table 7.3 presents the properties of the bio-ash brick fabricated using BFS and WBFA, alongside the requirements for bricks with various engineering purposes according to ASTM standards, and the comparison with bricks for different applications. Since the oven-dried density of bio-ash bricks is 2140 kg/m³, only normal weight concrete building block is listed for comparison with bio-ash brick.

Table 7.3 Technical properties of bio-ash bricks and comparison with bricks for different applications

Grade/Classification ^a	Average compressive strength (MPa)	Water absorption by 5-h boiling (%)	Water absorption	Saturation Coefficient
Bio-ash Bricks	22.69	13.54	9.34% 202 kg/m ³	0.69
Building bricks (ASTM C62)	SW	> 20.7	< 17.0	< 0.78
	MW	> 17.2	< 22.0	< 0.88
	NW	> 10.3	-	-
Concrete building brick (ASTM C55)	Normal weight (density > 2000 kg/m ³)	> 17.2	-	< 208kg/m ³
Paving brick (ASTM C902)	MX	> 20.7	-	< 14%
	NX	-	-	-

(a: The classification of building bricks and paving brick is mainly determined by the weathering resistance. For building bricks, SW, MW, and NW refer to severe weathering conditions, moderate weathering condition, and negligible weathering, respectively. For paving brick, MX implies that brick is intended for exterior use where resistance to freezing is not a factor, and NX implies that brick is for interior use where it is protected from freezing when wet)

In general, bio-ash brick exhibits satisfactory engineering properties. The average compressive strength reaches 22.69 MPa at 28 days, satisfying the requirement for applications in buildings and pavement, as specified in Table 7.3. Water adsorption plays an important role in influencing various aspects of brick from casting to service life, including the adhesion of mortars between bricks, the formation of ice on surfaces, and the growth of moss, among others [315]. The cold-water absorption of bio-ash brick is 9.34% (202 kg/cm³), meeting the requirements of concrete blocks and pedestrian bricks according to the ASTM standards. The 5-hour boiling water absorption and saturation coefficient of bio-ash bricks can also comply with the requirements for building bricks. As no requirement is mentioned for concrete blocks and pedestrian in boiling water absorption, a comparative evaluation in this regard is not feasible.

Overall, the physical properties of bio-ash bricks satisfy all the specifications for concrete bricks, building bricks, as well as pedestrian and light traffic paving bricks specified in ASTM standards, implying its potential for a wide range of engineering applications.

Product 2: BCC

The setting time of pastes is listed in Table 7.4. A slight increase in setting time is observed with more WBFA, which can be attributed to the increase in sulfate content with the addition of WBFA, as well as the increased water demand for pastes with WBFA to attain standard consistency. In EN 197-1, only the initial setting time of common cement is regulated in detail, with a requirement of no less than 60 minutes for cement with a strength class at 42.5 MPa, and no less than 75 minutes for cement with a strength class at 32.5 MPa. The initial setting time of BCC complies with this requirement.

The flexural and compressive strength of cement mortars are presented in Figure 7.2. Similar to the results in Chapter 5, replacing BFS with WBFA in BFS blended cement can be beneficial for strength development, especially at early ages (2 days). As shown in Figure 7.2 (a) and (b), in both the 'N-series' group and 'R-series' group, a clear increase in flexural strength is seen in mortars containing WBFA compared to those of reference mixtures (NC1 and RC1). Mortars with 15% of WBFA show the highest flexural strength. Specifically, a 69.01% increase in flexural strength in NC2 compared to NC1 at 2 days, and a 13.51% increment at 28 days. In the R-series, the flexural strength of RC2 is 49.58% higher than that of RC1 at 2 days, and 15.53% higher at 28 days.

Table 7.4 Setting time of BCC and comparison with requirements for common cement

	NC1	NC2	NC3	RC1	RC2	RC3	Strength Class (MPa)	
							32.5	42.5
Initial setting (min)	170	210	205	165	185	190	≥ 75	≥ 60
Final setting (min)	365	425	440	310	365	375	-	-

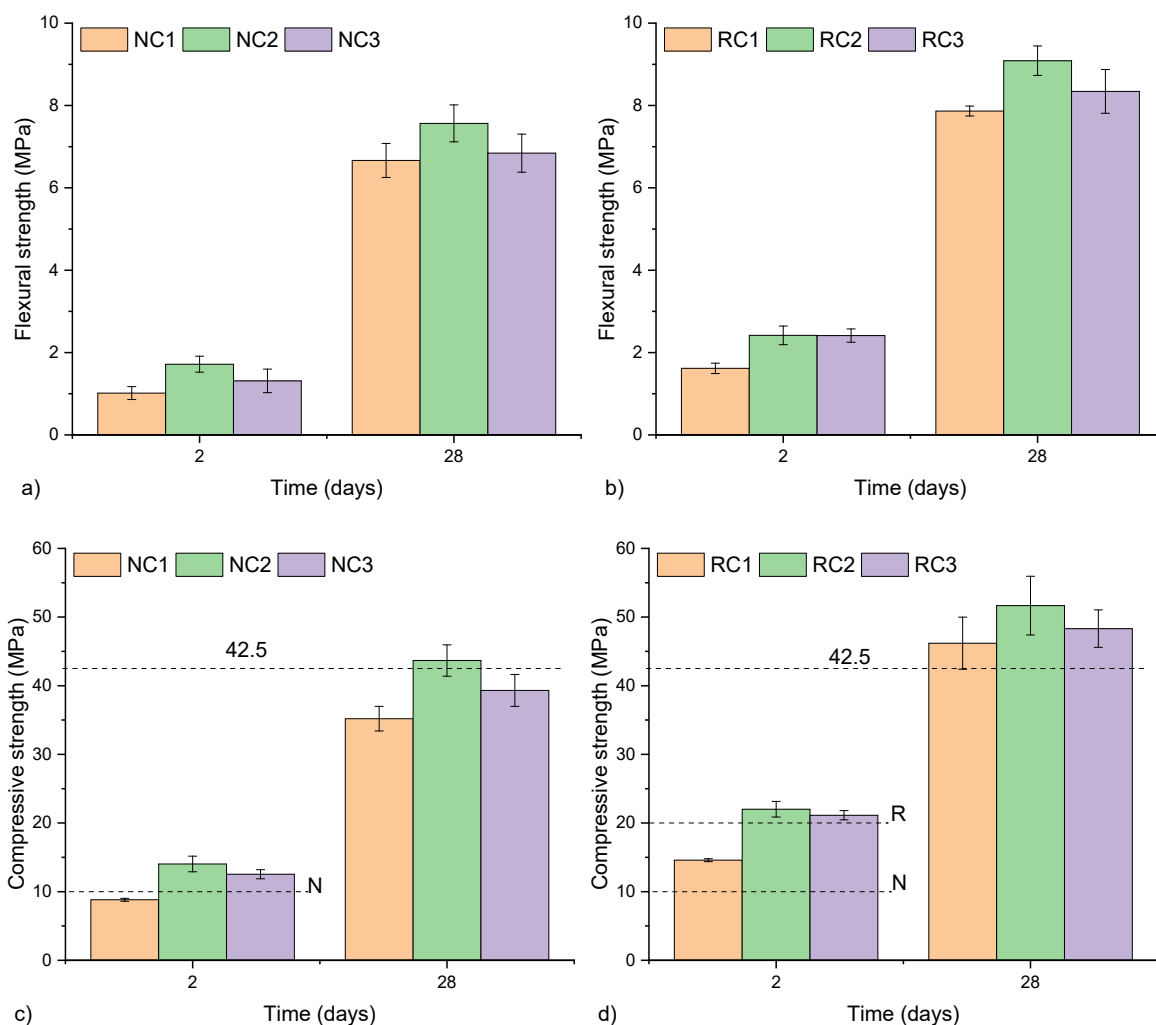


Figure 7.2 Flexural strength and compressive strength of mortars

While flexural strength is not required in common cement according to EN standards, the compressive strength of mortars is one of the most important parameters for cement classification. The compressive strength of mortars is shown in Figure 7.2 (c) and (d). Three dash lines in the figures indicate the requirements for ordinary early strength at 10 MPa (N), high early strength at 20 MPa (R) and strength class at 42.5 MPa, respectively.

In N-series mortar, reference mixture NC1 shows the low early strength of 8.82 MPa. With the addition of WBFA, a clear enhancement of early age strength is detected. The compressive strength of mortars NC2 and NC3 at 2 days can be above 10 MPa. Among the three mixtures, only NC2 attains compressive strength exceeding 42.5 MPa at 28 days, indicating compliance with the cement strength class of 42.5 N. NC1 and NC3 should only be assigned to the 32.5 L and 32.5 N grades, respectively.

A similar phenomenon is also seen in the R-series group. The reference mixture RC1 meets the 42.5 N strength requirement with 2-day compressive strength of 14.59 MPa and 28-day strength of 46.19 MPa. Comparatively, BCC exhibits enhanced strength development. RC2 and RC3 show the 2-day strength at 22.01 MPa and 21.13 MPa, and the 28-day strength at 51.67 MPa and 48.31 MPa, respectively. The strength grade of 'R-series' BCC mortar can be categorized as 42.5 R, given that both RC2 and RC3 exhibit early strengths above 20 MPa.

7.3 Life cycle assessment (LCA)

Based on the findings in Section 7.2, WBFA has been approved from a technical perspective with the capability to be used for manufacturing construction products. For the by-product valorization, in addition to assessing technical properties, it is crucial to evaluate the environmental impact of these products to determine whether the utilization process is justified. LCA of the specific products, therefore, can be an important approach for evaluating the utilization process based on the environmental perspective.

7.3.1 Goal and scope

The goal of the LCA is to evaluate the environmental impact of utilizing WBFA in the production of construction products, in the cases of bio-ash bricks and BCC as mentioned in Section 7.2. A cradle-to-gate analysis is conducted based on NEN-EN 15804 with CML-IA method [316], focusing primarily on material aspects, encompassing the sourcing of raw materials (A1) and the manufacturing of products (A3). All materials are considered locally available; thus, the transportation process (A2) is excluded.

The functional unit for bio-ash bricks is 1m³. The environmental influences of bio-ash bricks are compared with the commercially available brick database from their Environmental Product Declarations (EPDs). The resources of detailed EPDs are listed in Table A7.1.

For BCC, the functional unit is 1 ton, with a strength grade of 42.5 MPa at 28 days. Commercial cements CEM I 42.5 N and CEM III 42.5 N are used as the benchmarks, reference sample RC1 is also used as a comparison to BCC with addition of WBFA.

7.3.2 Life cycle inventory (LCI)

In total 11 environmental impact categories are assessed, with detailed categories and their corresponding abbreviations provided in Table A7.2. The environmental impacts of raw materials in these 11 categories have been collected from the NIBE EPD database [317] (sourced from Dutch Nationale Milieudatabase 3.8 and Ecoinvent 3.6) and presented in the same table.

For now, there is no environmental profile for WBFA in the current database. As WBFA is the by-product in biomass energy production that does not have an economic value, the environmental burden is considered negligible from a material perspective. A similar strategy has been also adopted in [80]. However, it is important to note that the pretreatment processes of WBFA, including drying and grinding described in Chapter 3, involve energy consumption. The environmental impact of these processes should be assessed and considered as part of the environmental impact of WBFA.

To quantify the environmental impact of the WBFA pretreatment process, the electricity consumption during the pretreatment is taken into account. The environmental profile of WBFA can therefore be calculated from the electricity consumption, by adopting the environmental profile of the Dutch medium voltage electricity supply, which is commonly used for industrial production [318].

The industrial instrument parameter configuration is directly adopted to determine the energy consumption of WBFA treatment. The WBFA treatment includes drying and grinding process.

- WBFA drying process

A rotary drum dryer is assumed to be used for the WBFA drying process. The energy consumption is estimated to be in the range of 1.35-6 kWh/t [319]. To avoid underestimation, the upper limit of the energy consumption, which is 6 kWh/t, is adopted as the parameter in this research.

- WBFA grinding process

It is important to note that there is a great disparity in equipment capacity between lab-scale grinding machines and industrial milling systems. To avoid the miscalculation of the energy used for WBFA grinding process, a raw slag grinding process is conducted using the same lab scale milling machine. Based on the particle size distribution (PSD) of slag ground for different time durations and comparing it with the PSD of commercially supplied BFS (results present in Appendix Figure S7.1), it is suggested that a grinding process of 3 hours is required to ensure the slag can be ground to obtain identical PSD with commercial slag. Considering that the WBFA grinding process lasts for 10 minutes as stated in Section 3.3.1, an equivalent energy consumption of the WBFA grinding process can be assessed. In the BFS production industry, the power consumption of the vertical roller mill system is approximately 45 kWh/t [320]. Consequently, for WBFA grinding, an energy consumption of 2.5 kWh/t of WBFA is anticipated.

In total, the electricity consumption of the pretreatment process of WBFA including drying and grinding is 8.5 kWh/t. The environmental impact of WBFA is then calculated based on the electricity consumption using the environmental profile of Dutch medium voltage electricity supply, as listed in Table A7.2.

Regarding energy consumption during product manufacturing, no additional steps are required for BCC once all of these materials are supplied as ground powders. In the case of bio-ash brick production, a commercial automatic interlocking brick machine is assumed to be used. The energy consumption for 1 m³ of bricks is about 1.85-5.21 kWh [321]. Assumption of 5.21 kWh is therefore used for LCA analysis.

The detailed inventories of 1 m³ non-fired bio-ash brick and 1 ton of BCC are shown in Figure 7.3 and 7.4, respectively.

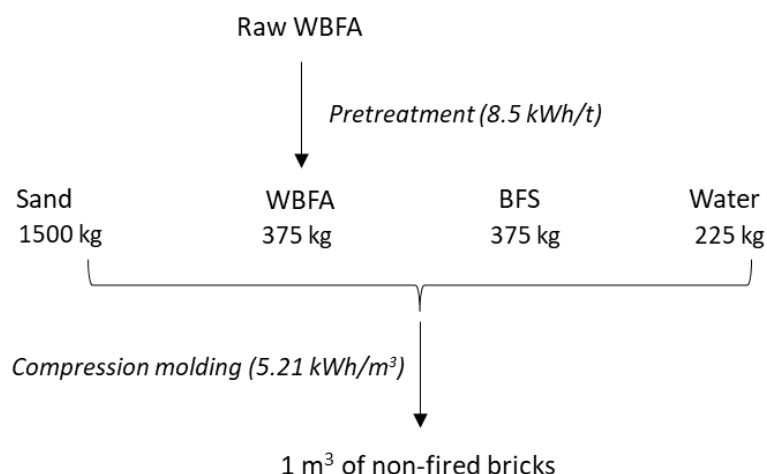


Figure 7.3 Inventory of 1 m³ non-fired bio-ash bricks

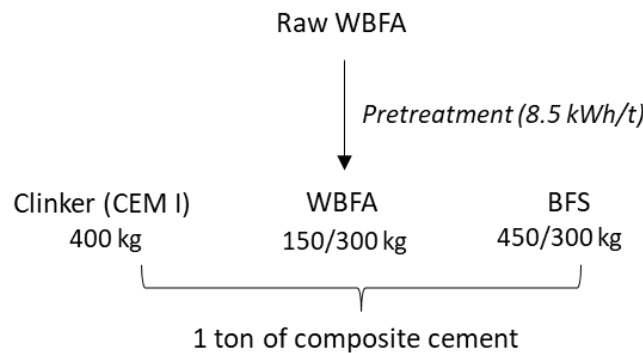


Figure 7.4 Inventory of 1 ton of BCC

7.3.3 Environmental cost indicator (ECI)

ECI is a single-point score used for evaluating the environmental performance of products/activities and is monetarily expressed in euros [322]. It indicates the environmental shadow cost that is required to compensate for the negative impact caused by the production of materials/activities and is required in the Netherlands for construction buildings. It is feasible to employ ECI as a weighting factor to compare various products in terms of environmental preference [323]. The ECI calculation can be determined using Equation 7.1:

$$ECI = \sum EI_i \times M_i \times m_i \quad (7.1)$$

where ECI indicates the total environmental cost indicator of the products under its function unit. The letter i refers to the specific process or material involving the products manufacturing. EI_i denotes as environmental impact category equivalents, M_i indicates the monetary value of the associated environmental impact category (see Table A7.1), m_i refers to the weight of the specific material or the amount of electricity used for manufacturing process under the functional unit in this research (see Figure 7.3 and 7.4).

7.4 Life cycle impact assessment

7.4.1 Bio-ash brick

7.4.1.1 Contribution analysis

An overview of the environmental performance of bio-ash brick as illustrated through 11 environmental indicators is presented in Table 7.5.

The relative percentages of each contributor (materials and manufacturing process) regarding their environmental impact in each individual environmental category are presented in Figure 7.5. It is clear that BFS contributes the most to the environmental impact, followed by sand, the manufacturing process, and WBFA in all aspects. BFS is normally considered to have less environmental burden when used in SCMs in construction materials [324,325]. However, due to the extremely low environmental impact of sand and WBFA, BFS stands out as the largest contributor in this scenario. It is important to note that the absolute value in all these categories is relatively low compared with commercial bricks. To clarify the environmental advantages of bio-ash brick, a comparison between bio-ash brick and commercial bricks is conducted as shown in Figure 7.6. Due to variations in the data sourced

from commercial bricks that often focus on different aspects, not all environmental indicators can be directly compared. Therefore, only GWP, ODP, AP, and EP that are widely available in the EDPs of products are compared. Detailed EDPs of commercial bricks are listed in Table A7.2.

Table 7.5 Environmental impact of 1 m³ bio-ash bricks

Category	abbr.	Unit	
Global Warming potential	GWP	kg CO ₂ eq	3.21E+01
Ozone layer Depletion potential	ODP	kg CFC11 eq	1.95E-06
Human Toxicity potential	HTP		1.81E+01
Freshwater Aquatic Eco-toxicity potential	FAETP		1.38E-01
Marine Aquatic Eco-toxicity potential	MAETP	kg 1,4-DB eq	4.56E+02
Terrestrial Eco-toxicity potential	TETP		6.59E-02
Photochemical Oxidation potential	POCP	kg ethylene eq	4.34E-02
Acidification potential	AP	kg SO ₂ eq	1.16E-01
Eutrophication potential	EP	kg PO ₄ eq	1.81E-02
Abiotic Depletion potential-fossil fuel	ADPFF		2.34E-01
Abiotic Depletion potential-non fossil fuel	ADPE	kg Sb eq	9.45E-05

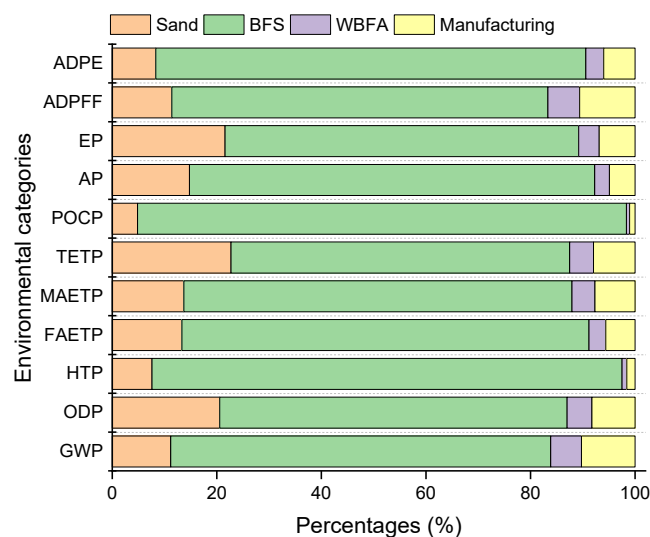


Figure 7.5 Relatively percentages of 11 environmental categories of bio-ash bricks contributed from materials

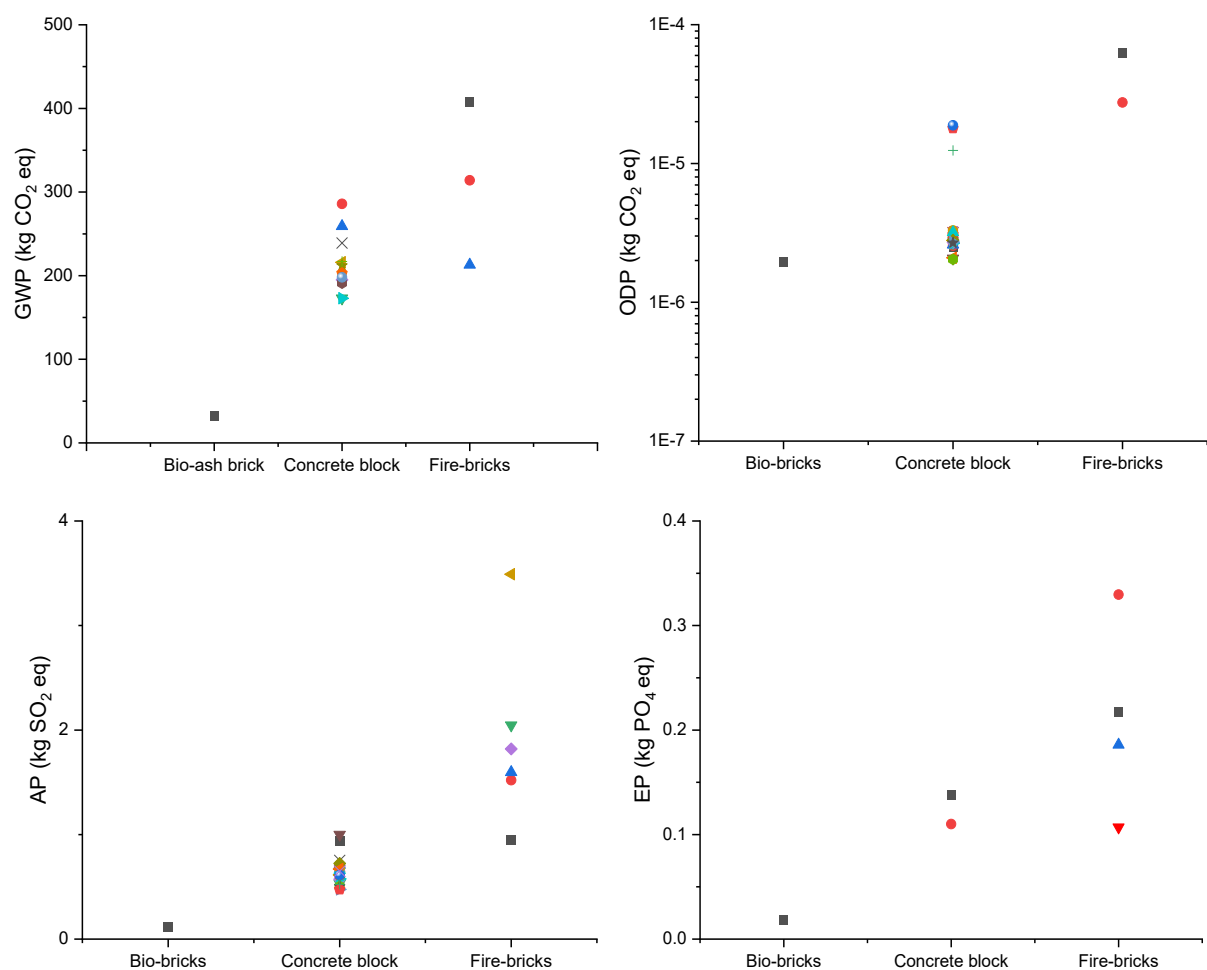


Figure 7.6 GWP (Global Warming potential), ODP (Ozone layer Depletion potential), AP (Acidification potential), and EP (Eutrophication potential) of bio-ash bricks and commercial bricks with data from EPD

The GWP of bio-ash bricks is only 32.07 CO₂ eq /m³, which is about at least 5 times lower than concrete blocks and fired clay bricks. The main reasons for the low GWP in bio-ash brick are the use of low-carbon raw materials and a less energy-intensive production process. Comparatively, concrete blocks typically require about 10% cement, which introduces a high GWP. For fired bricks, on the other hand, the burning process at high temperatures is the main contributor to their high GWP. This result highlights the significance of GWP reduction in bio-ash bricks compared with commercial bricks.

ODP indicates the reduction of ozone concentrations as a consequence of specific chemicals being released to the environment. The overall ODP of bio-ash bricks is 1.95E-06 kg CFC 11 eq/m³, which is comparable to that of most concrete blocks, and significantly lower than that of fired clay bricks. AP is the acidic substance that actively affects the soil, water, and construction materials, leading to a severe condition. The AP of bio-ash bricks is 1.16E-01 SO₂ eq kg/m³, much smaller than those in concrete block and clay bricks. This is because AP is mainly related to the acid gases release. Both cement production and clay brick manufacturing require high temperature condition. The burning of fuels might greatly contribute to the high AP of these two products. The EP is 1.81E-02 PO₄ eq kg/m³ in of bio-ash bricks, and is approximately 10 times smaller than those in concrete block and clay bricks.

In general, in all aspects, bio-ash brick has lower environmental impact than the commercial concrete brick and fired-clay bricks, highlighting its low environmental burden.

7.4.1.2 ECI analysis

The ECI of bio-ash bricks is about 4.03 euro/m³, indicating that the production of 1 m³ of bio-ash bricks requires a hidden cost of 4.03 euros to compensate its impact caused to the environment. It is worth highlighting that this value is relatively low when compared with commercial bricks. Although not all aspects of the contributors can be precisely calculated for comparison with bio-ash bricks due to limited data, a simplified ECI cost of commercial bricks obtained from the GWP, ODP, AP, and EP (if available) reveals a cost of at least 10 euros, as shown in Figure 7.7. This is already more than 2 times larger than the whole ECI of bio-ash bricks. The accumulation of environmental costs from the other indicators can further lead to a bigger gap between the ECI of bio-ash bricks and commercial ones. Bio-ash brick is proved with great environmental advantageous compared with commercial bricks based on the ECI analysis.

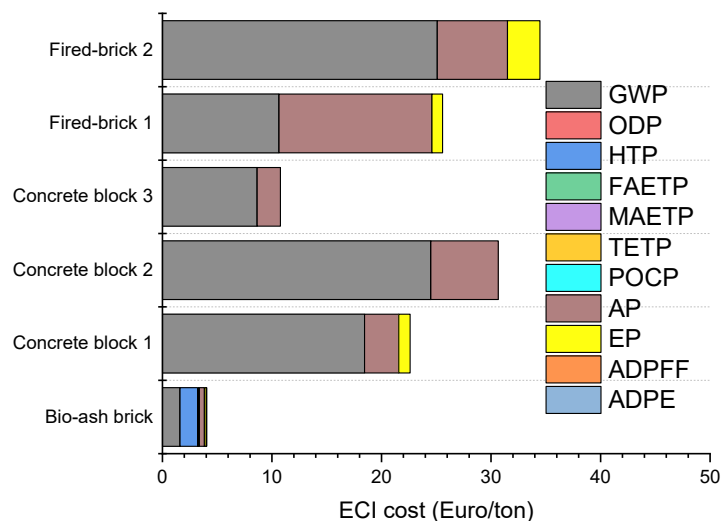


Figure 7.7 ECI cost of bio-ash brick and comparison with commercial bricks (The data for Fired Bricks 1 and 2 are sourced from the 13th and 15th types of fired bricks in Table A7.2; data for Concrete Bricks 1, 2, and 3 are sourced from the 1st, 8th, and 10th types, respectively.)

7.4.2 Bio-ash composite cement (BCC)

The designed strength class for BCC is 42.5 MPa. Based on the results in Section 7.2.3, the BCC for LCA analysis include NC2, RC2, and RC3 as stated in Table 7.2, and compared with reference mixture RC1.

7.4.2.1 Contribution analysis

Figure 7.8 compares the environmental impact across 11 different categories for three types of BCC, with a comparison of reference mixture RC1. Generally, there is a consistent reduction in the environmental impact across all 11 categories as the increasing substitution of BFS with WBFA. This reduction is attributed to the intrinsically lower environmental impact associated with WBFA in comparison to BFS. It is important to note that despite the same strength grade of R-series mixtures, BCC shows enhanced compressive strength at 2 days. The positive influence of WBFA on strength properties while simultaneously reducing environmental burdens should be highlighted.

NC2 that is composed of CEM I 42.5 N cement exhibits the same strength class as RC1 but demonstrates a considerably lower environmental impact across all aspects, except for TETP (Terrestrial Eco-Toxicity Potential). This discrepancy can be attributed to the employment of different types of cement. In most scenarios, CEM I 52.5R cement shows a higher environmental impact than CEM I 42.5N cement, as shown in Table A7.1. This can be explained by the variation of clinker compositions. To achieve a higher strength level, CEM I 52.5 R typically contains a greater proportion of alite and/or a higher specific surface area than that in CEM I 42.5 N [326,327]. Consequently, this leads to an anticipated higher environmental impact in CEM I 52.5 R. BCC contains CEM I 52.5R (RC2 and RC3) are, therefore, seen with greater values in most of environmental indicators compared with NC2.

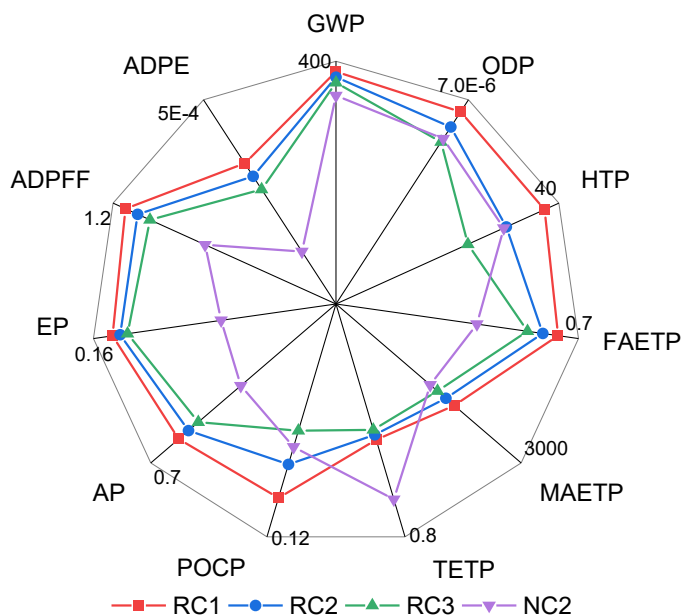


Figure 7.8 Comparison of 11 Environmental impact categories indicators of three types of BCC (RC2, RC3 and NC2) and reference mixture RC1

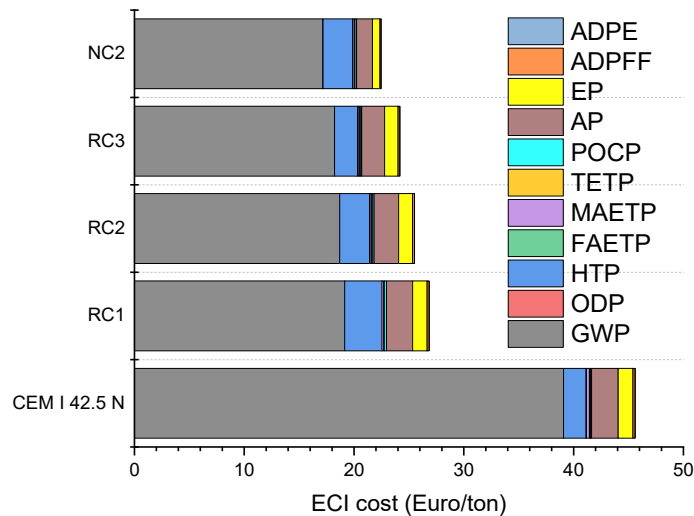


Figure 7.9 ECI calculation of various types of cement

7.4.2.2 ECI analysis

The ECI costs of BCC (RC2, RC3, NC2) are calculated with the illustration of specific contributions from 11 environmental categories. The results are listed in Figure 7.9 and are compared with reference mixture RC1 and commercial cement CEM I 42.5 N.

It can be seen that CEM I 42.5 N shows the largest ECI cost with a value of 45.60 euro/ton, in which GWP contributes about 85% of the total ECI costs. Reference mixture RC1 is found with the ECI cost at 26.84 euro/ton, which is 41.14% lower compared to CEM I. This is primarily attributed to the reduction in GWP resulting from the substitution of clinkers by BFS.

For BCC, by introducing WBFA for BFS replacement, a gradual decrease in the ECI cost is seen. RC2 and RC3 are determined with a ECI cost at 25.51 euro/ton and 24.18 euro/ton, respective. NC2, on the other hand, is observed with the lowest ECI cost among all, at 22.49 euro/ton. Compared with RC1, the ECI cost reduction ratios for RC2, RC3, and NC2 are 4.97%, 9.93%, and 16.30%, respectively. However, the reduction is less significant, which is mainly because that clinker phases are the primary contributor to the environmental cost in the cement production. The environmental benefits from WBFA are less significant when it is used for BFS replacement in cement production.

7.5 Discussions

7.5.1 Recommendations for improvement

7.5.1.1 Bio-ash brick

The advantages of bio-ash bricks over fired-clay bricks are mainly attributed to the exclusion of high temperature burning process. In comparison to concrete blocks, on the other hand, the exclusion of cement is of great benefit. It is interesting to note that for conventional concrete bricks, the binder constitutes only accounts for about 10% of the total weight. Comparatively, approximately 30% of the mass proportion in bio-ash bricks is attributed to the binder constituents. The overall environmental impact of bio-ash bricks is

significantly reduced due to the lower environmental impact of BFS and WBFA in nature compared with cement, which contributes to the overall sustainability of bio-ash bricks.

While bio-ash bricks already demonstrate a considerably lower environmental burden, it may be still possible to achieve a further reduction in its environmental impact. Further improvement can be suggested from the following perspectives:

- Increasing the WBFA to BFS ratio: As shown in Figure 7.5, BFS has the largest contribution in all 11 environmental categories. Lowering the proportion of BFS can effectively decrease the environmental impact of bio-ash bricks. Results reported in Chapter 4 indicate that binary pastes with a larger WBFA to BFS ratio might have a slower strength at early ages but a significant strength development in later stages. Bio-ash bricks with an increased WBFA to BFS ratio might also attain satisfactory property, where an extend of curing period should be considered.
- Increasing the proportions of sand: Since sand has a lower environmental impact than BFS, another option is to increase the sand proportions in the bio-ash bricks. However, it is important to note that increasing the sand content may lead to higher energy consumption during the manufacturing process. This could be due to the need for a higher compression force to achieve proper compaction of the brick. Therefore, the balance between the environmental impact resulting from sand proportions and the potential increase in manufacturing energy consumption should be carefully evaluated.

7.5.1.2 BCC

In this research, WBFA with a lower environmental impact is used to partially replace BFS in BFS blended cement, thus leading to a decrease in the environmental impact of BCC compared with the BFS blended cement. Further approaches can be applied to obtain a more sustainable cement.

- Pretreatment of WBFA: The environmental burden of WBFA comes from the energy consumption during the pretreatment process. The primary goal for the pretreatment process is to ensure that WBFA is free from metallic aluminium and free lime, which would cause unfavoured volume expansion. A lowest energy demanding process is employed during this process. Nevertheless, it is still commendable to consider an additional pretreatment process if it can lead to a better performance in the products. Previous results in Chapter 5 indicate that a finer particle size might lead to a denser particle packing in the microstructure and an improved strength. If applicable, grinding can be applied to upgrade the cement strength. Still, a comprehensive evaluation should be conducted to determine if the energy cost and performance benefits justify this step.
- Composition optimization: The idea of substituting BFS with WBFA originates from the investigation of BFS-WBFA binary pastes. However, WBFA might also be capable of cement replacement, although the mass proportion of cement replacement cannot be excessively high to ensure the comparable strength grade can be achieved. This method can effectively reduce the environmental impact, considering that cement has

the most significant environmental impact compared to slag and biomass fly ash. This should be addressed for future research.

7.5.2 Limitation of the LCA

7.5.2.1 *Transportation*

Transportation plays a significant role in increasing the environmental impact of final products. In cradle-to-gate analysis, the transportation of raw materials can exhibit variability in both distance and mode, depending on the accessibility of sources. This variability consequently leads to fluctuations in the environmental impact of the resulting products. As seen in Table A7.2, transportation is the least contributing factor in major indicators in the EPD of commercial bricks. Therefore, this suggests our research results are representative even when the transportation process is not considered. Nonetheless, it is essential to note that in practical application, the availability of materials should be given careful consideration, as long-distance transportation can still constitute a substantial component of the overall environmental impact of the final products.

7.5.2.2 *Research boundaries*

This LCA primarily focuses on a cradle-to-gate analysis, emphasising the environmental benefit of employing WBFA for the production of bio-ash bricks and BCC within the scope of this research. For a more comprehensive evaluation of the environmental impact of WBFA utilization, it is recommended to adopt a cradle-to-grave or even cradle-to-cradle analysis. To achieve this goal, however, more data and information should be provided. The durability of these products is one of the concerning factors to address the life span of the materials. It is firmly established that an extending service life can be beneficial from the environmental perspective, as fewer interventions are needed. However, durability evaluation should also be based on the application purpose as well as the prevailing environmental conditions during the service life. More research, therefore, should be conducted on these aspects to further provide sufficient data for a cradle-to-grave LCA analysis. Moreover, the leaching performance of these WBFA-containing construction products needs to be investigated in future research to gain knowledge on the release of heavy metals to the environment, thus providing detailed insight during the service life of the products. Future works are expected to focus on these aspects.

7.6 Conclusions

Based on the findings in Chapters 4 and 5 concerning utilizing WBFA in different binder systems, this chapter extends the scope by upscaling these binders for product manufacturing. The conclusions can be summarized as follows:

- Bio-ash bricks exhibit 28-days compressive strength at 22.69 MPa, with cold water adsorption at 9.34%, 5-hour boiling water adsorption at 13.54%. The physical properties of bio-ash bricks align with the ASTM standards designated for bricks used in various applications.
- The incorporation of WBFA as a substitute for BFS, up to 30% in BFS blended cement, positively contributes to the strength development of standard mortars. This improvement is characterized by a notable early strength gain, while maintaining the

same strength grade at 28 days. The formulation of BCC, comprising WBFA, BFS, and cement clinker, can be expected as a novel cement type for construction applications, with similar mass composition to CEM V cement.

- The environmental impact of WBFA concerning 11 environmental categories is calculated based on the electricity usage during its pretreatment. The results indicate a much lower environmental impact of WBFA in all aspects compared with that of BFS, indicating its potential as low environment burden mineral in construction industry.
- A cradle-to-gate Life Cycle Assessment (LCA) is conducted for both bio-ash bricks and BCC. In the case of bio-ash bricks, a noteworthy reduction in ECI costs is observed when compared to commercial bricks. To further reduce ECI costs in bio-ash bricks, it is recommended to augment the weight proportion of sand and WBFA. However, it is imperative to carefully consider potential compromises in physical properties and the energy required for moulding. In the case of BCC, a moderate decrease in ECI costs is observed in BCC when introducing WBFA as BFS replacement. Suggestions for ECI cost reduction can be additional grinding of WBFA to further improve the mechanical properties of BCC, or partially substituting cement with WBFA.

Appendix

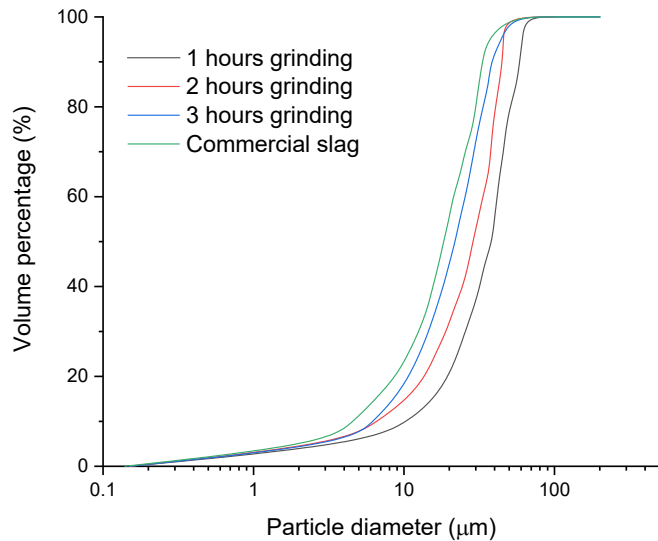


Figure A7.1 Particle size distribution of raw slag under different grinding durations by lab milling machine and comparison with commercial slag

Table A7.1 Environmental impacts categories and the associated value for raw materials per kg

Category	abbr.	Unit	Monetary value (euro/kg)	BFS	Sand	Electricity (medium voltage in NL)	WBFA	CEM I 52.5R	CEM I 42.5 N
Global Warming potential	GWP	kg CO ₂ eq	5.00E-02	6.06E-02	2.56E-03	6.33E-01	5.38E-03	8.57E-01	7.82E-01
Ozone layer Depletion potential	ODP	kg CFC11 eq	3.00E+01	3.71E-09	2.87E-10	3.11E-08	2.64E-10	1.09E-08	9.89E-09
Human Toxicity potential	HTP	kg 1,4-DB eq	9.00E-02	4.64E-02	9.82E-04	5.49E-02	4.67E-04	2.40E-02	2.29E-02
Freshwater Aquatic Eco-toxicity potential	FAETP		3.00E-02	3.06E-04	1.31E-05	1.48E-03	1.26E-05	1.14E-03	6.68E-04
Marine Aquatic Eco-toxicity potential	MAETP		1.00E-04	9.67E-01	4.46E-02	6.74E+00	5.73E-02	3.34E+00	2.70E+00
Terrestrial Eco-toxicity potential	TETP		6.00E-02	1.22E-04	1.07E-05	1.01E-03	8.57E-06	9.83E-04	1.54E-03
Photochemical Oxidation potential	POCP	kg ethylene eq	2.00E+00	1.16E-04	1.50E-06	8.81E-05	7.49E-07	7.58E-05	5.33E-05
Acidification potential	AP	kg SO ₂ eq	4.00E+00	2.56E-04	1.22E-05	1.09E-03	9.29E-06	1.10E-03	6.08E-04
Eutrophication potential	EP	kg PO ₄ eq	9.00E+00	3.50E-05	2.79E-06	2.39E-04	2.03E-06	3.16E-04	1.49E-04
Abiotic Depletion potential-fossil fuel	ADPFF	kg Sb eq	1.60E-01	4.80E-04	1.90E-05	4.77E-03	4.05E-05	2.11E-03	1.21E-03
Abiotic Depletion potential-non fossil fuel	ADPE		1.60E-01	2.22E-07	5.61E-09	1.09E-06	9.25E-09	5.28E-07	6.80E-08

Table A7.2 EDPs of commercial bricks (per m³)

Production approach	Number	Process	Environmental Indicator				File sources
			GWP kg CO ₂ eq	ODP kg CFC11 eq	AP kg SO ₂ eq	EP kg PO ₄ eq	
Concrete brick	1	A1-A3	3.69E+02	1.79E-05	7.82E-01	1.15E-01	https://www.marshalls.co.uk/commercial/epd-library
	2	A1-A3	2.86E+02	1.88E-05	1.27E+00	1.18E-01	
	3	A1-A3	2.59E+02	1.24E-05	5.92E-01	9.17E-02	
	4	A1	1.78E+02	4.63E-06	3.73E-01	-	https://www.astm.org/products-services/certification/environmental-product-declarations/epd-pcr/epd-for-jandris-block.html
		A2	4.87E+00	2E-10	6.61E-02	-	
		A3	2.76E+01	7.8E-07	2.75E-01	-	
	5	A1	2.71E+02	9.38E-05	8.30E-01	-	https://pcr-epd.s3.us-east-2.amazonaws.com/389.EPD_for_Hard_Block_Factory_EPD_2018-06-18.pdf
		A2	5.00E+01	1.29E-05	2.50E-01	-	
		A3	3.20E+01	8.39E-06	1.10E-01	-	
	6	A1	1.70E+02	8.90E-05	5.40E-01	-	
		A2	5.10E+01	1.31E-05	2.50E-01	-	
		A3	3.20E+01	8.32E-06	1.10E-01	-	
	7	A1	2.90E+02	9.52E-05	8.80E-01	-	
		A2	5.10E+01	1.30E-05	2.50E-01	-	
		A3	3.20E+01	8.45E-06	1.10E-01	-	
	8	A1	4.20E+02	8.07E-05	1.23E+00	-	
		A2	4.10E+01	1.05E-05	2.00E-01	-	
		A3	2.70E+01	6.79E-06	1.00E-01	-	

Table A7.2 EDPs of commercial bricks (per m³) (Continued)

Production approach	Number	Process	Environmental Indicator				File sources
			GWP kg CO ₂ eq	ODP kg CFC11 eq	AP kg SO ₂ eq	EP kg PO ₄ eq	
Concrete brick	9	A1	4.22E+02	8.04E-05	1.23E+00	-	https://pcr-epd.s3.us-east-2.amazonaws.com/389.EPD_for_Hard_Block_Factory_EPD_2018-06-18.pdf
		A2	4.10E+01	1.05E-05	2.10E-01	-	
		A3	2.70E+01	6.73E-06	1.00E-01	-	
	10	A1-A3	1.73E+02	2.52E-06	5.31E-01	-	https://pcr-epd.s3.us-east-2.amazonaws.com/619.EPD_FOR_Angelus_Block.pdf
	11	A1-A3	1.95E+02	2.56E-06	5.73E-01	-	
	12	A1-A3	2.16E+02	2.60E-06	6.14E-01	-	
Fired-brick	13	A1-A3	2.13E+02	1.85E-05	3.49E+00	1.07E-01	https://www.wienerberger.co.uk/content/dam/wienerberger/united-kingdom/marketing/documents-magazines/sustainability/correct/UK_EPD_UK_Clay_Brick_202402.pdf
	14	A1	1.42E+01	1.44E-06	1.18E-01	3.48E-02	https://www.igbc.ie/wp-content/uploads/2021/07/EPD-Kingscourt-Brick-12-07-2021-EPDIE-21-51.pdf
		A2	4.82E+00	8.87E-07	1.33E-02	1.99E-03	
		A3	1.93E+02	1.92E-05	3.62E-01	7.54E-02	
	15	A1-A3	5.02E+02	8.10E-07	1.60E+00	3.30E-01	https://www.epd.dk/uk/epd-database/randers-tegl-a-s/tile-brick-based-on-red-burning-clay-hammershoj/

(Note: the processes A1, A2, and A3 implies the extraction and processing of raw materials, transport to the production site, and manufacturing processes, respectively)

Chapter 8

Retrospection, conclusions, and prospects

8.1 Retrospection

In the beginning of this thesis, the present state and potential future advancements of biomass energy are illustrated. The accumulation of wood biomass fly ash (WBFA), one of the primary by-products of biomass energy, poses a significant challenge to the sustainable development of biomass energy. The high demand for raw materials in the construction industry, on the other hand, provides an opportunity for WBFA utilization, which benefits both the energy and construction industries.

The primary goal of this thesis is to enhance the utilization of WBFA for the development of sustainable low-carbon cementitious materials. To achieve this, it is essential to understand the properties of WBFA, conduct proper pretreatment for WBFA, and further propose proper utilization approaches based on the knowledge of WBFA and cementitious materials. Chapter 2 reviewed the characteristics of WBFA from a large number of cases in the literature. Besides, the up-to-date research on valorising WBFA in cementitious materials development is summarized. A WBFA classification method was proposed by associating their chemical compositions and current utilization approaches, providing a brief guideline on the utilization method for WBFA in cementitious materials. Still, it was found that the utilization of WBFA in the construction sector remained limited, due to its infeasibility to be directly used as conventional supplementary cementitious materials (SCMs) in cement or as precursors in alkali-activated materials (AAMs). WBFA only provided a limited contribution to hydrate formation.

The experimental research in this thesis starts by characterizing three types of WBFA collected in the Netherlands. By evaluating their properties, one type with representative physicochemical properties aligned with the literature review was selected. A pretreatment process was adopted to eliminate the metallic Al and free lime in WBFA, to prevent volume expansion when using WBFA in cementitious materials. The dissolution of WBFA was conducted in solutions with different alkalinites, in order to mimic the dissolution of elements Ca, Si, and Al, the most interesting elements for hydrates formulation in cementitious materials, from WBFA. The results suggested to use WBFA to enhance the reaction of pozzolanic materials instead of adopting WBFA as conventional SCMs. This strategy was further implemented in Chapter 4.

In Chapter 4, a clinker-free binder was formulated with WBFA and BFS, following the strategy proposed in Chapter 3. The positive findings in Chapter 4 further implied the possibility of using WBFA to replace BFS in BFS blended cement, which was investigated in Chapter 5. Results from Chapters 4 and 5 conveyed that WBFA can be used for developing cementitious materials for low strength and high strength applications, respectively. The

reaction kinetics, and microstructure development of these binders were studied thoroughly, enabling a comprehensive understanding of how WBFA functions in the binders, which can be used as knowledge to tailor the performance of these binders for different engineering practices.

In Chapter 6, the carbonation resistance of the binders developed in Chapters 4 and 5 was studied to obtain a further understanding on their performance from the durability perspective. By comparing the microstructure alteration of binders before and after carbonation, the governing factors for controlling the carbonation resistance of these binders were discussed, suggestions on improving carbonation resistance were provided accordingly.

In Chapter 7, construction products are developed based on the cementitious materials studied in Chapters 4 and 5, converting research results into engineering practices. The WBFA-BFS binary binder was upscaled to produce compressed bio-ash bricks. Meanwhile, the properties of BFS blended cement containing WBFA were evaluated according to common cement standard, in order to verify the feasibility of WBFA as a mineral constituent in cement production. The physical properties of these products can meet the requirements in standards. Meanwhile, the life cycle analysis for the two products shows the benefits of WBFA in developing cementitious materials. Overall, the results demonstrate that WBFA can be effectively utilized in cementitious materials, offering a win-win solution for both the biomass energy and construction sectors.

8.2 Conclusions

The main conclusions of this thesis can be summarized as follows:

WBFA characteristic and pretreatment:

- WBFA is commonly rich in calcium, alkalis, and sulfate, while containing a limited content of aluminosilicates. One of the most feasible WBFA samples was selected among three ashes for detailed investigation, based on its representative chemical compositions and low contamination content.
- A cost-effective two-step pretreatment process was proposed to eliminate the metallic aluminum and free lime in WBFA, improving its feasibility to be utilized in binder development. Analysis of the mineral compositions and dissolution results of the treated WBFA revealed low availability of aluminosilicates but high alkalinity, calcium, and sulfate content, which were advantageous for promoting aluminosilicate hydration. This formed the basis for WBFA utilization in WBFA-BFS binary binder and as a replacement for BFS in BFS blended pastes.

WBFA-BFS binary pastes:

- *Hydration kinetics*

Neither WBFA nor BFS can exhibit a hydration peak from the isothermal calorimetry test solely, while the combination of these two materials led to a clear cement-like heat release characteristic, indicating a substantial contents of hydrates generation.

An increase of WBFA in the pastes led to a slower initial reaction but proves beneficial for long term hydration, this conclusion can also be evidenced by results

of bound water contents from TGA test, and BFS reaction degrees from SEM-EDS mappings.

- *Microstructure*

The main hydration products in the binary pastes are C-S-H gels, ettringite, and Friedel's salt. Hydrotalcite was also observed as the secondary hydrate from the XRD and FTIR results. The packing of hydrates and anhydrous particles formed the microstructure of the binary pastes. Accumulation of hydrates during hydration leads to the refinement of pore structure with time, and pastes with more WBFA lead to a more significant porosity reduction at a later age, aligning well with the kinetics of binary pastes. However, the overall porosity of the binary pastes remained large, above 30% at 60 days from MIP test.

- *Mechanical properties*

A mixture with 50% of treated WBFA and 50% of BFS with a water to binder ratio at 0.40 exhibited the highest compressive strength, reaching about 40 MPa at 60 days. This indicated that the binary pastes can be used for moderate strength applications.

WBFA in BFS blended cement pastes:

- *Hydration kinetics*

WBFA can largely accelerate the hydration of both BFS and Portland cement at early age. This can be evidenced by the increased total heat release, largely increased bound water in pastes containing WBFA at 1 day and 7 days. At long term hydration, the reaction degrees of cement were comparable regardless of the proportion of WBFA based on the QXRD analysis, while an increased BFS reaction degree can be seen with the increment of WBFA based on the EDS-mapping analysis.

- *Microstructure*

In BFS blended cement, the main hydration products in the pastes were C-S-H gels, monosulfate and hydrotalcite after 28 days and onwards. When WBFA was introduced, besides C-S-H gels and hydrotalcite, it led to the formation of Friedel's salt and ettringite. By adding WBFA, the porosity of pastes significantly decreased at 1 day, owing to the accelerated hydration of cement and BFS with accumulation of more hydrates. For samples at 90 days, the increment of WBFA led to a gradual increase in porosity.

- *Mechanical properties*

The introduction of WBFA significantly enhanced the early age compressive strength of BFS blended pastes. For long term strength, replacing 15% of BFS with WBFA can still positively contribute to the compressive strength. The mixture with 30% of BFS replacement with WBFA only showed about 8% strength decrease at 90 days. This indicated the great significance of WBFA in promoting the low early-age strength of BFS blended cement while maintaining comparable long-term strength.

Carbonation resistance:

- WBFA-BFS binary pastes exhibited poorer carbonation resistance compared to cement pastes. The carbonation of binary pastes resulted in a strength loss of approximately 50% upon reaching complete carbonation. This was attributed to the decomposition of hydrates, including C-S-H gels, ettringite, and Friedel's salt. This

decomposition further led to the coarsening of pores, resulting in a decrease in strength.

- In BFS blended cement system, the introduction of WBFA led to a reduction in carbonation resistance. For all mixtures, the compressive strength initially increased due to the carbonation of portlandite converting to calcite with a volume increase. Later, the compressive strength started to decrease with the extension of carbonation exposure period. Similar to binary pastes carbonation, the decomposition of hydrates is observed. The strength of pastes after 70 days of accelerated carbonation is still comparable to samples before carbonation.
- Pore connectivity was found as a more important in controlling the carbonation resistance in the pastes, instead of the contents of carbonation buffering mineral portlandite. It was suggested that further grinding WBFA to reduce the porous structure of grains could enhance the carbonation resistance of WBFA-containing cementitious materials.

Environmental benefits:

- Bio-ash brick with satisfactory engineering properties is developed based on the binary WBFA-slag binder. The cradle-to-gate life cycle analysis (LCA) of bio-ash bricks reveals a significant reduction in environmental impact compared to commercially available bricks. The environmental cost indicator (ECI) for bio-ash bricks is less than 50% of that for commercial bricks.
- Bio-ash composite cement (BCC) is formulated by integrating WBFA into BFS blended cement as a replacement for BFS. From the perspective of cement composition, BCC can fit the scope of CEM V and CEM VI type of cement, depending on the proportion of WBFA. The physical properties of BCC meet the requirements for common cements, suggesting the potential of WBFA as a mineral constituent in cement production. The Cradle-to-gate LCA analysis demonstrates a reduced environmental impact in BCC compared to both OPC and BFS blended cement, highlighting the environmental benefits of valorizing WBFA in cement production.

8.3 Contributions of this thesis

- *New strategies for utilizing WBFA in cementitious materials have been proposed:*

Unlike previous research focusing on using WBFA to replace cement, this thesis proposes to use WBFA to enhance the reaction of pozzolanic materials. This was verified through the development of cement clinker-free WBFA-BFS binary pastes. This knowledge was further extended to BFS blended cement systems by replacing BFS with WBFA. The results, demonstrating higher early age strength and comparable long-term strength in pastes with WBFA, confirm the successful use of WBFA as a functional mineral in developing cementitious materials.

- *The detailed reaction process of WBFA containing binders was investigated:*

Through the investigation from reaction kinetics and microstructure evolution, this research provides a fundamental understanding of how WBFA affects the reactions in BFS and cement. These findings can offer valuable insights for tailoring the performance of WBFA-

containing cementitious materials according to specific application requirements. These can serve as theoretical knowledge for further implementation of utilizing WBFA in construction materials.

- *The carbonation of WBFA-containing cementitious materials was studied*

The impact of WBFA on the carbonation performance of cementitious materials was analysed. The governing factors affecting carbonation resistance when WBFA was introduced were concluded, and possible solutions were proposed accordingly. These findings expand the understanding of the performance of WBFA-containing cementitious materials, offering theoretical knowledge for industrial applications where carbonation needs to be considered.

- *Verified the engineering practice of using WBFA in preparing construction products:*

By developing Bio-ash brick and Bio-ash composite cement with qualified technical properties, this thesis verifies the applicability from an industrial perspective for employing WBFA in developing construction products. The environmental benefits determined through LCA further indicate the positive impact of using WBFA to develop low-carbon construction materials.

To sum up, this thesis provided systematic research on circulating WBFA in developing cementitious materials. It covers investigations spanning from raw materials characterization and binder formulation to understanding the fundamental reaction mechanisms and the carbonation process, culminating in the production of final products, emphasizing the benefits of utilizing WBFA in the construction sector. The ash studied represents a broad range of WBFA in terms of physicochemical properties, offering valuable insights for industrial applications and providing a methodology for WBFA utilizing in the construction sector. However, it is necessary to mention that due to the variety of WBFA, there are variations in chemical composition. For example, some ashes are rich in silica rather than calcium and alkalis, which fall outside the scope of this research. Additionally, some ashes may contain contaminants, particularly heavy metals, which might require further pretreatment processes. These can be extended for future research.

8.4 Prospects

Besides the scope of this thesis, there are some interesting research topics can be extended for future research.

- From both literature and current research, it can be seen that the quality of WBFA is relatively low for cementitious materials. This can be attributed to the high chloride content, heavy metals, relatively low reactivity, etc,. Further pretreatment on WBFA to improve its quality is suggested for future research.
- This research extensively incorporated WBFA into binder formulation with minimal costs in pretreatment, while the results implied that the porous microstructure in WBFA might be one of the factors impeded the performance of the WBFA-containing binder. To further improve the performance of these binders, further refinement on the grinding process can be studied. Meanwhile, optimizing the mixture design of the

binders considering both physical performance (from experimental results) and environmental cost (from LCA analysis) is suggested for future research.

- Integrating the experimental results into a numerical hydration model, for instance, CEMHYD3D, HYMOSTRUC or GEOMICRO 3D, is suggested in future research. This enables the prediction of the microstructure evolution and mechanical properties of WBFA-containing binders, promoting the efficiency of mixture designs.
- In this research, only BFS was used as the pozzolanic material to react with WBFA. It is advised to incorporation other pozzolanic materials to replace the gradually scarce BFS, for instance, calcined low-quality clay, red mud, and MSWI ash etc. This can further reduce the dependence on the currently used SCMs under limited supply. This brings great research and engineering interests.
- From the industrial point of view, it is suggested to conducted more case studies on using WBFA-containing binders for different construction products manufacturing. This can help the exploration the potential of these binders in engineering practice. Based on the application purpose, the research on durability of the products and further improvement, if necessary, can be conducted.
- The LCA study employed in this thesis is confined to a cradle-to-gate boundary. It is advisable to enhance the comprehensiveness of the analysis by conducting a more extensive LCA, such as a cradle-to-grave analysis. This would provide a holistic understanding of the environmental impact of building products incorporating WBFA.

Reference

- [1] M. Crippa, G. Oreggioni, D. Guizzardi, M. Muntean, E. Schaaf, E. Lo Vullo, E. Solazzo, F. Monforti-Ferrario, J.G.. Olivier, E. Vignati, Fossil CO₂ and GHG emissions of all world countries - 2019 Report Publications Office of the EU, 2019. <https://doi.org/10.2760/687800>.
- [2] IEA, CO₂ Emissions in 2022, Paris, 2023. <https://www.iea.org/news/global-co2-emissions-rebounded-to-their-highest-level-in-history-in-2021>.
- [3] Agora Energiewende and enervis, Phasing out coal in the EU 's power system by 2030. A policy action plan, (2021). https://static.agora-energiewende.de/fileadmin/Projekte/2020/2020_09_EU_Coal_Exit_2030/EU-Coal-phase-out-2030_Datenanhang.pdf.
- [4] Europe Beyond Coal, Overview: National coal phase-out announcements in Europe. Status January 2021, (2021) 1–7. <https://beyond-coal.eu/wp-content/uploads/2021/01/Overview-of-national-coal-phase-out-announcements-Europe-Beyond-Coal-January-2021.pdf>.
- [5] C. Sulaiman, A.S. Abdul-Rahim, C.A. Ofozor, Does wood biomass energy use reduce CO₂ emissions in European Union member countries? Evidence from 27 members, *J. Clean. Prod.* 253 (2020) 119996. <https://doi.org/10.1016/j.jclepro.2020.119996>.
- [6] Statistics Netherlands, Renewable energy use, 1990-2018, (n.d.). <https://www.clo.nl/en/indicators/en038535-renewable-energy-use>.
- [7] P. Lauri, P. Havlík, G. Kindermann, N. Forsell, H. Böttcher, M. Obersteiner, Woody biomass energy potential in 2050, *Energy Policy*. 66 (2014) 19–31. <https://doi.org/10.1016/j.enpol.2013.11.033>.
- [8] B. Hektor, S. Backéus, K. Andersson, Carbon balance for wood production from sustainably managed forests, *Biomass and Bioenergy*. 93 (2016) 1–5. <https://doi.org/10.1016/j.biombioe.2016.05.025>.
- [9] IEA, Net Zero by 2050: A Roadmap for the Global Energy Sector, Paris, 2021. <https://www.iea.org/reports/net-zero-by-2050>.
- [10] A.S. Frans Lamers, Marcel Cremers, Doris Matschegg, Christoph Schmidl, Kirsten Hannam, Paul Hazlett, Sebnem Madrali, Birgitte Primdal Dam, Roberta Roberto, Rob Mager, Kent Davidsson, Nicolai Bech, Hans-Joachim Feuerborn, Options for increased use of ash from biomass combustion and co-firing, *IEA Bioenergy*. (2018) 1–61.
- [11] S.K. Amin, S.A. El-Sherbiny, A.A.M.A. El-Magd, A. Belal, M.F. Abadir, Fabrication of geopolymers bricks using ceramic dust waste, *Constr. Build. Mater.* 157 (2017) 610–620. <https://doi.org/10.1016/j.conbuildmat.2017.09.052>.
- [12] Y. Hu, S. Liang, J. Yang, Y. Chen, N. Ye, Y. Ke, S. Tao, K. Xiao, J. Hu, H. Hou, W. Fan, S. Zhu, Y. Zhang, B. Xiao, Role of Fe species in geopolymers synthesized from alkali-thermal pretreated Fe-rich Bayer red mud, *Constr. Build. Mater.* 200 (2019) 398–407. <https://doi.org/10.1016/j.CONBUILDMAT.2018.12.122>.
- [13] Y. Li, X. Zeng, J. Zhou, H. Liu, Y. Gu, Z. Pan, Y. Zeng, Y. Zeng, Incorporation of disposed oil-contaminated soil in cement-based materials, *Resour. Conserv. Recycl.* 160 (2020). <https://doi.org/10.1016/j.resconrec.2020.104838>.
- [14] N. Sedira, J. Castro-Gomes, M. Magrinho, Red clay brick and tungsten mining waste-based alkali-activated binder: Microstructural and mechanical properties, *Constr. Build. Mater.* 190 (2018) 1034–1048. <https://doi.org/10.1016/j.conbuildmat.2018.09.153>.
- [15] G. Kürklü, G. Görhan, Investigation of usability of quarry dust waste in fly ash-based geopolymers adhesive mortar production, *Constr. Build. Mater.* (2019). <https://doi.org/10.1016/j.conbuildmat.2019.05.104>.
- [16] M.B. Ali, R. Saidur, M.S. Hossain, A review on emission analysis in cement industries, *Renew. Sustain.*

Energy Rev. 15 (2011) 2252–2261. <https://doi.org/10.1016/j.rser.2011.02.014>.

[17] Z. Giergiczny, Fly ash and slag, Cem. Concr. Res. 124 (2019). <https://doi.org/10.1016/j.cemconres.2019.105826>.

[18] A. Fuller, M. Stegmaier, N. Schulz, M. Menke, H. Schellhorn, F. Knödler, J. Maier, G. Scheffknecht, Use of wood dust fly ash from an industrial pulverized fuel facility for rendering, Constr. Build. Mater. 189 (2018) 825–848. <https://doi.org/10.1016/j.conbuildmat.2018.09.016>.

[19] N.M. Sigvardsen, M.R. Geiker, L.M. Ottosen, Reaction mechanisms of wood ash for use as a partial cement replacement, Constr. Build. Mater. 286 (2021) 122889. <https://doi.org/10.1016/j.conbuildmat.2021.122889>.

[20] V. Gupta, D.K. Pathak, S. Siddique, R. Kumar, S. Chaudhary, Study on the mineral phase characteristics of various Indian biomass and coal fly ash for its use in masonry construction products, Constr. Build. Mater. 235 (2020). <https://doi.org/10.1016/j.conbuildmat.2019.117413>.

[21] R. Rajamma, L. Senff, M.J. Ribeiro, J.A. Labrincha, R.J. Ball, G.C. Allen, V.M. Ferreira, Biomass fly ash effect on fresh and hardened state properties of cement based materials, Compos. Part B Eng. 77 (2015) 1–9. <https://doi.org/10.1016/j.compositesb.2015.03.019>.

[22] K.W. Kim, K.T. Park, F. Ates, H.G. Kim, B.H. Woo, Effect of pretreated biomass fly ash on the mechanical properties and durability of cement mortar, Case Stud. Constr. Mater. 18 (2023) e01754. <https://doi.org/10.1016/j.cscm.2022.e01754>.

[23] J. Šantek Bajto, N. Štirmer, S. Cerković, I. Carević, K. Kostanić Jurić, Pilot scale production of precast concrete elements with wood biomass ash, Materials (Basel). 14 (2021). <https://doi.org/10.3390/ma14216578>.

[24] NEN-EN 12390-12: Testing hardened concrete - Part 12: Determination of the carbonation resistance of concrete - Accelerated carbonation method, 12 (2021).

[25] G. Liang, Y. Li, C. Yang, C. Zi, Y. Zhang, D. Zhang, M. Wang, W. Zhao, Ash properties correlated with diverse types of biomass derived from power plants: an overview, Energy Sources, Part A Recover. Util. Environ. Eff. 00 (2020) 1–12. <https://doi.org/10.1080/15567036.2020.1804012>.

[26] J.I. Odzijewicz, E. Wołejko, U. Wydro, M. Wasil, A. Jabłońska-Trypuć, Utilization of Ashes from Biomass Combustion, Energies. 15 (2022) 9653. <https://doi.org/10.3390/en15249653>.

[27] S. V. Vassilev, D. Baxter, L.K. Andersen, C.G. Vassileva, An overview of the chemical composition of biomass, Fuel. 89 (2010) 913–933. <https://doi.org/10.1016/j.fuel.2009.10.022>.

[28] H. Spliethoff, Combustion Systems for Solid Fossil Fuels, in: 2010: pp. 221–359. https://doi.org/10.1007/978-3-642-02856-4_5.

[29] A. Demirbas, Potential applications of renewable energy sources, biomass combustion problems in boiler power systems and combustion related environmental issues, Prog. Energy Combust. Sci. 31 (2005) 171–192. <https://doi.org/10.1016/j.pecs.2005.02.002>.

[30] I. Obernberger, K. Supancic, Possibilities of ash utilisation from biomass combustion plants, in: Proc. 17th Eur. Biomass Conf. Exhib., Hamburg, 2009.

[31] O. Dahl, H. Nurmesniemi, R. Pöykiö, G. Watkins, Comparison of the characteristics of bottom ash and fly ash from a medium-size (32 MW) municipal district heating plant incinerating forest residues and peat in a fluidized-bed boiler, Fuel Process. Technol. 90 (2009) 871–878. <https://doi.org/10.1016/j.fuproc.2009.04.013>.

[32] F. Agrela, M. Cabrera, M.M. Morales, M. Zamorano, M. Alshaer, Biomass fly ash and biomass bottom ash, in: New Trends Eco-Efficient Recycl. Concr., Elsevier, 2019: pp. 23–58. <https://doi.org/10.1016/B978-0-08-102480-5.00002-6>.

[33] T.P. da Costa, P. Quinteiro, L.A. da C. Tarelho, L. Arroja, A.C. Dias, Environmental impacts of forest biomass-to-energy conversion technologies: Grate furnace vs. fluidised bed furnace, J. Clean. Prod. 171 (2018) 153–162. <https://doi.org/10.1016/j.jclepro.2017.09.287>.

[34] A. Panahi, M. Tarakcioglu, M. Schiemann, M. Delichatsios, Y.A. Levendis, On the particle sizing of torrefied biomass for co-firing with pulverized coal, *Combust. Flame.* 194 (2018) 72–84. <https://doi.org/10.1016/j.combustflame.2018.04.014>.

[35] M. Sami, K. Annamalai, M. Wooldridge, Co-firing of coal and biomass fuel blends, *Prog. Energy Combust. Sci.* 27 (2001) 171–214. [https://doi.org/10.1016/S0360-1285\(00\)00020-4](https://doi.org/10.1016/S0360-1285(00)00020-4).

[36] NEN-EN 450-1 Fly ash for concrete - Part 1: Definition, specifications and conformity criteria, 2012.

[37] H. Soud, Developments in particulate control for coal combustion, IEA Coal research, London, 1995.

[38] N. Maeda, T. Katakura, T. Fukasawa, A.-N. Huang, T. Kawano, K. Fukui, Morphology of woody biomass combustion ash and enrichment of potassium components by particle size classification, *Fuel Process. Technol.* 156 (2017) 1–8. <https://doi.org/10.1016/j.fuproc.2016.09.026>.

[39] G.C.H. Doudart de la Grée, M.V.A. Florea, A. Keulen, H.J.H. Brouwers, Contaminated biomass fly ashes - Characterization and treatment optimization for reuse as building materials, *Waste Manag.* 49 (2016) 96–109. <https://doi.org/10.1016/j.wasman.2015.12.023>.

[40] R.P. Girón, B. Ruiz, E. Fuente, R.R. Gil, I. Suárez-Ruiz, Properties of fly ash from forest biomass combustion, *Fuel.* 114 (2013) 71–77. <https://doi.org/10.1016/j.fuel.2012.04.042>.

[41] E.R. Teixeira, A. Camões, F.G. Branco, Valorisation of wood fly ash on concrete, *Resour. Conserv. Recycl.* 145 (2019) 292–310. <https://doi.org/10.1016/j.resconrec.2019.02.028>.

[42] R. Melotti, E. Santagata, M. Bassani, M. Salvo, S. Rizzo, A preliminary investigation into the physical and chemical properties of biomass ashes used as aggregate fillers for bituminous mixtures, *Waste Manag.* 33 (2013) 1906–1917. <https://doi.org/10.1016/j.wasman.2013.05.015>.

[43] S. Wang, L. Baxter, F. Fonseca, Biomass fly ash in concrete: SEM, EDX and ESEM analysis, *Fuel.* 87 (2008) 372–379. <https://doi.org/10.1016/j.fuel.2007.05.024>.

[44] I. Carević, A. Baričević, N. Štirmer, J. Šantek Bajto, Correlation between physical and chemical properties of wood biomass ash and cement composites performances, *Constr. Build. Mater.* 256 (2020) 119450. <https://doi.org/10.1016/j.conbuildmat.2020.119450>.

[45] J. Popławski, M. Lelusz, Assessment of Sieving as a Mean to Increase Utilization Rate of Biomass Fly Ash in Cement-Based Composites, *Appl. Sci.* 13 (2023). <https://doi.org/10.3390/app13031659>.

[46] Camia A, Giuntoli, J. Jonsson, R. Robert, The use of woody biomass for energy production in the EU, *Publ. Off. Eur. Union.* (2021) 178. <https://doi.org/10.2760/831621>.

[47] ASTM C618, Standard Specification for Coal Fly Ash and Raw or Calcined Natural Pozzolan for Use in Concrete, n.d. <https://doi.org/10.1520/C0618-22.2>.

[48] R.P. Girón, I. Suárez-Ruiz, B. Ruiz, E. Fuente, R.R. Gil, Fly Ash from the Combustion of Forest Biomass (*Eucalyptus globulus* Bark): Composition and Physicochemical Properties, *Energy & Fuels.* 26 (2012) 1540–1556. <https://doi.org/10.1021/ef201503u>.

[49] A. Fuller, M. Carbo, P. Savat, J. Kalivodova, J. Maier, G. Scheffknecht, Results of fly ash quality for disposal options from high thermal shares up to pure biomass combustion in a pilot-scale and large scale pulverized fuel power plants, *Renew. Energy.* 75 (2015) 899–910. <https://doi.org/10.1016/j.renene.2014.10.032>.

[50] J. Fořt, J. Šál, R. Ševčík, M. Doleželová, M. Keppert, M. Jerman, M. Záleská, V. Stehel, R. Černý, Biomass fly ash as an alternative to coal fly ash in blended cements: Functional aspects, *Constr. Build. Mater.* 271 (2021) 71–73. <https://doi.org/10.1016/j.conbuildmat.2020.121544>.

[51] I. Carević, M. Serdar, N. Štirmer, N. Ukrainczyk, Preliminary screening of wood biomass ashes for partial resources replacements in cementitious materials, *J. Clean. Prod.* 229 (2019) 1045–1064. <https://doi.org/10.1016/j.jclepro.2019.04.321>.

[52] M. Berra, T. Mangialardi, A.E. Paolini, Reuse of woody biomass fly ash in cement-based materials, *Constr. Build. Mater.* 76 (2015) 286–296. <https://doi.org/10.1016/j.conbuildmat.2014.11.052>.

[53] G. Ondrasek, M. Zovko, F. Kranjčec, R. Savić, D. Romić, Z. Rengel, Wood biomass fly ash ameliorates acidic, low-nutrient hydromorphic soil & reduces metal accumulation in maize, *J. Clean. Prod.* 283 (2021) 124650. <https://doi.org/10.1016/j.jclepro.2020.124650>.

[54] W.Y. Lin, A.K. Prabhakar, B.C. Mohan, C.H. Wang, A factorial experimental analysis of using wood fly ash as an alkaline activator along with coal fly ash for production of geopolymers-cementitious hybrids, *Sci. Total Environ.* 718 (2020). <https://doi.org/10.1016/j.scitotenv.2019.135289>.

[55] R.M. Novais, L.H. Buruberri, G. Ascensão, M.P. Seabra, J.A. Labrincha, Porous biomass fly ash-based geopolymers with tailored thermal conductivity, *J. Clean. Prod.* 119 (2016) 99–107. <https://doi.org/10.1016/j.jclepro.2016.01.083>.

[56] T. Ivanković, J. Hrenović, G. Itskos, N. Koukouzas, D. Kovačević, J. Milenković, Alkaline disinfection of urban wastewater and landfill leachate by wood fly ash, *Arch. Ind. Hyg. Toxicol.* 65 (2014) 365–375. <https://doi.org/10.2478/10004-1254-65-2014-2546>.

[57] B. Bouzar, Y. Mamindy-Pajany, Immobilization study of As, Cr, Mo, Pb, Sb, Se and Zn in geopolymers matrix: application to shooting range soil and biomass fly ash, *Int. J. Environ. Sci. Technol.* 20 (2023) 11891–11912. <https://doi.org/10.1007/s13762-023-04788-x>.

[58] F. Ates, K.T. Park, K.W. Kim, B.H. Woo, H.G. Kim, Effects of treated biomass wood fly ash as a partial substitute for fly ash in a geopolymers mortar system, *Constr. Build. Mater.* 376 (2023) 131063. <https://doi.org/10.1016/j.conbuildmat.2023.131063>.

[59] B. Nadia, K. Fatma, C. Nasser, Mechanical, thermal and durability investigation of compressed earth bricks stabilized with wood biomass ash, *Constr. Build. Mater.* 364 (2023) 129874. <https://doi.org/10.1016/j.conbuildmat.2022.129874>.

[60] A. De Rossi, L. Simão, M.J. Ribeiro, D. Hotza, R.F.P.M. Moreira, Study of cure conditions effect on the properties of wood biomass fly ash geopolymers, *J. Mater. Res. Technol.* 9 (2020) 7518–7528. <https://doi.org/10.1016/j.jmrt.2020.05.047>.

[61] K. Ohenoja, J. Pesonen, J. Yliniemi, M. Illikainen, Utilization of Fly Ashes from Fluidized Bed Combustion: A Review, *Sustainability* 12 (2020) 2988. <https://doi.org/10.3390/su12072988>.

[62] E.R. Teixeira, A. Camões, F.G. Branco, J.C. Matos, Effect of biomass fly ash on fresh and hardened properties of high volume fly ash mortars, *Crystals* 11 (2021) 1–21. <https://doi.org/10.3390/cryst11030233>.

[63] J. Fořt, J. Šál, J. Žák, R. Černý, Assessment of Wood-Based Fly Ash as Alternative Cement Replacement, *Sustainability* 12 (2020) 9580. <https://doi.org/10.3390/su12229580>.

[64] G.J.B. Silva, V.P. Santana, M. Wójcik, Investigation on mechanical and microstructural properties of alkali-activated materials made of wood biomass ash and glass powder, *Powder Technol.* 377 (2021) 900–912. <https://doi.org/10.1016/j.powtec.2020.09.048>.

[65] J. Acordi, A. Luza, D.C.N. Fabris, F. Raupp-Pereira, A. De Noni, O.R.K. Montedo, New waste-based supplementary cementitious materials: Mortars and concrete formulations, *Constr. Build. Mater.* 240 (2020). <https://doi.org/10.1016/j.conbuildmat.2019.117877>.

[66] I. Gabrijel, M. Skazlić, N. Štirmer, Long-Term Behavior of Concrete Containing Wood Biomass Fly Ash, *Appl. Sci.* 12 (2022). <https://doi.org/10.3390/app122412859>.

[67] N.M. Sigvardsen, M.R. Geiker, L.M. Ottosen, Phase development and mechanical response of low-level cement replacements with wood ash and washed wood ash, *Constr. Build. Mater.* 269 (2021). <https://doi.org/10.1016/j.conbuildmat.2020.121234>.

[68] N.M. Sigvardsen, G.M. Kirkelund, P.E. Jensen, M.R. Geiker, L.M. Ottosen, Impact of production parameters on physicochemical characteristics of wood ash for possible utilisation in cement-based materials, *Resour. Conserv. Recycl.* 145 (2019) 230–240. <https://doi.org/10.1016/j.resconrec.2019.02.034>.

[69] T. Bauer, M. Pelkonen, A. Lagerkvist, Co-digestion of sewage sludge and wood fly ash, *Environ. Technol.*

43 (2022) 1853–1859. <https://doi.org/10.1080/09593330.2020.1856937>.

[70] R. Weber, Y. Poyraz, M. Mancini, A. Schwabauer, Biomass fly-ash deposition: Dependence of deposition rate on probe/particle temperature in 115–1200 °C range, *Fuel.* 290 (2021). <https://doi.org/10.1016/j.fuel.2020.120033>.

[71] M. Wójcik, F. Stachowicz, A. Maślon, The Use of Wood Biomass Ash in Sewage Sludge Treatment in Terms of Its Agricultural Utilization, *Waste and Biomass Valorization.* 11 (2020) 753–768. <https://doi.org/10.1007/s12649-018-0518-0>.

[72] T.C. Esteves, R. Rajamma, D. Soares, A.S. Silva, V.M. Ferreira, J.A. Labrincha, Use of biomass fly ash for mitigation of alkali-silica reaction of cement mortars, *Constr. Build. Mater.* 26 (2012) 687–693. <https://doi.org/10.1016/j.conbuildmat.2011.06.075>.

[73] R. Rajamma, J.A. Labrincha, V.M. Ferreira, Alkali activation of biomass fly ash-metakaolin blends, *Fuel.* 98 (2012) 265–271. <https://doi.org/10.1016/j.fuel.2012.04.006>.

[74] S. Maschio, G. Tonello, L. Piani, E. Furlani, Fly and bottom ashes from biomass combustion as cement replacing components in mortars production: Rheological behaviour of the pastes and materials compression strength, *Chemosphere.* 85 (2011) 666–671. <https://doi.org/10.1016/j.chemosphere.2011.06.070>.

[75] R. Rajamma, R.J. Ball, L.A.C. Tarelho, G.C. Allen, J.A. Labrincha, V.M. Ferreira, Characterisation and use of biomass fly ash in cement-based materials, *J. Hazard. Mater.* 172 (2009) 1049–1060. <https://doi.org/10.1016/j.jhazmat.2009.07.109>.

[76] L. Tosti, A. van Zomeren, J.R. Pels, R.N.J. Comans, Technical and environmental performance of lower carbon footprint cement mortars containing biomass fly ash as a secondary cementitious material, *Resour. Conserv. Recycl.* 134 (2018) 25–33. <https://doi.org/10.1016/j.resconrec.2018.03.004>.

[77] S. Wang, A. Miller, E. Llamazos, F. Fonseca, L. Baxter, Biomass fly ash in concrete: Mixture proportioning and mechanical properties, *Fuel.* 87 (2008) 365–371. <https://doi.org/10.1016/j.fuel.2007.05.026>.

[78] N. Ukrainczyk, N. Vrbos, E.A.B. Koenders, Reuse of woody biomass ash waste in cementitious materials, *Chem. Biochem. Eng. Q.* 30 (2016) 137–148. <https://doi.org/10.15255/CABEQ.2015.2231>.

[79] J. Cuenca, J. Rodríguez, M. Martín-Morales, Z. Sánchez-Roldán, M. Zamorano, Effects of olive residue biomass fly ash as filler in self-compacting concrete, *Constr. Build. Mater.* 40 (2013) 702–709. <https://doi.org/10.1016/j.conbuildmat.2012.09.101>.

[80] E.R. Teixeira, R. Mateus, A. Camões, F.G. Branco, Quality and durability properties and life-cycle assessment of high volume biomass fly ash mortar, *Constr. Build. Mater.* 197 (2019) 195–207. <https://doi.org/10.1016/j.conbuildmat.2018.11.173>.

[81] A. Qureshi, Y. Jia, C. Maurice, B. Öhlander, Potential of fly ash for neutralisation of acid mine drainage, *Environ. Sci. Pollut. Res.* 23 (2016) 17083–17094. <https://doi.org/10.1007/s11356-016-6862-3>.

[82] M. Vely-Lizancos, M. Azenha, I. Martínez-Lage, P. Vázquez-Burgo, Addition of biomass ash in concrete: Effects on E-Modulus, electrical conductivity at early ages and their correlation, *Constr. Build. Mater.* 157 (2017) 1126–1132. <https://doi.org/10.1016/j.conbuildmat.2017.09.179>.

[83] R. Kaminskas, V. Cesnaukas, R. Kubiliute, Influence of biomass fly ash additive on blast-furnace cement hydration and hardening, *Adv. Cem. Res.* 29 (2017) 313–321. <https://doi.org/10.1680/jadcr.16.00190>.

[84] N.C. Cruz, S.M. Rodrigues, L. Carvalho, A.C. Duarte, E. Pereira, P.F.A.M. Römkens, L.A.C. Tarelho, Ashes from fluidized bed combustion of residual forest biomass: recycling to soil as a viable management option, *Environ. Sci. Pollut. Res.* 24 (2017) 14770–14781. <https://doi.org/10.1007/s11356-017-9013-6>.

[85] A.A. Khan, M. Aho, W. de Jong, P. Vainikka, P.J. Jansens, H. Spliethoff, Scale-up study on combustibility and emission formation with two biomass fuels (B quality wood and pepper plant residue) under BFB conditions, *Biomass and Bioenergy.* 32 (2008) 1311–1321. <https://doi.org/10.1016/j.biombioe.2008.03.011>.

[86] N. Koukouzas, J. Hämäläinen, D. Papanikolaou, A. Tourunen, T. Jäntti, Mineralogical and elemental composition of fly ash from pilot scale fluidised bed combustion of lignite, bituminous coal, wood chips and their blends, *Fuel*. 86 (2007) 2186–2193. <https://doi.org/10.1016/j.fuel.2007.03.036>.

[87] C. Maschowski, P. Kruspan, P. Garra, A. Talib Arif, G. Trouvé, R. Gieré, Physicochemical and mineralogical characterization of biomass ash from different power plants in the Upper Rhine Region, *Fuel*. 258 (2019) 116020. <https://doi.org/10.1016/j.fuel.2019.116020>.

[88] L. Etiégni, A.G. Campbell, Physical and chemical characteristics of wood ash, *Bioresour. Technol.* 37 (1991) 173–178. [https://doi.org/10.1016/0960-8524\(91\)90207-Z](https://doi.org/10.1016/0960-8524(91)90207-Z).

[89] NEN-EN 206 Concrete - Specification, performance, production and conformity, (2021).

[90] J. Fořt, E. Vejmelková, M. Keppert, P. Rovnaníková, P. Bezdička, R. Černý, Alkaline activation of low-reactivity ceramics: Peculiarities induced by the precursors' dual character, *Cem. Concr. Compos.* (2020). <https://doi.org/10.1016/j.cemconcomp.2019.103440>.

[91] B. Lothenbach, K. Scrivener, R.D. Hooton, Supplementary cementitious materials, *Cem. Concr. Res.* 41 (2011) 1244–1256. <https://doi.org/10.1016/j.cemconres.2010.12.001>.

[92] A.A. Khan, W. de Jong, P.J. Jansens, H. Spliethoff, Biomass combustion in fluidized bed boilers: Potential problems and remedies, *Fuel Process. Technol.* 90 (2009) 21–50. <https://doi.org/10.1016/j.fuproc.2008.07.012>.

[93] H. Bachmaier, D. Kuptz, H. Hartmann, Wood ashes from grate-fired heat and power plants: Evaluation of nutrient and heavy metal contents, *Sustain.* 13 (2021). <https://doi.org/10.3390/su13105482>.

[94] M. Berra, N.M. Ippolito, T. Mangialardi, A.E. Paolini, L. Piga, Leaching test procedure for assessing the compliance of the chemical and environmental requirements of hardened woody biomass fly ash cement mixtures, *Waste Manag.* 90 (2019) 10–16. <https://doi.org/10.1016/j.wasman.2019.04.038>.

[95] L.M. Ottosen, N.M. Sigvardsen, Heavy metal leaching from wood ash before and after hydration and carbonation, *Environ. Sci. Pollut. Res.* (2024). <https://doi.org/10.1007/s11356-024-33221-0>.

[96] M. Berra, G. De Casa, M. Dell'Orso, L. Galeotti, T. Mangialardi, A.E. Paolini, L. Piga, Reuse of Woody Biomass Fly Ash in Cement-Based Materials: Leaching Tests, in: *Recycl. Biomass Ashes*, Springer Berlin Heidelberg, Berlin, Heidelberg, 2011: pp. 133–146. https://doi.org/10.1007/978-3-642-19354-5_10.

[97] S. V. Vassilev, D. Baxter, L.K. Andersen, C.G. Vassileva, An overview of the composition and application of biomass ash. Part 1. Phase-mineral and chemical composition and classification, *Fuel*. 105 (2013) 40–76. <https://doi.org/10.1016/j.fuel.2012.09.041>.

[98] J.H. Park, J.H. Eom, S.L. Lee, S.W. Hwang, S.H. Kim, S.W. Kang, J.J. Yun, J.S. Cho, Y.H. Lee, D.C. Seo, Exploration of the potential capacity of fly ash and bottom ash derived from wood pellet-based thermal power plant for heavy metal removal, *Sci. Total Environ.* 740 (2020). <https://doi.org/10.1016/j.scitotenv.2020.140205>.

[99] R.T. Chancey, P. Stutzman, M.C.G. Juenger, D.W. Fowler, Comprehensive phase characterization of crystalline and amorphous phases of a Class F fly ash, *Cem. Concr. Res.* 40 (2010) 146–156. <https://doi.org/10.1016/j.cemconres.2009.08.029>.

[100] N.W. Chen-Tan, A. Van Riessen, C. V. Ly, D.C. Southam, Determining the reactivity of a fly ash for production of geopolymers, *J. Am. Ceram. Soc.* 92 (2009) 881–887. <https://doi.org/10.1111/j.1551-2916.2009.02948.x>.

[101] R. Rumman, M.R. Kamal, A. Bediwy, M.S. Alam, Partially burnt wood fly ash characterization and its application in low-carbon mortar and concrete, *Constr. Build. Mater.* 402 (2023) 132946. <https://doi.org/10.1016/j.conbuildmat.2023.132946>.

[102] E.R. Teixeira, A. Camões, F.G. Branco, Synergetic effect of biomass fly ash on improvement of high-volume coal fly ash concrete properties, *Constr. Build. Mater.* 314 (2022). <https://doi.org/10.1016/j.conbuildmat.2021.125680>.

[103] C.B. Cheah, M.H. Samsudin, M. Ramli, W.K. Part, L.E. Tan, The use of high calcium wood ash in the

preparation of Ground Granulated Blast Furnace Slag and Pulverized Fly Ash geopolymers: A complete microstructural and mechanical characterization, *J. Clean. Prod.* 156 (2017) 114–123. <https://doi.org/10.1016/j.jclepro.2017.04.026>.

[104] H.F.W. Taylor, *Cement chemistry*, 2nd ed., 1997. <https://doi.org/10.1680/cc.25929>.

[105] I.R. Dominguez, J. Gómez-Millán, M. Alvarez, S. De Aza, L. Contreras, A.H. De Aza, Build-up formation and corrosion of monolithic refractories in cement kiln preheaters, *J. Eur. Ceram. Soc.* 30 (2010) 1879–1885. <https://doi.org/10.1016/j.jeurceramsoc.2010.02.023>.

[106] L. Tosti, A. van Zomeren, J.R. Pels, R.N.J. Comans, Evaluating Biomass Ash Properties as Influenced by Feedstock and Thermal Conversion Technology towards Cement Clinker Production with a Lower Carbon Footprint, *Waste and Biomass Valorization*. 12 (2021) 4703–4719. <https://doi.org/10.1007/s12649-020-01339-0>.

[107] N. Carr, *Biomass Derived Binder*, 2019. <https://doi.org/https://doi.org/10.4233/uuid:12821467-3df9-40ab-a297-159497650b8c>.

[108] L.H. Buruberri, M.P. Seabra, J.A. Labrincha, Preparation of clinker from paper pulp industry wastes, *J. Hazard. Mater.* 286 (2015) 252–260. <https://doi.org/10.1016/j.jhazmat.2014.12.053>.

[109] H.A. Ali, D. Xuan, C.S. Poon, Assessment of long-term reactivity of initially lowly-reactive solid wastes as supplementary cementitious materials (SCMs), *Constr. Build. Mater.* 232 (2020). <https://doi.org/10.1016/j.conbuildmat.2019.117192>.

[110] G. Habert, S.A. Miller, V.M. John, J.L. Provis, A. Favier, A. Horvath, K.L. Scrivener, Environmental impacts and decarbonization strategies in the cement and concrete industries, *Nat. Rev. Earth Environ.* 1 (2020) 559–573. <https://doi.org/10.1038/s43017-020-0093-3>.

[111] V. Hallet, M.T. Pedersen, B. Lothenbach, F. Winnefeld, N. De Belie, Y. Pontikes, Hydration of blended cement with high volume iron-rich slag from non-ferrous metallurgy, *Cem. Concr. Res.* 151 (2022) 106624. <https://doi.org/10.1016/J.CEMCONRES.2021.106624>.

[112] V.H. Dodson, *Pozzolans and the Pozzolanic Reaction*, in: V.H. Dodson (Ed.), *Concr. Admixtures*, Springer US, Boston, MA, 1990: pp. 159–201. https://doi.org/10.1007/978-1-4757-4843-7_7.

[113] F. Massazza, *Pozzolana and pozzolanic cements*, Arnold London, 1998.

[114] S. Donatello, M. Tyrer, C.R. Cheeseman, Comparison of test methods to assess pozzolanic activity, *Cem. Concr. Compos.* 32 (2010) 121–127. <https://doi.org/10.1016/j.cemconcomp.2009.10.008>.

[115] W.B. Bonfim, H.M. de Paula, Characterization of different biomass ashes as supplementary cementitious material to produce coating mortar, *J. Clean. Prod.* 291 (2021). <https://doi.org/10.1016/j.jclepro.2021.125869>.

[116] V. Jittin, R. Rithuparna, A. Bahurudeen, B. Pachiappan, Synergistic use of typical agricultural and industrial by-products for ternary cement: A pathway for locally available resource utilisation, *J. Clean. Prod.* 279 (2021) 123448. <https://doi.org/10.1016/j.jclepro.2020.123448>.

[117] A. Khmiri, B. Samet, M. Chaabouni, A cross mixture design to optimise the formulation of a ground waste glass blended cement, *Constr. Build. Mater.* 28 (2012) 680–686. <https://doi.org/10.1016/j.conbuildmat.2011.10.032>.

[118] D. Vaičiukynienė, I. Pundienė, A. Kantautas, A. Augonis, E. Janavičius, V. Vaičiukynas, J. Alobeid, Synergistic effect of dry sludge from waste wash water of concrete plants and zeolitic by-product on the properties of ternary blended ordinary Portland cements, *J. Clean. Prod.* 244 (2020). <https://doi.org/10.1016/j.jclepro.2019.118493>.

[119] B. Lothenbach, G. Le Saout, E. Gallucci, K. Scrivener, Influence of limestone on the hydration of Portland cements, *Cem. Concr. Res.* 38 (2008) 848–860. <https://doi.org/10.1016/j.cemconres.2008.01.002>.

[120] S. Adu-Amankwah, M. Zajac, C. Stabler, B. Lothenbach, L. Black, Influence of limestone on the hydration of ternary slag cements, *Cem. Concr. Res.* 100 (2017) 96–109.

<https://doi.org/10.1016/J.CEMCONRES.2017.05.013>.

[121] E.R. Teixeira, A. Camões, F.G. Branco, J.B. Aguiar, R. Fangueiro, Recycling of biomass and coal fly ash as cement replacement material and its effect on hydration and carbonation of concrete, *Waste Manag.* 94 (2019) 39–48. <https://doi.org/10.1016/j.wasman.2019.05.044>.

[122] J. Balagosa, M.J. Lee, Y.W. Choo, H.S. Kim, J.M. Kim, Experimental Validation of the Cementation Mechanism of Wood Pellet Fly Ash Blended Binder in Weathered Granite Soil, *Materials (Basel).* 16 (2023) 17–19. <https://doi.org/10.3390/ma16196543>.

[123] I. Jawed, J. Skalny, Alkalies in cement: a review: II. Effects of alkalies on hydration and performance of Portland cement, *Cem. Concr. Res.* 8 (1978) 37–51.

[124] W.A. Gutteridge, J.A. Dalziel, Filler cement: The effect of the secondary component on the hydration of Portland cement: Part I. A fine non-hydraulic filler, *Cem. Concr. Res.* 20 (1990) 778–782. [https://doi.org/10.1016/0008-8846\(90\)90011-L](https://doi.org/10.1016/0008-8846(90)90011-L).

[125] X. Ouyang, Filler-hydrates Adhesion Properties in Cement Paste System Development of Sustainable Building Materials, Delft University of Technology, 2017. <https://doi.org/10.4233/uuid:4d613364-6f2e-4a61-be9f-a71a6c05ebdc>.

[126] C. Maschowski, P. Kruspan, A.T. Arif, P. Garra, G. Trouvé, R. Gieré, Use of biomass ash from different sources and processes in cement, *J. Sustain. Cem. Mater.* 9 (2020) 350–370. <https://doi.org/10.1080/21650373.2020.1764877>.

[127] G. Menéndez, V. Bonavetti, E.F. Irassar, Strength development of ternary blended cement with limestone filler and blast-furnace slag, *Cem. Concr. Compos.* 25 (2003) 61–67. [https://doi.org/10.1016/S0958-9465\(01\)00056-7](https://doi.org/10.1016/S0958-9465(01)00056-7).

[128] V. Rahhal, V. Bonavetti, L. Trusilewicz, C. Pedrajas, R. Talero, Role of the filler on Portland cement hydration at early ages, *Constr. Build. Mater.* 27 (2012) 82–90. <https://doi.org/10.1016/j.conbuildmat.2011.07.021>.

[129] C.B. Cheah, W.K. Part, M. Ramli, The long term engineering properties of cementless building block work containing large volume of wood ash and coal fly ash, *Constr. Build. Mater.* 143 (2017) 522–536. <https://doi.org/10.1016/j.conbuildmat.2017.03.162>.

[130] R. Rajamma, Incorporação de cinzas volantes de biomassa em materiais cimentícios Biomass fly ash incorporation in cement based materials, Universidade de Aveiro, 2011. <https://doi.org/10.16194/j.cnki.31-1059/g4.2011.07.016>.

[131] M. Velay-Lizancos, I. Martinez-Lage, M. Azenha, P. Vázquez-Burgo, Influence of temperature in the evolution of compressive strength and in its correlations with UPV in eco-concretes with recycled materials, *Constr. Build. Mater.* 124 (2016) 276–286. <https://doi.org/10.1016/j.conbuildmat.2016.07.104>.

[132] NEN-EN 197-1 Cement - Part 1: Composition, specifications and conformity criteria for common cements, (2018).

[133] R.J. Myers, S.A. Bernal, J.L. Provis, Phase diagrams for alkali-activated slag binders, *Cem. Concr. Res.* 95 (2017) 30–38. <https://doi.org/10.1016/J.CEMCONRES.2017.02.006>.

[134] J.L. Provis, Alkali-activated materials, *Cem. Concr. Res.* 114 (2018) 40–48. <https://doi.org/10.1016/j.cemconres.2017.02.009>.

[135] A. Gharzouni, B. Samet, S. Baklouti, E. Joussein, S. Rossignol, Addition of low reactive clay into metakaolin-based geopolymers formulation: Synthesis, existence domains and properties, *Powder Technol.* (2016). <https://doi.org/10.1016/j.powtec.2015.11.012>.

[136] E. Adesanya, K. Ohenoja, T. Luukkonen, P. Kinnunen, M. Illikainen, One-part geopolymers cement from slag and pretreated paper sludge, *J. Clean. Prod.* 185 (2018) 168–175. <https://doi.org/10.1016/j.jclepro.2018.03.007>.

[137] A. Peys, H. Rahier, Y. Pontikes, Potassium-rich biomass ashes as activators in metakaolin-based inorganic

polymers, *Appl. Clay Sci.* 119 (2016) 401–409. <https://doi.org/10.1016/j.clay.2015.11.003>.

[138] A. De Rossi, L. Simão, M.J. Ribeiro, R.M. Novais, J.A. Labrincha, D. Hotza, R.F.P.M. Moreira, In-situ synthesis of zeolites by geopolymmerization of biomass fly ash and metakaolin, *Mater. Lett.* 236 (2019) 644–648. <https://doi.org/10.1016/j.matlet.2018.11.016>.

[139] M.E. Küçük, T. Kinnarinen, A. Häkkinen, Dissolution kinetics of aluminosilicates from biomass ashes in alkaline solutions, *Ceram. Int.* 47 (2021) 11714–11726. <https://doi.org/10.1016/J.CERAMINT.2021.01.011>.

[140] B. Sun, G. Ye, G. de Schutter, A review: Reaction mechanism and strength of slag and fly ash-based alkali-activated materials, *Constr. Build. Mater.* 326 (2022) 126843. <https://doi.org/10.1016/j.conbuildmat.2022.126843>.

[141] C.J. Zhu, I. Pundienė, J. Pranckevičienė, M. Kligys, A. Korjakinis, L. Vitola, Influence of alkaline activator solution ratio on the properties of biomass fly ash-based alkali-activated materials, *J. Phys. Conf. Ser.* 2423 (2023) 012033. <https://doi.org/10.1088/1742-6596/2423/1/012033>.

[142] L. Pérez-Villarejo, E. Bonet-Martínez, D. Eliche-Quesada, P.J. Sánchez-Soto, J.M. Rincón-López, E. Castro-Galiano, Biomass fly ash and aluminium industry slags-based geopolymers, *Mater. Lett.* 229 (2018) 6–12. <https://doi.org/10.1016/j.matlet.2018.06.100>.

[143] M. Saeli, D.M. Tobaldi, M.P. Seabra, J.A. Labrincha, Mix design and mechanical performance of geopolymeric binders and mortars using biomass fly ash and alkaline effluent from paper-pulp industry, *J. Clean. Prod.* 208 (2019) 1188–1197. <https://doi.org/10.1016/j.jclepro.2018.10.213>.

[144] R.M. Novais, J. Carvalheiras, L. Senff, J.A. Labrincha, Upcycling unexplored dregs and biomass fly ash from the paper and pulp industry in the production of eco-friendly geopolymer mortars: A preliminary assessment, *Constr. Build. Mater.* 184 (2018) 464–472. <https://doi.org/10.1016/j.conbuildmat.2018.07.017>.

[145] S.S. Narani, S. Siddiqua, P. Perumal, Wood fly ash and blast furnace slag management by alkali-activation: Trace elements solidification and composite application, *J. Environ. Manage.* 354 (2024) 120341. <https://doi.org/10.1016/j.jenvman.2024.120341>.

[146] S. Jurado-Contreras, E. Bonet-Martínez, P.J. Sánchez-Soto, O. Gencel, D. Eliche-Quesada, Synthesis and characterization of alkali-activated materials containing biomass fly ash and metakaolin: effect of the soluble salt content of the residue, *Arch. Civ. Mech. Eng.* 22 (2022) 1–21. <https://doi.org/10.1007/s43452-022-00444-2>.

[147] O.A. Abdulkareem, M. Ramli, J.C. Matthews, Production of geopolymer mortar system containing high calcium biomass wood ash as a partial substitution to fly ash: An early age evaluation, *Compos. Part B Eng.* 174 (2019). <https://doi.org/10.1016/j.compositesb.2019.106941>.

[148] C.C. Ban, P.W. Ken, M. Ramli, The hybridizations of coal fly ash and wood ash for the fabrication of low alkalinity geopolymer load bearing block cured at ambient temperature, *Constr. Build. Mater.* 88 (2015) 41–55. <https://doi.org/10.1016/j.conbuildmat.2015.04.020>.

[149] T.H. Silva, L.F.S. Lara, G.J.B. Silva, J.L. Provis, A.C.S. Bezerra, Alkali-activated materials produced using high-calcium, high-carbon biomass ash, *Cem. Concr. Compos.* 132 (2022) 104646. <https://doi.org/10.1016/j.cemconcomp.2022.104646>.

[150] A. Mobili, F. Tittarelli, H. Rahier, One-part alkali-activated pastes and mortars prepared with metakaolin and biomass ash, *Appl. Sci.* 10 (2020). <https://doi.org/10.3390/app10165610>.

[151] T. Luukkonen, Z. Abdollahnejad, J. Yliniemi, P. Kinnunen, M. Illikainen, One-part alkali-activated materials: A review, *Cem. Concr. Res.* 103 (2018) 21–34. <https://doi.org/10.1016/J.CEMCONRES.2017.10.001>.

[152] C. Ouellet-Plamondon, G. Habert, Life cycle assessment (LCA) of alkali-activated cements and concretes, in: *Handb. Alkali-Activated Cem. Mortars Concr.*, Elsevier, 2015: pp. 663–686. <https://doi.org/10.1533/9781782422884.5.663>.

[153] S. V. Vassilev, D. Baxter, L.K. Andersen, C.G. Vassileva, T.J. Morgan, An overview of the organic and inorganic phase composition of biomass, *Fuel.* 94 (2012) 1–33. <https://doi.org/10.1016/j.fuel.2011.09.030>.

[154] J. Zhai, I.T. Burke, W.M. Mayes, D.I. Stewart, New insights into biomass combustion ash categorisation: A phylogenetic analysis, *Fuel.* 287 (2021) 119469. <https://doi.org/10.1016/j.fuel.2020.119469>.

[155] C.B. Cheah, M. Ramli, Mechanical strength, durability and drying shrinkage of structural mortar containing HCWA as partial replacement of cement, *Constr. Build. Mater.* 30 (2012) 320–329. <https://doi.org/10.1016/j.conbuildmat.2011.12.009>.

[156] NEN-EN 12880 Characterization of sludges - Determination of dry residue and water content, 12880 (2023).

[157] D. Min, H. Dongwen, L. Xianghui, T. Mingshu, Mechanism of expansion in hardened cement pastes with hard-burnt lime, *Cem. Concr. Res.* 26 (1996) 647–648. [https://doi.org/10.1016/0008-8846\(96\)00021-X](https://doi.org/10.1016/0008-8846(96)00021-X).

[158] EN 451-1, Method of testing fly ash - Part 1: Determination of free calcium oxide content, 1 (2017).

[159] X. Tian, F. Rao, C.A. León-Patiño, S. Song, Effects of aluminum on the expansion and microstructure of alkali-activated MSWI fly ash-based pastes, *Chemosphere.* 240 (2020) 124986. <https://doi.org/10.1016/J.CHEMOSPHERE.2019.124986>.

[160] P. Segui, J.E. Aubert, B. Husson, M. Measson, Characterization of wastepaper sludge ash for its valorization as a component of hydraulic binders, *Appl. Clay Sci.* 57 (2012) 79–85. <https://doi.org/10.1016/J.CLAY.2012.01.007>.

[161] E.H. Oelkers, S.R. Gislason, The mechanism, rates and consequences of basaltic glass dissolution: I. An experimental study of the dissolution rates of basaltic glass as a function of aqueous Al, Si and oxalic acid concentration at 25°C and pH = 3 and 11, *Geochim. Cosmochim. Acta.* 65 (2001) 3671–3681. [https://doi.org/10.1016/S0016-7037\(01\)00664-0](https://doi.org/10.1016/S0016-7037(01)00664-0).

[162] C. Kuenzel, N. Ranjbar, Dissolution mechanism of fly ash to quantify the reactive aluminosilicates in geopolymers, *Resour. Conserv. Recycl.* 150 (2019) 104421. <https://doi.org/10.1016/J.RESCONREC.2019.104421>.

[163] K.C. Newlands, M. Foss, T. Matschei, J. Skibsted, D.E. Macphee, Early stage dissolution characteristics of aluminosilicate glasses with blast furnace slag- and fly-ash-like compositions, *J. Am. Ceram. Soc.* 100 (2017) 1941–1955. <https://doi.org/10.1111/JACE.14716>.

[164] A. Mikuni, A.E. Ryuichi, K. Ae, K. Ikeda, Dissolution properties of some fly ash fillers applying to geopolymers in alkali solution, (n.d.). <https://doi.org/10.1007/s10853-006-0530-9>.

[165] D. Xuan, C.S. Poon, Removal of metallic Al and Al/Zn alloys in MSWI bottom ash by alkaline treatment, *J. Hazard. Mater.* 344 (2018) 73–80. <https://doi.org/10.1016/j.jhazmat.2017.10.002>.

[166] N. Doebelin, R. Kleeberg, Profex: A graphical user interface for the Rietveld refinement program BGMIN, *J. Appl. Crystallogr.* 48 (2015) 1573–1580. <https://doi.org/10.1107/S1600576715014685>.

[167] K. De Weerdt, H. Justnes, The effect of sea water on the phase assemblage of hydrated cement paste, *Cem. Concr. Compos.* 55 (2015) 215–222. <https://doi.org/10.1016/j.cemconcomp.2014.09.006>.

[168] F.A. Andersen, L. Brečević, G. Beuter, D.B. Dell'Amico, F. Calderazzo, N.J. Bjerrum, A.E. Underhill, Infrared Spectra of Amorphous and Crystalline Calcium Carbonate., *Acta Chem. Scand.* 45 (1991) 1018–1024. <https://doi.org/10.3891/acta.chem.scand.45-1018>.

[169] E.R. McCaslin, C.E. White, A parametric study of accelerated carbonation in alkali-activated slag, *Cem. Concr. Res.* 145 (2021) 106454. <https://doi.org/10.1016/j.cemconres.2021.106454>.

[170] M.D. Lane, Mid-infrared emission spectroscopy of sulfate and sulfate-bearing minerals, *Am. Mineral.* 92 (2007) 1–18. <https://doi.org/10.2138/am.2007.2170>.

[171] J.T. Kloprogge, R.D. Schuiling, Z. Ding, L. Hickey, D. Wharton, R.L. Frost, Vibrational spectroscopic study of syngenite formed during the treatment of liquid manure with sulphuric acid, *Vib. Spectrosc.* 28 (2002)

209–221. [https://doi.org/10.1016/S0924-2031\(01\)00139-4](https://doi.org/10.1016/S0924-2031(01)00139-4).

[172] W.R. Taylor, Application of infrared spectroscopy to studies of silicate glass structure: Examples from the melilite glasses and the systems Na₂O-SiO₂ and Na₂O-Al₂O₃-SiO₂, *J. Earth Syst. Sci.* 99 (1990) 99–117. <https://doi.org/10.1007/BF02871899>.

[173] Z. Zhang, H. Wang, J.L. Provis, Quantitative study of the reactivity of fly ash in geopolymers by ftir, *J. Sustain. Cem. Mater.* 1 (2012) 154–166. <https://doi.org/10.1080/21650373.2012.752620>.

[174] S. Zhang, A. Keulen, K. Arbi, G. Ye, Waste glass as partial mineral precursor in alkali-activated slag/fly ash system, *Cem. Concr. Res.* 102 (2017) 29–40. <https://doi.org/10.1016/j.cemconres.2017.08.012>.

[175] M.Y.A. Mollah, W. Yu, R. Schennach, D.L. Cocke, A Fourier transform infrared spectroscopic investigation of the early hydration of Portland cement and the influence of sodium lignosulfonate, *Cem. Concr. Res.* 30 (2000) 267–273. [https://doi.org/10.1016/S0008-8846\(99\)00243-4](https://doi.org/10.1016/S0008-8846(99)00243-4).

[176] X. Wang, W. Ni, R. Jin, B. Liu, Formation of Friedel's salt using steel slag and potash mine brine water, *Constr. Build. Mater.* 220 (2019) 119–127. <https://doi.org/10.1016/j.conbuildmat.2019.05.195>.

[177] A. Jose, M.R. Nivitha, J.M. Krishnan, R.G. Robinson, Characterization of cement stabilized pond ash using FTIR spectroscopy, *Constr. Build. Mater.* 263 (2020) 120136. <https://doi.org/10.1016/J.CONBUILDMAT.2020.120136>.

[178] S. Kumar, R. Kumar, Mechanical activation of fly ash: Effect on reaction, structure and properties of resulting geopolymer, *Ceram. Int.* 37 (2011) 533–541. <https://doi.org/10.1016/j.ceramint.2010.09.038>.

[179] S. V. Dimitrova, D.R. Mehanjiev, Interaction of blast-furnace slag with heavy metal ions in water solutions, *Water Res.* 34 (2000) 1957–1961. [https://doi.org/10.1016/S0043-1354\(99\)00328-0](https://doi.org/10.1016/S0043-1354(99)00328-0).

[180] K.C. Reddy, K.V.L. Subramaniam, Blast Furnace Slag Hydration in an Alkaline Medium: Influence of Sodium Content and Sodium Hydroxide Molarity, *J. Mater. Civ. Eng.* 32 (2020) 04020371. [https://doi.org/10.1061/\(asce\)mt.1943-5533.0003455](https://doi.org/10.1061/(asce)mt.1943-5533.0003455).

[181] H. Uvegi, P. Chaunsali, B. Traynor, E. Olivetti, Reactivity of industrial wastes as measured through ICP-OES: A case study on siliceous Indian biomass ash, *J. Am. Ceram. Soc.* 102 (2019) 7678–7688. <https://doi.org/10.1111/JACE.16628>.

[182] K. Ohenoja, P. Tanskanen, V. Wigren, P. Kinnunen, M. Körkkö, O. Peltosaari, J. Österbacka, M. Illikainen, Self-hardening of fly ashes from a bubbling fluidized bed combustion of peat, forest industry residuals, and wastes, *Fuel*. 165 (2016) 440–446. <https://doi.org/10.1016/j.fuel.2015.10.093>.

[183] M. Illikainen, P. Tanskanen, P. Kinnunen, M. Körkkö, O. Peltosaari, V. Wigren, J. Österbacka, B. Talling, J. Niinimäki, Reactivity and self-hardening of fly ash from the fluidized bed combustion of wood and peat, *Fuel*. 135 (2014) 69–75. <https://doi.org/10.1016/j.fuel.2014.06.029>.

[184] I. Garcia-Lodeiro, A. Palomo, A. Fernández-Jiménez, D.E. MacPhee, Compatibility studies between N-A-S-H and C-A-S-H gels. Study in the ternary diagram Na₂O-CaO-Al₂O₃-SiO₂-H₂O, *Cem. Concr. Res.* 41 (2011) 923–931. <https://doi.org/10.1016/j.cemconres.2011.05.006>.

[185] I. García-Lodeiro, A. Fernández-Jiménez, A. Palomo, D.E. MacPhee, Effect of calcium additions on N-A-S-H cementitious gels, *J. Am. Ceram. Soc.* 93 (2010) 1934–1940. <https://doi.org/10.1111/j.1551-2916.2010.03668.x>.

[186] R.V.R. San Nicolas, B. Walkley, J.S.J. van Deventer, Fly ash-based geopolymers chemistry and behavior, in: *Coal Combust. Prod.*, Elsevier, 2017: pp. 185–214. <https://doi.org/10.1016/B978-0-08-100945-1.00007-1>.

[187] R. Xiao, X. Jiang, M. Zhang, P. Polaczyk, B. Huang, Analytical investigation of phase assemblages of alkali-activated materials in CaO-SiO₂-Al₂O₃ systems: The management of reaction products and designing of precursors, *Mater. Des.* 194 (2020) 108975. <https://doi.org/10.1016/j.matdes.2020.108975>.

[188] Ministry of Infrastructure and Water Management Netherland, *Soil Quality Regulation*, (2006) 1-170. <https://www.government.nl/ministries/ministry-of-infrastructure-and-water-management>.

[189] R.S. Barneyback, S. Diamond, Expression and analysis of pore fluids from hardened cement pastes and mortars, *Cem. Concr. Res.* 11 (1981) 279–285. [https://doi.org/10.1016/0008-8846\(81\)90069-7](https://doi.org/10.1016/0008-8846(81)90069-7).

[190] C. Dehghanian, M. Arjmandi, Influence of slag blended cement concrete on chloride diffusion rate, *Cem. Concr. Res.* 27 (1997) 937–945. [https://doi.org/10.1016/S0008-8846\(97\)00064-1](https://doi.org/10.1016/S0008-8846(97)00064-1).

[191] P.S. Mangat, J.M. Khatib, B.T. Molloy, Microstructure, chloride diffusion and reinforcement corrosion in blended cement paste and concrete, *Cem. Concr. Compos.* 16 (1994) 73–81. [https://doi.org/10.1016/0958-9465\(94\)90002-7](https://doi.org/10.1016/0958-9465(94)90002-7).

[192] R. Snellings, J. Chwast, Ö. Cizer, N. De Belie, Y. Dhandapani, P. Durdzinski, J. Elsen, J. Haufe, D. Hooton, C. Patapy, M. Santhanam, K. Scrivener, D. Snoeck, L. Steger, S. Tongbo, A. Vollpracht, F. Winnefeld, B. Lothenbach, RILEM TC-238 SCM recommendation on hydration stoppage by solvent exchange for the study of hydrate assemblages, *Mater. Struct. Constr.* 51 (2018). <https://doi.org/10.1617/s11527-018-1298-5>.

[193] E.W. Washburn, Note on a Method of Determining the Distribution of Pore Sizes in a Porous Material, *Proc. Natl. Acad. Sci.* 7 (1921) 115–116. <https://doi.org/10.1073/pnas.7.4.115>.

[194] H.S. Wong, M.K. Head, N.R. Buenfeld, Pore segmentation of cement-based materials from backscattered electron images, *Cem. Concr. Res.* 36 (2006) 1083–1090. <https://doi.org/10.1016/j.cemconres.2005.10.006>.

[195] K. Scrivener, R. Snellings, B. Lothenbach, *A Practical Guide to Microstructural Analysis of Cementitious Materials*, CRC Press, 2018. <https://doi.org/10.1201/b19074>.

[196] J.S. Lumley, R.S. Gollop, G.K. Moir, H.F.W. Taylor, Degrees of reaction of the slag in some blends with Portland cements, *Cem. Concr. Res.* 26 (1996) 139–151. [https://doi.org/10.1016/0008-8846\(95\)00190-5](https://doi.org/10.1016/0008-8846(95)00190-5).

[197] J.I. Escalante-Garcia, J.H. Sharp, The chemical composition and microstructure of hydration products in blended cements, *Cem. Concr. Compos.* 26 (2004) 967–976. <https://doi.org/10.1016/j.cemconcomp.2004.02.036>.

[198] Y. Zhang, O. Çopuroğlu, Role of the grain size on the hydration characteristics of slag in an aged field concrete, *Cem. Concr. Res.* 162 (2022). <https://doi.org/10.1016/j.cemconres.2022.106985>.

[199] V. Kocaba, E. Gallucci, K.L. Scrivener, Methods for determination of degree of reaction of slag in blended cement pastes, *Cem. Concr. Res.* 42 (2012) 511–525. <https://doi.org/10.1016/j.cemconres.2011.11.010>.

[200] G. Ye, *Experimental Study and Numerical Simulation of the Development of the Microstructure and Permeability of Cementitious Materials*, 2003.

[201] Z. Li, T. Lu, X. Liang, H. Dong, J. Granja, M. Azenha, G. Ye, Mechanisms of autogenous shrinkage of alkali-activated slag and fly ash pastes, *Cem. Concr. Res.* 135 (2020). <https://doi.org/10.1016/j.cemconres.2020.106107>.

[202] M. Chabannes, H. Kazemi-kamyab, J. Trigallez, R. Snellings, Performance and microstructure development of lime – calcined fluvial sediment binders under different curing conditions, *Cem. Concr. Res.* 160 (2022) 106903. <https://doi.org/10.1016/j.cemconres.2022.106903>.

[203] A. Schöler, B. Lothenbach, F. Winnefeld, M. Ben Haha, M. Zajac, H.M. Ludwig, Early hydration of SCM-blended Portland cements: A pore solution and isothermal calorimetry study, *Cem. Concr. Res.* 93 (2017) 71–82. <https://doi.org/10.1016/J.CEMCONRES.2016.11.013>.

[204] S. Adu-Amankwah, L. Black, J. Skocek, M. Ben Haha, M. Zajac, Effect of sulfate additions on hydration and performance of ternary slag-limestone composite cements, *Constr. Build. Mater.* 164 (2018) 451–462. <https://doi.org/10.1016/j.conbuildmat.2017.12.165>.

[205] D. Jansen, F. Goetz-Neunhoeffer, C. Stabler, J. Neubauer, A remastered external standard method applied to the quantification of early OPC hydration, *Cem. Concr. Res.* 41 (2011) 602–608. <https://doi.org/10.1016/j.cemconres.2011.03.004>.

[206] H. Nguyen, P. Kinnunen, K. Gijbels, V. Carvelli, H. Sreenivasan, A.M. Kantola, V.V. Telkki, W. Schroevers,

M. Illikainen, Ettringite-based binder from ladle slag and gypsum – The effect of citric acid on fresh and hardened state properties, *Cem. Concr. Res.* 123 (2019) 105800. <https://doi.org/10.1016/j.cemconres.2019.105800>.

[207] T. Wagner, D.A. Kulik, F.F. Hingerl, S. V Dmytrieva, GEM-SELEKTOR GEOCHEMICAL MODELING PACKAGE: TSolMod LIBRARY AND DATA INTERFACE FOR MULTICOMPONENT PHASE MODELS, *Can. Mineral.* 50 (2012) 1173–1195. <https://doi.org/10.3749/canmin.50.5.1173>.

[208] D.A. Kulik, T. Wagner, S. V. Dmytrieva, G. Kosakowski, F.F. Hingerl, K. V. Chudnenko, U.R. Berner, GEM-Selektor geochemical modeling package: Revised algorithm and GEMS3K numerical kernel for coupled simulation codes, *Comput. Geosci.* 17 (2013) 1–24. <https://doi.org/10.1007/s10596-012-9310-6>.

[209] B. Lothenbach, D.A. Kulik, T. Matschei, M. Balonis, L. Baquerizo, B. Dilnese, G.D. Miron, R.J. Myers, Cemdata18: A chemical thermodynamic database for hydrated Portland cements and alkali-activated materials, *Cem. Concr. Res.* 115 (2019) 472–506. <https://doi.org/10.1016/j.cemconres.2018.04.018>.

[210] B. Lothenbach, Thermodynamic equilibrium calculations in cementitious systems, *Mater. Struct.* 43 (2010) 1413–1433. <https://doi.org/10.1617/s11527-010-9592-x>.

[211] D. Rothstein, J.J. Thomas, B.J. Christensen, H.M. Jennings, Solubility behavior of Ca-, S-, Al-, and Si-bearing solid phases in Portland cement pore solutions as a function of hydration time, *Cem. Concr. Res.* 32 (2002) 1663–1671. [https://doi.org/10.1016/S0008-8846\(02\)00855-4](https://doi.org/10.1016/S0008-8846(02)00855-4).

[212] X. Li, J. Bizzozero, C. Hesse, Impact of C-S-H seeding on hydration and strength of slag blended cement, *Cem. Concr. Res.* 161 (2022) 106935. <https://doi.org/10.1016/j.cemconres.2022.106935>.

[213] Z. Shi, M.R. Geiker, B. Lothenbach, K. De Weerdt, S.F. Garzón, K. Enemark-Rasmussen, J. Skibsted, Friedel's salt profiles from thermogravimetric analysis and thermodynamic modelling of Portland cement-based mortars exposed to sodium chloride solution, *Cem. Concr. Compos.* 78 (2017) 73–83. <https://doi.org/10.1016/j.cemconcomp.2017.01.002>.

[214] M. Balonis, B. Lothenbach, G. Le Saout, F.P. Glasser, Impact of chloride on the mineralogy of hydrated Portland cement systems, *Cem. Concr. Res.* 40 (2010) 1009–1022. <https://doi.org/10.1016/j.cemconres.2010.03.002>.

[215] S.-D. Wang, K.L. Scrivener, Hydration products of alkali activated slag cement, *Cem. Concr. Res.* 25 (1995) 561–571. [https://doi.org/10.1016/0008-8846\(95\)00045-E](https://doi.org/10.1016/0008-8846(95)00045-E).

[216] P. Yu, R.J. Kirkpatrick, B. Poe, P.F. McMillan, X. Cong, Structure of Calcium Silicate Hydrate (C-S-H): Near-, Mid-, and Far-Infrared Spectroscopy, *J. Am. Ceram. Soc.* 48 (1999) 742–748.

[217] I. García-Lodeiro, A. Fernández-Jiménez, M.T. Blanco, A. Palomo, FTIR study of the sol-gel synthesis of cementitious gels: C-S-H and N-A-S-H, *J. Sol-Gel Sci. Technol.* 45 (2008) 63–72. <https://doi.org/10.1007/s10971-007-1643-6>.

[218] E. Scholtzová, L. Kucková, J. Kožíšek, D. Tunega, Structural and spectroscopic characterization of ettringite mineral –combined DFT and experimental study, *J. Mol. Struct.* 1100 (2015) 215–224. <https://doi.org/10.1016/J.MOLSTRUC.2015.06.075>.

[219] Fernández, J.L. García Calvo, M.C. Alonso, Ordinary Portland Cement composition for the optimization of the synergies of supplementary cementitious materials of ternary binders in hydration processes, *Cem. Concr. Compos.* 89 (2018) 238–250. <https://doi.org/10.1016/J.CEMCONCOMP.2017.12.016>.

[220] B. Lothenbach, E. Wieland, A thermodynamic approach to the hydration of sulphate-resisting Portland cement, *Waste Manag.* 26 (2006) 706–719. <https://doi.org/10.1016/j.wasman.2006.01.023>.

[221] Z.-L. Jiang, Y.-J. Pan, J.-F. Lu, Y. Wang, Pore Structure Characterization of Cement-Based Materials by Different Experimental Methods and its Influence on Permeability Evaluation, *Cem. Concr. Res.* 159 (2022) 106892. <https://doi.org/10.2139/ssrn.4019251>.

[222] P. Kumar Mehta, Paulo J. M. Monteiro, CONCRETE Microstructure, Properties and Materials, 2016.

[223] D.A. Silva, V.M. John, J.L.D. Ribeiro, H.R. Roman, Pore size distribution of hydrated cement pastes

modified with polymers, *Cem. Concr. Res.* 31 (2001) 1177–1184. [https://doi.org/10.1016/S0008-8846\(01\)00549-X](https://doi.org/10.1016/S0008-8846(01)00549-X).

[224] S. Igarashi, M. Kawamura, A. Watanabe, Analysis of cement pastes and mortars by a combination of backscatter-based SEM image analysis and calculations based on the Powers model, *Cem. Concr. Compos.* 26 (2004) 977–985. <https://doi.org/10.1016/j.cemconcomp.2004.02.031>.

[225] M.H.N. Yio, J.C. Phelan, H.S. Wong, N.R. Buenfeld, Determining the slag fraction, water/binder ratio and degree of hydration in hardened cement pastes, *Cem. Concr. Res.* 56 (2014) 171–181. <https://doi.org/10.1016/j.cemconres.2013.12.002>.

[226] F. Georget, W. Wilson, K.L. Scrivener, edxia: Microstructure characterisation from quantified SEM-EDS hypermaps, *Cem. Concr. Res.* 141 (2021) 106327. <https://doi.org/10.1016/j.cemconres.2020.106327>.

[227] M. Nedeljković, Z. Li, G. Ye, Setting, strength, and autogenous shrinkage of alkali-activated fly ash and slag pastes: Effect of slag content, *Materials (Basel)* 11 (2018). <https://doi.org/10.3390/ma11112121>.

[228] X. Hu, C. Shi, Z. Shi, L. Zhang, Compressive strength, pore structure and chloride transport properties of alkali-activated slag/fly ash mortars, *Cem. Concr. Compos.* (2019). <https://doi.org/10.1016/j.cemconcomp.2019.103392>.

[229] O. Burciaga-Díaz, Parameters affecting the properties and microstructure of quicklime (CaO) - Activated slag cement pastes, *Cem. Concr. Compos.* 103 (2019) 104–111. <https://doi.org/10.1016/J.CEMCONCOMP.2019.05.002>.

[230] B. Yuan, Q.L. Yu, H.J.H. Brouwers, Evaluation of slag characteristics on the reaction kinetics and mechanical properties of Na₂CO₃ activated slag, *Constr. Build. Mater.* 131 (2017) 334–346. <https://doi.org/10.1016/j.conbuildmat.2016.11.074>.

[231] K. Scrivener, A. Ouzia, P. Juillard, A. Kunhi Mohamed, Advances in understanding cement hydration mechanisms, *Cem. Concr. Res.* 124 (2019) 105823. <https://doi.org/10.1016/j.cemconres.2019.105823>.

[232] F. Delage, D. Ghaleb, J.L. Dussossoy, O. Chevallier, E. Vernaz, A mechanistic model for understanding nuclear waste glass dissolution, *J. Nucl. Mater.* 190 (1992) 191–197. [https://doi.org/10.1016/0022-3115\(92\)90086-Z](https://doi.org/10.1016/0022-3115(92)90086-Z).

[233] A. Schindler, K. Folliard, Heat of Hydration Models for Cementitious Materials, *ACI Mater. J.* 102 (2005) 77–90. <https://doi.org/10.14359/14246>.

[234] Y. Zuo, M. Nedeljković, G. Ye, Coupled thermodynamic modelling and experimental study of sodium hydroxide activated slag, *Constr. Build. Mater.* 188 (2018) 262–279. <https://doi.org/10.1016/j.conbuildmat.2018.08.087>.

[235] Y. Sun, Z.H. Wang, D.J. Park, Y.K. Chen, H.S. Kim, W.S. Kim, H.S. Lee, Mathematical determination of the maximum heat release for fly ash cement paste: Effect of heat flow monitoring time, calculation approach and fly ash content, *Thermochim. Acta.* 726 (2023) 179553. <https://doi.org/10.1016/j.tca.2023.179553>.

[236] S. Chithiraputhiran, N. Neithalath, Isothermal reaction kinetics and temperature dependence of alkali activation of slag, fly ash and their blends, *Constr. Build. Mater.* 45 (2013) 233–242. <https://doi.org/10.1016/j.conbuildmat.2013.03.061>.

[237] L. Steger, S. Blotevogel, L. Frouin, C. Patapy, M. Cyr, Experimental evidence for the acceleration of slag hydration in blended cements by the addition of CaCl₂, *Cem. Concr. Res.* 149 (2021) 2–10. <https://doi.org/10.1016/j.cemconres.2021.106558>.

[238] V. Kocaba, Development and evaluation of methods to follow microstructural development of cementitious systems including slags, 2009. <https://doi.org/https://doi.org/10.5075/epfl-thesis-4523>.

[239] E. John, B. Lothenbach, Cement hydration mechanisms through time – a review, *J. Mater. Sci.* 58 (2023) 9805–9833. <https://doi.org/10.1007/s10853-023-08651-9>.

[240] F. Zunino, K. Scrivener, The influence of sulfate addition on hydration kinetics and C-S-H morphology of C₃S and C₃S/C₃A systems, *Cem. Concr. Res.* 160 (2022) 106930.

[https://doi.org/10.1016/j.cemconres.2022.106930.](https://doi.org/10.1016/j.cemconres.2022.106930)

[241] F. Zunino, K. Scrivener, Factors influencing the sulfate balance in pure phase C3S/C3A systems, *Cem. Concr. Res.* 133 (2020) 106085. <https://doi.org/10.1016/j.cemconres.2020.106085>.

[242] F. Zunino, K. Scrivener, Insights on the role of alumina content and the filler effect on the sulfate requirement of PC and blended cements, *Cem. Concr. Res.* 160 (2022) 106929. <https://doi.org/10.1016/j.cemconres.2022.106929>.

[243] E. Berodier, Impact of the Supplementary Cementitious Materials on the kinetics and microstructural development of cement hydration, PhD Thesis. 6417 (2015) 154. <https://doi.org/https://doi.org/10.5075/epfl-thesis-6417>.

[244] Y. Zhang, Z. Wan, L.M. de Lima Junior, O. Çopuroğlu, Early age hydration of model slag cement: Interaction among C3S, gypsum and slag with different Al₂O₃ contents, *Cem. Concr. Res.* 161 (2022). <https://doi.org/10.1016/j.cemconres.2022.106954>.

[245] J. da S. Andrade Neto, A.G. De la Torre, A.P. Kirchheim, Effects of sulfates on the hydration of Portland cement – A review, *Constr. Build. Mater.* 279 (2021) 122428. <https://doi.org/10.1016/j.conbuildmat.2021.122428>.

[246] A. Vollpracht, B. Lothenbach, R. Snellings, J. Haufe, The pore solution of blended cements: a review, *Mater. Struct. Constr.* 49 (2016) 3341–3367. <https://doi.org/10.1617/s11527-015-0724-1>.

[247] J. Fu, A.M. Jones, M.W. Bligh, C. Holt, L.M. Keyte, F. Moghaddam, S.J. Foster, T.D. Waite, Mechanisms of enhancement in early hydration by sodium sulfate in a slag-cement blend – Insights from pore solution chemistry, *Cem. Concr. Res.* 135 (2020). <https://doi.org/10.1016/J.CEMCONRES.2020.106110>.

[248] R. Taylor, I.G. Richardson, R.M.D. Brydson, Composition and microstructure of 20-year-old ordinary Portland cement–ground granulated blast-furnace slag blends containing 0 to 100% slag, *Cem. Concr. Res.* 40 (2010) 971–983. <https://doi.org/10.1016/j.cemconres.2010.02.012>.

[249] X. Zhu, I.G. Richardson, Morphology-structural change of C-A-S-H gel in blended cements, *Cem. Concr. Res.* 168 (2023) 107156. <https://doi.org/10.1016/j.cemconres.2023.107156>.

[250] P. Li, W. Li, Z. Sun, L. Shen, D. Sheng, Development of sustainable concrete incorporating seawater: A critical review on cement hydration, microstructure and mechanical strength, *Cem. Concr. Compos.* 121 (2021) 104100. <https://doi.org/10.1016/j.cemconcomp.2021.104100>.

[251] J. Wang, Y. Xie, X. Zhong, L. Li, Test and simulation of cement hydration degree for shotcrete with alkaline and alkali-free accelerators, *Cem. Concr. Compos.* 112 (2020) 103684. <https://doi.org/10.1016/j.cemconcomp.2020.103684>.

[252] L. Huang, P. Yan, Effect of alkali content in cement on its hydration kinetics and mechanical properties, *Constr. Build. Mater.* 228 (2019) 116833. <https://doi.org/10.1016/j.conbuildmat.2019.116833>.

[253] M. Horgnies, J.J. Chen, C. Bouillon, Overview about the use of fourier transform infrared spectroscopy to study cementitious materials, *WIT Trans. Eng. Sci.* 77 (2013) 251–262. <https://doi.org/10.2495/MC130221>.

[254] A. Mendes, W.P. Gates, J.G. Sanjayan, F. Collins, NMR, XRD, IR and synchrotron NEXAFS spectroscopic studies of OPC and OPC/slag cement paste hydrates, *Mater. Struct. Constr.* 44 (2011) 1773–1791. <https://doi.org/10.1617/s11527-011-9737-6>.

[255] G. Möschner, B. Lothenbach, F. Winnefeld, A. Ulrich, R. Figi, R. Kretzschmar, Solid solution between Al- ettringite and Fe- ettringite (Ca₆[Al₁ - xFe_x(OH)₆]₂(SO₄)₃·26H₂O), *Cem. Concr. Res.* 39 (2009) 482–489. <https://doi.org/10.1016/j.cemconres.2009.03.001>.

[256] E. L'Hôpital, B. Lothenbach, K. Scrivener, D.A. Kulik, Alkali uptake in calcium alumina silicate hydrate (C-A-S-H), *Cem. Concr. Res.* 85 (2016) 122–136. <https://doi.org/10.1016/j.cemconres.2016.03.009>.

[257] J. Li, W. Zhang, P.J.M. Monteiro, Structure and Intrinsic Mechanical Properties of Nanocrystalline Calcium Silicate Hydrate, *ACS Sustain. Chem. Eng.* 8 (2020) 12453–12461.

<https://doi.org/10.1021/acssuschemeng.0c03230>.

[258] J. Wang, C. Gao, J. Tang, Z. Hu, J. Liu, The multi-scale mechanical properties of calcium-silicate-hydrate, *Cem. Concr. Compos.* 140 (2023) 105097. <https://doi.org/10.1016/j.cemconcomp.2023.105097>.

[259] M.J. Abdolhosseini Qomi, K.J. Krakowiak, M. Bauchy, K.L. Stewart, R. Shahsavari, D. Jagannathan, D.B. Brommer, A. Baronnet, M.J. Buehler, S. Yip, F.J. Ulm, K.J. Van Vliet, R.J.M. Pellenq, Combinatorial molecular optimization of cement hydrates, *Nat. Commun.* 5 (2014) 1–10. <https://doi.org/10.1038/ncomms5960>.

[260] R. Shahsavari, M.J. Buehler, R.J.M. Pellenq, F.-J. Ulm, First-Principles Study of Elastic Constants and Interlayer Interactions of Complex Hydrated Oxides: Case Study of Tobermorite and Jennite, *J. Am. Ceram. Soc.* 92 (2009) 2323–2330. <https://doi.org/10.1111/j.1551-2916.2009.03199.x>.

[261] L.E. Copeland, D.L. Kantro, G.J. Verbeck, Chemistry of hydration of Portland cement, *Citeseer*, 1960.

[262] V.T. Ngala, C.L. Page, EFFECTS OF CARBONATION ON PORE STRUCTURE AND DIFFUSIONAL PROPERTIES OF HYDRATED CEMENT PASTES, *Cem. Concr. Res.* 27 (1997) 995–1007. [https://doi.org/10.1016/S0008-8846\(97\)00102-6](https://doi.org/10.1016/S0008-8846(97)00102-6).

[263] B. Šavija, M. Luković, Carbonation of cement paste: Understanding, challenges, and opportunities, *Constr. Build. Mater.* 117 (2016) 285–301. <https://doi.org/10.1016/j.conbuildmat.2016.04.138>.

[264] S.A. Bernal, R.M. de Gutierrez, J.L. Provis, V. Rose, Effect of silicate modulus and metakaolin incorporation on the carbonation of alkali silicate-activated slags, *Cem. Concr. Res.* 40 (2010) 898–907. <https://doi.org/10.1016/j.cemconres.2010.02.003>.

[265] C. Ying, L. Peng, Y. Zhiwu, L. Siyang, H. Cheng, L. Dapeng, Research on the performance evolution of concrete under the coupling effects of sulfate attack and carbonation, *J. Mater. Res. Technol.* 26 (2023) 4670–4695. <https://doi.org/10.1016/j.jmrt.2023.08.206>.

[266] H. Justnes, J. Skocek, T.A. Østnor, C.J. Engelsen, O. Skjølvold, Microstructural changes of hydrated cement blended with fly ash upon carbonation, *Cem. Concr. Res.* 137 (2020) 106192. <https://doi.org/10.1016/j.cemconres.2020.106192>.

[267] M. Nedeljković, B. Ghiassi, S. Melzer, C. Kooij, S. van der Laan, G. Ye, CO₂ binding capacity of alkali-activated fly ash and slag pastes, *Ceram. Int.* 44 (2018) 19646–19660. <https://doi.org/10.1016/j.ceramint.2018.07.216>.

[268] C.L. Page, K. W. J. Treadaway, Aspects of electrochemistry of steel in concrete, *Nature*. 5862 (1982) 109–115.

[269] S. von Greve-Dierfeld, B. Lothenbach, A. Vollpracht, B. Wu, B. Huet, C. Andrade, C. Medina, C. Thiel, E. Gruyaert, H. Vanoutrive, I.F. Saéz del Bosque, I. Ignjatovic, J. Elsen, J.L. Provis, K. Scrivener, K.C. Thienel, K. Sideris, M. Zajac, N. Alderete, Ö. Cizer, P. Van den Heede, R.D. Hooton, S. Kamali-Bernard, S.A. Bernal, Z. Zhao, Z. Shi, N. De Belie, Understanding the carbonation of concrete with supplementary cementitious materials: a critical review by RILEM TC 281-CCC, 2020. <https://doi.org/10.1617/s11527-020-01558-w>.

[270] Z. Liu, P. Van den Heede, C. Zhang, X. Shi, L. Wang, J. Li, Y. Yao, B. Lothenbach, N. De Belie, Carbonation of blast furnace slag concrete at different CO₂ concentrations: Carbonation rate, phase assemblage, microstructure and thermodynamic modelling, *Cem. Concr. Res.* 169 (2023) 107161. <https://doi.org/10.1016/j.cemconres.2023.107161>.

[271] G.J.G. Gluth, X. Ke, A. Vollpracht, L. Weiler, S.A. Bernal, M. Cyr, K. Dombrowski-Daube, D.A. Geddes, C. Grengg, C. Le Galliard, M. Nedeljkovic, J.L. Provis, L. Valentini, B. Walkley, Carbonation rate of alkali-activated concretes and high-volume SCM concretes: a literature data analysis by RILEM TC 281-CCC, *Mater. Struct.* 55 (2022) 225. <https://doi.org/10.1617/s11527-022-02041-4>.

[272] A. Morandieu, M. Thiéry, P. Dangla, Investigation of the carbonation mechanism of CH and C-S-H in terms of kinetics, microstructure changes and moisture properties, *Cem. Concr. Res.* 56 (2014) 153–170. <https://doi.org/10.1016/j.cemconres.2013.11.015>.

[273] B. Wu, Carbonation of C-S-H gel and its Effects on the Carbonation Rate in Blended Cement Paste - An

Experimental and Modelling Study, 2023. <https://doi.org/10.4233/uuid>.

[274] M. Nedeljković, B. Ghiassi, S. van der Laan, Z. Li, G. Ye, Effect of curing conditions on the pore solution and carbonation resistance of alkali-activated fly ash and slag pastes, *Cem. Concr. Res.* 116 (2019) 146–158. <https://doi.org/10.1016/j.cemconres.2018.11.011>.

[275] P.H.R. Borges, J.O. Costa, N.B. Milestone, C.J. Lynsdale, R.E. Streatfield, Carbonation of CH and C-S-H in composite cement pastes containing high amounts of BFS, *Cem. Concr. Res.* 40 (2010) 284–292. <https://doi.org/10.1016/j.cemconres.2009.10.020>.

[276] H. Vanoutrive, P. Van den Heede, N. Alderete, C. Andrade, T. Bansal, A. Camões, Ö. Cizer, N. De Belie, V. Ducman, M. Etxeberria, L. Frederickx, C. Grengg, I. Ignjatović, T.-C. Ling, Z. Liu, I. Garcia-Lodeiro, B. Lothenbach, C. Medina Martinez, J. Sanchez-Montero, K. Olonade, A. Palomo, Q.T. Phung, N. Rebollo, M. Sakoparnig, K. Sideris, C. Thiel, T. Visalakshi, A. Vollpracht, S. von Greve-Dierfeld, J. Wei, B. Wu, M. Zajac, Z. Zhao, E. Gruyaert, Report of RILEM TC 281-CCC: outcomes of a round robin on the resistance to accelerated carbonation of Portland, Portland-fly ash and blast-furnace blended cements, *Mater. Struct.* 55 (2022) 99. <https://doi.org/10.1617/s11527-022-01927-7>.

[277] Q. Zhou, F.P. Glasser, Kinetics and mechanism of the carbonation of ettringite, *Adv. Cem. Res.* 12 (2000) 131–136. <https://doi.org/10.1680/adcr.2000.12.3.131>.

[278] T. Nishikawa, K. Suzuki, S. Ito, K. Sato, T. Takebe, Decomposition of synthesized ettringite by carbonation, *Cem. Concr. Res.* 22 (1992) 6–14. [https://doi.org/10.1016/0008-8846\(92\)90130-N](https://doi.org/10.1016/0008-8846(92)90130-N).

[279] H. Justnes, J. Skocek, T.A. Østnor, C.J. Engelsen, O. Skjølvold, Microstructural changes of hydrated cement blended with fly ash upon carbonation, *Cem. Concr. Res.* 137 (2020) 106192. <https://doi.org/10.1016/j.cemconres.2020.106192>.

[280] S. Miyata, Anion-Exchange Properties of Hydrotalcite-Like Compounds, *Clays Clay Miner.* 31 (1983) 305–311. <https://doi.org/10.1346/CCMN.1983.0310409>.

[281] A.K. Suryavanshi, R. Narayan Swamy, Stability of Friedel's salt in carbonated concrete structural elements, *Cem. Concr. Res.* 26 (1996) 729–741. [https://doi.org/10.1016/S0008-8846\(96\)85010-1](https://doi.org/10.1016/S0008-8846(96)85010-1).

[282] X. Ke, S.A. Bernal, J.L. Provis, Uptake of chloride and carbonate by Mg-Al and Ca-Al layered double hydroxides in simulated pore solutions of alkali-activated slag cement, *Cem. Concr. Res.* 100 (2017) 1–13. <https://doi.org/10.1016/j.cemconres.2017.05.015>.

[283] C.W. Hargis, B. Lothenbach, C.J. Müller, F. Winnefeld, Carbonation of calcium sulfoaluminate mortars, *Cem. Concr. Compos.* 80 (2017) 123–134. <https://doi.org/10.1016/j.cemconcomp.2017.03.003>.

[284] S. Walsperger, P.D. Cobden, O. V. Safonova, Y. Wu, E.J. Anthony, High CO₂ Storage Capacity in Alkali-Promoted Hydrotalcite-Based Material: In Situ Detection of Reversible Formation of Magnesium Carbonate, *Chem. – A Eur. J.* 16 (2010) 12694–12700. <https://doi.org/10.1002/chem.201000687>.

[285] K. Morimoto, S. Anraku, J. Hoshino, T. Yoneda, T. Sato, Surface complexation reactions of inorganic anions on hydrotalcite-like compounds, *J. Colloid Interface Sci.* 384 (2012) 99–104. <https://doi.org/10.1016/j.jcis.2012.06.072>.

[286] Y. Zhang, O. Çopuroğlu, The role of hydrotalcite-like phase and monosulfate in slag cement paste during atmospheric and accelerated carbonation, *Cem. Concr. Compos.* 132 (2022) 104642. <https://doi.org/10.1016/j.cemconcomp.2022.104642>.

[287] M. Palacios, F. Puertas, Effect of Carbonation on Alkali-Activated Slag Paste, *J. Am. Ceram. Soc.* 89 (2006) 3211–3221. <https://doi.org/10.1111/j.1551-2916.2006.01214.x>.

[288] A. Hidalgo, C. Domingo, C. Garcia, S. Petit, C. Andrade, C. Alonso, Microstructural changes induced in Portland cement-based materials due to natural and supercritical carbonation, *J. Mater. Sci.* 43 (2008) 3101–3111. <https://doi.org/10.1007/s10853-008-2521-5>.

[289] N. Mehta, J. Gaëtan, P. Giura, T. Azaïs, K. Benzerara, Detection of biogenic amorphous calcium carbonate (ACC) formed by bacteria using FTIR spectroscopy, *Spectrochim. Acta - Part A Mol. Biomol. Spectrosc.* 278 (2022) 121262. <https://doi.org/10.1016/j.saa.2022.121262>.

[290] D. Chakrabarty, S. Mahapatra, Aragonite crystals with unconventional morphologies, *J. Mater. Chem.* 9 (1999) 2953–2957. <https://doi.org/10.1039/a905407c>.

[291] N. Li, N. Farzadnia, C. Shi, Microstructural changes in alkali-activated slag mortars induced by accelerated carbonation, *Cem. Concr. Res.* 100 (2017) 214–226. <https://doi.org/10.1016/j.cemconres.2017.07.008>.

[292] X. Liu, P. Feng, Y. Cai, X. Yu, C. Yu, Q. Ran, Carbonation behavior of calcium silicate hydrate (C-S-H): Its potential for CO₂ capture, *Chem. Eng. J.* 431 (2022) 134243. <https://doi.org/10.1016/j.cej.2021.134243>.

[293] W. Cao, W. Yi, J. Peng, J. Li, S. Yin, Recycling of phosphogypsum to prepare gypsum plaster: Effect of calcination temperature, *J. Build. Eng.* 45 (2022) 103511. <https://doi.org/10.1016/j.jobe.2021.103511>.

[294] M. Thiery, G. Villain, P. Dangla, G. Platret, Investigation of the carbonation front shape on cementitious materials: Effects of the chemical kinetics, *Cem. Concr. Res.* 37 (2007) 1047–1058. <https://doi.org/10.1016/j.cemconres.2007.04.002>.

[295] G. Villain, M. Thiery, G. Platret, Measurement methods of carbonation profiles in concrete: Thermogravimetry, chemical analysis and gammadensimetry, *Cem. Concr. Res.* 37 (2007) 1182–1192. <https://doi.org/10.1016/j.cemconres.2007.04.015>.

[296] M. Nedeljković, Carbonation mechanism of alkali-activated fly ash and slag materials In view of long-term performance predictions, 2019. <https://doi.org/10.4233/uuid>.

[297] B. Chen, M. Horgnies, B. Huet, V. Morin, K. Johannes, F. Kuznik, Comparative kinetics study on carbonation of ettringite and meta-ettringite based materials, *Cem. Concr. Res.* 137 (2020) 106209. <https://doi.org/10.1016/j.cemconres.2020.106209>.

[298] F. Puertas, M. Palacios, T. Vázquez, Carbonation process of alkali-activated slag mortars, *J. Mater. Sci.* 41 (2006) 3071–3082. <https://doi.org/10.1007/s10853-005-1821-2>.

[299] M. Castellote, C. Andrade, X. Turrillas, J. Campo, G.J. Cuello, Accelerated carbonation of cement pastes in situ monitored by neutron diffraction, *Cem. Concr. Res.* 38 (2008) 1365–1373. <https://doi.org/10.1016/j.cemconres.2008.07.002>.

[300] B. Wu, G. Ye, Development of porosity of cement paste blended with supplementary cementitious materials after carbonation, *Constr. Build. Mater.* 145 (2017) 52–61. <https://doi.org/10.1016/j.conbuildmat.2017.03.176>.

[301] V. Shah, K. Scrivener, B. Bhattacharjee, S. Bishnoi, Changes in microstructure characteristics of cement paste on carbonation, *Cem. Concr. Res.* 109 (2018) 184–197. <https://doi.org/10.1016/j.cemconres.2018.04.016>.

[302] F. Georget, W. Wilson, K. Scrivener, edxia through the Glueviz interface, (2020) 1–10. <https://doi.org/https://doi.org/10.5281/zenodo.3686068>.

[303] J.E. Rossen, K.L. Scrivener, Optimization of SEM-EDS to determine the C–A–S–H composition in matured cement paste samples, *Mater. Charact.* 123 (2017) 294–306. <https://doi.org/10.1016/j.matchar.2016.11.041>.

[304] Y. Sargam, K. Wang, Quantifying dispersion of nanosilica in hardened cement matrix using a novel SEM-EDS and image analysis-based methodology, *Cem. Concr. Res.* 147 (2021) 106524. <https://doi.org/10.1016/j.cemconres.2021.106524>.

[305] Y. Zhang, The effect of blast furnace slag chemistry on carbonation characteristics of cement-slag systems, 2022. <https://doi.org/https://doi.org/10.4233/uuid:6732d452-5d85-4f06-a816-37d4e43f749b>.

[306] B. Johannesson, P. Utgenannt, Microstructural changes caused by carbonation of cement mortar, *Cem. Concr. Res.* 31 (2001) 925–931. [https://doi.org/10.1016/S0008-8846\(01\)00498-7](https://doi.org/10.1016/S0008-8846(01)00498-7).

[307] H. Vanourtrive, P. Minne, I. Van de Voorde, Ö. Cizer, E. Gruyaert, Carbonation of cement paste with GGBFS: Effect of curing duration, replacement level and CO₂ concentration on the reaction products and CO₂ buffer capacity, *Cem. Concr. Compos.* 129 (2022). <https://doi.org/10.1016/j.cemconcomp.2022.104449>.

[308] M. Schneider, M. Romer, M. Tschudin, H. Bolio, Sustainable cement production-present and future, *Cem. Concr. Res.* 41 (2011) 642–650. <https://doi.org/10.1016/j.cemconres.2011.03.019>.

[309] M.A. Ilgin, S.M. Gupta, Environmentally conscious manufacturing and product recovery (ECMPRO): A review of the state of the art, *J. Environ. Manage.* 91 (2010) 563–591. <https://doi.org/10.1016/j.jenvman.2009.09.037>.

[310] M. Buyle, J. Braet, A. Audenaert, Life cycle assessment in the construction sector: A review, *Renew. Sustain. Energy Rev.* 26 (2013) 379–388. <https://doi.org/10.1016/j.rser.2013.05.001>.

[311] X. Li, Y. Zhu, Z. Zhang, An LCA-based environmental impact assessment model for construction processes, *Build. Environ.* 45 (2010) 766–775. <https://doi.org/10.1016/j.buildenv.2009.08.010>.

[312] O. Ortiz, F. Castells, G. Sonnemann, Sustainability in the construction industry: A review of recent developments based on LCA, *Constr. Build. Mater.* 23 (2009) 28–39. <https://doi.org/10.1016/j.conbuildmat.2007.11.012>.

[313] NEN-EN 196-3 Methods of testing cement - Part 3: Determination of setting times and soundness, 2016.

[314] NEN-EN 196-1 Methods of testing cement - Part 1: Determination of strength, 2016.

[315] C.F. Lin, C.H. Wu, H.M. Ho, Recovery of municipal waste incineration bottom ash and water treatment sludge to water permeable pavement materials, *Waste Manag.* 26 (2006) 970–978. <https://doi.org/10.1016/j.wasman.2005.09.014>.

[316] B. Robert, E.B. Brown, *Handbook on Life Cycle Assessment: Operational Guide to the ISO Standards*, Springer Netherlands, Dordrecht, 2002. <https://doi.org/10.1007/0-306-48055-7>.

[317] NIBE B.V., Environmental Product Declaration (EPD) Database for the Netherlands Market, (n.d.).

[318] J. Schmidt, S. Merciai, M. Thrane, R. Dalgaard, Inventory of country specific electricity in LCA-Consequential and attributional scenarios., Aalborg, 2011.

[319] Fly Ash Dryer: All things you need to know, (2023). <https://www.mortarplant.com/fly-ash-dryer-all-things-you-need-to-know/>.

[320] GGBS Production Line, (n.d.). <https://cementplantsupplier.com/cement-solutions/ggbs-production-line/>.

[321] Automatic interlocking brick machine compressed interlocking clay earth mud bricks making machine, (n.d.). https://www.alibaba.com/product-detail/automatic-interlocking-brick-machine-compressed-interlocking_1600603148224.html?spm=a2700.7724857.0.0.507910719F16UO.

[322] Milieudatabase Stichting Nationale, Rekenregels en richtlijnen bepaling Milieuprestatie Bouwwerken, 0 (2021) 1–27. https://milieudatabase.nl/wp-content/uploads/2021/11/Rekenregels_en_richtlijnen_deel_1_november_2021-1.pdf.

[323] S. Zhang, Q. Feng, D. Wang, G. Ye, Environmental Impact Evaluation of a Slag/Fly Ash-Based Strain Hardening Geopolymer Composite (SHGC), in: SP-349 11th ACI/RILEM Int. Conf. Cem. Mater. Altern. Bind. Sustain. Concr., American Concrete Institute, 2021. <https://doi.org/10.14359/51732779>.

[324] Y. Li, Y. Liu, X. Gong, Z. Nie, S. Cui, Z. Wang, W. Chen, Environmental impact analysis of blast furnace slag applied to ordinary Portland cement production, *J. Clean. Prod.* 120 (2016) 221–230. <https://doi.org/10.1016/j.jclepro.2015.12.071>.

[325] Y. Kim, A. Hanif, M. Usman, M.J. Munir, S.M.S. Kazmi, S. Kim, Slag waste incorporation in high early strength concrete as cement replacement: Environmental impact and influence on hydration & durability attributes, *J. Clean. Prod.* 172 (2018) 3056–3065. <https://doi.org/10.1016/j.jclepro.2017.11.105>.

[326] Y.M. Zhang, T.J. Napier-Munn, Effects of particle size distribution, surface area and chemical composition on Portland cement strength, *Powder Technol.* 83 (1995) 245–252. [https://doi.org/10.1016/0032-5910\(94\)02964-P](https://doi.org/10.1016/0032-5910(94)02964-P).

[327] I.B. Celik, M. Oner, N.M. Can, The influence of grinding technique on the liberation of clinker minerals and cement properties, *Cem. Concr. Res.* 37 (2007) 1334–1340. <https://doi.org/10.1016/j.cemconres.2007.06.004>.

Acknowledgements

This PhD program is supported by China Scholarship Council (CSC), for which I am deeply grateful.

It is a long but short journey. Although I took more time than expected to complete my PhD, I can still vividly recall my first morning arriving in Delft as if it were today. All things would eventually come to an end, no matter good or bad. Doing a PhD has been not only about research but also a process of self-discovery, through different experiences and people. There are too many memories with people I encountered with, whom I would need to show my sincere acknowledgements.

First and foremost, I would like to express my sincere acknowledgements to my promoter, Prof. Guang Ye, for giving me the opportunity to work on a doctoral project in the CMMB group. Thank you for providing me an open environment that allowed me to conduct research with great freedom. I am grateful for your guidance and constructive comments, which significantly improved my thesis. Working with you has inspired me in aspects, your rigorous attitudes towards scientific work will serve as a model in my future career.

My deep acknowledgements also go to my promoter, Prof. Erik Schlangen, for your insightful comments and suggestions on both my research and thesis. Since much of my research took place in Microlab, I am grateful for your organization in Microlab, providing such a wonderful lab environment, where I truly enjoyed working.

I also extend my sincere thanks to Dr. Hua Dong, who acted as my daily supervisor throughout my PhD journey. You were always willing to help, providing valuable suggestions on my project. Your critical thinking and efficient working attitude greatly influenced me.

I am thankful to all of my committee members and the chairman for their time in reviewing my thesis, offering valuable feedback, and attending my PhD defence.

My gratitude extends to Dr. Mladena Luković and Dr. Gabrie Meesters, who attended my Go-No-Go meeting, providing helpful suggestions and comments.

Special thanks go to Prof. Mirja Illikainen for hosting me a short visit to the University of Oulu. I am grateful to Dr. Katja Kilpimaa for her support in Oulu, and to Patrick Lemounga Ninla, Elijah Damilola Adesanya, Hoang Nguyen, He Niu for the enjoyable discussions and help in the lab. This visit was funded by ADAM2, to which I am also thankful.

I deeply appreciate the help from the Microlab technicians. Maiko, you are the most energetic person in the lab, always full of passion, and always caring for our safety. Thank you for organizing activities and drinks at PSOR, which brought the Microlab community together. John, thank you for assisting me during experiments, especially with ICP test handling numerous samples. Arjan, I am grateful for your help with BSE-EDS mapping, which involved hundreds of tests. Ton, I am grateful for your assistance in the casting room whenever I need, and your early morning help with pore solutions extractions, often starting at 7 a.m.

I also appreciate the secretarial team: Jaap Meijer, Claire de Bruin, Jacqueline Bergenhenegouwen, Iris Nederhof-van Woggelum, and Sandra Schuchmann-Hagman for your support and efforts in providing us a comfortable working environment.

Special thanks to my first officemates in 6.72: Yong Zhang, Hao Huang, Farhad Pargar, Gabriel Hoder, and Marija Nedeljkovic for your warm welcome and for sharing your PhD experience. Later, in 6.06, I enjoyed working with Hongzhi Zhang, Wenjuan Lyu, Shi Xu, Xingliang Yao, Zhi Wan, Guilherme da Silva Munhoz, Jinbao Xie, and Jeroen van Oosten. A special acknowledgment goes to Zhi Wan for our shared coffee (liquor) breaks and laughter, and to Guilherme for organizing our office dinners and parties, sharing ideas and happiness.

I would like to express my deep thanks to the Microlabers, with a special shout-out to CMMB group. My thanks go to Zhenming Li, who gave me a tour when I joined in the lab and taught me some lab equipment in my first year. We had much fun in collaborations, discussions, and sports. Besides your accomplishment in research so far, your talents in crosstalk are also impressive. Yun Chen, Chen Liu, and Hu Shi, thank you for the research collaboration and for the friendship that has brought so many joyful moments. My appreciation goes to Jiayi Chen for his help with image analysis, and I also thank Shizhe Zhang, Boyu Chen, Luiz Miranda de Lima Junior, Shan He, and Yu Zhang for engaging discussions on research topics. Sep Hesselmans is acknowledged for summary translation into Dutch. My acknowledgements go to my colleagues in Microlab: Prof. Klaas van Breugel, Dr. Oguzhan Copuroglu, Dr. Branko Šavija, Dr Mohammad Fotouhi, Dr. Gozde Ozerkan, Dr. Dessi Koleva, Zhiwei Qian, Tianshi Lu, Bei Wu, Xuliang Hou, Mayank Gupta, Fernando Mendonca Filho, Emanuele Rossi, Yidong Gan, Yu Chen, Yibing Zuo, Yask Kulshreshtha, Bart Hendrix, Jeannette van den Bos, Max Veeger, Ze Chang, Albina Kostiuchenko, Wen Zhou, Rowin Bol, Zhaozheng Meng, Burcu Aytekin Turkoglu, Zhiyuan Xu, Yading Xu, Claudia Romero Rodriguez, Ameya Kamat, Farnaz Aghabeyk, Minfei Liang, Anne Linde van Overmeir, Patrick Holthuizen, Ali Ghaderiaram, Irving Alfredo Flores Beltran, Yu Zeng, Haoming Wu, Eyüphan Küçükalfa, and Sebastian Kuniewski. Thanks for your support and friendship. Each coffee break chat, cake sharing, and snack strengthened my workday.

I would like to thank Mineralz for the research funding support, as well as colleagues: Rob Bleijerveld, Marc Brito van Zijl, and Jens Ruijg, for engaging in research discussions and sharing insights from an industry perspective.

I would like to thank everyone I met outside of my PhD work. Xiaohui Liang and Bo Li, you were the first friends I met when I arrived in Delft, and we shared memorable times talking, playing games, and even attempting the gym (even though it lasted only two months). Thanks for your friendship and time together. I am grateful for joyful moments with friends Xiuli Wang, Yitao Huang, Lu Cheng, Pei He, Lubin Huo, Chi Jin, Fanxiang Xu, and Miao Fu. Thank you for enriching my leisure time.

I want to express my gratitude to my family. Thanks for your unconditional love, supports and understanding. I wish that my two grandfathers would be happy to attend my defence ceremony, if they ever could.

Lastly, I would like to express my heartfelt gratitude to my wife, Yaowen. I am incredibly lucky to have you in my life, sharing both happiness and sorrow together. Despite the many years of long-distance relationship, your support and love have been my source of strength, helping me to get through whatever I encountered. I believe that distance will no longer be a part of our lives in our coming future, and I am excited to explore the world with you.

Xuhui Liang, Oct 2024, in Delft

Curriculum Vitae

Name: Xuhui LIANG (梁旭輝)
Date of Birth: 12 April 1993
Email: xhliang0412@gmail.com

09/2018 – 12/2024	PhD candidate Microlab, Faculty of Civil Engineering and Geoscience Delft University of Technology
11/2019 – 12/2019	Visiting researcher Fibre and Particle Engineering, Faculty of Technology University of Oulu
09/2015 – 06/2018	Master of Science School of Materials Science and Engineering Chongqing University
09/2011 - 06/2015	Bachelor of Engineering School of Chemistry and Chemical Engineering Guizhou University

Propositions

accompanying the dissertation

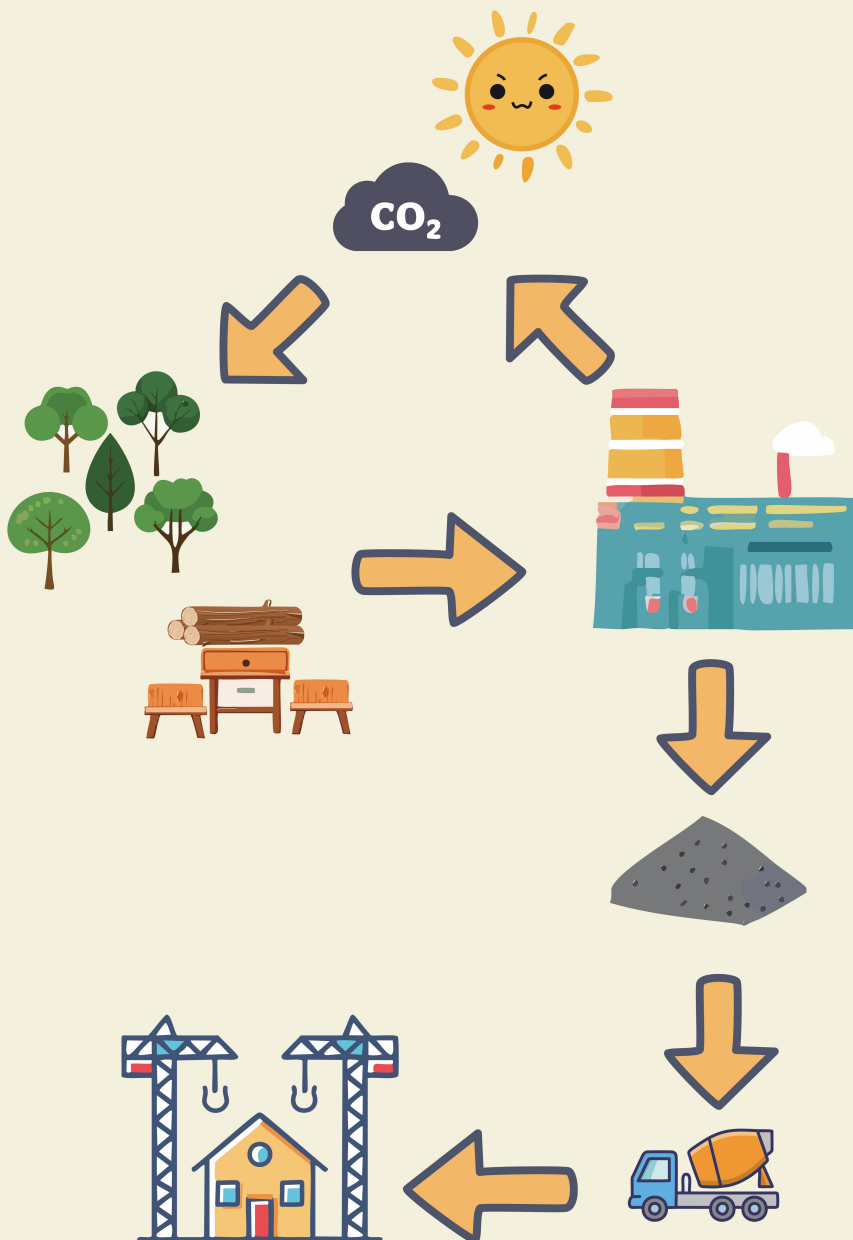
Valorization of Wood Biomass Fly Ash for the Development of Sustainable Low-carbon Cementitious Materials

By

Xuhui LIANG

1. The term 'by-product' should be used for wood biomass fly ash instead of 'industrial waste' when it is used in the construction industry. (This proposition pertains to this dissertation)
2. Government decisions and commercial interests, rather than solely research results, determine the roadmap for the valorization of industrial by-products. (This proposition pertains to this dissertation)
3. Enhancing a particular property in cementitious materials often involves the trade-offs with other properties, much like our life.
4. All knowledge is provisional, temporary, capable of refutation at any moment (Karl Popper)
5. Trial and error impart more insights than literature alone.
6. The greater your knowledge, the humbler you become.
7. Acknowledging limitations holds more significance than simply recognizing accomplishments.
8. Emotion management is more crucial than time management when pursuing a PhD.

These propositions are regarded as opposable and defendable, and have been approved by the promoters Prof.dr. G. Ye and Prof.dr.ir. E. Schlangen



9 789463 846769